REPUBLIQUE ALGERIENNE DEMOCRATIQUE ET POPULAIRE
Ministère de l'Enseignement Supérieur et de la Recherche Scientifique

École Nationale Polytechnique
Département de Génie Chimique

Université de Sherbrooke
Faculté de génie

Département de Génie Chimique et de Génie Biotechnologique

Thèse de Doctorat en cotutelle

En Génie Chimique

Présenté par :

Abir AZARA

PRODUCTION DE NANOFILAMENTS DE CARBONE À PARTIR DE GAZ PRODUIT PAR PYROLYSE DES DÉCHETS PLASTIQUES, EN UTILISANT UNE NOUVELLE CONFIGURATION DE RÉACTEUR

Soutenue le 15 novembre 2022 devant le jury composé de :

Roch Lefebvre (président, professeur titulaire à l'UdeS)

Nicolas ABATZOGLOU (Directeur, professeur titulaire à l'UdeS)

François GITZHOFER (Codirecteur, professeur associé à l'UdeS)

El Hadi BENYOUSSEF (Codirecteur, professeur à l'ENP)

Faroudja MOHELLEBI (Codirectrice, professeure à l'ENP)

Fairouz KIES (Évaluatrice, maitre de conférences à l'ENP)

Grégory PATIENCE (Évaluateur, professeur titulaire à Polytechnique Montréal)

Federico GALLI (Rapporteur, professeur adjoint à l'UdeS)

ENP 2022

REPUBLIQUE ALGERIENNE DEMOCRATIQUE ET POPULAIRE
Ministère de l'Enseignement Supérieur et de la Recherche Scientifique

École Nationale Polytechnique
Département de Génie Chimique

Université de Sherbrooke
Faculté de génie

Département de Génie Chimique et de Génie Biotechnologique

Thèse de Doctorat en cotutelle

En Génie Chimique

Présenté par :

Abir AZARA

PRODUCTION DE NANOFILAMENTS DE CARBONE À PARTIR DE GAZ PRODUIT PAR PYROLYSE DES DÉCHETS PLASTIQUES, EN UTILISANT UNE NOUVELLE CONFIGURATION DE RÉACTEUR

Soutenue le 15 novembre 2022 devant le jury composé de :

Roch Lefebvre (président, professeur titulaire à l'UdeS)

Nicolas ABATZOGLOU (Directeur, professeur titulaire à l'UdeS)

François GITZHOFER (Codirecteur, professeur associé à l'UdeS)

El Hadi BENYOUSSEF (Codirecteur, professeur à l'ENP)

Faroudja MOHELLEBI (Codirectrice, professeure à l'ENP)

Fairouz KIES (Évaluatrice, maitre de conférences à l'ENP)

Grégory PATIENCE (Évaluateur, professeur titulaire à Polytechnique Montréal)

Federico GALLI (Rapporteur, professeur adjoint à l'UdeS)

ENP 2022

ملخص باللغة العربي

المشروع الذي هو موضوع هذه الدكتوراه هو جزء من مشروع كبير بين جامعة شير بروك والعديد من الشركاء الصناعيين.

الهدف العام للمشروع هو تطوير وتوسيع نطاق عملية تصنيع ألياف الكربون النانوية من الغازات الناتجة عن الانحلال الحراري للنفايات البلاستيكية. تحقيقا لهذه الغاية، تم تطوير مفاعل جديد واختباره على نطاق تجريبي. تعتمد العملية على استخدام البوليمرات غير القابلة لإعادة التدوير (التي يتم دفنها أو حرقها) كمواد وسيطة لإنتاج غاز سيتم استخدامه كمادة وسيطة في المفاعل الجديد لإنتاج ألياف الكربون النانوية وذلك عن طريق عزل ثاني أكسيد الكربون.

يعتبر عزل ثاني أكسيد الكربون، أحد غازات الدفيئة، على شكل ألياف الكربون النانوية، الفائدة الأكثر إثارة للاهتمام. من ناحية أخرى، تعتبر ألياف الكربون النانوية عاملًا رئيسيًا في الجدوى الاقتصادية للعملية على نطاق صناعي، نظرًا لخصائصها الرائعة، وهي: التوصيل الكهربائي، والتوصيل الحراري، والمقاومة الميكانيكية.

تم تطوير واختبار مفاعل تصنيع ألياف الكربون النانوية خلال هذا المشروع. يمر التطوير بعدة مراحل، وهي: تصميم المفاعل وتصنيعه وتركيب المعدات وربطها وبدء العملية وأداء الاختبارات وفق بروتوكول أمان. فضلا عن التدخل لحل مشاكل التشغيل المختلفة.

تم إجراء تفاعل إعادة التكوين الجاف في المفاعل الجديد عند 600 درجة مئوية، باستخدام 500 جم من المحفز. تم استخدام الإيثيلين كغاز تمثيلي للغاز الناتج عن الانحلال الحراري للنفايات البلاستيكية، نظرًا لأن الأخير يتكون أساسًا من الهيدروكربونات غير المشبعة.

بالرغم من حدوث بعض المشكلات، فإن النتائج التجريبية الأولية لتشغيل المفاعل بالإيثيلين التي تم الحصول عليها واعدة للغاية وتؤكد قابلية تشغيل العملية. التحسينات ضرورية من أجل العمل بشكل مستمر لفترة أطول والوصول إلى إنتاج 1 كجم / ساعة من ألياف الكربون النانوية.

الكلمات الرئيسية: المواد النانوية، ألياف الكربون النانوية، نفايات البلاستيك، إعادة تدوير البوليمر، الحفز، هندسة الطرائق، هندسة كيميائية

Résumé en anglais

The project that is the subject of this PhD is part of the NanoF-PoRes project, which is a major synergistic project between the University of Sherbrooke and several partners, namely: PRIMA Quebec, KWI Polymers and Soleno.

The overall objective of the project is the development and scaling up of a process for the synthesis of carbon nanofilaments from the products of plastic waste pyrolysis. To this end, new reactor configurations have been developed and tested on a pilot scale. The process is based on the use of non-recyclable polymers (which are landfilled) as raw materials to produce synthesis gas which will be used as raw material in the new reactor where it will go through a dry reforming reaction to produce carbon nanofilaments. The sequestration of CO_2, a greenhouse gas, in the form of carbon, seems to be one of the most interesting benefits of the dry reforming reaction of carbonaceous gases. Regarding carbon nanofilaments, they are considered to be the key factor in the economic feasibility of the process on an industrial scale, due to their remarkable properties, namely electrical conductivity, thermal conductivity, and mechanical resistance.

The carbon nanofilaments synthesis kg-lab reactor was developed and tested during this project. The development and scale-up go through several steps, namely the design of the reactor, its manufacture, the installation of equipment, start-up of the process and the performance of tests according to a standard operability protocol as well as troubleshooting.

The dry reforming reaction is carried out in the reactor at 600 °C, using 500 g of catalyst deposited inside the reactor. Ethylene was used as a surrogate molecule of the gas produced from the pyrolysis of plastic waste, since the latter is mainly composed of unsaturated hydrocarbons.

Although some problems have occurred, the preliminary experimental results of the operation of the reactor with ethylene obtained so far are very promising and confirm the operability of the process. Improvements are necessary in order to operate continuously and for longer time in order to reach a production of 1kg/h of carbon nanofilaments.

Key words: Nanomaterials, Carbon Nanofilaments, Waste plastics, Polymers Recycling, Catalysis, Process Engineering, Dry Reforming.

Résumé en français

Le projet qui fait l'objet de ce Doctorat fait partie d'un grand projet « NanoF-PoRes » synergique entre l'université de Sherbrooke et plusieurs partenaires à savoir : PRIMA Québec, KWI Polymers et Soleno.

L'objectif global du projet est le développement et la mise à l'échelle d'un procédé de synthèse de nanofilaments de carbone à partir de gaz produits par pyrolyse des déchets plastiques. À cet effet, une nouvelle configuration de réacteur a été développée et testée à échelle pilote. Le processus est basé sur l'utilisation des polymères non recyclables (qui sont mis en décharge ou incinérés) comme matières premières pour produire le gaz de synthèse qui sera utilisé comme matière première dans le nouveau réacteur où il est reformé à sec pour produire les nanofilaments de carbone. La séquestration du CO_2, un gaz à effet de serre, sous forme de nanofilaments de carbone est le bénéfice le plus intéressant de la réaction de reformage à sec des gaz carbonés. Les nanofilaments de carbone, quant à eux, sont considérés comme le facteur clé de la faisabilité économique du procédé à l'échelle industrielle, en raison de leurs propriétés remarquables à savoir : la conductivité électrique, la conductivité thermique et la résistance mécanique.

Le réacteur kg-lab de synthèse de nanofilaments de carbone a été développé et testé au cours de ce projet. Le développement et la mise à l'échelle passent par plusieurs étapes que sont : la conception du réacteur, sa fabrication, l'installation des équipements et leur raccordement, la mise en marche du procédé et la réalisation des tests selon un protocole de sécurité ainsi que l'intervention pour régler les différents problèmes de fonctionnement.

La réaction de reformage à sec a été conduite dans le nouveau réacteur à 600 °C, en utilisant 500 g de catalyseur déposé à l'intérieur du réacteur. L'éthylène a été utilisé comme molécule représentative du gaz produit par pyrolyse des déchets plastiques, étant donné que ce dernier est composé majoritairement d'hydrocarbures insaturés.

Même si quelques problèmes sont survenus, les résultats expérimentaux préliminaires du fonctionnement du réacteur avec de l'éthylène obtenus sont très prometteurs et confirment l'opérabilité du procédé. Des améliorations s'avèrent nécessaires afin de fonctionner en continu plus longtemps et d'atteindre une production de 1kg/h de nanofilaments de carbone.

Mots-clés : Nanomatériaux, Nanofilaments de carbone, Déchets plastiques, Recyclage des polymères, Catalyse, Génie des procédés, Reformage à sec.

Remerciements

Mes remerciements s'adressent en premier lieu à mon Dieu pour m'avoir donné, l'esprit et les moyens d'arriver à ce stade de connaissance.

Je tiens à remercier mes superviseurs, les professeurs : Nicolas Abatzoglou, François Gitzhofer, El Hadi Benyoussef et la professeure Faroudja Mohellebi qui m'ont accompagnée tout au long de cette recherche avec beaucoup de patience, de pédagogie et d'engagement. Qu'ils trouvent ici, l'expression de ma gratitude, de ma reconnaissance éternelle et de ma profonde admiration pour leurs qualités scientifiques et humaines, pour leurs disponibilités et leurs conseils avisés. C'est à la fois un privilège et une expérience exceptionnelle d'avoir bénéficié de leurs savoirs.

Je remercie vivement le professeur Federico Galli de l'université de Sherbrooke, le professeur Grégory Patience de l'École Polytechnique de Montréal et madame Fairouz Kies maitre de conférences à l'École Polytechnique d'Alger, qui ont bien voulu me faire l'honneur de participer au jury et pour le temps qu'ils ont accordé à l'évaluation de ce travail.

Mes remerciements s'adressent également à nos partenaires industriel, M. Yves Laroche, M. Pierre Breton, et surtout Docteur Jasmin Blanchard, dont j'ai bénéficié des conseils et de l'expérience tout au long de ce projet.

Un grand merci s'adresse à tous les membres du GRTP, les professeurs Inès Esma Achouri et Ryan Gosselin pour leur support scientifique ; les techniciens : Jacque Gagné, Shahram Navaee Ardeh, Alexandre Couture, Marc couture et Henri Gauvin pour leur support technique ; et mes collègues : Salma Belbessai, Mostafa Chamoumi, Frank Blondel, James Aloha, Abdullah Ly, Komlan Koumbogle, Yuwei Zhang et tous les nouveaux étudiants qui se sont joints au groupe. Grâce à eux, mon parcours de Doctorat était plus détendu, plus agréable et plus enrichissant.

J'exprime aussi toute ma reconnaissance à tous les enseignants et le personnel des départements du Génie Chimique de l'École Nationale Polytechnique d'Alger et de l'Université de Sherbrooke qui ont contribué à ma formation avec beaucoup de compétence et de dévouement. Je remercie particulièrement le personnel de la plateforme de recherche et d'analyses des matériaux de l'université de Sherbrooke, dont Stéphane Gutierrez, Charles Bertrand, Carl St-Louis et Sonia Blais.

Mon plus grand merci revient naturellement à ma famille, et plus particulièrement à mes parents et mon mari pour leurs encouragements et leur soutien tout au long de mon cursus universitaire.

Je remercie chaleureusement sans les citer, toutes les personnes qui m'ont soutenue et qui ont aussi contribué, de près ou de loin, à la concrétisation de ce travail.

Table des matières

Liste des tableaux

Liste de figures

Liste des acronymes

ASME	American Society of Mechanical Engineers
ATG	Analyse thermogravimétrique
BE	Barrières de sécurité existantes
BET	Brunauer-Emmett-Teller
CC	Craquage catalytique
CP	Conséquences potentielles
DCI	Diamètre du cylindre interne
DEX	Spectrométrie de rayons X à dispersion d'énergie
DR	Dry reforming (reformage à sec)
DR	Diamètre du réacteur
DRF	Degré de résistance au feu
DRX	Diffraction des rayons X
DS	Diamètre de sortie
EPI	Équipements de protection individuelle
HCI	Hauteur du cylindre intérieur
HR	Hauteur du réacteur
HS	Hauteur de la sortie
HTS	Hauteur de tombée de solides
ICFB	Internal Circulating Fluidized Bed (lit fluidisé de circulation interne)
LES	Limite supérieure d'explosivité
LIE	Limite inférieure d'explosivité
MEB	Microscopie électronique à balayage
MET	Microscopie électronique à transmission
NFC	Nanofilaments de carbone
NTC	Nanotubes de carbone
RBA	Recommandations de barrières de sécurité additionnelles
RLE	Recommended Limit Exposure (limite d'exposition recommandée)
RPT	Réduction programmée de température
VECD	Valeur d'exposition de courte durée
VEMP	Valeur d'exposition moyenne pondérée

Note : les abréviations anglaises sont dans les corps des articles.

CHAPITRE 1
INTRODUCTION

CHAPITRE 1 INTRODUCTION

1.1 Mise en contexte et problématique

Le CO_2, gaz à effet de serre, contribue grandement au réchauffement de la terre ainsi qu'au changements climatiques ce qui présente une grande menace pour l'environnement. Plusieurs études ont été menées afin de trouver un moyen pour réduire son taux dans l'atmosphère. Parmi ces moyens, la capture ou la séquestration du CO_2 a connu un grand essor. Il existe plusieurs types de séquestration : géologique, artificielle et chimique. L'une des voies chimiques largement étudiée consiste en la séquestration du CO_2 sous forme de nanofilaments de carbone (NFC) en utilisant le procédé de reformage à sec. D'autres parts, la consommation de matières plastiques dans le monde ne fait qu'augmenter, ce qui s'accompagne d'une augmentation drastique des déchets plastiques dont la gestion est devenue incontournable. Le recyclage mécanique est la principale solution pour le traitement de ces déchets. Les déchets non recyclables mécaniquement sont traités par plusieurs voies à savoir : l'incinération ou l'enfouissement, ce qui est nuisible à l'environnement. La voie chimique présente une excellente alternative à l'enfouissement et à l'incinération. Elle consiste à convertir les déchets plastiques par réaction chimique comme la gazéification ou la pyrolyse puis le reformage à sec, en produits chimiques à valeur ajoutée, tels que le gaz de synthèse et les NFC. Le gaz de synthèse composé principalement de CO et de H_2 constitue un élément de base dans l'industrie chimique, il est utilisé pour la production d'hydrogène et la synthèse de Fischer Tropsch. Ce gaz peut être aussi utilisé pour combler les besoins énergétiques du procédé rendant ainsi le procédé rentable et autosuffisant. Les NFC sont considérés comme le facteur clé de la faisabilité économique du processus à l'échelle industrielle, grâce à leur grande valeur. Les premières recherches pour la production des NFC ont été motivées par le besoin d'inhiber la croissance de ce carbone en raison des problèmes causés par son accumulation sur le catalyseur à savoir : le blocage du réacteur, la réduction des propriétés de transfert de chaleur et la désactivation du catalyseur (Baker & Albright, 1983). Des études subséquentes ont démontré que les NFC possèdent des propriétés intéressantes qui comprennent une résistance mécanique, une conductivité électrique et une conductivité thermique élevées. Il a été démontré qu'ils peuvent être utilisés comme additifs dans des matrices polymériques pour améliorer leurs propriétés, remplaçant ainsi les additifs

onéreux et couteux qui sont utilisés actuellement pour l'amélioration des propriétés des polymères. En plus, les NFC devraient permettre une réduction du matériau requis pour produire une résistance et une rigidité donnée, fournissant ainsi un poids léger des matrices polymériques. Ce sont ces caractéristiques qui ont stimulé les efforts de recherche pour optimiser et contrôler la formation de ce type de carbone (Baker, 2016). Le groupe de recherche GRTP s'est intéressé depuis des années à la production des nanofilaments de carbone à partir du reformage à sec de différents types d'alimentations (Blanchard et al., 2008; Jankhah et al., 2008a; Jankhah et al., 2008b). Dans le cadre de ce projet de Doctorat, un nouveau type d'alimentation, se présentant sous la forme d'un gaz produit par pyrolyse des déchets plastiques, sera reformé à sec pour produire les NFC. Par conséquent, ce procédé pourrait faire face à une problématique à la fois économique et environnementale.

Les réacteurs utilisés pour ce type de réaction sont multiples, du lit fixe au lit fluidisé, passant par les réacteurs rotatifs et ceux à membrane. La réaction de reformage est endothermique et nécessite un grand apport en énergie ce qui reste un défi majeur de la faisabilité économique du processus à grande échelle. L'utilisation des réacteurs à lits fixe présente un inconvénient majeur, en effet, les quantités de carbone déposées sur le catalyseur provoquent le blocage dans le réacteur nécessitant ainsi des arrêts fréquents du processus. Le développement d'un réacteur avec une conception appropriée fonctionnant en mode continu, permettant l'addition, le retrait du catalyseur et la récupération facile du carbone déposé est indispensable en termes industriels. Au cours de la dernière décennie, l'attention s'est portée sur l'étude des réacteurs à lit fluidisé en raison de la facilité de récupération des NFC et de leurs excellentes propriétés de transfert de chaleur et de masse. Cependant, ce type de réacteur présente aussi des problèmes. Au cours du processus, la grande variation de la densité du lit dans le réacteur, l'attrition des particules de catalyseur et la rupture des structures carbonées ont été clairement mises en évidence par (Pinilla et al., 2009; Pirard et al., 2013). Pour pallier ces problèmes, les chercheurs se sont penchés alors sur le développement de nouveaux réacteurs pour que le procédé de reformage puisse être réalisé industriellement. Le but de ce projet s'inscrit dans le cadre de cette optique.

1.2 Définition du projet de recherche

Les réacteurs déjà utilisés pour la réaction de reformage à sec et la réaction de production des NFC, sont fiables à l'échelle laboratoire, mais présentent beaucoup d'inconvénients qui rendent ce processus non faisable à échelle industrielle. La réaction de reformage à sec de l'éthylène, donnée par l'équation (1.1), est fortement endothermique et la chaleur doit être fournie uniformément.

$$C_2H_4 + 2CO_2 \rightarrow 4CO + 2H_2 \quad (\Delta H_{298} = 292.5 \text{ MJ/kmol}) \quad (1.1)$$

D'autres réactions peuvent avoir lieu également, à savoir les réactions de (1.2) à (1.5) :

Décomposition de l'éthylène :

$$C_2H_4 \rightarrow 2C + 2H_2 \quad (\Delta H\_298 = -52.5 \text{ MJ/kmol}) \quad (1.2)$$

Réaction inverse du gaz à l'eau :

$$CO_2 + H_2 \rightleftharpoons CO + H_2O \quad (\Delta H\_298 = 41.0 \text{ MJ/kmol}) \quad (1.3)$$

Réaction du Boudouard :

$$2CO \rightleftharpoons CO_2 + C \quad (\Delta H\_298 = -172.0 \text{ MJ/kmol}) \quad (1.4)$$

Réaction du gazéification du carbone :

$$C + H_2O \rightarrow CO + H_2 \quad (\Delta H\_298 = 131.3 \text{ MJ/kmol}) \quad (1.5)$$

À petite échelle, le transfert de chaleur est simple et peut se faire électriquement. À grande échelle, le transfert de chaleur devient un défi majeur. Un autre problème réside dans la récupération des nanofilaments de carbone. Cette difficulté se rencontre en particulier dans les réacteurs à lit fixe. Avdeeva et al (Avdeeva et al., 2004) ont utilisé une technique de séparation des NFC du reste du catalyseur qui consiste en l'élimination de toutes les particules de catalyseur métallique présentes dans les fibres par attaque acide avec du HCL et ce, pendant 72h. Ensuite, les échantillons récupérés ont été soigneusement lavés à l'eau distillée et séchés à 110 °C. Blanchard et al. (Blanchard et al., 2008), ont utilisé un réacteur ayant un lit sous forme de feuillets d'acier convenablement positionnés à l'intérieur du réacteur (sous forme d'étoile verticale) pour faire la réaction de reformage à sec de l'éthanol et produire des NFC. Une telle configuration permet la récupération facile des NFC qui peut se faire mécaniquement après l'arrêt de la réaction qui est défini par la perte de charge dans le lit. La nouvelle configuration du réacteur qui comprend un lit fluide et un lit mobile

semblerait être efficace pour pallier le problème de la récupération des NFC. En effet, l'avantage de la nouvelle configuration serait la récupération facile des NFC, sans altérer la réactivité du catalyseur, car le détachement des NFC formés des particules du catalyseur se fait mécaniquement pendant la phase du lit jaillissant. Les NFC détachés sont entrainés avec l'effluent gazeux à la sortie du réacteur puis sont filtrés pour être ensuite récupérés par des impulsions de gaz. Un autre avantage de cette configuration serait aussi la maximisation de la production de NFC grâce au contact continu du gaz réactif avec les particules du catalyseur. Encore plus, la section du lit fluidisé favorise les échanges de chaleur et de matière ce qui assure l'uniformité de la température et l'homogénéité du matériau formé. L'éthylène est utilisé comme molécule modèle représentative du gaz produit lors de la pyrolyse des déchets plastiques. Sa réaction avec le CO_2 en présence du catalyseur et en utilisant les conditions opératoires convenables, donnerait lieu à la formation des NFC. Ces derniers ont des propriétés thermiques, électriques et mécaniques remarquables. Une fois introduits dans des matrices polymériques, ils amélioreraient leurs propriétés.

Dans le cadre de ce projet, un nouveau type d'alimentation, se présentant sous la forme d'un gaz produit par pyrolyse des déchets plastiques, sera reformé à sec pour produire les NFC et ce, en utilisant une nouvelle configuration de réacteur qui comporte un lit mobile et un lit fluide. Grâce au contact continu du gaz réactif avec les particules du catalyseur et grâce aux échanges de chaleur et de matière favorisés dans la section du lit fluidisé, cette configuration aurait comme avantages majeurs la facilité de la récupération des NFC et la maximisation de leur production.

1.3 Objectifs du projet de recherche

1.3.1 Objectif général

L'objectif général de ce projet est la mise à l'échelle d'un procédé de production des NFC à partir des fluides dérivés d'un procédé de pyrolyse autothermique de résidus plastiques. Les trois éléments principaux de cet objectif sont :

i. La conception et la construction d'une nouvelle configuration de réacteur hybride, combinant un lit fluidisé à un lit mobile .
ii. L'opération dudit réacteur hybride avec des réactifs représentatifs des gaz pyrolytiques pour prouver le concept à l'échelle kg-lab.

iii. La description des problèmes opérationnels et les efforts d'optimisation incluant celles accomplies et les recommandations pour les prochaines étapes.

1.3.2 Objectifs spécifiques

Pour arriver à l'objectif général décrit ci-dessus, plusieurs étapes qui constituent les objectifs spécifiques furent choisis et présentés ci-dessous. Ils ont été accompagnés de jalons préétablis et ajustés tout au long de cet effort ambitieux dans la cadre académique de cette étude.

1- Conception du réacteur
   - Concevoir et fabriquer le réacteur de synthèse de NFC.
   - Construire un banc d'essai à froid pour l'étude fluido-dynamique.

2- Élaboration d'un protocole de sécurité (procédure opérationnelle sécuritaire)
   - Définir et mettre en place des pratiques de travail sécuritaire avec des équipement d'échelle pilote kg-lab.
   - Définir et mettre en place des pratiques de travail sécuritaire lors de la manipulation des NFC.

3- Mise en marche (opérationnalisation) du procédé et évaluation de son fonctionnement
   - Installer et instrumenter les différentes unités du procédé et assurer leur raccordement.
   - Déterminer le protocole opératoire du réacteur pour assurer son fonctionnement en régime permanent.

4- Production des NFC à échelle kilo-lab
   - Effectuer des tests de production des NFC.
   - Caractériser les NFC.

1.4 Contributions originales

1. L'originalité de ce projet de recherche réside dans l'utilisation d'un réacteur de production de NFC d'une nouvelle configuration constituée d'un lit fluidisé et d'un lit mobile; ladite configuration offre des avantages en termes de production et de récupération de ces NFC. Ces derniers sont produits tant dans la partie fluidisée que dans la partie du lit mobile. L'opération de ce réacteur assure le détachement continu de ces NFC et leur récupération avec les gaz sortant du réacteur. Ainsi, le système

peut être opéré en mode de régime permanent contrairement aux réacteurs actuels utilisant la configuration du type « lit fixe ».

1.5 Plan du document

Le document comporte 6 chapitres.

Le **CHAPITRE 1** est une introduction comportant plusieurs parties : la mise en contexte et la problématique y sont abordées pour bien situer la recherche effectuée. Ensuite, le projet de recherche est défini pour dégager l'utilité et l'intérêt de travailler avec cette nouvelle configuration de réacteur et de produire les NFC. Les objectifs de recherche sont énoncés. Enfin, le point a été mis sur l'originalité de ce travail de recherche.

Le **CHAPITRE 2** est un article scientifique qui présente une synthèse critique de la littérature, des articles scientifiques et des brevets sont passés en revue pour situer le projet dans le domaine de production des NFC à partir des déchets plastiques. La première section de cet article est consacrée à un résumé général des nanomatériaux de carbone, y compris la compréhension actuelle de leurs mécanismes de croissance, la différence entre les différents types et les conditions qui contrôlent leur croissance. La deuxième partie vise à synthétiser les données publiées dans la littérature scientifique au cours de la dernière décennie sur la production des nanomatériaux de carbone filamenteux à partir de la pyrolyse de déchets plastiques. Les différentes conceptions de réacteurs utilisées sont examinées et les effets de différents paramètres, y compris le catalyseur utilisé et les paramètres du procédé, sur le rendement et la qualité des NFC à partir de divers types de déchets plastiques sont discutés.

Le **CHAPITRE 3** présente la méthodologie ainsi que le cheminement adopté pour effectuer l'étude de ce projet. Après une petite introduction, les étapes suivies pour la conception du réacteur sont présentées. Pour bien comprendre le fonctionnement du réacteur, une description de sa configuration sera détaillée et une explication exhaustive des différents phénomènes qui ont lieu entre la phase gaz et le solide sera élaborée. La mise en marche du procédé partie importante de ce projet, sera présentée en détail. En effet, elle consiste en la construction du laboratoire où les tests ont eu lieu et de toutes les étapes suivies pour l'installation du procédé et ce, jusqu'à son fonctionnement. Enfin, les enjeux de santé et sécurité seront présentés. Un autre aspect important qui a impacté le déroulement de ce projet

est la résolution des différents problèmes techniques qui sont survenus au cours des premières manipulations. La dernière partie de ce chapitre est dédiée à la description du travail fait pour faire face à ces problèmes.

Le **CHAPITRE 4** est un article scientifique qui porte sur l'étude préliminaire qui a été effectuée à l'échelle laboratoire pour la production des NFC via la réaction de reformage à sec de l'éthylène. Cette étude a servi à démontrer l'avantage de l'utilisation du CO_2, à part l'avantage environnemental qui porte sur la séquestration d'un gaz à effet de serre.

Le **CHAPITRE 5** est un article scientifique ayant trait aux principaux résultats de l'étude hydrodynamique effectuée avec le banc d'essai à froid et à l'étude qui prouve la fonctionnalité de ce nouveau procédé par la présentation des résultats expérimentaux obtenus en utilisant le réacteur pilote et l'éthylène comme matière première.

Le **CHAPITRE 6** permet de conclure en faisant un bref retour sur les principaux résultats et les recommandations émises afin d'améliorer le procédé.

À la fin du document, les annexes et la bibliographie sont présenté. Concernant la bibliographie, le style bibliographique utilisé est le style (auteur, date) et il provient de l'association américaine de psychologie (American Psychological Association APA 7th édition).

CHAPITRE 2
ÉTAT DE L'ART

CHAPITRE 2 ÉTAT DE L'ART

2.1. Avant-propos

Auteurs et affiliation

A. Azara : Étudiante en Doctorat, Université de Sherbrooke, Faculté de Génie, Département de Génie Chimique et de Génie Biotechnologique.

S. Belbessai : Étudiante en Doctorat, Université de Sherbrooke, Faculté de Génie, Département de Génie Chimique et de Génie Biotechnologique.

N. Abatzoglou : Professeur, Université de Sherbrooke, Faculté de génie, Département de génie Chimique et de Génie Biotechnologique.

Date d'acceptation : 18 Décembre 2021.

État de l'acceptation : version finale publiée.

Revue :Journal of Environmental Chemical engineering

Référence : (Azara et al., 2022)

Titre français : Revue de la littérature sur la synthèse des nanomatériaux de carbone filamenteux via la conversion catalytique des produits de pyrolyse des déchets plastiques

Contribution au document :Cet article contribue à la thèse en élaborant l'état de l'art dans le domaine de production des NFC à partir des déchets plastiques.

Résumé français :

Les déchets plastiques posent des problèmes importants pour l'environnement et les écosystèmes en raison de leur nature non biodégradable. Outre le recyclage mécanique et thermique, le recyclage thermochimique peut convertir les déchets plastiques en produits de grande valeur. Les procédés de pyrolyse et de gazéification peuvent convertir les déchets plastiques en produits liquides et gazeux pouvant être utilisés pour la synthèse de divers produits. Par ailleurs, ces mêmes produits peuvent être utilisés pour produire des nanomatériaux de carbone filamenteux, c'est-à-dire des nanotubes de carbone (NTC) et des

nanofilaments de carbone (NCF). Malgré les progrès significatifs réalisés dans le domaine de la synthèse de carbone filamenteux, une compréhension complète de tous les aspects du mécanisme de croissance n'est toujours pas disponible et, par conséquent, il n'y a pas de contrôle structurel évident. Par conséquent, la première section de cet article est consacrée à un résumé général des nanocarbones filamenteux, y compris la compréhension actuelle de leurs mécanismes de croissance, la différence entre les différents types et les conditions qui contrôlent leur croissance. La deuxième partie vise à synthétiser les données publiées dans la littérature scientifique au cours de la dernière décennie sur la production des nanocarbones filamenteux à partir de la pyrolyse de déchets plastiques. Les différentes conceptions de réacteurs utilisées pour convertir les déchets plastiques en nanocarbones filamenteux sont examinées et les effets de différents paramètres, y compris le catalyseur utilisé et les paramètres du procédé, sur le rendement et la qualité du carbone à partir de divers types de déchets plastiques sont discutés. Enfin, les différentes applications de ces nanomatériaux sont passées en revue.

2.2. Article: A review of filamentous carbon nanomaterial synthesis via catalytic conversion of waste plastic pyrolysis products

Abir Azara[1,2], Salma Belbessai[1,2] and Nicolas Abatzoglou [1,*]

[1] Department of Chemical & Biotechnological Engineering, Université de Sherbrooke, 2500 Boulevard de l'Université, Sherbrooke, QC J1K 2R1, Canada.

[2] Laboratoire de Valorisation des Énergies Fossiles, École National Polytechnique, 10 Avenue Hassen Badi El Harrach BP182, Alger 16200, Algeria.

[*] Corresponding author: nicolas.abatzoglou@usherbrooke.ca

2.2.1. Abstract

Waste plastics pose challenging issues to the environment and ecosystems due to their non-biodegradable nature. Aside from mechanical and thermal recycling, thermochemical recycling can convert waste plastics to high-value products. Pyrolysis and gasification processes can convert waste plastics to liquid and gaseous streams that can be used for the synthesis of various products (the waste-refinery concept). Moreover, these same streams can be used to produce filamentous carbon nanomaterials (CNM), that is, carbon nanotubes (CNT) and carbon nanofilaments (CNF). Despite the significant progress made in the field of filamentous CNM synthesis, a full understanding of all aspects of the growth mechanism is still unavailable and, thus, there is no obvious structural control. Consequently, the first section of this article is dedicated to a general summary of CNM, including the current understanding of their growth mechanisms, the difference between the various types, and the conditions which control their growth. The second section aims to synthesize the data published in the scientific literature over the past decade on the production of filamentous CNM from the pyrolysis of waste plastics. The different reactor designs used to convert waste plastics to CNM are considered, and the effects of different parameters, including the catalyst used and process parameters, on the yield and quality of CNM from various types of waste plastics are discussed. Finally, applications for CNM are reviewed.

Highlights

- Filamentous CNM can be produced from waste plastic.
- This review focuses on the two-stage pyrolysis–catalysis process.
- Continuous production of CNM and H_2 from real waste plastics is a big challenge.
- Temperature of pyrolysis and catalysis are key factors.

- Steam is needed at the right proportion to improve hydrogen yield and CNM quality.
- Techno-economic assessment is necessary for scale-up and evaluation of sustainability.

Graphic abstract

Keywords: Carbon nanotubes, carbon nanofilaments, waste plastics, pyrolysis, catalysis, hydrogen.[1]

Abbreviations: B-CNT, Bamboo-like carbon nanotubes; BET, Brunauer–Emmett–Teller; CS-CNF, Cap-stack carbon nanofilaments; CF, Carbon fiber; CNC, Carbon nanocages; CNF, Carbon nanofilaments; CNM, Carbon nanomaterials; CNS, Carbon nanospheres; CNT, Carbon nanotubes; CC, Catalytic cracking; T_c, Catalytic temperature; CVD, Chemical vapor deposition; DR, Dry reforming; EDLC, Electrochemical double-layer capacitors; FTIR , Fourier-transform infrared spectroscopy; FCC, Fluid catalytic cracking; FBR, Fluidized bed reactor; GC, Glassy carbon; HDPE, High density polyethylene; HC-CNF, Hollow-core carbon nanofilaments; HC, Hydrocarbons; ICP, Induction-coupled plasma; LDPE, Low density polyethylene; MB, Methylene blue; MP, Mixed plastics; MOC, Motor oil container; MWCNT, Multi-walled carbon nanotubes; MPW, Municipal plastic waste; MSW, Municipal solid waste; ORR, O_2 reduction reaction; P-CNF, Platelet carbon nanofilaments; PCDD/F, Platelet carbon nanofilaments; PE, Polyethylene; PET, Polyethylene terephthalate; PP, polypropylene; PS, polystyrene; PTFE, Polytetrafluoroethylene; PVC, Polyvinyl chloride; T_p, Pyrolysis temperature; SEM, Scanning electron microscopy; SWCNT, Single-walled carbon nanotubes; SS, Stainless steel; TPO, Temperature programmed oxidation; TGA, Thermogravimetric analysis; TEM,

2.2.2. Introduction

Plastics are one of the most used materials globally because they are notably lightweight, chemically resistant, and have low production costs. Most plastics produced are used once and disposed of, becoming waste, most of which is not biodegradable (Kunwar et al., 2016). The accumulation of this waste on land and in water is becoming one of the most serious current environmental issues, known as "white pollution." Thus, plastic waste management has become essential. Conventional methods such as incineration and landfill are not sustainable and cause loss of resources (Al-Salem et al., 2017; Kunwar et al., 2016), which has led researchers to develop plastic upcycling technologies, consisting of converting these waste materials into value-added products, such as H_2 and CNM (Aboul-Enein et al., 2018; Aboul-Enein & Awadallah, 2018, 2019; Acomb et al., 2016; Yao et al., 2017; Yao, Zhang, et al., 2018).

CNM possess remarkable properties, including high mechanical strength and high electrical and thermal conductivities. Due to these properties, efforts have been made to optimize and control the formation of this type of carbon for use in several industrial applications (Baker, 2016). The first method used for the production of CNM is chemical vapor deposition (CVD) from hydrocarbons (HC); this type of CNM is referred to as vapor growth carbon filaments (VGCF) if the diameter was greater than 500 nm and vapor growth CNF (VGCNF) if the diameter was less than 500 nm (Endo & Koyama, 1977). Hyperion Catalysis was the first company to produce a commercially manufactured CNT named FIBRIL at an industrial scale, using a nano-sized catalyst for growth in reactors with flowing HC at high temperatures (David Moy & Asif Chishti, 1998). In the 1990s, Applied Science Inc., in collaboration with General Motors Research, began to market VGCNF called Pyrograf III at USD 200/kg. Pyrograf III is a highly graphitic and low-cost CNF, with a diameter ranging from 70 to 200 nm and a length of up to 200 microns (Pyrograf®-III, 2018).

Carbon-based molecules such as CO, C_2H_4, and CH_4, are usually used as carbon precursors for CNM synthesis. Currently, attention is focused on producing these HC from the pyrolysis of waste plastics in order to contribute to the fight against white pollution.

Transmission electron microscopy; VGCF, Vapor growth carbon filaments; VGCNF, Vapor growth carbon nanofilaments; VLS, Vapor-Liquid-Solid; XRD, X-ray powder diffraction.

Different thermochemical processes can be used, including pyrolysis–catalysis and catalytic carbonization (Lopez et al., 2018). Catalytic carbonization is a one-stage process where waste plastics are directly pyrolyzed and converted to CNM in the presence of a catalyst in a one-pot reactor (Gong et al., 2012, 2014; Gong, Liu, Jiang, Chen, et al., 2015). The pyrolysis–catalysis process is a two-stage process: first, the pyrolysis of plastics to form condensable and non-condensable gases, and second, the growth of CNM from the decomposition of these products in the presence of catalysts. There are also different ways to conduct the two-stage process, (i) in one reactor with two separate zones for pyrolysis and catalysis where all the HC products derived from the pyrolysis of the waste plastics pass directly to the catalysis zone and interact with the catalyst to produce CNM, and (ii) in two separate reactors with or without an intermediate condensation step; the condensation step is used to remove condensable gases that can be used for many applications such as fuel in diesel engines (Kaimal & Vijayabalan, 2015; S. Lee et al., 2015), and only non-condensable gases will be catalytically converted to CNM and H_2 in the catalysis reactor.

The pyrolysis–catalysis of waste plastics leads to the formation of different types of CNM, including CNT, CNF, carbon nanocages (CNC), and carbon nanospheres (CNS). However, this review will cover only filamentous CNM production, namely, CNT and CNF. To improve the catalytic activity, there are several parameters to be controlled, which present some challenges due to their interdependency in affecting CNM yield and quality. The reactor configuration is crucial: the differences between using all the pyrolysis products or removing the condensable gases before the catalysis step is widely studied to find the optimal way to produce CNM. Different reactor configurations have been developed and tested for possible deployment and commercialization of the technology on a larger scale. The waste plastics used as a feedstock can be a single type or a mixture of types, which produce different yields and different gas compositions, directly affecting CNM yields and quality. The catalyst used, as well as the process parameters, are also shown to be critical. For example, the morphology, graphitization, wall thickness, and length of the CNM are influenced by the nature and the size of the metal catalyst (Nahil et al., 2015), the catalyst support (Bazargan & McKay, 2012), and the steam input (Acomb et al., 2014).

An exhaustive literature review is essential to understand the effect of each parameter based on the studies reported in the literature in the last decade. Therefore, this review will focus on recent efforts in upcycling plastic waste into CNM via pyrolysis–catalysis process. First, the background of CNM will be introduced, including their types, growth mechanisms, factors impacting their morphology, and, finally, their properties and general uses. Typical methods and reactors used for producing CNM from waste plastics will then be reviewed, followed by the impact of different factors, including the type of plastic, the catalyst, and the temperature, then CNM specific applications will be presented. At the end of this review, challenges encountered in scaling up the process and suggested solutions will be discussed.

The novelty of this article is mainly the fact that this review covers not only the production of CNM from waste plastics by means of two-stage pyrolysis–catalysis processes, but also synthesizes the knowledge relative to the way different morphologies of CNM are produced. The latter is not well reported in the literature.

2.2.3. CNM background

Morphology

There are different types of filamentous CNM, as shown in Figure 2. *1*. Morphologies (a), (b), and (c) are CNT: (a) a single sheet of graphene that is rolled up to form a hollow cylinder is called a single-walled carbon nanotube (SWCNT), while (b) consists of several cylindrical sheets of graphene that are concentrated to form multi-walled carbon nanotubes (MWCNT), while morphology (c), called bamboo-like CNT (B-CNT) and sometimes also considered as a CNF, has a core that is separated by graphitic layers at a periodic interval. Morphologies (d), (e), and (f) are CNF which differ from CNT due to the angle between the growth axis and the graphene layers. CNT have a zero angle, while CNF have a non-zero angle (Desmaris et al., 2015). Morphologies (d) and (e) are called fishbone or herringbone CNF, solid core and hollow core, respectively. The former is called a cap-stack CNF (CS-CNF) because the graphene sheets are bent into the shape of a cap and stacked, and the projected view (Figure 2. *1*(d)) shows the graphene sheets making an oblique angle with respect to the nanofiber axis. The latter, hollow-core CNF (HC-CNF), has an inner cavity when the apex of the cap becomes discontinuous because of energetic requirements. (f) shows the platelet CNF (P-CNF), where the graphene sheets are stacked perpendicular to the

growth axis. Several other CNM conformations have been observed, such as octopus, bidirectional, helical, branched, and coiled (Baker et al., 1973, 1975; Boehm, 1973; Kawaguchi et al., 1992). These different growth types will be discussed further in this review.

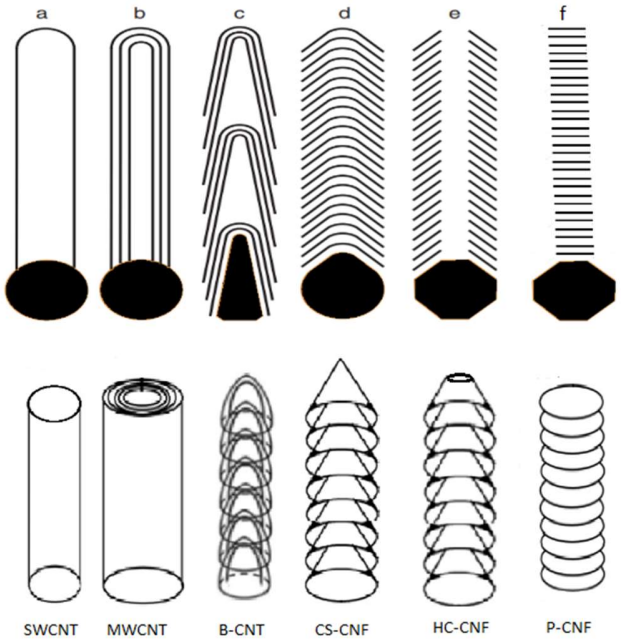

Figure 2. 1 Different morphologies of CNM, the bottom row is a 3D view, while the top row is a projected view with catalyst particle embedded at the tip." (inspired by (Jiang et al., 2007)).

Synthesis and mechanisms

There are two main methods to release carbon atoms from carbonaceous precursor molecules: chemical and physical. For the physical methods, such as arc discharge, electrospinning, and laser ablation, high-energy input is required, making them very expensive. Chemical methods are more advantageous than physical ones in terms of scale-up, cost, and temperature. CVD is the most frequently utilized process: the carbon precursors decompose at high temperatures on the surface of catalyst particles to produce atomic carbon, which subsequently precipitates as graphitic nanofilaments. Some methods combine physical and chemical methods, such as plasma-enhanced chemical vapor deposition (PECVD). CVD can be divided into two methods, thin-film growth that involves a catalyst dispersed on a support and the floating catalyst method where volatile organometallic compounds such as

ferrocene and iron pentacarbonyl are used as catalysts (Moisala et al., 2003). The catalyst can also be a powder, and the process is then called "catalytic decomposition." CO and HC are usually used as carbon feedstock. When CO is used, atomic carbon is formed from the disproportionation reaction of CO, also called the Boudouard reaction. When HC are used, atomic carbon comes from the catalytic or thermal decomposition of the HC. Saturated HC are very stable, and this stability decreases with an increased number of carbon atoms; methane is the most stable saturated HC, and its thermal decomposition begins at approximately 900°C (Moisala et al., 2003). Unsaturated HC are less stable and more reactive due to their π-bonds. They decompose readily at high T, and their reaction products may also undergo further decomposition; therefore, they are favored for the growth of CNM compared to saturated HC (Y.-Q. Xu et al., 2006).

The mechanism of CNM growth in catalytic processes has been the subject of several controversies. Baker et al. (Baker et al., 1972) were the first authors to propose a mechanism. According to them, the CNM growth mechanism is composed of three steps:

1. **Adsorption and surface reaction step:** The HC is decomposed on a specific crystallographic facet of the metal catalyst particle.
2. **Dissolution and diffusion step:** The carbon is dissolved through the bulk of the particle to form a "metal–carbon" solid-state solution.
3. **Saturation and precipitation step:** The limit of solubility of carbon in the metal at the reaction temperature is reached, leading to the precipitation of carbon on another crystallographic facet to form a graphene sheet. The stacking of these sheets gives rise to the CNM.

The rate-limiting step of this mechanism is the diffusion of carbon through the bulk of the metal catalyst because the activation energies for CNM growth are close to those for the diffusion of carbon through the corresponding metals (Baker, 2016). Another reason is that the growth rate of CNM decreases when the diameter of the catalyst particle increases. The driving force for the diffusion of carbon is believed to be the concentration gradient. According to Sacco et al. (Sacco et al., 1984) and Alstrup et al. (Alstrup, 1988), an unstable metal carbide phase forms at the gas–catalyst interface, and its decomposition leads to the supersaturation of carbon in the frontal regions of the catalyst particle, thus creating a

concentration gradient. The exothermic decomposition of the HC at the front facet and the endothermic precipitation of solid carbon at the rear facet cause a temperature gradient in the particle. The carbon structure will continue to grow until the decomposition of the HC ceases due to the formation of carbon around the catalyst, preventing the gas from contacting it. Two criticisms of this mechanism should be noted, the first is that the decomposition of HC is not always exothermic, such as methane, and yet carbon is formed from its decomposition. The second criticism is that a temperature gradient is unlikely in such small metal particles (Teo et al., 2003).

Oberlin et al. (Oberlin et al., 1976) proposed another similar mechanism, suggesting that carbon diffusion occurs over the catalyst surface rather than within the catalyst bulk since the energy barrier of surface diffusion is lower than that of bulk diffusion. These authors assume that the mechanism proposed by Baker et al. does not satisfactorily explain the anisotropy of CNM growth or the growth of HC-CNF.

Dai et al. (Dai et al., 1996) have described the growth of SWCNT and MWCNT using the yarmulke mechanism due to the resemblance of the process to the yarmulke, a skullcap worn in certain cultures. The condition needed to grow CNT versus CNF is the size of the catalytic particles, which must be of the order of a few to a few tens of nanometers. Small nanoparticles have a very high number of surface atoms, which creates a very high surface energy per atom. To diminish this energy, the carbon atoms assemble as a graphene cap on the surface of the particle, with the edge strongly chemisorbed to the particle. In this mechanism, open graphene edges with energetically costly dangling bonds are avoided at all stages of growth. New incoming carbon atoms are gradually added to the edges of the cap, eventually causing the cap to lift off the particle to form a hollow tube which continues to grow away from the particle, resulting in a hollow tube. The driving force for the lifting process is the free energy released when the strain built up in the carbon cap around the spherical surface of the catalyst nanoparticle is relaxed. A new cap can form underneath the previous one to produce MWCNT, and the older cap is lifted to form a cylindrical tube whose open end remains chemisorbed to the catalytic particle. When the strain due to the increasing curvature of new layers becomes too great, nucleation will stop. This mechanism is especially

valid for small particles rather than larger particles because detaching a cap to grow a tube is more expensive in terms of energy for the larger cap than for the smaller cap.

Other authors (Gavillet et al., 2001; Jiang et al., 2007; Loiseau et al., 2003) have proposed another mechanism that relies on the vapor–liquid–solid (VLS) model, a model first introduced in the 1960s to explain the growth of silicon whiskers (Wagner & Ellis, 1964). This model involves a vapor-phase precursor (HC), the liquid phase carbon–metal solution, and solid-phase CNM and has been used to explain the growth of individual SWCNT and SWCNT bundles (Gavillet et al., 2001; Loiseau et al., 2003), as well as MWCNT (Jiang et al., 2007). This model proposes a quasi-liquid metallic particle in which the diffusion is very fast and thus cannot be the rate-limiting step. For this model, the limiting step is the surface reaction since the activation energy of the reaction has been found to be close to that of the heterogeneous decomposition of HC, and the rate is not very sensitive to variation in the diameter of the catalyst particle (Jiang et al., 2007). Due to the nanometer-scale size, the high heat transport and carbon diffusion coefficients through the catalyst, the temperature and carbon concentration across the catalyst are uniform. These authors are not the only ones who suggested a quasi-liquid state of the catalyst during CNM growth, many recent experiments (X. Chen et al., 2004; Y. Li et al., 1999, 2011; Schaper et al., 2004) have shown that the metal catalyst particle is in a quasi-liquid state, and it undergoes a reshaping process during the growth of the different types of CNM.

Relying on these results, one can ask these questions:

- Which of these mechanisms accounts more for CNM growth? Is there a different mechanism for each type of CNM?
- What are the factors that impact CNM growth and determine their morphology?
- Does the metallic particle exist in a quasi-liquid state? And how could it be so at temperatures far below its melting point?
- What is the active phase for the growth of CNM, the metallic form or the carbide form?

To answer these questions, it is important to understand the different phenomena which occur during CNM growth. There are three different regions related to the growth of CNM:

i) The catalyst–gas interface,

ii) The bulk of the catalyst,

iii) The catalyst–solid carbon interface.

Thus, in order to develop a comprehensive understanding of the growth and control of CNM structures, the phenomena that occur in each region will be reviewed in the next section.

Factors impacting CNM growth

Factors related to the catalyst–gas interface

The initiation step in the CNM growth process is a crucial step, which influences the subsequent steps. One of the major factors associated with the initiation of CNM growth is the decomposition of the carbon-containing reactive gas. The different factors that impact that process are:

The crystallographic orientation of the atoms of the metal particle has been shown to play an important role in the ability of the catalyst to decompose reactive gases (Koestner et al., 1982). As the first step in the CNM growth mechanism, the HC must undergo dissociative chemisorption on the surface of the metal. However, the interaction between the HC or CO and the catalyst does not always lead to the formation of the CNM. Audier et al. (Audier et al., 1983a, 1983b, 1983c) studied carbon growth from the disproportionation of CO on fcc-structured Fe-Co and Fe-Ni alloys and bcc-structured Fe-Co alloys. Using transmission electron microscopy/selected area electron diffraction (TEM/SAED) technique, they have found that the gas decomposes on the (100) facet for the bcc-structured alloys and the (111) facet for the fcc-structured ones. Using the same technique, Yang and Chen (R. T. Yang & Chen, 1989) have proven that the Ni and Fe (100) and (110) facets are the most suitable for interaction with HC molecules.

The introduction of other metallic components into the main metal of the catalyst influences the growth of the CNM (Baker, 2016). There are two structural configurations for the adsorption of HC such as ethylene or acetylene: the "parallel" configuration as depicted in Figure 2. *2* **(**a), or the "end-on" configuration as in Figure 2. *2* **(**b). The first configuration promotes the polymerization reaction because parallel ethylene species will eventually become close, interact and condense to form encapsulating carbon, while the second configuration promotes the transformation into "ethylidyne (CH_3C)," which will then decompose to give atomic carbon and methane (M. S. Kim et al., 1991). Monometallic

catalysts generally tend to adsorb HC in configuration (a), whereas bimetallic catalysts or those containing adatoms that do not chemisorb HC tend to favor the second configuration. Krishnankutty et al. (Krishnankutty et al., 1996) have proven that adding copper to any of the transition metals, especially iron, increases the carbon yield compared to that from pure iron under the same conditions. When the adsorption takes place at an iron atom with the nearest neighbor being a copper atom that is not capable of chemisorbing the HC and therefore is unoccupied, the adsorption occurs in the "end-up" configuration. In other studies, it was found that if only 1.0 wt.% of Ag was added to powdered Co, a significant increase in the production of carbon nanofibers from the decomposition of ethylene was observed (Chambers et al., 1996).

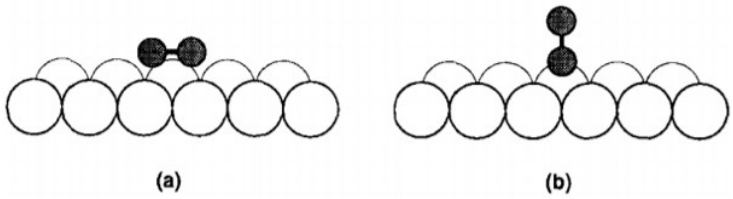

Figure 2. 2 Ethylene adsorption at the surface of a metal catalyst in (a) "parallel" and (b) "end-on" configurations (M. S. Kim et al., 1991).

The chemical nature of the gaseous environment can considerably influence the different steps of the CNM growth process. Luo et al. (Luo et al., 2000) have conducted tests using the same nickel-based catalyst and the reactive gases CH_4/N_2, CO/N_2, and $CO_2/CH_4/N_2$. They observed the formation of two types of carbon, encapsulating and filamentous, with the latter being formed mostly in the presence of CO. These results are in accordance with those of Azara et al. (Azara et al., 2019), who studied ethylene catalytic cracking (CC) (C_2H_4/Ar) and ethylene dry reforming (DR) (C_2H_4/CO_2). During the CC reaction, CNF with irregular shapes as well as encapsulating carbon were formed; meanwhile, during the DR reactions, where CO was present, only CS-CNF were formed. The encapsulating carbon is usually formed at relatively low T when the adsorbed HC accumulate on the surface of the catalyst and the C_nH_m* radicals slowly polymerize. Filamentous carbon is formed from the catalytic decomposition of HC, and pyrolytic carbon is formed from HC thermal decomposition at high T. The question is why the addition of CO/CO_2 to the reactant gas prevents the formation of encapsulating carbon. Indeed, the presence of some gases in the composition of the

reactive gas induces electronic disturbances that affect the arrangement of the atoms in the crystallographic facet of the catalyst and consequently determine the adsorption mode, and thus the decomposition of the reactive gas. It has been found that when CO is present in the reactive gas, the adsorption of HC takes place in the "end-up" configuration, which prevents the polymerization of HC (Dupuis, 2005). Several studies have indicated that the activity of the metal catalyst for the formation of CNM can be promoted by introducing controlled amounts of certain other gases such as hydrogen, sulfur, and chlorine (Chambers & Baker, 1997; M. S. Kim et al., 1993). Martin-Gullon et al. (Martin-Gullon et al., 2006) produced CNF using Ni catalyst and natural gas as a feedstock by adding H_2S. When sulfur was not used, only soot was obtained, but when sulfur is added to the reactive feed, highly graphitic CS-CNF were formed. It is well known that the adsorption of sulfur onto a metal surface can lead to poisoning and premature deactivation of the catalyst (Rostrup-Nielsen, 1984). However, it is also reported in the literature that very low sulfur concentrations improve the performance of a metal catalyst (Reyniers & Froment, 1995). The presence of H_2 in the mixture of reactants has also played a key role in the growth of CNM (Rodriguez, 1993). Nolan et al. (Nolan et al., 1998) asserted that the inclined angle of graphene planes relative to the axis depends on the presence of hydrogen. According to this work, H_2 satisfies the valences at the edge atoms of the cones in a typical CNF. With an increasing concentration of hydrogen, the angle of orientation between the graphene basal planes and the axis of the tube (θ) increases. Their tests exposed a Ni/SiO_2-Al_2O_3 catalyst to a mixture of $CO/CO_2/N_2$ with H_2 concentrations between 0% and 3% and a temperature range of 745 K to 785 K. They observed different morphologies of nanofilaments, CNT were obtained without hydrogen, while CNF with dangling bonds were formed when H_2 was present (Nolan et al., 1998).

Factors related to the bulk of the catalyst

Two main aspects of the bulk of the catalyst should be studied: the physical state (solid or quasi-liquid) and the chemical state (carbide or metal). The state of the catalyst is also influenced by the phenomena which occur in the catalyst–gas and catalyst–solid carbon interfaces.

As we have seen in the VLS model, the physical state is assumed to be quasi-liquid. This quasi-liquid state of the metal is not related to the melting state of the bulk metal. The melting point of nickel is 1455°C, that of copper is 1085°C, and that of iron is 1538°C, all of which

are far below the reaction temperatures. The presence of the metal in the quasi-liquid state at temperatures around 700°C is caused by the interfacial effect between the graphene sheets and the crystallographic facet of the metal particle, which causes the bonds between the metal atoms to weaken and break, allowing the metal to melt and spread on the carbon (Schaper et al., 2004). However, this high mobility of the surface atoms would not have been possible if the particle size had not been nanometer-scale. Nanometer-scale catalyst particles behave differently from the corresponding bulk material because they have a high specific surface area, high surface energy, and high mobility, and they easily undergo surface reconstruction. The relationship between the melting temperature of a particle (T_m) and its radius (r) is given by the following equation (Moisala et al., 2003):

$$T_m = T_0 - \frac{2T_0}{\Delta H_{diffusion}\,\rho_s\, r}\left[\sigma_{S1} + (1 - \frac{\rho_s}{\rho_l})\sigma_l\right] \qquad (2.\ 1)$$

where:

T_0: the bulk melting temperature

$\Delta H_{diffusion}$ the latent heat of fusion

σ_{S1} is the solid–liquid interfacial energy

σ_l is the surface energy of the liquid

ρ_s *and* ρ_l are the densities of the solid and the liquid metal, respectively

From this equation, the melting temperature is reduced from the bulk value with decreasing particle diameter. Krivoruchko and Zaikovskii have observed that the catalyst particle has a solid core surrounded by liquid state carbon–metal solution and have suggested a surface melting catalyst (Krivoruchko & Zaikovskii, 1998).

The second aspect of the catalyst particle is its chemical state. Many earlier studies have identified metal carbides as the crystals at the tip of the CNM, suggesting that carbides are the precursors of these materials (Oberlin et al., 1976; Sacco et al., 1984). However, when Baker et al. (Baker et al., 1982) used high-purity cementite as a starting catalyst, the growth of carbon nanofibers was not observed. Recent studies have proven that, upon carbon dissolution, a metastable solution of Fe-C forms, and further decomposes to Fe_3C and atomic

carbon (Krivoruchko & Zaikovskii, 1998) or metallic Fe and atomic carbon (Moisala et al., 2003) depending on the carbon concentration. Jiang et al. (Jiang et al., 2007) have found that the carbon concentration on an iron catalyst is greater than 25%, which is unusual according to the Fe-C phase diagram. These findings led them to propose another $T_{eutectic}$ at a higher carbon concentration and an Fe–C solution, which will decompose into Fe_3C and graphene layers. Jourdain et al. (Jourdain et al., 2002) have also shown that the carbon concentration in a Ni/Fe catalyst used for MWCNT growth is very high, above 25%. The solubility of carbon in metals also increases with decreasing catalyst particle diameter (Moisala et al., 2003). From all these findings, metallic iron is the active phase for HC decomposition or CO disproportionation to produce atomic carbon. This atomic carbon will diffuse through the metal until saturation; then, a carbon-metal solution with an unusually high carbon concentration will form and subsequently decompose to carbon and metal carbide.

Factors related to the catalyst–carbon interface

Not all catalyst facets promote carbon precipitation. Dissolved carbon will precipitate in the form of graphene on certain facets of metals, which favor an epitaxial fit between the two components (R. T. Yang & Chen, 1989). Yang and Chen (R. T. Yang & Chen, 1989) found that for Ni-based catalysts, the most favored crystallographic facets for the precipitation of carbon were Ni (111) and Ni (311) because they provide a stronger epitaxial fit with graphene. This finding has been confirmed by Vinciguerra et al. (Vinciguerra et al., 2003) who showed that for Fe (bcc), the (1−1 0) facets are the most suitable for the growth of carbon because they have separations that overlap with the lattices of graphene sheets, and for cobalt and nickel (fcc), the appropriate facet is (111).

The forces involved in the interaction between graphene and metal, in addition to their nanometer-scale size and the temperature, cause the particle to be in a quasi-liquid state, which cause its reshaping. The interaction between a metal and a support in a gas environment can be expressed by Young's equation (Rodriguez, 1993):

$$\gamma_{SG} = \gamma_{MS} + \gamma_{MG} \cos\theta \qquad (2.2)$$

where S, M, and G refer to the support, the metal, and the gas, respectively. In the case of an interaction between a metallic surface and carbon, the support here is considered to be graphite and γ_{SG} is the graphite surface energy; γ_{MS} is the metal-graphite interfacial energy; γ_{MG} is the metal surface energy; and θ is the contact angle. Figure 2. *3* is a schematic

representation of the forces involved in the interaction between metal and a graphite surface; these forces determine the contact angle, θ (Rodriguez, 1993).

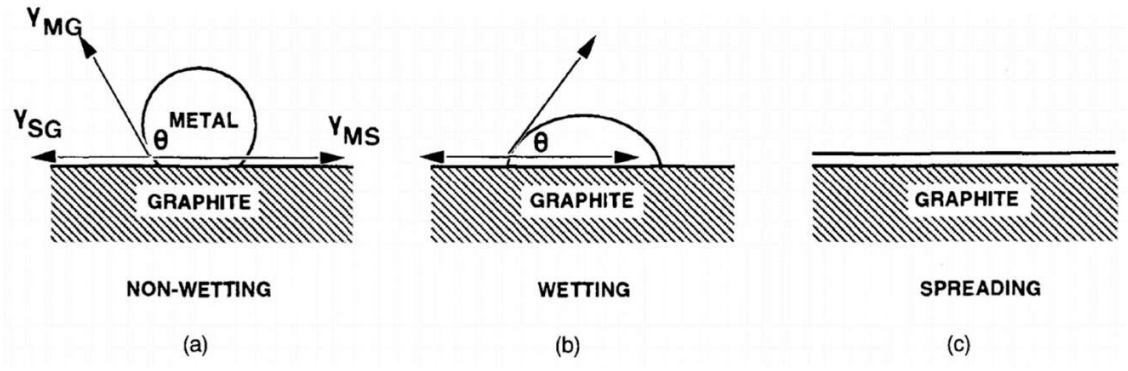

Figure 2. 3 Interaction between surface metal and graphite (permission granted by Springer Nature) (Rodriguez, 1993).

Thus, the changes in the shape of the catalyst particle are a function of the metal wetting degree on the graphite; when weak forces occur between the metal and the graphite, θ is higher than 90° and there is no wetting, the particle remains hemispherical, and the graphene sheet is adjacent to the metal particle (Figure 2. *3* (a)), when strong forces occur between the two components, θ is lower than 90° and wetting occurs (Figure 2. *3* (b)). The metal spreads over the graphite surface when the adhesion exceeds the cohesion inside the particle ($\gamma_{MS} > \gamma_{SG} + \gamma_{MG}$), and the graphene sheets are parallel to the surface from which they grew (Figure 2. *3* (c)**)**. For the particles to pass from a non-wetting state to a wetting state, atomic mobility must exist in the particles. This mobility is enabled by the nanometer-scale size of the particle and its unusually high concentration of carbon, as discussed in the previous section.

As in the metal–gas interface, the addition of adatoms to the host metal and the presence of other gases has an influence on the metal–carbon interface. Studies of the behavior of certain metal–graphene interfaces have proven that when copper is added to the host metal, the interfacial energy increases, and the bimetallic catalyst spreads, leading to the formation of CNF (M. S. Kim et al., 1992). Hydrogen also is known to cause the reconstruction of certain crystallographic facets of the metal, as in Fe and Ni (Hammer et al., 1993; Müller, 1993).

Other factors (temperature and partial pressure of HC)

Baker et al. (Baker et al., 1975) studied the effect of the temperature on the yield of CNM produced from the cobalt-catalyzed decomposition of acetylene and found that the maximum yield occurred at 725°C. The temperature affects the HC decomposition as well as the diffusion rate of carbon through the catalyst. To accelerate the catalytic decomposition and the carbon diffusion rate, high T are preferable to low T. However, a high T favors the thermal decomposition of HC and increases the amount of pyrolytic carbon; thus, a moderate T of around 700°C is favored for higher CNM yield. The temperature also plays an important role in metal dispersion on the support surface and metal particle size during the growth process, impacting the CNM diameter and morphology, which are related. A high T will promote the agglomeration and sintering of catalytic particles; thus, they will have a larger size leading to the growth of CNM with larger diameters. The sintering phenomenon is even more heightened when the catalyst–support interaction is weak. A strong catalyst–support interaction also seems to have a negative impact on the growth of the CNM because it reduces the surface that is accessible for HC, and the diffusion path length is relatively short, and carbon atoms may not be supplied uniformly over the whole region of the catalyst particles, causing perturbations that lead to the formation of defects on the structure of the CNM (Baker, 1989).

The same authors (Baker et al., 1975) have conducted a second series of experiments using the same catalyst, where the temperature of the samples was kept at a constant 725°C, while the acetylene pressure varied in the range of 6 to 200 Torr. As the pressure increased, the yield of CNM increased and then decreased; the maximum efficiency occurred at 60–100 Torr. Above 100 Torr, more encapsulating carbon was formed than filamentous carbon. In fact, at high HC partial pressure, the excessive amount of carbon precursor led to an accumulation of HC radicals at the gas–catalyst interface, which tended to undergo gas-phase polymerization and accumulate on the surface as encapsulating carbon.

Catalyst morphology vs. CNM morphology

Many factors impact the reshaping process of the catalyst particles and, thus, the type of CNM formed. In the next section, we will elaborate on the dependence between the shape and the size of the catalyst particles and those of the CNM.

CNM diameter and CNT vs. CNF

The diameter of the CNM produced is correlated to the diameter of the metal particle from which it is formed (Baker et al., 1972, 1973). If the catalyst is a metallic powder or foil, CNF will form with a wide and unpredictable size distribution. To produce nanofibers of precise and well-controlled size, it is necessary to use supported catalysts and control the size of the metal particles. There are different methods for the preparation of such catalysts, which will be discussed later.

Lamouroux et al. (Lamouroux et al., 2007) studied the evolution of the diameter of CNM as a function of the diameter of the catalytic particles. They found that the CNM diameter was almost the same as the nanoparticle diameter, and at diameters of 5 nm, no more CNT were produced, and instead, MWCNT are favored (Figure 2. *4*).

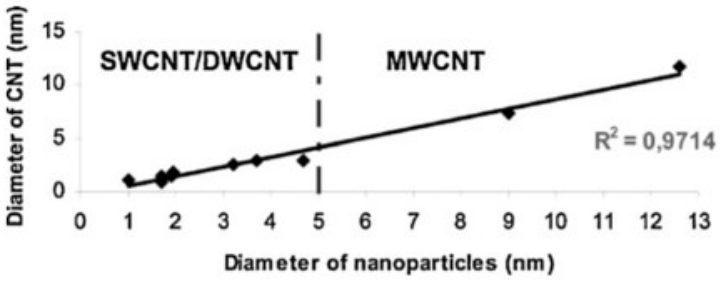

Figure 2. 4 Correlation between the size of the catalyst and the CNM diameter (permission granted by Taylor & Francis) (Lamouroux et al., 2007).

Li et al. (Y. Li et al., 2001) have used Fe-Mo nanoparticles with a diameter varying between 3 and 14 nm as catalysts for the growth of SWCNT. Their results indicate that 8 nm is the upper limit catalyst diameter for SWCNT nucleation. At diameters above 8.5 nm, no more SWCNT were observed. Cheung et al. (Cheung et al., 2002) studied the growth of CNT from the decomposition of C_2H_4 on 3, 9, and 13 nm iron nanoclusters. SWCNT were nucleated only from the 3 and 9 nm clusters, while MWCNT were observed from the 13 nm clusters. However, SWCNT has been produced from larger catalyst particles, with an upper bound of a diameter of few tens nm (Teo et al., 2003). The main determining factor of the growth of CNT compared to the growth of CNF is the size of the catalytic particles, which must be of the order of a few to a few tens of nanometers. The metallic nanoparticles have a high surface energy, and to decrease it, the carbon tends to assemble into a graphene cap,

which leads to the growth of an SWCNT as indicated in the previously discussed yarmulke mechanism (section 0) (Dupuis, 2005).

Mono, bidirectional and multidirectional growth

TEM studies have demonstrated that nanofibers exist in various conformations, some of which are shown in Figure 2. *5*, the nanofibers were generated in a bidirectional mode where carbon precipitation occurred from opposite facets of the catalyst particle, which remained embedded in the structure throughout the growth period. Kinetic analysis of the growth sequences obtained using controlled atmosphere electron microscopy (Nolan et al., 1998) has demonstrated that both sides of the structure develop at identical rates. It has been found that the catalyst particles associated with this growth always had a symmetrical shape and diamond configuration (M. S. Kim et al., 1991). If different CNF grow from neighboring facets of the same crystal, an octopus-like morphology will form (Figure 2. *5* (a)) (Rodriguez et al., 1995; Ting & Liu, 2003).

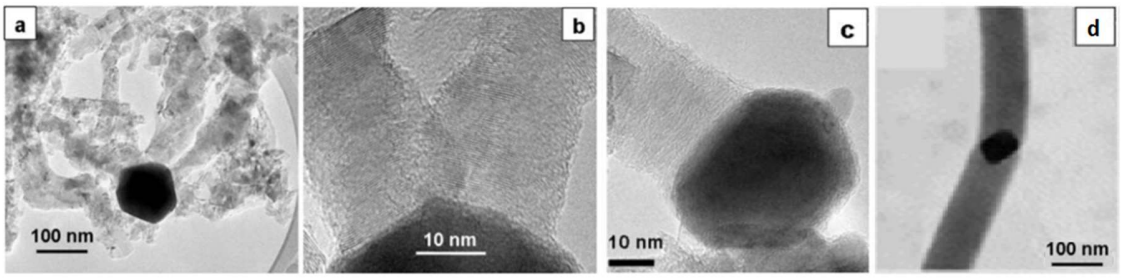

Figure 2. 5 (a) Multidirectional (octopus-like), (b) and (d) bidirectional and (c) monodirectional CNM (permission granted by the Royal society of chemistry) (Monthioux et al., 2007).

Platelet vs. herringbone CNF

Both platelets and herringbone CNF are produced from polyhedral and faceted crystals. CS-CNF without a hollow core are composed of a curved graphene sheet that grows from adjacent facets of the same crystal, which imposes a curvature on the graphene sheet. To allow the formation of a graphene sheet having a bowl shape, at least three adjacent facets should be involved in the growth of CNF. If only two facets are involved, an "open book" morphology would be generated, which is very unlikely (Monthioux et al., 2007). The bending angle of the graphene sheets is close to the angle between these crystal facets. This angle should not be sharper than 80–90° because there is a limit to the acceptable strain

supported by the curved graphene sheet. When the angle is too small, a high bending strain is induced in the graphene sheet, and to release the excessive strain, the apex becomes discontinuous, and a hole appears, thereby creating an inner cavity, making a HC-CNF (Monthioux et al., 2007). In this case, the energetic cost to create the edge carbons (i.e., allowing dangling bonds) is lower than the energetic cost of bending the graphene sheets.

Both platelet and herringbone CNF are possible when the crystal diameters range between 40 and 100 nm (Monthioux et al., 2007). There is a threshold value for the ratio of the edge carbon atoms over core carbon atoms, which determines the formation of herringbone instead of platelet CNF. Typically, growing a single herringbone nanofiber from 3 adjacent crystal facets instead of growing 3 platelet nanofibers from each facet reduces the number of edge atoms threefold.

According to Monthioux et al. (Monthioux et al., 2007), catalyst particles can be classified according to two morphological characteristics: the extension of the crystal faces, F_ϕ, and the angle between them, F_α. The driving force to switch between these morphologies is related to the competition between the energetic cost of edge atoms with dangling bonds and that of the curved graphene sheet. In their work, they have defined two parameters, I_{nf}, which is the unsaturated factor related to the level of unsaturated graphene sheets, and S_{nf}, which is the strain factor related to the topological deformation of the graphene sheets.

$$I_{nf} = \frac{edge\ atoms}{total\ atoms} \qquad (2.\ 3)$$

$$S_{nf} = 1 - \frac{\alpha}{180^\circ} \qquad (2.\ 4)$$

where α is the angle of the graphene sheets in the projected image of CNM.

The free energy of the system is proportional to these two factors. S_{nf} prevails over I_{nf} since minimizing the strain is more important than minimizing the number of edge atoms. Table 2. *1* summarizes the relationship between the catalyst morphological parameters F_ϕ and F_α and the type of CNM, as well as the related parameters and S_{nf}.

Table 2. 1 CNM types according to the catalyst morphological parameters F_ϕ and F_α, as well as the related parameters I_{nf} and S_{nf} (Monthioux et al., 2007).

F_ϕ	**<40 nm**	**40–100 nm**	**>80 nm**

F_α				
>80°	S_{nf}	0,5–1	0,5–1	1
	I_{nf}	High	Low	Low
	Morphology	CS-CNF	CS-CNF	P-CNF
<90°	S_{nf}	<0,5	1	1
	I_{nf}	High	High	Low
	Morphology	HC-CNF	P-CNF	P-CNF
20–60°	S_{nf}	<0,5		
	I_{nf}	from high to low		
	Morphology	HC-CNF		

HC-CNF can be formed from elongated, conical, and pear-shaped catalyst particles. The conical tip of the crystal is not pointed but instead truncated, and the facet located in the tip of the cone appears to be inactive with respect to the formation of graphene. Contrary to what is observed for crystals with isometric facets, the diameter of the hollow core of the CNF formed from elongated conical crystals is well defined and depends on the facet of the tip of the cone (Figure 2. *6*) (Monthioux et al., 2007).

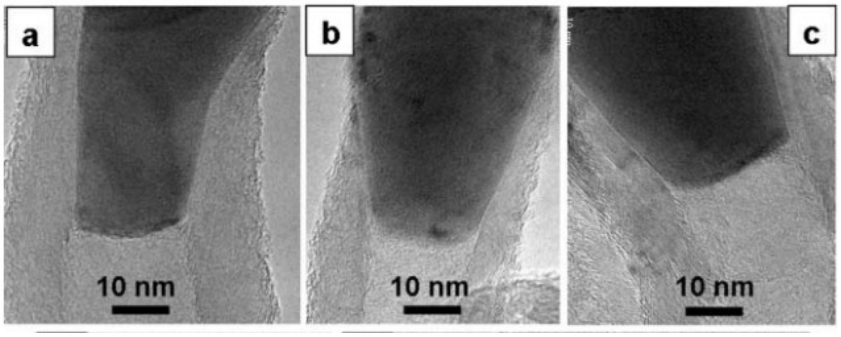

Figure 2. 6 HC-CNF growing from elongated metal particles (permission granted by the Royal society of chemistry) (Monthioux et al., 2007).

Bamboo-like CNT

Bamboo-like CNT are composed of hollow compartments separated at a regular pitch that develop along the axis, as shown in Figure 2. *1*-(c). Compared to other CNT morphologies, bamboo-like CNTs have a high specific surface area and high defect density which gives them the characteristics of a good adsorbent (Wang et al., 2016; Wiśniewski et al., 2012) and an excellent material for the H_2 and Li storage battery electrodes (L. Chen et al., 2013; X. Xu et al., 2015). They can be produced by several routes such as dry reforming

(Dębek et al., 2016; Martin-Gullon et al., 2006; Siew et al., 2015), catalytic cracking (J. Chen et al., 2001; Y. Li et al., 1999; Shen & Lua, 2015), hydrothermal (Kang et al., 2005) and alcohothermal process (Tang & Luo, 2018). The formation of bamboo-type CNTs is attributed to the quasi-liquid phase of the catalyst particles and to capillary forces at the catalyst-carbon interface. in fact, the capillary forces act as a driving force for the metal particle to jump in the near liquid state to form the bamboo-type CNTs (Jia et al., 2017). Chen et al. (J. Chen et al., 2001) proposed a mechanism for the formation of bamboo-like CNT. First, a continuous wall and cavity are formed by inserting new carbon layers at the carbon–metal interface. As the insertion proceeds, a driving force is increasingly exerted on the metal particle in the direction of carbon growth due to the low wetting affinity between the metal and the forming graphene cap. When the stress is greater than the cohesive force of the carbon and the metal, the metal particle jumps to detach itself from the graphene cap, then the process restarts periodically.

Straight vs. helical growth

Under some conditions, the growth rate is unbalanced and peculiar morphologies such as helical nanofilaments can form (Figure 2. *7*). Helical CNM also fall into different categories, including helix, braid, spiral, coil, and spring (Shaikjee & Coville, 2012). Helical growth of CNT has been reported to be due to the insertion of a series of pentagons and heptagons within the hexagonal matrix of the graphene nanotube. Dunlap (Dunlap, 1994) has shown that the curvature in the structure, called a "knee," is formed by the insertion of a pentagon on the convex side (positive curvature) and a heptagon on the concave side (negative curvature) of the graphene nanotube. This model can only be used to explain single wall helices or, at best, two wall helices (Setton & Setton, 1997). Ramachandran and Sathyamurthy (Ramachandran & Sathyamurthy, 2006) have suggested that the hexagonal matrix of graphene can be distorted by rotation at a small angle without incorporating pentagons or hexagons. This continuous distortion of subsequent layers results in a coiled nanotube. For CNF, the formation of a coil-like shape is probably caused by inequal precipitation on some catalyst particle surfaces, which have faster carbon deposition rates than neighboring surfaces (Zheng et al., 2004). This disturbance of the precipitation characteristics of carbon from the catalyst particle can be caused by the participation of compounds such as sulfur or phosphorus, which introduce an element of asymmetry into the

system (Martin-Gullon et al., 2006). Thus, helical growth of CNF could be achieved when a catalyst particle is faceted with different crystallographic surfaces having variable precipitation characteristics that would lead to anisotropic growth. Another factor that may lead to the formation of a helical structure is the carbon precursor. For most research that produced helical CNM, acetylene (C_2H_2) was the dominant raw material used, and when other HC were used, helical CNM are not obtained in great quantity (Raghubanshi & Dikio, 2015; Shaikjee & Coville, 2012).

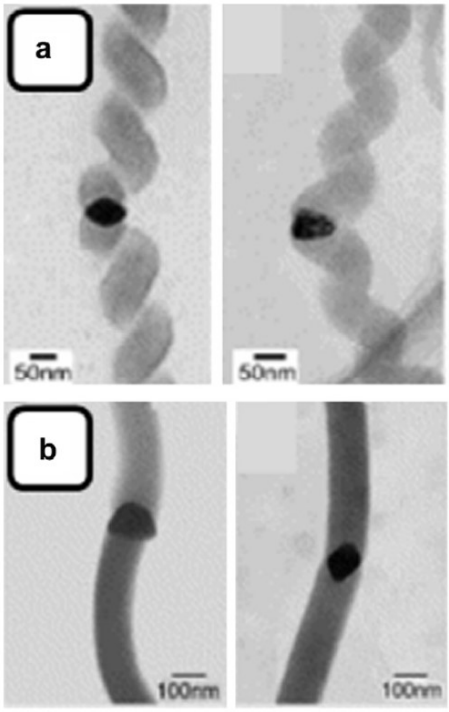

Figure 2. 7 Regular faceted particles giving rise to (a) helical nanofibers and (b) linear nanofibers (Monthioux et al., 2007).

Catalyst preparation

Different forms of catalysts have been used to produce CNM, including metallic powder, metallic foils, and supported metal on substrates (Baker et al., 2001). Transition metals (Fe, Ni, and Co), as well as their alloys, are usually used for heterogeneous reactions, and their organometallic compound or metallocene (i.e., ferrocene, nickelocene, and cobaltocene) are used for homogeneous reactions. The capacity of these metals for carbon formation is related to their ability to decompose carbonaceous gases and the high diffusion rate of carbon in these metals at high temperatures (Romero et al., 2008). Metal dispersed on a substrate is

usually used for CVD reactions, and it is easy to control the size of the metallic particles formed. The first step of their preparation is to deposit a thin layer of the active metal on the surface of the substrate using methods such as spray coating, sputtering, and spin-coating (Teo et al., 2003). The second step is heating at high T to generate ultrafine metal particles (<10 nm in diameter). Another method is to spray organometallic compounds on the surface of the substrate. Powder catalysts are used in flow reactors, where they are placed in a boat, as a fixed packed bed, or as a fluidized bed. There are different methods for their preparation; the most common is the precipitation of the metal precursors, such as metal salts (nitrates, sulfates, and chlorides), on a support (typically alumina and silica), followed by drying, calcining, grinding, and sieving in order to have an oxide catalyst with a specific diameter distribution.

After preparation, the particle size distribution is only a rough estimate of the true particle size of the catalyst during CNM growth because the catalyst particle size inevitably changes due to several factors. For example, particle size can increase because of sintering phenomena or decrease due to reduction by H_2. Two main factors directly impact sintering behavior: the strength of the metal–support interaction and the temperature. In order to limit the effect of the sintering behavior of metal particles, the support material used should interact relatively strongly with the active metal, and the reaction temperature should not be very high (Rodriguez, 1993). Once the catalyst has been placed in the synthesis oven, the system is heated to the reaction temperature in an inert gas such as argon or nitrogen. When the reaction temperature is reached, hydrogen is used to reduce the catalyst to a metallic form before the reaction occurs, decreasing the size of the metallic particles. The reduction can also occur due to the hydrogen produced during the reaction. As a result of these processes, there will be a distribution of the particle diameters, and the distribution of the CNM diameters will be random. This type of catalyst is usually used for mass production, and it can be removed from CNM by acid dissolution (Teo et al., 2003).

CNM properties and applications

CNT, especially SWCNT with their high aspect ratio, have remarkable properties. However, CNF also possess some of these special properties, including high thermal conductivity, high tensile strength, and high electric conductivity, and they are an excellent

alternative to CNT since they are cheaper and can be produced more easily at a large scale (Al-Saleh & Sundararaj, 2011). Regarding the mechanical properties, the chemical bonds in a CNF are of two types: covalent bonds between the carbon atoms of the graphene sheet, and van der Waals bonds between the graphene planes, giving CNF remarkable mechanical properties. As for electrical properties, electrical conduction occurs through the sp^2 hybridization of the carbon atoms and the presence of delocalized electrons that can move freely throughout the carbon structure. Table 2. *2* outlines the different properties of CNM.

Table 2. 2 CNM properties (Al-Saleh & Sundararaj, 2011).

Property	**VGCNF**[a]	**SWCNT**[b]	**MWCNT**[b]	**CF**[c]
Diameter (nm)	50–200	<10	5–50	7300
Aspect ratio	250–2000	100–10000	100–10000	440
Density (g/cm^3)	2	~1,3[d]	~1,75[e]	1,74
Thermal conductivity (W/m K)	1950	3000–6000[f]	3000–6000[f]	20
Electrical resistivity (Ω cm)	1×10^{-4}	1×10^{-3} – 1×10^{-4}	2×10^{-3} – 1×10^{-4}	$1,7 \times 10^{-3}$
Tensile strength (GPa)	2,92	50–500[g]	10–60[g]	3,8
Tensile modulus (GPa)	240	1500	1000	227

[a] from references: (Breuer & Sundararaj, 2004) (Tibbetts et al., 2007) (Endo et al., 2001) (Finegan & Tibbetts, 2001), [b] from references: (Winey & Vaia, 2007), [c] from references: (Keith et al., 2005), [d] from references: (Coleman et al., 2006), [e] from references: (Shaffer & Windle, 1999), [f] from references:(P. Kim et al., 2001), [g] from references: (Xie et al., 2005).

These properties have extreme importance for applications such as composite additives, energy storage devices, and environmental cleaning.

Composites

CNF can substitute for additives used in composites, such as carbon fibers, due to their extraordinary intrinsic properties, particularly their mechanical strength and electrical and thermal conductivities. Incorporating CNF into polymers would enhance the material properties, reducing the volume needed to produce a given strength and stiffness, thus

providing weight and cost savings. Various polymers such as epoxy resin, polystyrene (PS), and polyethylene (PE) have been widely used with carbon nanofibers to produce composites. One of the major challenges during the composite synthesis process is the dispersion of nanofibers in the polymer matrix. CNF are mixed with the polymers at an appropriate temperature, following which the mixture is extruded (Zeng et al., 2004); or they can be mixed with the polymer in a solvent, ultrasound is used to disperse the nanofibers and homogenize the solution, then the solvent is evaporated, and a powder is obtained (Lai et al., 2004). The functionalization of CNF is also necessary before incorporation, as it allows the formation of chemical bonds and improves compatibility with the polymer matrix. Functionalization consists of grafting reactive oxygenated or halogenated groups on the wall of the CNF, most often using baths of nitric acid mixed with sulfuric acid (Bitter et al., 2003). CNF can also be incorporated into ceramics to improve their mechanical properties, including tensile strength, toughness, and resistance to friction (Vincent, 2008).

CNF-reinforced composites have been widely used as electrodes in batteries. The main requirement for high-performance batteries is electrodes with high porosity, which allows them to contain sufficient electrolytes and satisfy the fast and long-term ion transport requirements. Ji et al. (Ji et al., 2009) succeeded in preparing porous carbon nanofibers with large accessible surface area and well-developed pore structures. They were prepared by electrospinning and subsequent heat and chemical treatments. They have been directly used as anodes in lithium-ion batteries without adding inactive materials, such as polymer binders or electronic conductors.

Adsorption

The thin filamentous shape of CNF has a large number of shallow pores in the surface regions, giving them the ideal capacity for rapid adsorption of a large amount of gas. Additionally, CNF can be functionalized with a variety of functional groups to improve their adsorbent properties. Fauteux-Lefebvre et al. (Fauteux-Lefebvre et al., 2015) synthesized iron-functionalized nanofilaments and tested them for use in the desulfurization of He gas containing 500 ppm of H_2S. In this study, the concentration of H_2S decreased to 1.5 ppm, and the carbon played two important roles: it acted both as a sulfur adsorbent and as a nanometer-scale support, which disperses iron efficiently in the form of oxide, improving the rate and efficiency of the H_2S capture.

Catalysis

The combination of several properties, including surface area, porosity, electrical and thermal conductivities, corrosion resistance, and thermal stability, makes CNF good candidates for use as a catalyst (Mestl et al., 2001) and catalyst support (Serp et al., 2003). CNM-supported catalysts are widely used for the Fischer–Tropsch reaction, and they have excellent activity and selectivity compared to conventional catalyst supports such as alumina or silica (Bahome et al., 2005, 2007; Bezemer et al., 2006). Since CNF exhibit relatively inert surfaces, pre-treatments are necessary to achieve the desired interaction with metals; therefore, surface functionalization is essential. The homogeneous deposition of cobalt on a support of carbon nanofibers was studied by Bezemer et al. (Bezemer et al., 2006), and a strong interaction has been found between cobalt and CNF activated by treatment with nitric acid at high pH. This CNM-supported catalyst was used for the Fischer–Tropsch reaction, and the C_5+ selectivity was about 53% by weight, demonstrating the usefulness and promise of CNF as a support material for the Fischer–Tropsch reaction.

Field-effect emitter

A field-effect emitter should have a high aspect ratio structure, low working function, and stable chemical properties because, at a high aspect ratio, a large amplification of electric field can be generated to achieve electron emission in low-stress electric fields. CNF seem to be a good candidate for field-effect emitters because they have a large aspect ratio as well as a small radius of curvature at their tips which is suitable for use in electronic field emission. Li et al. (H. Li et al., 2005) have cultured CNF on tungsten filament substrates by plasma-reinforced hot filament CVD. The emission property of the CNF has been measured, and the results showed that the corresponding emission current density is 20 mA/cm^2.

Supercapacitors

Some CNF have an interesting porous structure, different from conventional CNF, which has potential for energy storage. Therefore, these CNF are very attractive for use as an electrode material for supercapacitors, especially electrochemical double-layer capacitors (EDLC). Tao et al. (Tao et al., 2006) synthesized CNF with a porous structure and used them as polarized electrodes with 6 M KOH as the electrolyte for an EDLC. To prepare the carbon electrodes, 95 wt.% of purified CNF and 5 wt.% polytetrafluoroethylene (PTFE) were mixed, and the mixture was pressed into pellets. The specific capacitance of CNF was about 297

F/g, comparable to the performance of the best carbon materials. The EDLC stores charges at the electrode–electrolyte interface, and a large ion-accessible surface area is favorable for achieving a higher specific capacitance. Porous CNF have these characteristics, including a high specific surface area and good electrical conductivity, which make them an excellent material for EDLC.

Summary of overall trends for CNM growth

It is made clear in the manuscript that the factor which dominantly determines whether CNT or CNF are formed is the metal particle size, which depends on the catalyst preparation (type of support used, dispersion method), pre-treatment (H_2 reduction), and temperature. Regarding CNF, it is not yet fully understood which factor(s) is (are) the dominant one(s). All factors mentioned are interdependent and their impacts are cumulative. The metal catalyst particle is in a quasi-liquid state, and it undergoes a reshaping process during the growth, and depending on the final shape of the particle, different types of CNM are formed. So, we cannot predict satisfactorily the form of CNF formed as function of all impacting factors. Moreover, nearly all mechanisms occur simultaneously, and this is why, under the same operating conditions, different forms are obtained. Ideally, each mechanism should be studied separately under different reaction conditions, but this is experimentally impossible for the moment. Such a study should be done at nanoscale in order to see how the pure catalysts crystal types influence the mechanistic pathways under various reaction regimes.

Here are some conclusions deduced from what we presented before:

CNM types and growth mechanism

- Different types of filamentous carbon exist; SWCNT and MWCNT have an angle of 0° between the growth axis and the graphene layers, while CNF have a non-zero angle.
- Different mechanisms have been proposed for CNM growth: bulk diffusion, surface diffusion, the yarmulke model, and the VLS model.
- All growth mechanisms involve the catalytic decomposition of carbon feedstock (HC or CO), carbon diffusion, and carbon precipitation.
- Baker's model proposes that the diffusion occurs through the bulk of the catalyst, while Oberlin proposes that the carbon diffuses over the catalyst surface. For both models, diffusion is the rate-limiting step.

- The yarmulke mechanism accounts for CNT growth from very small nanometer-scale particles.
- The VLS model involves three phases: a vapor phase (HC or CO), a liquid phase (the catalyst), and a solid phase (CNM). For this model, the rate-limiting step is the surface reaction.
- The VLS model seems to be the most plausible for CNF growth because the quasi-liquid state of the catalyst has been proven by many authors.
- There are three different regions related to the growth of CNM. To develop a comprehensive understanding of the growth and control of the CNM structure, we should understand the different phenomena occurring in each region.
- The first region related to the CNM formation is the catalyst–gas interface, which determines how the HC bind and decompose. The second region is the bulk of the catalyst, in which the physical state and the chemistry dictate the carbon dissolution and the rate of diffusion through the particle. The last region is the catalyst–carbon interface, the interaction at which is responsible for the structural characteristics of the formed CNM.

Catalyst–gas interface

- Initially, the carbonaceous gas must undergo dissociative chemisorption at certain crystallographic facets of the catalytic particle to produce a significant amount of atomic carbon.
- The amount of atomic carbon produced directly impacts the amount of CNM produced.
- The reactivity of the metallic catalyst toward the dissociative chemisorption of carbonaceous gases can be enhanced by adding adatoms or co-adsorption of certain gases.
- Fe and Ni (100) and (110) are the most suitable facets for HC decomposition.
- Bimetallic catalysts favor the "end-up" HC adsorption configuration, which leads to the formation of filamentous carbon; monometallic catalysts tend to favor the "parallel" configuration, which leads to the formation of encapsulating carbon.
- Bimetallic catalysts are preferred to be made of a combination of transition metals and adatoms that are not capable of chemisorbing HC, such as Cu and Ag.
- The nature of the gas phase is also important. HC and CO are usually used as carbon sources.

- Unsaturated HC are more reactive and are favored for CNM growth.
- The presence of CO/CO_2 in the reactive gas prevents the polymerization of HC and thus prevents the formation of encapsulating carbon.
- H_2 is known to satisfy the valence of the dangling bonds of edge atoms, which permits the formation of CNF.

The bulk of the catalyst

- The catalyst exists in a quasi-liquid state at relatively high T (above 700°C) because of its nanometer-scale size, which allows the high mobility of surface atoms, leading the metal to spread on the graphene sheet.
- This high mobility is due to the interfacial effect between the graphene sheet and the catalyst surface, which causes the weakening and breaking of metal bonds.
- Some authors suggested that only the surface of the particle exists in a quasi-liquid state.
- Both metal melting point and carbon concentration depend on the particle size; at nanometer-scale size, the melting point decreases, and the carbon concentration increases.
- For iron-based catalysts, the metal is the active phase for producing atomic carbon from HC decomposition, and after saturation with carbon, a metal–carbon quasi-liquid solution with a high carbon concentration will decompose into carbon and carbide.

Catalyst–carbon interface

- Carbon forms on metallic facets, which provide a strong epitaxial fit with graphene.
- For Ni-based catalysts, the most favored crystallographic facets for the precipitation of carbon are Ni (111) and Ni (311); for Fe-based catalysts, the (1−1 0) facets are the most suitable planes for the growth of carbon because they have the appropriate distances to overlap with the lattice of the graphene sheet, and for Co-based catalysts, the appropriate plane is (111).
- The forces between the metallic surface and graphene sheet put the particle in a quasi-liquid state, which facilitates its reshaping process.
- The addition of adatoms, for example, Cu and some gases, such as H_2, can also impact the reshaping process of the catalyst.

Other factors

- Other factors impacting CNM growth are temperature and metal–support interaction, as well as HC feed rate and pressure.
- High temperature accelerates the HC decomposition and carbon diffusion rate but also accentuates the sintering phenomena and HC thermal decomposition, which leads to the formation of pyrolytic carbon and larger-diameter CNM.
- A weak catalyst–support interaction favors the sintering phenomena, while a strong interaction decreases the surface accessible to the HC.
- The low partial pressure of HC yields less atomic carbon and, thus, a lower yield of CNM, while high partial pressure of HC leads to the formation of encapsulating carbon.

Catalyst morphology vs. CNM morphology

- The size of the catalytic particle is the most important factor for the nucleation of SWCNT. When the catalyst particles are a few tens of nanometers, CNT is produced instead of CNF, especially in the absence of dangling bonds terminating species, such as H_2.
- The particle shape has an impact on the type of CNM formed. The decomposition occurs in one facet and the precipitation in another one, and the graphene layer grows parallel to the surface.
- The catalyst particle usually has a spherical shape following preparation. However, under certain conditions, the catalyst particle is reconstructed into different shapes, which drive the formation of different types of CNF.
- Monodirectional growth occurs when the carbon precipitates from a single facet, bidirectional growth occurs from 2 opposing facets of a symmetric diamond-shaped particle at an identical rate, and multidirectional or octopus-like CNM forms when the growth occurs from different neighboring facets of the same crystal.
- Polyhedral and faceted particles produce both P-CNF and CS-CNF. P-CNF grow from a single facet, while CS-CNF grow from at least three adjacent facets.
- HC-CNF are formed when the graphene sheet apex becomes discontinuous.
- The driving force of switching between the different morphologies is related to the energetic costs of curving a graphene sheet and the existence of edge atoms with dangling bonds.

- Minimizing the strain of curving the graphene sheet has priority over minimizing the number of edge atoms.
- For large particles (around 100 nm), there is competition between P-CNF and CS-CNF. The determining feature is the angle between the facets. CS-CNF is preferred for angles between adjacent crystal facets of about 80–100° since the strain supported by the curved sheet will not be high, while sharper angles favor the platelet texture.
- For intermediate-sized particles (around 50 nm), CNF tend to form in both herringbone morphologies, solid and hollow core. The determining factor here is also related to the maximum bending strain of a graphene sheet, which is also related to the angle between the crystal facets. Angles between 80–90° allow the formation of CS-CNF, while sharper angles between facets favor the formation of HC-CNF.
- When catalyst crystals are elongated and terminated with a truncated cone, CNF form according to the hollow core herringbone morphology. The inner cavity is well defined and has a diameter that depends on the inactive facet at the cone apex.
- CNM helical growth is achieved when the crystallographic facets of the catalytic particle have different precipitation characteristics that lead to anisotropic growth.

2.2.4. CNM synthesis from waste plastic via the pyrolysis–catalysis process

Reactor design

The first factor impacting CNM yield is the reactor design, and different configurations of the two-stage process are described in this article. There are different ways to conduct the pyrolysis–catalysis process. The first model, which is exclusively used for laboratory-scale synthesis, uses one reactor, which is a two-stage, fixed bed, semi-batch reactor system where the two stages are independently heated and controlled, as shown in Figure 2. *8*. In the first stage, waste plastics are not continuously fed but are held in a quartz boat or on a stainless steel (SS) mesh. The catalyst is usually supported by a SS wire mesh on a perforated plate placed in the middle of the second catalytic stage, which is preheated to a certain catalysis temperature, T_c. When the second-stage temperature is reached, the boat containing the plastic sample is introduced in the middle of the first reactor and is heated until the pyrolysis temperature, T_p, is reached. An inert gas is used as a carrier gas (Acomb et al., 2016; Yao et

al., 2017; Yao, Zhang, et al., 2018). In this type of reactor, all the HC produced from plastic pyrolysis (both condensable and non-condensable gases) are used to grow CNM.

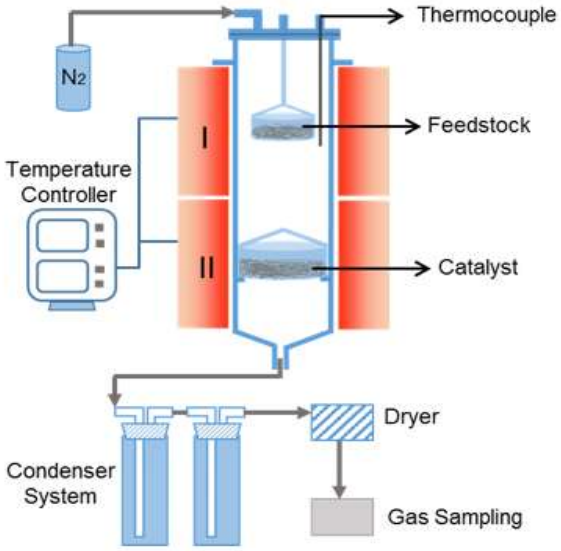

Figure 2. 8 Schematic diagram of the pyrolysis–catalysis semi-batch two-stage reactor adapted from (Yao & Wang, 2020).

The second type of reactor conducts pyrolysis and catalysis in two separate reactors, working in a continuous mode and enabling the production of a greater volume of CNM and the possibility of subsequent commercialization of the process.

The pyrolysis of waste plastics produces a mixture of gases with a wide range of molecular weights; the mixture is more complex when mixed plastics are used as the feedstock. To overcome this problem, an intermediate step has been introduced to condense gases with high molecular weight into pyrolysis oil so that only small molecules in the gas phase (C_4 and less) enter the catalytic reactor. The pyrolysis of plastics takes place in the first reactor, which is heated to a certain T_p, then the products pass through a condenser at room temperature to remove the condensable oils. Finally, the non-condensable gases enter the second-stage reactor, where the synthesis of CNM on a catalyst bed occurs at a certain T_c (Aboul-Enein et al., 2017, 2018; Veksha et al., 2017, 2018). Other authors have used distillation instead of condensation, including Borsodi et al. (Borsodi et al., 2016), who studied the production of CNM from different virgin and waste plastics (HDPE, PP, PS, PA, PVC, and municipal plastic waste). They used a double-stage process as shown in Figure 2. *9*; the first step was pyrolysis in an electrically heated tubular reactor that contained a special

screw to reduce coke deposition at 560–570°C without catalysts. An atmospheric distillation column was used to separate the pyrolysis products into gases, pyrolysis oil, and heavy oil. The non-condensable gases were fed into a catalytic CVD reactor at 700°C.

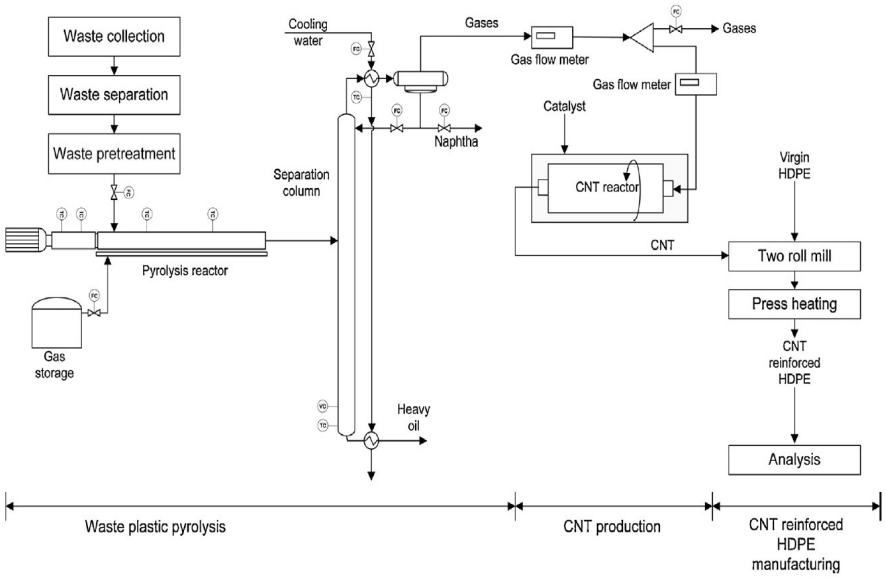

Figure 2. 9 Schematic diagram of the pyrolysis–catalysis continuous process using two separate reactors with an intermediate distillation step adapted from (Borsodi et al., 2016).

The introduction of a condensation or distillation step is advantageous for improving the quality of the CNM formed since low molecular weight molecules, especially unsaturated ones, have been reported to be better precursors than long-chain HC and aromatics for filamentous carbon formation (Argyle & Bartholomew, 2015). However, the disadvantage of this configuration is the reduced yield of CNM, which occurs because a large part of the carbon contained in the plastic is removed with the pyrolytic oil before entering the catalysis reactor. To overcome this problem, other authors have developed a new design that cracks the condensable HC instead of removing them, leading to the transformation of most plastics into light HC gases (Aboul-Enein & Awadallah, 2018, 2019).

The use of fixed bed reactors, which require low cost and simple design technologies, remains limited on a laboratory scale, as they have the disadvantages of poor heat transfer rates and poor gas–solid contact. This limitation remains a major challenge for the economic feasibility of the process scale-up. In addition, the quantities of carbon deposited on the catalyst cause blockage in the reactor, necessitating frequent stoppages. Developing a reactor

with a suitable design, which can operate in continuous mode, allow the addition and removal of the catalyst, and the easy recovery of the deposited carbon, is indispensable in industrial terms.

Over the past decade, attention has shifted to the study of fluidized bed reactors (FBR) due to the ease of recovery of CNM and their excellent heat and mass transfer properties. For example, Barbarias et al. (Barbarias et al., 2018) have performed the pyrolysis of waste plastics in a conical spouted bed reactor at 500°C. Then, pyrolysis volatiles were reformed in a FBR at 700°C (Figure 2. *10*).

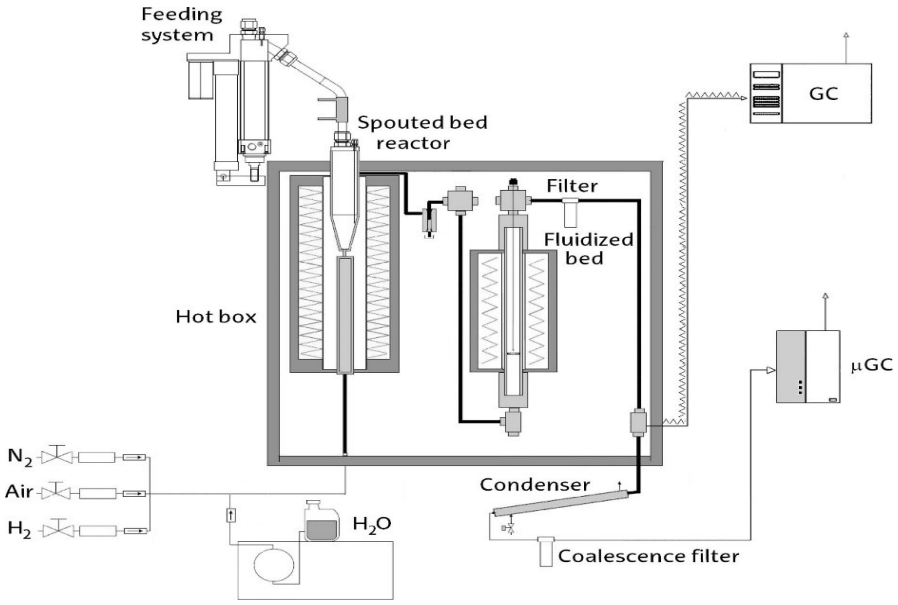

Figure 2. 10 Scheme of the pyrolysis and in-line reforming bench-scale plant (Barbarias et al., 2018).

Lui et al. (J. Liu et al., 2011) used a two-stage reaction system: a screw feeder was used to feed the waste polypropylene (PP) continuously into a screw kiln reactor for the pyrolysis reaction, followed by a condenser to condense pyrolysis oil, and the non-condensable gases pass through a moving-bed reactor for CNM production (Figure 2. *11*).

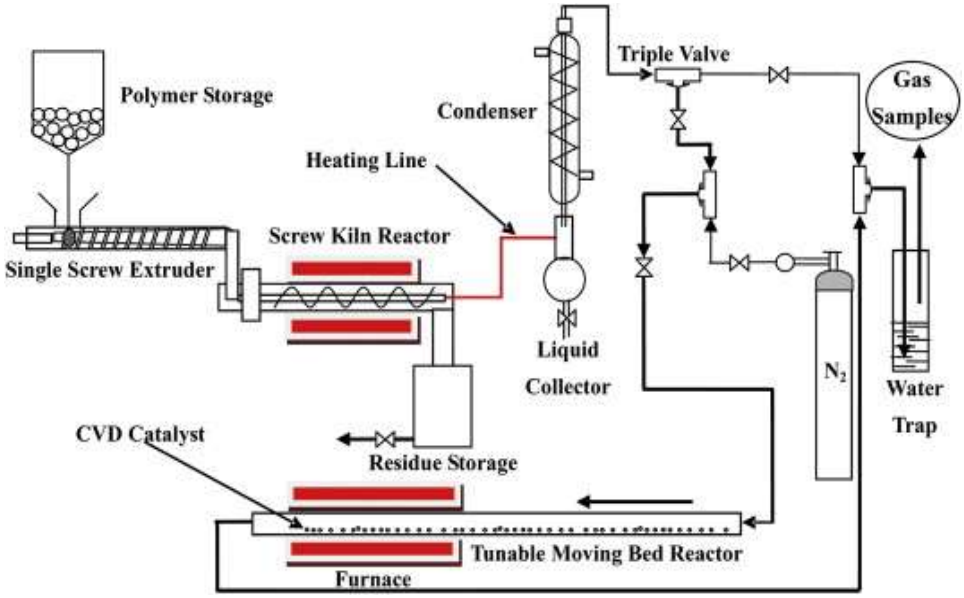

Figure 2. 11 Schematic diagram of the pyrolysis–catalysis continuous process using two separate reactors with an intermediate condensation step adapted from (J. Liu et al., 2011).

Yang et al. (R.-X. Yang et al., 2015) used a fluidized bed gasifier where the plastic waste (PP+PE) was continuously supplied, and the produced gases were filtered using a cyclone and column filter to remove the solid particulates, and they were passed through three parallel fixed bed catalytic reactors (Figure 2. 12) to co-produce H_2 and CNT.

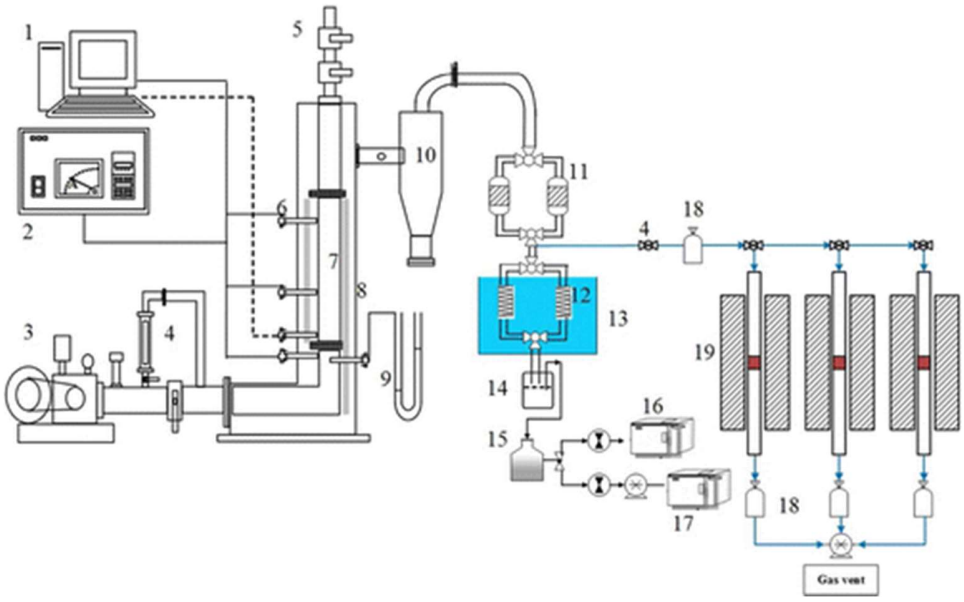

Figure 2. 12 Diagrammatic illustration of the gasification system: (1) computer, (2) TIC, (3) blower, (4) flow meter, (5) feeder, (6) thermocouple, (7) sand bed, (8) electric resistance, (9) U manometer, (10) cyclone, (11) column filter, (12) trapping tube, (13) cooler, (14) gas-washing bottles, (15) backup absorber, (16) Gas chromatogram/Thermal conductivity detector, (17) Gas chromatogram/Flame ionization detector, (18) sampling place, and (19) catalysis reactor cyclone and column filter to remove particulates and (R.-X. Yang et al., 2015).

Other researchers have developed novel configurations; for example, Bajad et al. (G. S. Bajad et al., 2017) have developed a new reactor configuration that consisted of several compartments to convert plastic waste into liquid HC, MWCNT, and H_2-rich synthesis gas. Their reactor design is based on co-central cores, as shown in Figure 2. *13*. The pyrolysis of plastic waste was carried out in the external chamber of the reactor, the products exited the reactor and passed to a condenser where oil and water will condense, to be evacuated from the bottom, and the non-condensable gases returned to the reactor where they catalytically decomposed into MWCNT in the internal chamber. Heat has been provided in the annulus to heat both chambers and reduce the need for energy.

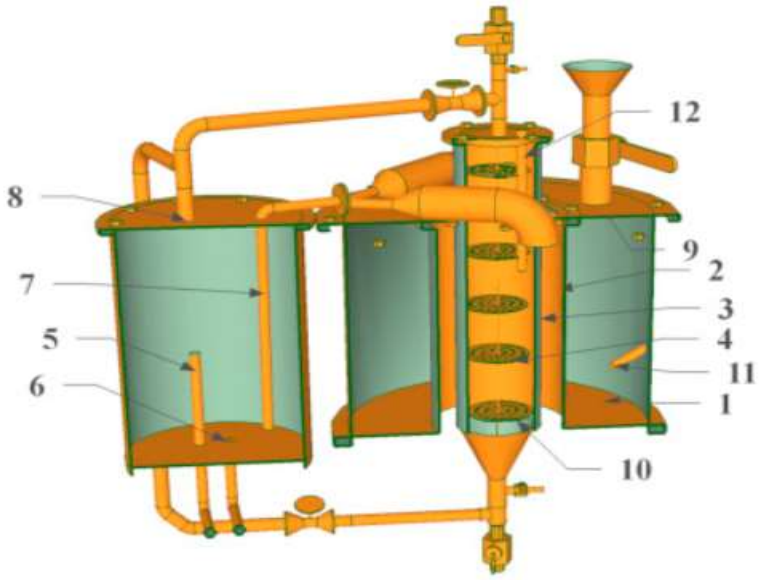

Figure 2. 13 Reactor cut section showing inner chambers and catalyst tray arrangement. (1 – pyrolysis chamber, 2 – heating chamber, 3 – CNT chamber, 4 – catalyst tray, 5 – oil drain line, 6 – water drain line, 7 – pyrolysis gas line to condenser, 8–non condensable gases to CNT chamber, 9 – Plastic feeder, 10 – first tray, 11 & 12 – thermo well) (G. S. Bajad et al., 2017).

Feedstock

Pyrolysis gases can be produced from a single plastic or a mixture of plastics. The resulting gas composition and yields vary with the type of feedstock plastic, but it is typically composed mainly of unsaturated gases such as ethylene, propylene, and butene, which makes it suitable to produce H_2 and CNM. PE and PP are usually used as precursors because of their high carbon content [110], and their main pyrolysis products are alkenes (Wampler, 1989). However, real-world waste plastics, especially municipal waste plastics, are composed of a mixture of polymers. Thus, the composition of the gas produced from their pyrolysis is complex and contains contaminants such as HCl, which originates from polyvinyl chloride (PVC). These contaminants are not desired for upstream processes, and a removal step is required (Bhaskar et al., 2003; Karayıldırım et al., 2005; Zhou et al., 2004). A dechlorination process is needed to reduce the chlorine content in the pyrolysis products. There are several methods of dechlorination, such as stepwise pyrolysis (i.e., two-step pyrolysis), catalytic pyrolysis, or the addition of chlorine adsorbents during the reactions. In stepwise pyrolysis,

the plastic is heated at a low temperature to decompose PVC and capture HCl. In the second stage, the remainder solid phase is heated to high temperatures. López et al. (López et al., 2011) have performed the stepwise pyrolysis of a mixture of plastics containing PVC. They reported that more than 50 wt% of the chlorine could be removed. However, the authors have noticed that stepwise pyrolysis leads to the formation of heavy hydrocarbons. Some researchers investigated the effect of superheated steam with catalysts and adsorbents on the dechlorination of PVC. Nishibata et al. (Nishibata et al., 2020) have found that the CaO catalyst/adsorbent caused more dechlorination than other metal oxides, including Fe_3O_4, SiO_2, Al_2O, $Ca(OH)_2$, and MgO, in the presence of superheated steam. The temperature is increased by the exothermic reaction of CaO with steam, which promotes the PVC degradation. The newly formed HCl reacts with CaO and $Ca(OH)_2$ to form calcium chlorides such as $CaCl_2$ and CaClOH. Other studies have also shown that, in superheated steam, metal oxides have better dechlorination ability than solid acid catalysts such as zeolite and alkali adsorbents (Hapipi et al., 2018). Most industrial applications use additives in the plastic feedstock to remove HCl (Plastics, 2021). They also use an alkaline solution to wash the gas in a scrubber to remove all acids present in the stream (Scheirs, 2006). Agilyx (Plastics, 2021) is the only current technology capable of handling plastic waste containing up to 70% PVC. This is achieved by stepwise pyrolysis. In the first step, the plastic is heated under vacuum inside a batch reactor. In this pre-treatment step, the moisture and the HCl are separated from the feedstock (DeWhitt, 2012).

Aboul-Enein et al. (Aboul-Enein et al., 2018) synthesized CNM via pyrolysis of different types of plastic waste (high density PE (HDPE), low density PE (LDPE), PP, PS, and PET) using a two-stage process with an intermediate condensation step to remove the oil. Pyrolysis was carried out at 700°C**,** and a catalytic reaction occurred at 650°C over a Ni–Mo/Al_2O_3 catalyst. The yields of non-condensable gases passing to the catalytic reactor were 72,5, 70,7, 62, 35,5, and 22,4% for LDPE, PP, HDPE, PET, and PS, respectively, which were directly correlated with the CNM yield from the catalytic reactor. In addition, PET or PS waste pyrolysis gave the largest amount of residue and char. The pyrolysis of PP and LDPE produced a high gas yield due to the presence of branched chains, the decomposition of which gives HC of lower molecular weight. HDPE has a linear carbon chain, making it more difficult to break down into HC lighter than other polyolefins (Syamsiro et al., 2014). In

contrast, PET has a high oxygen content, and its pyrolysis leads to the formation of oxygenated and aromatic compounds and lower concentrations of gaseous HC (Day & Wiles, 1984), while PS pyrolysis leads to the production of a large liquid fraction containing mainly styrene, toluene, and ethylbenzene (Miandad et al., 2017). The morphology and crystallinity of the CNM produced also depend on the plastic waste used. MWCNT with a high degree of graphitization were obtained from PP and LDPE, while HDPE led to the formation of MWCNT with a rugged surface. When PET waste was used, less crystalline MWCNT with uniform diameters were produced, and from PS waste, only a few MWCNT with structural defects were observed (Aboul-Enein et al., 2018).

Veksha et al. (Veksha et al., 2017) investigated the production of CNM from LDPE, PP, PS, PET, and a mixture of four plastics (MP), containing 40 wt.% LDPE, 40 wt.% PP, 10 wt.% PS, and 10 wt.% PET in a separate two-stage system with an intermediate condenser to remove condensable oils. T_p was 600°C, and the catalysis reaction using a Ni-$CaCO_3$ catalyst occurred at either 500 or 800°C. Neither PS nor PET yielded good results in terms of the quality and quantity of CNM produced. For PE and PP, similar yields of MWCNT with similar properties were produced at 800°C regardless of the plastic feedstock. At this high temperature, before reaching the catalyst bed, the non-condensable gases underwent an additional decomposition into intermediate products (i.e., methane and ethylene), which made the composition quasi-similar, no matter which plastic feedstock was used. At 500°C, the composition of the non-condensable pyrolysis gases did not change after entering the catalytic reactor; therefore, the CNM produced had different yields and structures. This difference implies that the influence of plastic type on CNM properties is more pronounced at a lower synthesis temperature. The carbon yield was 31% for PP, 21% for LDPE in the form of MWCNT, and 3% for the MP in the form of a mixture of CNC and MWCNT, in addition to amorphous and encapsulating carbons. The lower carbon yield using MP was attributed to the presence of PET and PS, while the lower carbon yield from LDPE compared to PP was attributed to the lower concentration of unsaturated HC in the LDPE pyrolysis gas at T_p = 600°C.

Real-world waste plastics were also investigated (Aboul-Enein & Awadallah, 2019; Wu et al., 2014; Wu & Williams, 2010b; Yao, Zhang, et al., 2018). Yao et al. (Yao, Zhang, et al., 2018) have studied the production of CNM and H_2 from a mixture of real-world plastics

using a Ni-Fe/Al_2O_3 catalyst. The mixed plastic waste composition comprised 40 wt.% sample bottles (mainly HDPE), 35 wt.% plastic bags (mainly LDPE), 20 wt.% preservative boxes (mainly PP), and 5 wt.% lunch boxes (mainly PS). The pyrolysis–catalysis process was conducted in a two-stage fixed bed reactor without an intermediate condensation stage, T_p was about 500°C, and T_c was 800°C. They found that the deposited carbon was mainly filamentous with a high yield (287 $mg/g_{plastic}$); however, a large quantity of amorphous carbon was also observed.

The addition of other gases to the pyrolysis gas has been reported to improve the yield and quality of the CNM. Several studies have shown that the addition of steam or other oxygenated compounds (i.e., ethanol or CO_2) can promote the growth of filamentous carbon by removing the amorphous carbon that coats the catalyst particles (Acomb et al., 2014; Futaba et al., 2009a, 2009b; Guellati et al., 2012; Wu et al., 2014). Guellati et al. (Guellati et al., 2012) have demonstrated that adding a small amount of ethanol (up to 9 vol%) improved the growth rate and quality of the vertically aligned MWCNT. Moreover, the addition of steam or CO_2 in the second stage to trigger steam reforming and dry reforming, respectively, has been widely studied. The presence of CO or CO_2 in the gas passing to the second stage can result from the presence of oxygen in the feedstock (i.e., PET) or if a gasification step is used to decompose plastics instead of pyrolysis. Yang et al. (R.-X. Yang et al., 2015) have studied the gasification of plastic waste (PP+PE) by air which yielded a mixture of different gaseous products (H_2, CO, CO_2, CH_4, and C_2–C_5 gaseous HC), which were conducted to 3 parallel fixed bed reactors of Ni-Al_2O_3 catalyst, where decomposition occurred. When the reaction temperature increased from 600 to 750°C, both CH_4 and C_2–C_5 HC concentrations in the outlet gas decreased, and the H_2 production rate, H_2 yield, and CNM yield increased. At high temperatures, the dry reforming of methane, dry reforming of HC, and direct decomposition of HC are favored. Thermogravimetric analysis (TGA) has indicated that CNM growth at 680°C possessed a higher degree of graphitization (R.-X. Yang et al., 2015). However, the presence of CO_2 at higher catalysis temperatures has a negative impact on CNM yield since the reverse Boudouard reaction is favored. Saad et al. (Saad et al., 2015) have observed that the addition of CO_2 during the pyrolysis–catalysis of HDPE with Ni-Mg-Al at 800°C led to the reduction of carbon deposition from 43.5 g/100g plastics to 15 g/100g.

The same authors have presented the same results using another catalyst, Ni-Al (Saad, Nahil, Wu, et al., 2015).

Wu et al. (Wu et al., 2014) have studied the influence of steam on the pyrolysis–catalysis process of different types of plastics. The plastics consisted of a mixture of MOC, commercial waste HDPE, and HDPE waste containing 1 wt.% PVC. The PVC present in the waste HDPE reduced the CNM yield and increased the fraction of amorphous carbon over filamentous carbon. The addition of steam in the process resulted in a significant decrease in the overall carbon yield, and the fraction of filamentous carbon over amorphous carbon increased (Table 2. *3*), which means that the steam reacted more with the amorphous carbon than the filamentous carbon. In addition, smoother MWCNT were observed in the scanning electron microscopy (SEM) analysis when steam was present during the process. Nahil et al.(Nahil et al., 2015) have also reported that the addition of steam reduces the carbon yield due to the gasification of the deposited carbon. However, the quality of the carbon in terms of purity and morphology seemed to be improved. They have also reported that at a high steam injection rate, MWCNT could barely be observed.

Table 2. 3 Production of carbons from pyrolysis-reforming of motor oil containers (MOC) and commercial waste HDPE using Ni-Mn-Al catalyst (Wu et al., 2014).

	Motor Oil Containers		**Commercial Waste HDPE**		**Commercial Waste HDPE Mixed With 1 wt.% PVC (HDPE/PVC)**	
	no steam	**with steam**	**no steam**	**with steam**	**no steam**	**with steam**
Amorphous carbon (AC) (g/100g plastics)	12,2	5,2	15,4	2,4	20,9	4,7

Filamentous carbon FC (g/100g plastics)	33,8	16,8	32,6	16,6	25,1	11,3
ratio AC/FC	0,37	0,31	0,47	0,15	0,83	0,42
Filamentous carbon type	MWCNT with an average length of 1 µm	Smooth and uniform MWCNT with an average length of 10 µm	MWCNT with an average length of 1 µm	More crystalline, smooth, and uniform MWCNT with an average length of 10 µm	MWCNT, which were entangled more densely	
Total carbon (wt%)	46.0	22.0	48.0	19.0	46.0	16.0

Another key factor in CNM production, besides the nature of the feedstock, is the rate at which the feedstock is used. Acomb et al. (Acomb et al., 2015) have reported that the yield of CNM obtained decreased as the amount of feedstock used increased, 29,2 wt.%, 17,9 wt.%, and 13,12 wt.% from 0,5 g, 1 g, and 1,25 g of LDPE, respectively. However, the amount of deposited carbon relative to the weight of the catalyst increases, as 292 mg $C/g_{catalyst}$ was formed at 0,5 g LDPE and 358 mg $C/g_{catalyst}$ at 1 g LDPE. Therefore, at higher feedstock rates, the percentage of feedstock converted is reduced; however, a larger amount of CNT per gram of catalyst is obtained. When the mass of plastics increases, the flow of the gases passing to the second catalytic stage increases, and with the same catalyst weight, the space velocity will increase, and, consequently, the residence time will decrease. Thus, not

all gases can access the catalyst surface to decompose, yielding fewer deposited solids and a larger amount of HC in the exit gas since they do not have the opportunity to react (Acomb et al., 2015).

Catalysts

Transition metal-based catalysts (Ni, Fe, and Co) are the most commonly used. Monometallic, bimetallic, and trimetallic catalysts have been tested. The catalyst support is also an important factor for the synthesis of CNM. Interaction with the support can stabilize the dispersion and the size distribution of the metal particles (K. A. Shah & Tali, 2016).

Monometallic catalysts

Many researchers have investigated monometallic catalysts. Acomb et al. (Acomb et al., 2016) have studied the effect of different transition metal-based catalysts (Ni, Fe, Co, and Cu) supported by alumina for the production of CNM from the pyrolysis–catalysis of LDPE. Using Ni, Fe, and Co catalysts, filamentous carbon was formed, mainly as MWCNT, but also as amorphous carbon with different yields. Both Ni and Fe catalysts gave a significant filamentous carbon yield, in contrast to Co, which had a very low yield, and Cu, which yielded no filamentous carbon. The difference in yield was attributed to the metal–support interactions, which were strong for Fe and Ni and very weak for Co and Cu, and led to the formation of large particles, reducing the growth rate because of the low surface area. Although the Fe catalyst had a similar metal–support interaction to the Ni catalyst, proved by temperature programmed reduction (TPR), its yield was higher, which indicates that the metal–support interaction is not the only factor impacting the MWCNT yield. Fe has a large carbon solubility compared to other metals, which could explain the higher yields since the solubility increases the amount of carbon available for CNM growth (W.-W. Liu et al., 2013; Moisala et al., 2003). Thus, the higher yield when an Fe-based catalyst was used results from the combination of two factors, desirable catalyst–support interaction and large carbon solubility. Other advantages of Fe-based catalysts are that their preparation is less expensive because Fe precursors are less expensive and they are environmentally friendly (Torres et al., 2014).

Yao et al. (Yao, Zhang, et al., 2018) have also shown that the Fe/Al_2O_3 catalyst produced the highest CNM yield compared to other metal catalysts. Using Raman spectral analysis,

they have observed that the carbon deposited over a Ni-based catalyst has a lower quality in terms of graphitization when compared to an Fe-based catalyst. They have also studied the influence of different types of supports, γ-Al_2O_3 and α-Al_2O_3. Better yields and morphology have been reported with the use of γ-Al_2O_3 supports, as presented in Table 2. *4* and Table 2. *5*. This difference between the γ and α alumina may be due to the smaller size of the metal particles of Ni and Fe deposited on the γ-Al_2O_3 support than those of the α-Al_2O_3 support. And as discussed in section 0, the catalyst particle size is a crucial factor for the growth of CNM.

Table 2. 4 Separate double stage processes without intermediate step (influence of catalyst)

Feedstock	**Catalyst**		**T of pyrolysis (°C)**	**T of catalysis (°C)**	**Filamentous carbon formed**		**Amorphous carbon yield (g/100g plastic)**	**Reference**
	Active metal	**Support**			**Morphology (diameter)**	**Yield (g/100g plastic)**		
LDPE	Ni	γ-Al_2O_3	600	800	MWCNT (15–30 nm)	4,57	4,99	(Acomb et al., 2016)
	Fe				MWCNT (5–30 nm)	17,9	0,08	
	Co				long thin MWCNT (5– 20 nm)	0,6	6,8	
	Cu				none	none	4,7	

	Fe	Al_3O_3	800	750	MWCNT	6,4 (vol %)[a]	n. d.	. (Arnaiz et al., 2013)
	Fe	γ-Al_2O_3	600	800	More densely packed MWCNT (20–30nm)	17,9	1	(Acomb et al., 2015)
				700	MWCNT (20–30nm)	21,3	0,5	
				900	Thick CS-CNF (30–60 nm)	2	4,5	
HDPE	Ni	Stainless steel mesh	500	800	MWCNT and CS-CNF	33,4	0,56	(Zhang et al., 2017)
	Ni	ZSM5-30	500	850	Filamentous carbon	10,61	n. d.	(Yao, Yang, et al., 2018)
	Ni	ceramic	500	600	CNT (10 nm)	7,2	2,1	(X. Liu et al., 2018)
				700	large number of long CNT	6	1,2	

				800	Few CNT (21.2 nm)	1,2	1,2	
PP	Fe	SiO_2	600	800	Large MWCNT (98 nm)	29 [b]	n. d.	(X. Liu et al., 2017)
	Ni				MWCNT (23 nm)	16 [b]	n. d.	
	Ni-Mn	Al_2O_3	500	800	Smooth and thin filamentous carbons with an (~20 nm)	62	n. d.	(Nahil et al., 2015)
	Ni-Ca				Difficult to observe filamentous carbons	n, d,	n. d.	
	Ni-Ce							
	Ni-Zn							
	Ni-Mg							
	Ni-	-	500	800	MWCNT (~30 nm)	52,6	5,1	

	Mn-Al (1:1:1)							(Wu et al., 2016)
	Ni-Mn-Al (2:1:2)					41,8	4,8	
Mixed plastic waste	Fe	γ-Al_2O_3	500	800	Smoother and smaller diameter bamboo-like CNT	19,5	13	(Yao, Zhang, et al., 2018)
		α-Al_2O_3			Bamboo-like CNT	19	16,2	
	Ni	γ-Al_2O_3			MWCNT (20 nm)	14	7,1	
		α-Al_2O_3			Bamboo-like CNT (40–50 nm)	10	15	
Mixed	Ni		500	800	MWCNT (20 nm)	14	7,1	(Yao, Zhang

plastics	Ni-Fe	γ-Al_2O_3		800	MWCNT with a large range of diameters	28,7	12	, et al., 2018)
				700	Bamboo-like CNT (20–40 nm)	25,8	17,4	
				900	CS-CNF	36	80	
Real MP (40 wt.% sample bottles (mainly HDPE), 35 wt.% plastic bags (mainly LDPE),	Ni-Fe (1:1)	γ-Al_2O_3	500	800	MWCNT (10–40 nm) with 3–10 nm wall thicknesses .) MWCNT formed on Ni-Fe (2:1), and Ni-Fe (3:1) were much thinner than those formed on Ni-Fe (1:3) and Ni-Fe (1:2)	45,8	n. d.	(Yao et al., 2017)
	Ni-Fe (1:2)					49,9	n. d.	
	Ni-Fe (1:3)					50,9	n. d.	
	Ni-Fe					45,1	n. d.	

20 wt.% preservative boxes (mainly PP) and 5 wt.% lunch boxes (mainly PS).)	(2:1)							
	Ni-Fe (3:1)					45,8	n. d.	

[a] Percent with respect to carbon volume in ethylene and propylene feeds (carbon in CNT/carbon in feed HC stream).
[b] Total carbon, including filamentous and amorphous

Table 2. 5 Separate double stage processes with intermediate step to remove pyrolysis oil (influence of catalyst)

Feedstock	**Catalyst**		**T of pyrolysis (°C)**	**T of catalysis (°C)**	**Filamentous carbon formed**		**Amorphous carbon yield**	**Reference**
	Active m	**Support**			**Morphology**	**Yield (g/100g**		

	et al					**plastic)**	**(g/100g plastic)**	
LDPE	Fe	MgO	400 °C	750 °C	Large-diameter CNF and MWCNT as well as very thin CNT	41,2	n. d.	(Abou l-Enein & Awad allah, 2018)
	Fe-Mo (40 % de Mo)				CNF-CNT hybrid materials	97,6	n. d.	
	Ni	$CaCO_3$	600	500	mainly MWCNT	21	n. d.	(Veksha et al., 2017)
				800	MWCNT with different diameters	23	n. d.	
PP	Ni	La_2O_3	500	700	MWCNT with different diameters	34,8	n. d.	(Abou l-Enein

	Ni-Cu				a mixture of large-diameter CNF and MWCNT	51,9	n. d.	et al., 2018)
	Fe	silica-alumina	570	700	uniform diameter MWCNT	13	n. d.	(Borsodi et al., 2016)
	Ni	$CaCO_3$	600	500	mainly MWCNT	32	n. d.	(Veksha et al., 2017)
				800	larger-diameter MWCNT	25	n. d.	
Mixed plastics (PE, PP, PS, PVC, and PET, obtained from shopping bags,	Ni–Mo	MgO	700	800	MWCNT with well-aligned graphene walls	11,05	n. d.	(G. Bajad et al., 2017)

chemical containers, PS–foams, vinyl pipes, and soft drink bottles, respectively)								
0,5 waste HDPE + 0,5 waste PP	Fe	silica-alumina	570	700	uniform diameter MWCNT	11	n. d.	(Borsodi et al., 2016)
93,1 %HDPE +4,9						17	n. d.	

%PP +0,2 %PVC+1, 8%label and paper								
MP (0,4 LDPE, 0,4 PP, 0,1 PS and 0,1 PET)	Ni	$CaCO_3$	600	500	MWCNT and nanocages	3	n. d.	(Veksha et al., 2017)
				800	larger-diameter MWCNT	23	n. d.	

Bimetallic and trimetallic catalysts

The addition of one or two other metals to the main metal of the catalyst has been widely studied because these bimetallic or trimetallic catalysts have a desirable synergy between the metals, which gives them good stability, smaller metal particle size (Kaya et al., 2015), and other advantages as discussed in section 0.

Yao et al. (Yao et al., 2017) have studied the pyrolysis–catalysis of mixed plastics using a two-stage fixed bed reactor with Ni and Fe catalysts in varying molar ratios. The bimetallic Ni-Fe catalysts were prepared with metal nitrates and γ-Al_2O_3 using the impregnation method. The thermal stability and graphitization of the carbon formed were enhanced when the Ni to Fe molar ratio was increased. In addition, the CNT produced were

found to be thinner when the amount of Ni in the catalyst was increased. Additional Ni enhanced the interaction between the metal oxides and Al_2O_3, which better dispersed the Ni on the surface of the support and yielded better CNM, as a strong metal–support interaction leads to well-dispersed small catalyst particles and prevents their sintering (Cargnello et al., 2013).

Aboul-Enein et al. (Aboul-Enein et al., 2018) have studied the effect of adding Cu to a Ni-La_2O_3 catalyst on the decomposition of the non-condensable gases produced from the pyrolysis of PP. In this study, the highly dispersed Ni particles were responsible for the growth of MWCNT, while the bimetallic Ni-Cu alloy was in a quasi-liquid state, which increased the metal particle sizes and led to the formation of large-diameter CS-CNF. The La_2O_3 support played a crucial role by maintaining good dispersion of Ni particles on its surface, which led to the formation of narrow MWCNT with uniform diameters. However, the Ni-Cu alloy particles either elongated or contracted during the decomposition of the HC as a result of their quasi-liquid state nature, promoting the formation of large-diameter CNF. Metal particles in a quasi-liquid state can be fragmented and hence encapsulated within the nanocarbon structure.

The same authors (Aboul-Enein & Awadallah, 2018) have studied the effects of adding Mo to Fe catalysts. The carbon yield and quality were found to be better using Fe-Mo-MgO compared to Fe-MgO. When using Fe-MgO, a mixture of MWCNT and large CNF were produced due to the heterogeneity in particle sizes. The non-interacting Fe_2O_3 species rapidly agglomerated during the pre-reduction step to form large metallic Fe particles, which caused the growth of large-diameter CNF. Meanwhile, the highly dispersed Fe particles in $FeMgO_4$ were responsible for the growth of MWCNT. The addition of Mo enhanced the dispersion and stabilization of the metal particle sites, which enhanced the interactions between all of the catalyst components to form various composite oxide species and led to high activity and the growth of narrower hollow MWCNT with relatively uniform outer diameters ranging from 10 nm to 30 nm. Several other studies have reported that the addition of Mo to Fe-based catalysts promoted their catalytic activity by protecting the Fe particles from agglomeration (Ago et al., 2006; Lamouroux et al., 2007; Yoshida et al., 2009).

Nahil et al.(Nahil et al., 2015) investigated the production of CNM from the pyrolysis–catalysis of PP in the presence of steam using ternary mixed oxide types of Ni-

Metal-Al catalyst (molar ratio 1:1:1), where the metal was Zn, Mg, Ca, Ce, or Mn. Long, smooth, and thin filamentous carbons with an average diameter of about 20 nm were produced only with Ni-Mn-Al. The other catalysts produced more amorphous carbon than filamentous carbon. The addition of Mn to Ni proved to be beneficial. Wu and Williams have performed pyrolysis–catalysis experiments to produce CNM from PP (Wu et al., 2016). The T_p of the first stage was 500°C, while the catalytic bed was heated to 800°C with the injection of water. Ni-Mn-Al catalysts with Ni:Mn:Al molar ratios of 2:1:2 and 1:1:1 were used. The majority of the CNM deposited on the two catalysts were MWCNT with a diameter of ~30 nm, in addition to amorphous carbon. For the Ni:Mn:Al 1:1:1 catalyst with a higher Mn content, the filamentous carbon yield was higher, 52,6 wt.% versus 41,8 wt.%. However, with Ni:Mn:Al 2:1:2, the carbon had better quality, according to temperature programmed oxidation (TPO) analyses.

Catalyst removal and CNM recovery

During CNM synthesis, the catalytically active components of the catalysts are rather consumed (metal load of the nanocarbons). However, since these catalysts are rather non-expensive, such a consumption is not highly detrimental financially. Moreover, the presence of a small quantity of metals (good heat, electrical and magnetic conductivity) confers highly appreciated characteristics to the nanocarbons.

However, a purification step consisting of separating catalyst particles, support material, and amorphous carbon from the CNM is required (Hou et al., 2002). In order to separate the metal particles from the CNM after the reaction, acid washing is required. Some authors have used $CaCO_3$ as a support to facilitate the acid washing step (Cheng et al., 2006; Couteau et al., 2003). During the reaction, $CaCO_3$ decomposes into CaO and CO_2. Therefore, after the reaction, the main by-product was CaO, which is easily soluble in dilute acids (Couteau et al., 2003).

Novel catalysts have been used to facilitate the recovery of CNM. Zhang et al. have studied the pyrolysis–catalysis of HDPE in a two-stage fixed bed reactor using an Ni-impregnated stainless steel (SS) mesh (Zhang et al., 2017). The carbon deposited was easily removed by physical separation from the mesh catalyst. SS meshes have been widely used as catalysts for the synthesis of CNM from HC; however, pre-treatment has been found to be necessary to improve the production of CNM. Zhuo et al. (Zhuo et al., 2014) have oxidized

316L SS wire mesh in air at 800°C and used it as a substrate catalyst for CNM synthesis from PE pyrolysis gases. The pre-treated SS wire mesh produced MWCNT forests with an average MWCNT length of 20 μm and 21 nm in diameter. Panahi et al. (Panahi et al., 2019) have used SS-304, SS-316, and SS-316L wirecloths as the catalyst and substrate for the production of CNM from the pyrolysis of different polymers in a two-stage quartz reactor. The polymers were pyrolyzed at 800°C in nitrogen, and their gaseous products were passed over the fixed SS catalyst substrates preheated at 800°C. These steels contain a high chromium concentration, which forms a passive chromium oxide layer when in contact with O_2, protecting the surface from corrosion. To break up this chromium oxide layer, increase the SS surface roughness, and activate it to catalyze the growth of CNM, they used a multi-step pre-treatment that included hydrochloric acid washing, heat treatment at high temperature in various gases, and rapid quenching. The authors found that the SS-316 treated with acid wash for 10 min and air oxidation at 800°C for 1 min, followed by rapid air-quenching, gave the highest MWCNT yield with the highest purity.

Influence of temperature

Both T_p and T_c have an impact on the CNM yield and morphology. Liu et al. (J. Liu et al., 2011) have studied the conversion of PP into MWCNT and a hydrogen-rich gas in a two-stage pyrolysis–catalysis process using a NiO catalyst. The influence of T_p (550–750°C) and T_c (500–800°C) on the performance of the system was investigated. At a fixed T_p of 750°C, the filamentous carbon yield increased from 23,7 to 34,1 g/100 g of PP when T_c increased from 500 to 700°C; then it decreased to 32,2 g/100 g of PP with further increase of T_c to 800°C. The catalytic reaction dominated over the thermal reaction at low T_c (between 500–700°C). Consequently, the hydrogen concentration and yield of carbon products increased. At higher T_c, the thermal decomposition of the HC mixture can produce more methane than hydrogen, and therefore, the yield of solid carbon decreases. MWCNT were formed at 700 and 800°C with a uniform diameter distribution and higher graphitization compared to those produced at lower T_c. The advantage of the unsupported NiO catalyst was that, during the reaction, it was reduced to metallic Ni, and the sintering problem was not observed at high T. In contrast, when T_p increased, the heavy HC further decomposed, resulting in a higher gas yield and lower amounts of pyrolysis oil.

The composition of the pyrolysis gas changed with temperature. The concentrations of H_2, methane, and ethylene increased with the temperature because the propylene and butene in the pyrolysis gas cracked at high temperatures. The concentrations of C_3 and C_4 alkenes in the pyrolysis gas reached a maximum at 650°C, which means that alkenes crack at a temperature higher than 650°C. The MWCNT yield had the same trend of alkene concentrations: from 550 to 650°C, it increased because the overall yield of pyrolysis gas and the concentration of alkenes increased. Above 650°C, the carbon yield decreased, even if the amount of pyrolysis gas increased, because the alkene concentration decreased, which is expected because unsaturated gases produce more CNM than methane. Regarding their structure, CNM with large outer diameters and narrow inner diameters appeared in the samples obtained at 650 and 700°C.

Yao et al. (Yao, Zhang, et al., 2018) have proven that increasing the T_c over a Ni-Fe/γ-Al_2O_3 catalyst favored the growth of filamentous carbon over amorphous carbon and converted the morphology from hollow core to solid core CNM. However, from Raman spectral analysis, the quality and graphitization of CNM were best at 800°C. It has been reported that the continued growth of good-quality CNM is related to the rate of carbon supply, which must be adequate (Lu & Liu, 2006). The temperature influences the decomposition rate of HC and, thus, the amount of atomic carbon available for growth. In this work, a temperature of 800°C generated a more suitable carbon rate for the growth of CNM than the lower temperature of 700°C. However, a higher temperature (900°C) provided an excessive feed of carbon, which was not in accordance with the precipitation rate and caused the poisoning of the metal particles by encapsulating carbon. In another work, Liu et al. (X. Liu et al., 2018) have used a Ni-Al_2O_3 catalyst to produce CNM from the pyrolysis–catalysis of HDPE in a two-stage fixed bed reactor. HDPE was pyrolyzed at 500°C at the first stage, and different T_c were studied in the second stage (600°C, 700°C, and 800°C). The smallest standard deviation of CNM diameters and the highest filamentous to amorphous carbon ratio were obtained at 700°C. Increasing T_c promotes the diffusion rate of the carbon atoms, and therefore, CNM are synthesized with fewer defects. However, a very high temperature would promote the sintering of the metallic particles and increase their size, which will impact the activity of the catalyst by reducing its surface area.

Acomb et al. (Acomb et al., 2015) used a two-stage process where LDPE pyrolysis gases were passed directly onto the second catalytic stage. Fe-γAl_2O_3 was used as a catalyst. The impact of T_c was investigated at a fixed T_p of 600°C. T_c varied between 700, 800, and 900°C. At 700°C, MWCNT and amorphous carbon were formed. At 800°C, thicker and more densely packed MWCNT with diameters ~20–30 nm were formed, and no amorphous carbon was observed. At 900°C, more carbon deposition was observed; however, the crystalline quality of this carbon had deteriorated. CS-CNF with less ordered carbon walls were formed, with larger diameters of 30–60 nm.

Arnaiz et al. (Arnaiz et al., 2013) studied the production of CNM by CVD in a range of temperatures from 600 to 800°C using non-condensable effluent gas obtained from PE pyrolysis as the carbon source and Fe-Al_3O_3 as a catalyst. The highest carbon yield was achieved at 650°C, while a better crystallinity was obtained at 750°C. A sufficiently high temperature is necessary for adequate kinetics and diffusion rates through the metal particle; however, a very high T will cause the sintering of the nanoparticles, inactivating them. Furthermore, an excess of carbon atoms can cause them to accumulate and form encapsulating carbon, which will deactivate catalytic sites.

Co-production of CNM and H_2

The pyrolysis–catalysis of waste plastics has dual applications, which consist of producing not only CNM but also H_2. Several studies have focused on the co-production of CNM and H_2. Liu et al. (X. Liu et al., 2017) have investigated the performance of Ni/SiO_2 and Fe/SiO_2 catalysts when producing H_2 and CNM from the catalytic gasification of waste PP, using a two-stage fixed bed reaction system. The pyrolysis was conducted at 600°C, and the second catalytic stage temperature was 800°C. The Fe-based catalyst resulted in the highest H_2 production (25,60 mmol/g plastic) and the highest carbon yield (29 wt.%). The addition of steam has been found to reduce the carbon yield, but it increased the H_2 yield. Wu and Williams (Wu et al., 2016) performed pyrolysis/catalytic steam-reforming experiments to produce CNM and H_2 from PP. T_p was 500°C, while the catalytic bed of Ni:Mn:Al 1:1:1 catalyst was heated to 800°C with an injection of water. The H_2 production was 56.6 mmol/g of plastic. As reported in the literature, Ni species on the catalyst surface are effective in reforming reactions, and in the presence of H_2O, steam reforming of light HC

(e.g., CH_4 and C_2H_4) occurred and resulted in high production of H_2. Yao et al. (Yao, Zhang, et al., 2018) have also proven in their work that higher steam inputs into the second stage catalytic reactor resulted in higher H_2 yields due to higher HC levels but much lower carbon yields due to gasification. Wu et al. (Wu et al., 2014) have reported the production of 81,8 mmol/g plastic in the pyrolysis-reforming of real-world waste plastics (MOC composed of 69% HDPE, 15% LDPE, 10% PP, 1% PS, and 5% residual oil), a lower yield than that produced from HDPE (94.4 mmol/g). It has been reported in the literature that PP and PE generate higher H_2 yields during the pyrolysis-gasification process in the presence of a Ni-based catalyst because their pyrolysis produces more alkenes, which are easily reformed to H_2 in the presence of steam. The presence of sulfur and residual motor oil has also been suggested to cause lower gas and H_2 production.

The temperature of the reaction also has an impact on the H_2 produced. An increase in the reaction temperature results in an increase in the H_2 yield (Acomb et al., 2015). As the temperature is raised, the C_2–C_4 HC decompose further to form CH_4 and H_2. At low temperatures, it has been proven that a larger quantity of amorphous carbon forms and could deactivate the catalyst, resulting in a low yield of H_2 (Wu & Williams, 2010a).

Characterization of plastic-derived CNM

Several analytical technics can be used to characterize plastic-derived CNM. To study the morphology of the CNM formed, SEM and TEM are used. Figure 2. *14* shows typical SEM and TEM images for carbon formed from LDPE pyrolysis gases using an Fe/γAl_2O_3 catalyst at two different temperatures. The SEM image of the sample obtained at 700°C shows filamentous carbon and amorphous carbon. The corresponding TEM image shows that the filamentous carbons are MWCNT, and their diameters and length are around 20–30 nm and up to a number of microns, respectively. The amorphous and encapsulating carbon observed using SEM are also seen. At 800°C, the SEM image shows filamentous carbon, which is more densely packed, and no amorphous carbon was observed. The corresponding TEM image shows that the filamentous carbons are MWCNT, with dimensions similar to those formed at 700°C (Acomb et al., 2015).

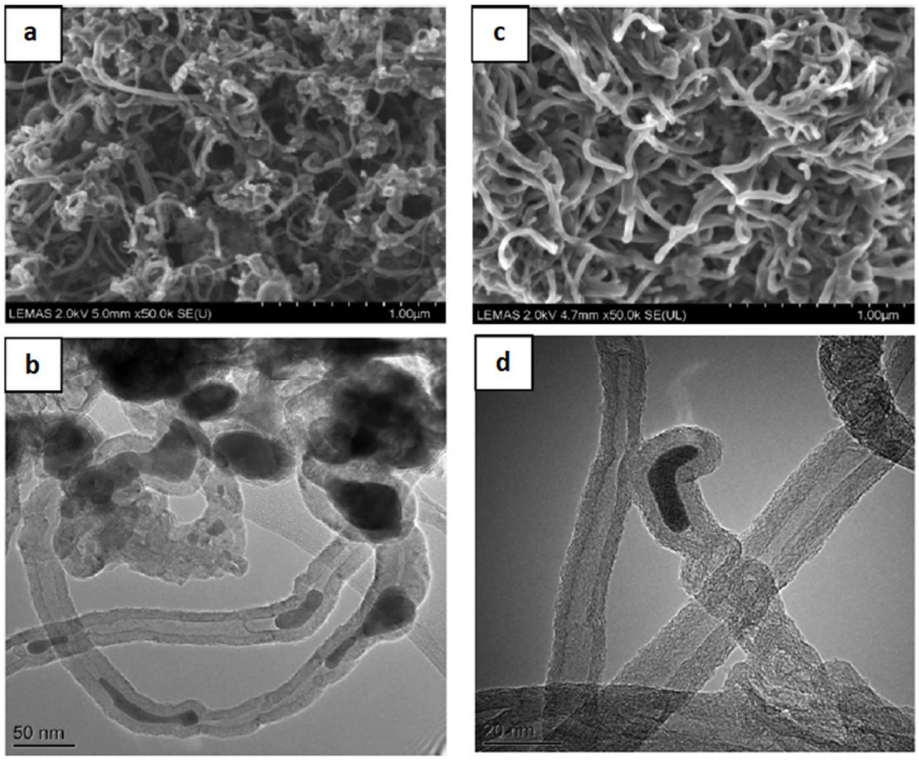

Figure 2. 14 Scanning electron microscopy and transmission electron microscopy images of carbon deposition on the catalyst at catalyst (growth) temperatures of (a) and (b) 700°C, (c) and (d) 800°C (Acomb et al., 2015).

Another technique used is Raman spectral analysis. The two main peaks at ~1580 cm^{-1} (G peak) and ~1350 cm^{-1} (D peak) in the Raman spectra of CNM are the resonance peak of graphite and the scattering peak of the disordered component, respectively. The intensity ratio (I_G/I_D) provides information about the presence of defects in the graphene sheets, and it can be used to characterize the crystallinity and degree of graphitization of the CNM. The higher the value of I_G/I_D, the higher is the quality and crystallinity of the CNM. The G' peak observed at ~2700 cm^{-1} is associated with the process of two-photon elastic scattering, and a higher ratio of ($I_{G'}/I_G$) also implies higher CNM purity (Yao, Zhang, et al., 2018). Figure 2. 15 presents the Raman analysis from the same samples in Figure 2. 14 (Acomb et al., 2015). The I_G/I_D ratio is lower for a catalyst temperature of 700°C, with a value of 1,66, than for 800°C, with a value of 1,97. This difference indicates that the crystallinity of the carbon deposited at this lower temperature is lower, which corroborates the SEM and TEM results.

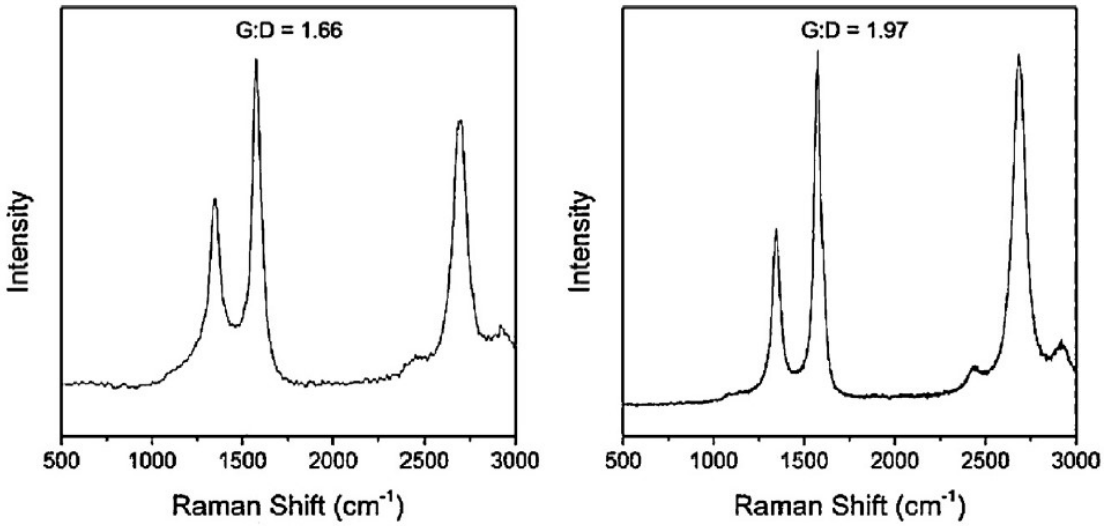

Figure 2. 15 Raman spectra of carbon deposits obtained from catalyst temperatures of (a) 700°C, (b) 800°C (Acomb et al., 2015).

In order to determine the amount of carbon deposited and the relative amounts of filamentous carbon and amorphous carbon produced, TPO or TGA has been used. Three stages of carbon oxidation have been identified: i) amorphous carbon at low T (~500°C), ii) filamentous carbon with small diameters at medium T (~650°C) and iii) filamentous carbon with large diameters and more layers at higher T (~750°C) (Zhang et al., 2017). However, the presence of residual metal in the CNM structure can catalyze carbon gasification and possibly lower the temperature at which the maximum gasification rate occurs. The presence of surface defects can also affect the oxidation temperature (Serp et al., 2003). Figure 2. 16 shows the derivative TPO plots. Two distinct peaks are present, one between 350 and 450°C, attributed to the amorphous carbon, and another between 500 and 700°C, attributed to the filamentous carbon (Acomb et al., 2015).

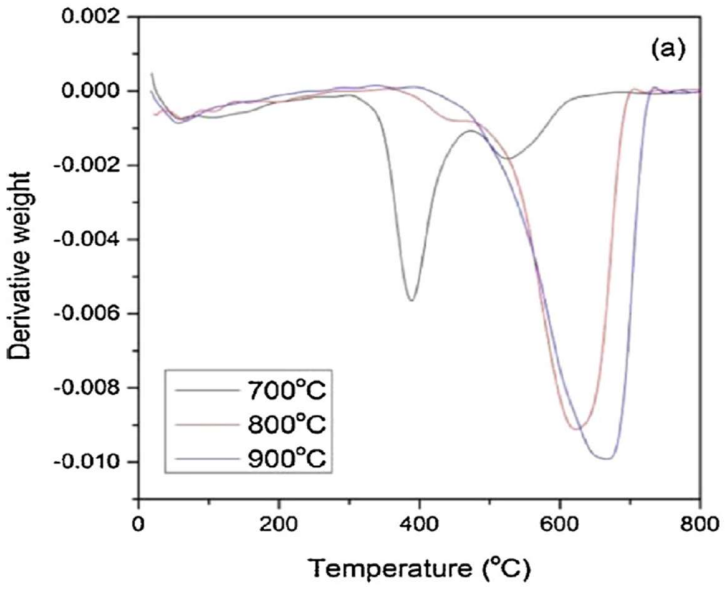

Figure 2. 16 Derivative temperature programmed oxidation (TPO) thermograms showing the effect of catalyst temperature (Acomb et al., 2015).

X-Ray diffraction (XRD) analysis can also be used to determine the crystallinity of the deposited carbon. The diffraction peak at $2\theta = 26°$ refers to the d_{002} of the graphitic framework, which corresponds to the interplanar distance between the graphene sheets. When this peak is sharp and intense, it indicates highly crystalline carbon. The textural properties of the synthesized CNM can also be investigated using N_2 physisorption.

Applications of CNM produced from plastic waste

CNM produced from plastic waste can be used for the same applications mentioned in section 0. However, this section presents the studies that have directly reported the application of CNM derived from plastic waste.

MWCNT produced by the pyrolysis–catalysis of PP were added at 2% by weight to LDPE to form a composite material (Wu et al., 2016). The mechanical properties of the resulting composite material were significantly improved over those of the original LDPE. The tensile and flexural strength of virgin LDPE were 11,4 and 7,5 MPa, respectively. For the MWCNT-LDPE composite, the tensile strength increased to 13,1 MPa, while the flexural strength increased to 9,3 MPa (Wu et al., 2016). The same work also reported that the MWCNT-LDPE composite showed much greater stiffness. LDPE had a tensile modulus of 348 MPa and a flexural modulus of 495 MPa; however, the tensile and flexural moduli of the

composite were significantly higher, 527.4MPa and 582.0 MPa, respectively (Wu et al., 2016). The authors confirmed that the homogeneous dispersion of CNM onto the polymer matrix plays a crucial role in reinforcing the composites.

In another work, Moo et al. (Moo et al., 2019) used LDPE (100%), PP (100%), and mixed plastics (MP; 40% LDPE, 40% P, 10% PS, and 10% PET) as a feedstock for the synthesis of CNM. Plastics were pyrolyzed at 600°C in a horizontal reactor, and the non-condensable gases were converted in the vertical reactor at 500–800°C in a packed bed reactor (PBR) with NiO supported on $CaCO_3$ as a catalyst. They tested the use of the CNM produced as an electrode material in a fuel cell: more specifically, as a cathode where the O_2 reduction reaction (ORR) occurs. The electrode surfaces modified with MWCNT synthesized from MP at 500°C have the lowest onset ORR potential of −0,11 V, which was significantly better than a glassy carbon (GC) electrode with an onset ORR potential of −0,19 V and comparable to platinum on a carbon (C/Pt) electrocatalyst at −0,10 V. MWCNT synthesized from MP at 500°C had more edge defects than the sample produced at 800°C, which means that the edge defects are active sites for ORR. The edge defects, consisting of carbon atoms with dangling bonds, allowed the adsorption of diatomic oxygen and, eventually, its reduction (Hossain et al., 1989).

Wen et al. (Wen et al., 2014) produced MWCNT from PP and mixed it with acetylene black and PTFE. The mixture was used as an electrode material for supercapacitors, and 6 M KOH aqueous solution was used as the electrolyte. The synthesized MWCNT had a large Brunauer, Emmett et Teller (BET) specific surface area and pore volume, and it displayed good electrochemical performance with a high capacitance.

Gong et al. (Gong et al., 2015) produced CS-CNF from PP, activated using KOH to obtain a porous structure, and used for the adsorption of methylene blue (MB) from wastewater. Activation with KOH endowed the porous CS-CNF with a high specific surface area (558,7 m^2/g) and a large pore volume (1,993 cm^3/g) due to the formation of numerous holes with a diameter of several to ten nanometers connecting the tube to the outside. The activation also etched some of the oblique layers, endowing the CNF with abundant surface functional groups. The porous CNF showed high performance in the adsorption of MB with an adsorption capacity of about 319,1 mg/g. Multiple adsorption mechanisms took place,

including pore filling, hydrogen bonding and electrostatic interactions between MB and porous CNF (Gong et al., 2015). CS-CNF were synthesized by the same authors and were oxidized to prepare acid-treated CS-CNF, which showed excellent performance in the adsorption of heavy metal ions and organic dyes (Gong et al., 2014).

Summary of factors impacting CNM synthesis from waste plastic via the pyrolysis–catalysis process

Reactor design

- Separate reactors for pyrolysis and catalysis allow better control of the process; for example, the temperature of each stage is independently controlled.
- Light HC are more suitable for the production of CNM, so a configuration that allows only the use of non-condensable gases is favored.
- An intermediate step between pyrolysis and catalysis reactors is favored to remove heavy HC, whether it is a condensation, distillation, or recracking step.
- Adding a condensation step will decrease the yield of CNM since a large quantity of carbon will be withdrawn with the condensate oil, but the advantage of this configuration is the production of this value-added product widely used in the industry.
- Adding a recracking step, which consists of cracking heavy HC into light HC, is the best option to convert the maximum possible amount of carbon from waste plastic into CNM.
- Continuous systems, in particular, fluidized bed reactors, are more suitable for scale-up and industrial production due to their several advantages, which include excellent heat and mass transfer, easy recovery of CNM, and easy removal of catalyst to be recycled and reused.

Feedstock

- CNM yield is directly related to the amount of HC gases, which is also related to the type of plastic waste used as feedstock.
- Unsaturated gases are easier to decompose than stable saturated HC, so it is better to use plastics whose pyrolysis gives lighter unsaturated HC.
- Real-world waste plastics are a mixture of different types of plastics, and the gas produced is complex and contains contaminants.

- Pre-treatment steps are required to simplify the composition of the gas entering the catalysis reactor and remove all the contaminants that would negatively impact the quality and quantity of the CNM produced.
- PP and PE pyrolysis at a certain T gives more HC of lower molecular weight, so the gas yield will be higher than the oil yield compared to other plastics, which means that a higher CNM yield would be obtained.
- PP and LDPE pyrolysis at a certain T produce a high gas yield due to the presence of branched chains. HDPE has a linear carbon chain, making it more difficult to decompose into lighter HC than other polyolefins.
- PS pyrolysis leads to the production of a large condensable fraction rich with aromatics, especially styrene.
- PET has a high oxygen content, and its pyrolysis leads to the formation of oxygenated and aromatic compounds.
- PVC pyrolysis produces HCl, which has a negative impact on the quality of the CNM.
- To make the quality and quantity of carbon independent of feedstock type, the reaction should be carried out at high T to decompose the most HC into small HC, such as ethylene and methane.
- When steam is added, it will act as a mild oxidizing agent and oxidize amorphous carbon first and then filamentous carbon, resulting in decreased amounts of amorphous carbon. A lower amount of steam may also enhance the quality of the CNM. However, at higher steam injection rates, most of the carbon would be removed.
- When CO_2 is added, at high T the reverse Boudouard reaction is favored, and C yield will decrease.
- When the feedstock/catalyst ratio is varied by increasing the amount of plastic used, the carbon yield decreases.

Catalyst

- Iron-, cobalt-, and nickel-based catalysts are most commonly used for CNM production.
- The strong interaction between the metal and the support and well-dispersed metal catalyst particles both affect the particle sizes and have been shown to result in better yields and quality of CNM.

- A strong metal–support is good for preventing the coalescence of metal particles and the enlargement of their diameter; however, a very strong metal–support interaction reduces the surface area of the catalyst. A metal–support interaction that is too weak would cause the sintering of metal during high-temperature reactions.
- Mixed metal catalysts gave better performance than single metal catalysts.
- Using alumina supports, the Fe catalyst generated more carbon and CNT than Ni, but the Ni-Fe catalyst gave the best results.
- The addition of Mo to Fe and Ni catalysts enhanced the yield and quality of CNM.
- Acid washing is required to purify CNM from residual metal.
- SS meshes are favored to easily remove the carbon deposited by physical separation.

Summary on the effects of temperature

- A higher T_p produces a less complex gas mixture rich in light HC, which is suitable for CNM growth.
- T_c is a crucial parameter because an increase of T_c yields more filamentous carbon due to its impact on HC decomposition and the carbon diffusion rate.
- At temperatures that are too high, an increased supply of pyrolysis gases causes excessive carbon feeding, which leads to catalyst poisoning by encapsulating carbon.
- High temperatures also favor the sintering phenomena of the catalyst.
- The temperature also helps dampen the effect of the difference on the type of feedstocks used, providing carbon with more uniform properties.

2.2.5. Outlook and conclusion

Filamentous CNM are high-value products with advantageous properties, and H_2 is a clean energy vector. These two valuable products are used for multiple industrial applications, and several efforts have been made to produce them. Using waste plastics as a feedstock to produce them is an appealing option, preventing white pollution. Different thermochemical processes produce CNM from waste plastics, and this review focused on the two-stage pyrolysis–catalysis process. In particular, the influence of different parameters, including reactor design, feedstock type, the catalyst used, and reaction conditions, on both the yield and quality of the CNM has been reviewed. Although promising results have been obtained at the laboratory scale, there are certain challenges to be addressed before implementing this process on a commercial scale. These challenges are 1) continuous

production of CNM and H_2, 2) using real-world waste plastics despite their complex compositions and the presence of impurities, and 3) the relatively high temperatures required for the process.

The design of reactors for the production of CNM should move from batch reactors to continuous systems, which facilitate the manipulation of the system and enable larger-scale production of CNM. Moreover, larger pilot-scale reactor systems should be developed to prove the feasibility of the process at an industrial scale, and innovative configurations should be developed to improve the energy efficiency of the system.

The type of plastic used has a direct impact on the quality of CNM produced. For the scale-up of production, product quality specifications depend on the market demand and the end-use application of these CNM. For example, some applications do not need high-quality CNM, in which case a lower quality bulk CNM from real-world mixed plastic waste feedstock will be tolerated. However, for other industrial applications, high-quality CNM is required despite the low yield. If the application needs a very high quality of CNM, presorting may be necessary to produce a suitable plastic raw material for the pyrolysis–catalysis plant. Sorting plastics is necessary not only to control the composition of the plastics stream but also to remove contaminants, the presence of which may reduce the plant efficiency. However, the additional costs generated by this pre-treatment should also be considered.

Regarding the influence of process parameters, the catalyst used, the temperature of pyrolysis, and the temperature of catalysis have been shown to be key factors. To obtain the desired product, these parameters must be adjusted appropriately. Again, it is essential to match the process conditions to the quality and quantity specifications of the CNM required by the market. Hydrogen is usually produced as a co-product with CNM; in such cases, steam is added to improve hydrogen yield and CNM quality by oxidizing amorphous carbon, which is more reactive than graphitized carbon. However, at a higher steam input, the CNM can be oxidized, and the yield is reduced. Therefore, a detailed techno-economic assessment must be carried out before considering the scale-up to an industrial level to ensure the environmental and economic sustainability of the process.

CHAPITRE 3
MÉTHODOLOGIE ET CHEMINEMENT

CHAPITRE 3 MÉTHODOLOGIE ET CHEMINEMENT

3.1. Introduction

La méthodologie est principalement axée sur le développement, l'évaluation et l'optimisation du procédé. Elle couvre deux volets essentiels : le volet réacteur et le volet procédé et production des NFC.

3.1.1. Volet réacteur

Un nouveau réacteur a été développé dans le cadre de cette étude. La conception du réacteur est passée par plusieurs étapes : la première étape a consisté en un dimensionnement basé sur les lois régissant les phénomènes ayant lieu à l'intérieur du réacteur à savoir tout ce qui a trait à la fluidisation. La deuxième étape a porté sur la fabrication de ce nouveau réacteur. Les vaisseaux industriels qui fonctionnent à haute pression et à haute température sont assujettis à des lois, des règlements et des normes de construction et d'utilisation. Le souci principal est de rendre leurs utilisations sécuritaires dans le lieu de travail. L'épaisseur de la paroi, le matériau de construction, les dimensions des brides ainsi que le nombre de boulons dépendent de plusieurs facteurs dont la température et la pression. La société américaine des ingénieurs mécaniques « *American Society of Mechanical Engineers* » ASME énoncent des normes et des réglementations qui constituent des lignes directrices pour la fabrication des équipements sous pression pour préserver la santé et la sécurité en milieu de travail. Ce sont ces normes qui ont été adoptées pour la fabrication du réacteur de production des NFC. La troisième étape de ce volet réacteur a consisté en son installation dans le laboratoire, en son raccordement avec les équipements périphériques qui constituent le procédé, en sa mise en marche en appliquant un protocole opératoire de sécurité pour enfin procéder à des tests de production des NFC.

Pour l'étude fluidodynamique, un modèle à froid « *mock-up* » à base de Plexiglas a été construit avec les mêmes dimensions que le réacteur à chaud. Comprendre l'hydrodynamique des réacteurs avec une nouvelle configuration est primordial pour le choix des conditions optimales d'un fonctionnement approprié. L'utilisation d'un modèle à froid avec du Plexiglas est aussi un moyen efficace pour visualiser les phénomènes complexes qui se produisent

entre la phase gazeuse et les particules solides. Il a également aidé à la prise de décisions lorsque des modifications dans la configuration du réacteur se sont avérées nécessaires.

3.1.2. Volet procédé et production des nanofilaments de carbone

Avant de passer à l'échelle kilo-lab, des manipulations à l'échelle g-lab ont été réalisées.

Production des NFC de carbone dans le réacteur différentiel

Afin d'étudier la réaction du reformage à sec de l'éthylène et de juger de la qualité des NFC produits, des tests de production des NFC en présence d'un catalyseur à base de résidu minier ont été effectués dans un réacteur différentiel. Les résultats de cette étude sont présentés dans la chapitre 4. Cette étude a permis de comprendre d'une part le processus de déroulement de la réaction de reformage à sec et d'autre part de voir l'impact de l'ajout de CO_2 dans le milieu réactionnel et ce, sur la qualité des NFC formés. En outre, cette étude a permis de se familiariser avec les différentes techniques de caractérisation des NFC.

Production des NFC de carbone dans le réacteur hybride

Après installation du réacteur, après la mise à l'échelle de tout le système et la validation de son fonctionnement en toute sécurité, des tests de reformage à sec ont été effectués en utilisant l'éthylène comme gaz représentatif des gaz produits lors de la pyrolyse des déchets plastiques. Les résultats de cette étude sont présentés dans la chapitre 5. En revanche, au cours des premiers tests, des difficultés de fonctionnement sont apparues qui ont suscité des changements nécessaires à la résolution des problèmes de fonctionnement rencontrés (voir partie 3.4).

3.2. Conception du réacteur

3.2.1. Description du fonctionnement du réacteur

Le réacteur est composé de deux cylindres concentriques. Il est doté de deux sorties latérales et d'une base conique (Figure 3. 1). Le lit catalytique est composé d'un lit fixe se trouvant dans l'annulaire et d'un lit fluidisé se situant à l'intérieur du cylindre interne. Le gaz entre par le bas et fluidise le catalyseur à l'intérieur du cylindre interne; une partie du catalyseur tombe à la surface du lit dans l'annulaire. Parallèlement à ce mouvement, le vide entre le cylindre interne et la base conique permet au catalyseur de tomber en dessous du cylindre

interne et d'être emporté par le gaz montant ce qui assure la recirculation du catalyseur entre les deux lits.

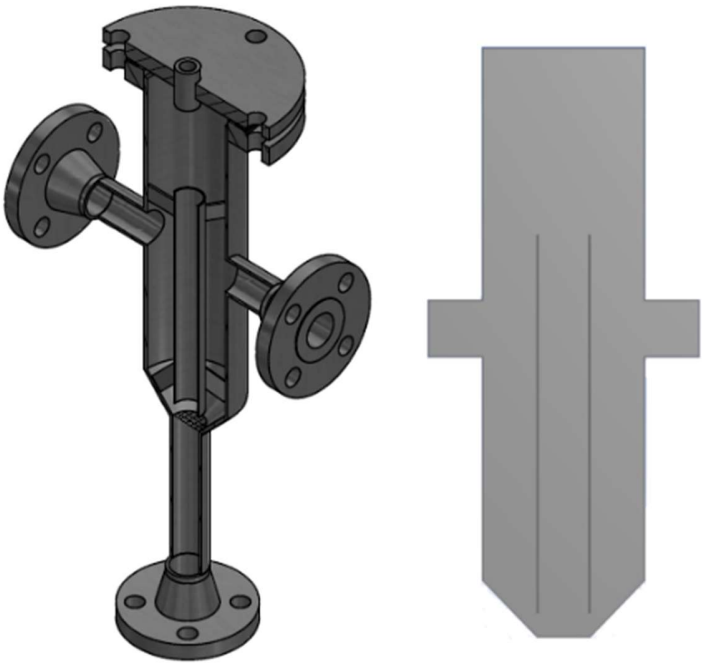

Figure 3. 1 Géométrie du réacteur

Le réacteur est apparenté à un réacteur de type Wurster, qui est un réacteur à lit jaillissant avec un cylindre de jet à l'intérieur appelé tube d'aspiration ou *draft tube*. En effet, la vitesse de gaz dans le cylindre interne doit être de façon à obtenir au moins un lit fluidisé bouillonnant où l'éjection des particules va avoir lieu. De plus, la hauteur du cylindre interne du réacteur doit correspondre à la hauteur d'expansion du lit fluidisé bouillonnant de façon à ce qu'une certaine partie des solides déborde du cylindre interne et que les particules éjectées tombent à la surface du lit dans l'annulaire.

Le débit de gaz (Q) envoyé du bas de réacteur se divise en deux courants (Q_1) et (Q_2) (Figure 3. 2):

1- Le premier (Q_1) traverse l'espace de tombée des solides et passe par le lit fixe dans l'annulaire et se dirige vers la sortie.
2- Le deuxième (Q_2) va verticalement jusqu'au bout du cylindre interne pour changer ensuite de direction et aller à travers le catalyseur dans l'annulaire pour enfin sortir; le catalyseur est fluidisé jusqu'à ce qu'il déborde du cylindre interne et se dépose en haut

du lit dans l'annulaire. Parallèlement à ce mouvement, le catalyseur tombe encore dans la partie inférieure du cylindre interne pour être entrainé encore une fois. De ce fait, le catalyseur va constamment circuler entre le cylindre interne et l'annulaire et le lit dans l'annulaire va avoir un mouvement descendant lent. Les NFC vont se produire lors du contact du catalyseur avec le gaz, et pendant la circulation du catalyseur ils vont être détachés des particules de catalyseur par friction et ils seront entrainés par le gaz.

$$Q = Q_1 + Q_2 \qquad (3.\ 1)$$

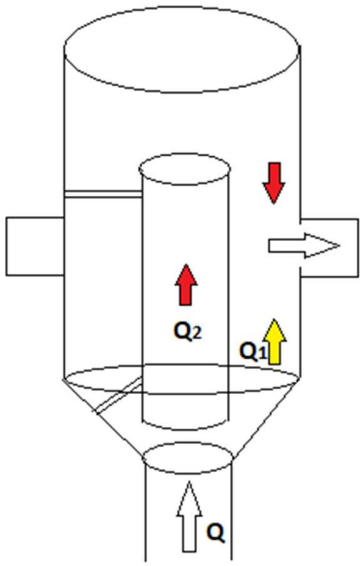

Figure 3. 2 Partage des débits de Gaz.

Le partage des débits est dicté par la perte de charge à travers les deux passages. Le débit de gaz parcourant une distance (L) à travers un milieu poreux (γ) dépend de la résistance d'écoulement du fluide selon la loi de Darcy :

$$Q_v = \frac{\gamma A}{\mu} \frac{\Delta P}{L} \qquad (3.\ 2)$$

$$Q_v = A\ U_0 \qquad (3.\ 3)$$

Ce qui donne

$$\Delta P = \frac{L}{\gamma}\ U_0 \mu \qquad (3.\ 4)$$

$$\Delta P = \frac{L}{\gamma} \frac{Q_v}{A} \mu \qquad (3.\ 5)$$

Avec :

ΔP: perte de charge (Pa).

Q_v : Débit volumique (m^3/s).

U_0: Vitesse du gaz (m/s).

γ : Perméabilité (m^{-2}).

A : Section de lac colonne (m^2).

μ : Viscosité du fluide (Pa.s).

L : Distance parcourue par le gaz (m).

En faisant l'analogie avec les lois de l'électricité notamment la loi d'Ohm (équation 3.6), nous avons :

$$\Delta V = R\, I \qquad (3.6)$$

$$\Delta P = R\,(U_0\,\mu) \begin{cases} \text{I à } U_0\,\mu = \frac{Q_v}{A}\mu \\ \Delta\text{V à } \Delta P \\ \text{R à } \frac{L}{\gamma} \end{cases}$$

R représente la résistance à l'écoulement du gaz. Comme le réacteur est symétrique, on peut considérer : $R_{1a} = R_{1b}$ et $R_{3a} = R_{3b}$ (Figure 3. 3).

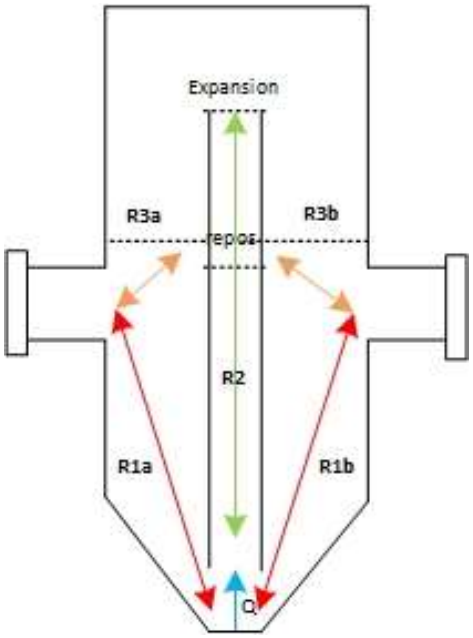

Figure 3. 3 Analogie avec les résistances électriques équivalentes.

Comme montré dans la Figure 3. 4, la perte de charge dans le cylindre externe ΔP_{ext} est égale à la somme de la perte de charge dans le cylindre interne ΔP_{int} et la perte de charge de la transition entre le cylindre interne et la sortie du réacteur $\Delta P_{transit}$ (équation 3. 7).

$$\Delta P_{ext} = \Delta P_{int} + \Delta P_{transit} \qquad (3.\ 7)$$

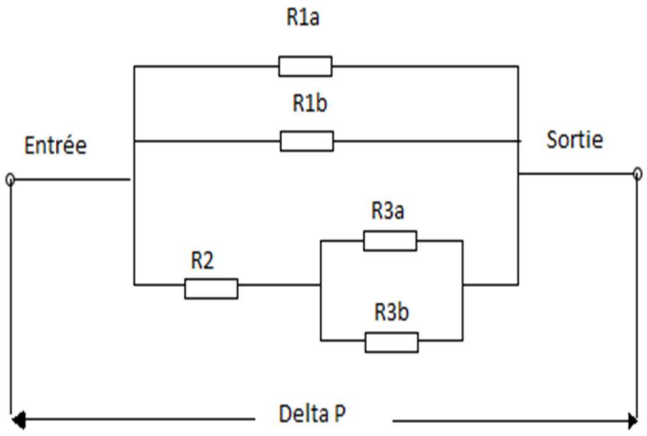

Figure 3. 4 Résistance d'écoulement du gaz du réacteur.

3.2.2. Dimensionnement du réacteur

La Figure 3. 5 met en relief toutes les dimensions qui doivent être calculées.

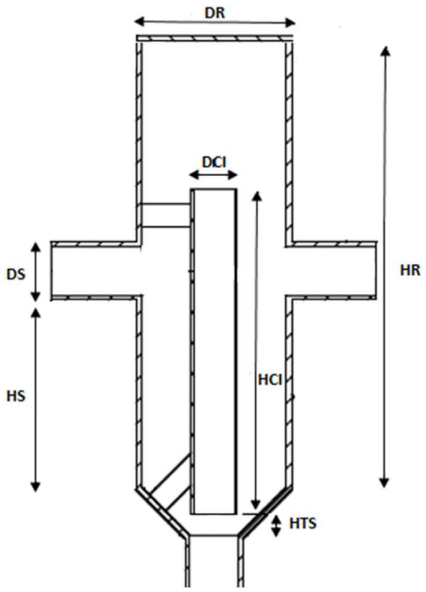

Figure 3. 5 Dimensions du réacteur

DCI : diamètre du cylindre interne (cm).

DR : diamètre du réacteur(cm).

DS : diamètre de sortie (cm).

HCI : hauteur du cylindre intérieur (cm).

HR : hauteur du réacteur (cm).

HS : hauteur de la sortie (cm).

HTS : hauteur de tombée de solides (cm).

Les étapes de calcul suivent l'algorithme montré de la Figure 3. 6. Un rappel sur le phénomène de fluidisation et les différentes équations utilisées dans le calcul, ainsi que toutes les étapes de calcul sont présentés en annexe A.

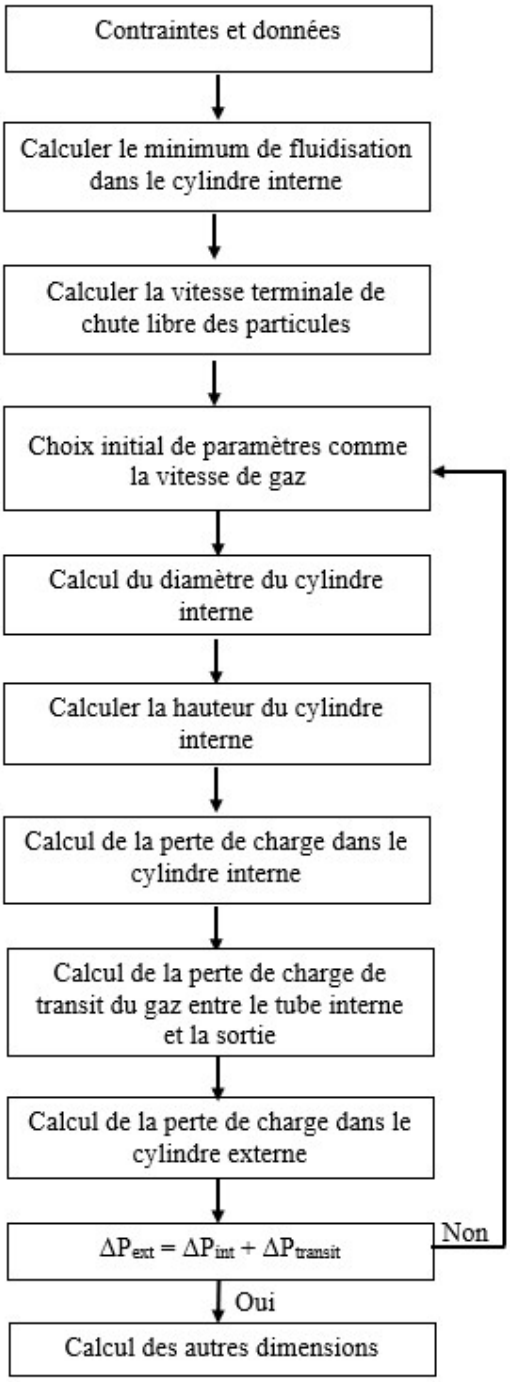

Figure 3. 6 Algorithme de dimensionnement du réacteur.

3.3. Mise en marche du processus

3.3.1. Construction du nouveau laboratoire

L'université de Sherbrooke a investi des fonds importants dans la construction du nouveau laboratoire qui abrite les travaux du groupe GRTP. Le groupe GRTP présidé par le professeur Nicolas Abatzoglou avec l'aide et l'expertise de trois autres professeurs, à savoir : le professeur François Gitzhofer, le professeur Ryan Gosselin et la professeure Esma Ines Achouri.

Il est composé de trois laboratoires :

- Laboratoire thermochimique et catalytique,
- Laboratoire de plasma,
- Laboratoire pharmaceutique.

Le laboratoire était prêt en 2019 mais les travaux de recherche n'ont commencé qu'en 2021. L'installation des équipements et leurs raccordements a pris certes du temps mais la cause principale du retard accumulé était la fermeture de l'université en mars 2020 du fait de la pandémie Covid 19.

3.3.2. Diagramme du procédé

Le schéma de tuyauterie et instrumentation du procédé est présenté en Figure 3. 7. Il se divise en quatre parties:

1- Section 1 : Réaction de reformage à sec,
2- Section 2 : Filtration,
3- Section 3 : Récupération des NFC,
4- Section 4 : Déshumidification de l'effluent gazeux.

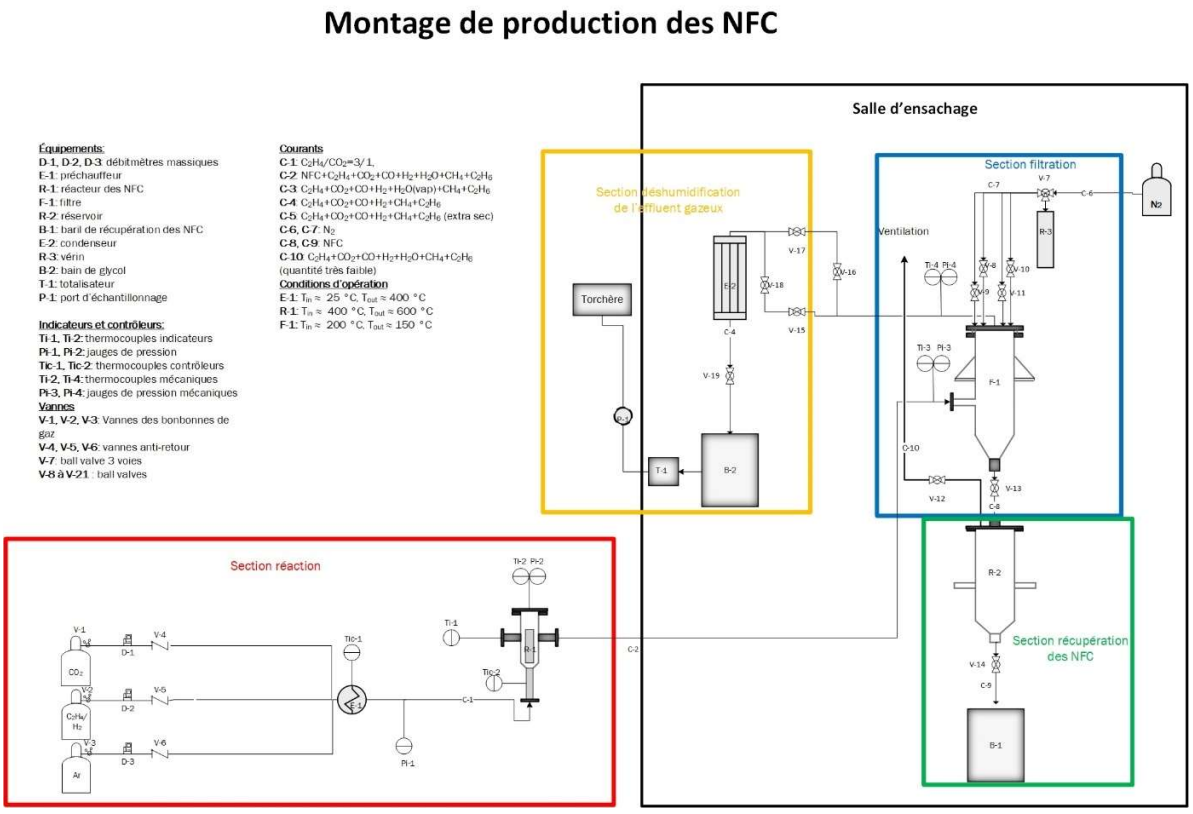

Figure 3. 7 Schéma de tuyauterie et instrumentation du procédé de production des NFC.

Section réaction

C'est dans cette section où la réaction a lieu. Les gaz sont acheminés à partir de bouteilles de gaz commerciales (fournies par LINDE) : C_2H_4 (99%), CO_2 (99%), H_2 (99%), et Ar (99%) jusqu'aux vannes principales (V-1,V-2 et V-3) qui sont reliées à leurs tours à des détendeurs permettant de mieux contrôler la pression se rendant aux débitmètres massiques. Trois débitmètres massiques ALICAT (D-1, D-2 et D-3) ont été utilisés pour contrôler les débits de gaz à l'entrée du préchauffeur. Des valves anti-retour (V-4, V-5 et V-6) ont été installées sur les trois lignes d'alimentation des différents gaz pour empêcher le retour du gaz au cas où la pression augmenterait et protéger ainsi les débitmètres massiques. Le préchauffeur (E1) est un cylindre qui se termine par un étranglement avec un coude à 90°. Il sert à amener le mélange de gaz alimenté à une température proche de celle de la réaction. Une bande chauffante contrôlée est utilisé à cet effet. Les gaz à la sortie du préchauffeur entrent dans le réacteur (R1) par le bas qui est un tube muni d'une bride. Le catalyseur est déposé à l'intérieur du réacteur et est supporté par un support de même diamètre que le tube contenant une grille

très fine. Le réacteur s'ouvre en haut par simple retrait d'une grande bride permettant ainsi l'accès au réacteur à des fins d'introduction de catalyseur, de nettoyage et de vidange. Deux tubes de sortie se trouvent de part et d'autre du réacteur, l'un sert à insérer un thermocouple et l'autre mène au système de filtration. Une bande chauffante en céramique avec contrôle de la température sert à fournir l'énergie nécessaire pour atteindre la température de réaction.

Les principaux équipements et instruments de la section 1 sont présentés dans les tableaux Tableau 3. 1 et Tableau 3. 2 respectivement.

Tableau 3. 1 Liste des équipements de la section 1.

Section	Équipement	Code	Spécifications techniques
1	Préchauffeur	E1	• Conçu selon la norme ASME Section VIII div 1. • Tous les trous de boulons des brides doivent chevaucher les axes principaux de l'équipement. • Toutes les soudures doivent être effectuées conformément à la section IX de l'ASME. • Les brides sont conformes à la norme ASME B16.5. • Les accouplements sont conformes à la norme ASME B16.11. • Matériau de construction : SS 321H.
	Réacteur	R1	

Tableau 3. 2 Liste des instruments de la section 1.

Section	Équipement	Code	Description
1	Débitmètres massiques	D-1, D-2, D-3	À pression différentielle
	Vannes	V-1, V-2, V-3	À bille de ½ de pouce

	Vannes	V-4, V-5, V-6	Anti-retours de ¼ de pouce
	Thermocouples indicateurs	Ti-1, Ti-2	Type K
	Thermocouples indicateurs contrôleurs	Tic-1, Tic-2	Type K
	Jauge de pression	Pi-1, Pi-2	Transducteurs de pression

Section filtration et récupération des NFC

Les NFC sont détachés du catalyseur en raison du frottement des particules de catalyseurs et entraînés avec le gaz sortant pour entrer dans la section de filtration où ils sont séparés du gaz à l'aide de filtres métalliques d'efficacité élevée pouvant atteindre environ (90%). Le gâteau formé sur les cylindres métalliques est délogé sous l'action des impulsions de N_2 assurées par le vérin (R3) et les NFC sont collectés dans le réservoir (R2) de la section de récupération. Il est à noter que la section de filtration et celle de récupération des NFC se trouvent à l'intérieur d'une salle d'ensachage conçue de manière appropriée et adaptée à la manipulation des nanomatériaux.

La salle d'ensachage est un local à pression négative muni d'un système de ventilation et de traitement de l'air contaminé par les NFC. La pression intérieure de l'air est plus basse que celle de l'air à l'extérieur du local. Ainsi, tout mouvement d'air va s'effectuer vers la chambre depuis les locaux voisins ce qui empêche la diffusion de l'air contaminé. L'évacuation en continu de l'air de ce local permet de réduire les NFC en suspension dans l'air et donc de limiter le risque de contamination des personnes qui entrent dans la pièce. L'évacuation est reliée à un filtre pour décontaminer l'air évacué. Cette salle a aussi un degré de résistance au feu DRF de 2 heures, pour empêcher la propagation de feu en cas d'incendie.

Les principaux équipements et instruments des section 2 et 3 sont présentés dans les tableaux Tableau 3. 3 et Tableau 3. 4 et respectivement.

Tableau 3. 3 Liste des équipements des sections 2 et 3.

Section	Équipement	Code	Spécifications techniques
	Filtre	n.d	• Cartouche métallique poreuse en SS 316L. d'épaisseur 0,062 pouce, 2 pouce de diamètre et 10 pouce de longueur.
2 et 3	Enceinte du filtre	F1	• Diamètre 12 pouce, longueur 40 pouce. • Matériau de construction : SS304. • Les brides sont conformes à la norme ASME B16.5.
	Réservoir	R2	• Diamètre 12 pouce, longueur 63 pouce. • Matériau de construction : SS304 • Les brides sont conformes à la norme ASME B16.5.

Tableau 3. 4 Liste des instruments des sections 2 et 3.

Section	Équipement	Code	Type
2 et 3	Vanne	V-7	À bille à trois voix de 3/8 de pouce
	Vanne	V-8 à V-12	À bille de 3/8 de pouce
	Vanne	V-13, V-14	À bille de 2,5 pouce
	Thermocouples indicateurs	Ti-3, Ti-4	Mécanique
	Jauge de pression	Pi-3, Pi-4	Manomètres

Section déshumidification de l'effluent gazeux

La dernière section comprend un condenseur pour déshumidifier l'effluent gazeux et le conditionnement final se fait à travers un bain de glycol pour l'élimination complète de la vapeur d'eau et de toutes autres impuretés. Enfin, il sera brulé en utilisant une torchère sans flamme et sans fumée. Le débit des produits est mesuré à l'aide d'un totalisateur et sa composition est analysée par chromatographie en phase gazeuse (Scion 400 Series GC).

Les principaux équipements et instruments de la section 4 sont présentés dans les tableaux Tableau 3. *5* et Tableau 3. *6* et respectivement.

Tableau 3. 5 Liste des équipements de la section 4.

Section	Équipement	Code	Spécifications techniques
4	Bain de glycol	B1	• Matériau de construction : SS 316 • Capacité : 70 l d'EG
	Condenseur	E2	• Matériau de construction : SS 316
	Totalisateur	T1	Débitmètre mécanique
	Torchère	B1	Sans flamme et sans fumé

Tableau 3. 6 Liste des instruments de la section 4

Section	Instrument	Code	Type
4	Vanne	V-15 au V-19	À bille de 3/8 de pouce
	Point de prélèvement	P-1	Septum

Les paramètres opérationnels des équipements

Les différents équipements utilisés dans le procédé sont conçus pour travailler dans des conditions opératoires de température et de pression bien précises. Le Tableau 3. 7 regroupe les conditions opératoires de tous les équipements du procédé.

Tableau 3. 7 Température et pression d'opération des principales unités du procédé.

Équipement	**Opération**	**Paramètres opérationnels**
E1	Préchauffage du gaz alimenté	• Pression de design interne 3,94 atm (58 psig). • Pression de travail maximale autorisée : 3,94 atmg à 500 °C • Température de design : 500 °C

R1	Réaction de reformage à sec et production des NFC	• Pression de design interne 4 atm (60 psig). • Pression de travail maximale autorisée : 4 atm à 704 °C • Température de design : 704 °C
F1	Filtration de l'effluent gazeux	• Température : 250 °C • Pression : 2,72 atm
R2	Récupération des NFC	• Température : 250 °C • Pression : 2,72 atm
B1	Déshumidification et lavage de l'effluent gazeux	• Température et pression ambiantes
E2	Déshumidification de l'effluent gazeux	• Température et pression ambiantes

3.3.3. Installation des équipements

Un travail d'équipe a été nécessaire à la réalisation de l'installation telle que présentée en Figure 3. 8. Ceci a consisté principalement à la sélection du matériel, équipements et instruments de mesure, à l'élaboration des différentes commandes, au montage et installation du matériel reçu et enfin au raccordement des différents composants du procédé. Le travail était partagé par section comme suit :

Section réaction

1- Installation du système d'alimentation composé de débitmètres massiques, de vannes anti-retours et de tuyaux de raccordement,
2- Installation d'un support métallique pour le réacteur et le préchauffeur,
3- Usinage des tuyaux (un horizontal, un vertical et un T entre les deux) et des brides entre le réacteur et le filtre.
4- Installation des tuyaux et brides entre le réacteur et le filtre,
5- Installation de thermocouples et de jauges de pression,

6- Installation du panneau électrique,
7- Faire un trou dans le mur pour passer le tuyau du réacteur à la salle d'ensachage.

Section filtration

1- Installation d'un support métallique pour le filtre,
2- Mise en place du filtre sur le support sur la mezzanine,
3- Installation du système d'impulsions : vérin, tuyaux, les 4 vannes à bille, la vanne à bille à trois voies et la bonbonne de N_2,
4- Installation des filtres dans leur enceinte : 4 cylindres de métal fritté ont été utilisés pour filtrer le gaz,
5- Installation des tuyaux entre le filtre et le condenseur et la bride à la sortie du filtre,
6- Installation de thermocouples et de manomètres.

Section récupération

1- Installation du réservoir en dessous du filtre avec une vanne à bille entre les deux,
2- Installation du tuyau de ventilation du réservoir,
3- Installation de la vanne à bille en dessous du réservoir.

Section déshumidification

1- Installation du condenseur et du bain de glycol,
2- Installation des tuyaux de raccordement ente les deux,
3- Installation du totalisateur,

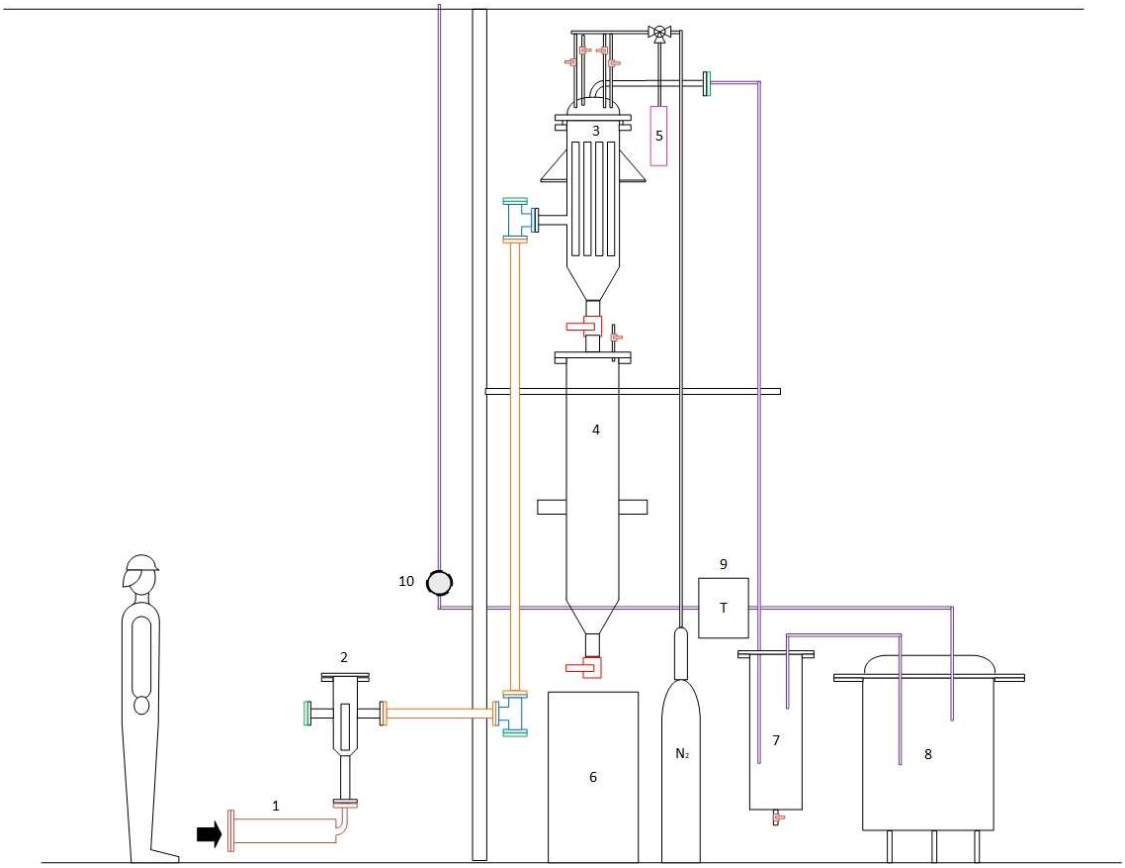

Figure 3. 8 Schéma du procédé. 1-Préchauffeur, 2-Réacteur, 3-Filtre, 4-Resrvoir de récupération des NFC, 5-Vérin, 6-Baril de récupération des NFC, 7-Condenseur, 8-Bain de glycol, 9-Totalisateur, 10-Point d'échantillonnage.

3.3.4. Protocole d'opération (SOP)

La logique des séquences d'action du protocole de la réaction est présentée ci-dessous :

1) Préparation des tests

- ✓ Préparer le catalyseur et le mettre dans le réacteur,
- ✓ S'assurer que les bonbonnes de gaz sont suffisamment pleines,
- ✓ Allumer l'ordinateur pour l'acquisition des données,
- ✓ Dégager les accès vers le réacteur,
- ✓ Porter les EPI.

2) Inspection des fuites avec un gaz inerte (N_2) et mise en marche

- ✓ Avant le début de la réaction il faut faire une inspection des fuites avec alimentation de gaz inerte (N_2) à température ambiante,
- ✓ Mise en marche : le chauffage est déclenché sous atmosphère inerte jusqu'à atteindre la température de réaction (régime transitoire-1).

3) Opération en régime permanent

- ✓ Une fois la température de réaction est atteinte, les gaz réactifs sont alimentés,
- ✓ Une perturbation de la température aura lieu à cause de l'enthalpie de réaction (régime transitoire-2 de courte durée),
- ✓ Retour au régime permanent.

4) Fin des tests et mise au repos

- ✓ Arrêt de l'alimentation des gaz réactifs
- ✓ Alimentation en gaz inerte pour évacuer tous les autres gaz
- ✓ Arrêt du chauffage et refroidissement sous atmosphère inerte

5) Arrêt d'urgence

Arrêt d'alimentation des gaz réactifs immédiat, alimentation en gaz inerte et arrêt du chauffage en cas de :

- ✓ Fuite de gaz,
- ✓ Surchauffe ou surpression.

Protocole détaillé de la réaction (Annexe B).

Protocole de vidange (Annexe C).

3.3.5. Santé et sécurité

Risque lié aux réactifs et produits gazeux

Les réactifs utilisés sont les gaz : CO_2, C_2H_4 et N_2. Les majeurs produits obtenus sont : NFC, CO, H_2, CH_4, C_2H_6, H_2O.

La plupart de ces gaz présentent plusieurs dangers, à savoir : toxicité, asphyxie et inflammabilité.

Toxicité

Au Québec, les valeurs d'exposition admissibles des contaminants de l'air sont celles qui sont prescrites par le Règlement sur la santé et la sécurité du travail RSST (S-2.1, r.19.01). Il y'a deux types :

Valeur d'Exposition Moyenne Pondérée (VEMP): la concentration moyenne, pondérée pour une période de 8 heures par jour, en fonction d'une semaine de 40 heures, d'une substance chimique (sous forme de gaz, poussières, fumées, vapeurs ou brouillards) présente dans l'air au niveau de la zone respiratoire du travailleur.

Valeur d'Exposition de Courte durée (VECD) : la concentration moyenne, pondérée sur 15 minutes, pour une exposition à une substance chimique (sous forme de gaz, poussières, fumées, vapeurs ou brouillards) présente dans l'air au niveau de la zone respiratoire du travailleur, qui ne doit pas être dépassée durant la journée de travail, même si la valeur d'exposition moyenne pondérée est respectée.

Les valeurs de chaque gaz sont regroupées dans le Tableau 3. 8.

Tableau 3. 8 VEMP et VECD des gaz utilisés dans le procédé (Ministère, 2020).

Gaz	VEMP (ppm)	VECD (ppm)
CO_2	5000	30 000
CO	35	200
C_2H_4	Asphyxiant simple	
H_2	Asphyxiant simple	
CH_4	Asphyxiant simple	
C_2H_6	Asphyxiant simple	
N_2	Asphyxiant simple	

Asphyxie

Asphyxiants simples

Comme mentionné au Tableau 3. *8*, l'azote, le méthane, l'éthane, l'éthylène, l'hydrogène et même le dioxyde de carbone sont classés comme asphyxiants simples. L'air que nous respirons contient habituellement près de 21 % d'oxygène. Si la concentration de ces gaz dans l'air atteint une certaine valeur, ils peuvent alors le réduire. De faibles teneurs en oxygène

(égales ou inférieures à 19,5 %) peuvent entrainer des symptômes d'asphyxie (perte de connaissance ou de motricité). Ce risque d'asphyxie peut se produire en cas d'émissions de gaz ou de fuite dans une atmosphère confinée ou d'inhalation directe par erreur.

Asphyxiants biochimiques

À la différence des gaz asphyxiants simples, ils sont pourvus d'actions physiologiques. En effet, ils empêchent le transport de l'oxygène ou son utilisation tissulaire. Ils provoquent l'asphyxie même pour d'assez faibles concentrations dans l'air inspiré. L'asphyxie biochimique est une hypoxie due à des anomalies circulatoires ou sanguines. Ces anomalies peuvent concerner entre autres une atteinte de l'hémoglobine qui peut être affectée aussi par la perturbation du transport de l'oxygène par suite de la liaison avec le fer de l'hémoglobine, comme c'est le cas du monoxyde de carbone CO.

Inflammabilité et explosivité

Un gaz inflammable est un gaz qui peut facilement s'enflammer et causer des incendies ou des explosions (en présence des deux autres éléments du triangle du feu à savoir : l'air et une source d'ignition qui peut être une flamme, une friction, une surface chaude, les interrupteurs d'appareil d'éclairage et même l'électricité statique). On définit ainsi des concentrations limites d'inflammabilité qui constituent les limites du domaine d'explosivité de chaque gaz. On parle alors de limite inférieure d'explosivité (LIE) ou de limite supérieure d'explosivité (LSE).

Limite inférieure d'explosivité (LIE)

C'est la concentration minimale de gaz dans l'air qui s'enflammera ou qui explosera au contact d'une source d'inflammation.

Limite supérieure d'explosivité (LSE)

C'est la concentration maximale de gaz dans l'air qui s'enflammera ou qui explosera au contact d'une source d'inflammation.

Point d'auto-inflammation (ou d'auto-ignition)

C'est la température à partir de laquelle une substance s'enflamme spontanément en l'absence d'une source d'ignition, dans l'atmosphère normale.

Le Tableau 3. 9 regroupe les valeurs de ces trois paramètres pour quelques gaz utilisés dans cette étude.

Tableau 3. 9 LIE, LSE et température d'auto-ignition de quelques gaz utilisés dans le procédé (Ministère, 2020).

Gaz	Limites d'inflammabilité (%V) dans un mélange avec air		Température d'auto-inflammation (°C)
	Inférieure	Supérieure	
CH_4	5	15	535
CO	12,5	74	605
H_2	4	75	500
C_2H_4	2,7	36	450
C_2H_6	3	12,5	472

Risques liés aux nanofilaments de carbone

Actuellement, les nanomatériaux sont considérés comme des produits innovants voire miracles, il n'en demeure pas moins qu'il faille considérer les aspects liés à la santé et à la sécurité. Les nanoparticules se trouvant dans un milieu solide ou liquide sont inertes. Le danger réside en fait dans leur aérosolisation. Libres dans l'atmosphère, ils peuvent être facilement inhalés par l'être humain et pénétrer dans la région alvéolaire profonde des poumons, là où se produisent les échanges gazeux ce qui pourrait provoquer des disfonctionnements. L'inhalation est la voie d'exposition la plus fréquente pour les nanoparticules fabriquées, et celle qui représente le risque d'exposition le plus commun dans la plupart des milieux de travail. Les nanoparticules libres peuvent aussi pénétrer dans le corps par absorptions dermique, oculaire ou par ingestion (National Institute for Occupational Safety and Health, 2018).

Les résultats d'études récentes sur des animaux indiquent que les nanotubes de carbone (NTC) et les nanofibres de carbone (NFC) peuvent présenter un risque respiratoire (National Institute for Occupational Safety and Health, 2018). Il n'y a pas un seul type de NFC; un type peut différer d'un autre par sa forme, sa taille, sa composition chimique (pourcentage de catalyseurs métalliques résiduels ou la fonctionnalisation des NTC et NFC) et d'autres caractéristiques physiques et chimiques. Ces variations de composition et de taille ont accru la complexité de la compréhension de leur potentiel de danger. L'exposition professionnelle aux NTC et NFC peut se produire non seulement au cours de leur fabrication, mais également au moment d'incorporer ces matériaux dans d'autres produits et applications. Un certain nombre d'études de recherche sur des animaux ont montré des effets pulmonaires indésirables à des doses de masse relativement faibles de NTC et de NFC, y compris des inflammations pulmonaires, des granulomes (tumeurs vasculaires inflammatoire) ainsi que des fibroses pulmonaires comme indiqué dans le Tableau 3. 10. Bien que l'on ne sache pas si des effets néfastes similaires sur la santé se produisent chez l'homme après une exposition à ces nanocarbones, les résultats d'études de recherche animale indiquent la nécessité de minimiser l'exposition des travailleurs (National Institute for Occupational Safety and Health, 2018).

Tableau 3. 10 Résultats d'études publiées sur la toxicologie par inhalation à court terme du SWCNT et du CNF.

Conception de l'étude et exposition/dose				Effets pulmonaires observés		
Référence	Espèce	Voie d'exposition	Exposition ou dose	Granulome	Inflammation	Fibrose
(Shvedova et al., 2008)	Souris	Inhalation	SWCNT - 5 mg/m^3, 5 h/jour pendant 4 jours (évaluation : 1, 7 et	+	+	+

			28 jours après l'expositi on)			
(DeLor me et al., 2012)	Rats	Inhalatio n uniquem ent par le nez	CNF- 0,54, 2,5 ou 25 mg/m^3, 6 h/jour pendant 90 jours (évaluati on : 1 et 90 jours après l'expositi on)	-	- (0,54 mg/m^3) + (2,5 et 25 mg/m^3)	-

+ : effet observé
- :aucun effet observé

En ce qui concerne la sécurité en milieu de travail, les NFC présentent aussi des risques d'explosion. En présence d'oxygène et d'une source d'ignition, un nuage de fines particules dispersées à une certaine concentration dans un espace clos ou restreint (confinement) est explosible, ce qui forme le pentagone d'explosion des poussière (Figure 3. 9). Cette restriction de l'espace permet une accumulation de la pression, augmentant ainsi la probabilité d'explosion (CCHST, 2020).

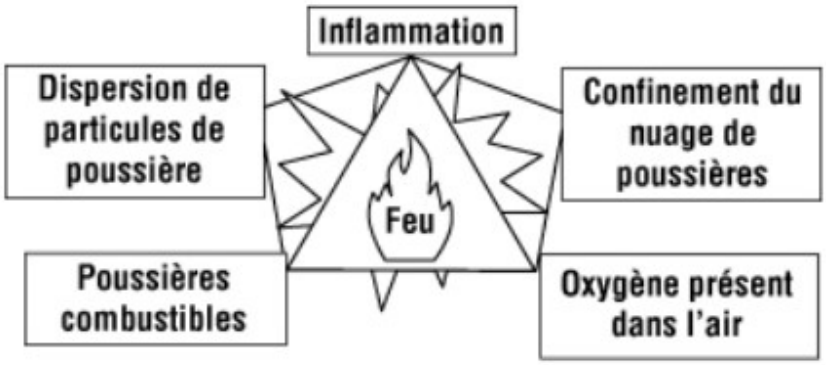

Figure 3. 9 Pentagone de l'explosion de poussières (CCHST, 2020).

Recommandations (National Institute for Occupational Safety and Health, 2018)

Certaines actions en termes de sécurité en milieu professionnel doivent obligatoirement être exécutées. En effet, il faut impérativement :

1. Évaluer l'exposition des travailleurs aux NFC. Les limites recommandées d'exposition aux nanoparticules sont très basses (par exemple pour les NTC, le National Institute for Occupational Safety and Health suggère une moyenne pondérée dans le temps de 1microgram/mètre^3 pour 8 heures de travail par jour),
2. Mener des évaluations complètes de l'exposition (y compris les expositions à d'autres dangers potentiels) dans le cadre d'un programme global de surveillance des dangers.
3. Élaborer des lignes directrices pour la sélection, l'installation et l'évaluation des contrôles techniques (p. Ex. Ventilation locale par aspiration, systèmes de collecte de poussière).
4. Éduquer et former les travailleurs à la reconnaissance des expositions potentielles et à l'utilisation de bonnes pratiques de travail dans la manipulation des NFC en vrac, ainsi que des matériaux contenant des NFC.
5. Mettre en œuvre un programme de surveillance médicale pour les travailleurs potentiellement exposés aux NFC avec réalisation de tests de dépistage médical spécifiques.
6. Encouragez les travailleurs à se laver les mains avant de manger, de fumer ou de quitter le lieu de travail.
7. Donner la possibilité aux travailleurs de prendre une douche et de changer de vêtements. Des zones de stockage des vêtements autres que ceux de travail doivent être prévues afin de prévenir la contamination croisée accidentelle d'autres zones.

Analyse What-if

Le procédé de production des NFC comporte plusieurs risques pour la santé et la sécurité des manipulateurs. Une analyse What-if est effectuée pour évaluer les risques liés aux deux sections principales du processus à savoir la section de la réaction et de la section de la filtration.

Les risques les plus importants, comme mentionnés précédemment, sont : l'incendie, l'explosion, l'intoxication et l'asphyxie.

Le réacteur

Que se passe-t-il Si une fuite du réacteur survient ?

- **CP (conséquences potentielles)** : Une fuite de gaz inflammable, qui, en présence de l'air et d'une source d'ignition pourrait provoquer un incendie.
- **BE (barrières de sécurité existantes)** : Un test de fuite par le biais de l'utilisation d'un gaz inerte et une inspection du réacteur et de tous les tuyaux qui l'entourent doivent être faits avant chaque début de manipulation.
- **RBA (recommandations de barrières de sécurité additionnelles)** : Comme l'espace où se trouve le réacteur est ouvert, un détecteur portatif s'avère indispensable pour détecter les fuites.

Que se passe-t-il Si une surpression ou une surchauffe survient ?

- **CP** : Bris et perte de confinement et déversement des produits gazeux et des NFC .
- **BE** : Le matériau de construction du réacteur ainsi que l'épaisseur respectent les normes ASME. L'instrumentation (thermocouples, jauges de pression) et l'acquisition des données à tout moment permettent de suivre l'évolution de la T et de la P et d'intervenir rapidement si une augmentation est remarquée,
- **RBA** : Maintenance fréquente sur l'instrumentation et le réacteur.

Le filtre

Que se passe-t-il Si une fuite dans le filtre survient ?

- **CP** : En présence d'air et d'une source d'ignition, une fuite de gaz inflammable pourrait provoquer un incendie,

- **BE** : Des détecteurs de gaz sont installés près du filtre et la salle dans laquelle se trouve le filtre est coupe-feu.
- **RBA** : Un test de fuite par le biais de l'utilisation d'un gaz inerte et une inspection du réacteur et de tous les tuyaux qui l'entourent doivent être faits avant chaque début de manipulation.

Que se passe-t-il Si une surpression survient ?

- **CP** : Bris et perte de confinement et déversement des produits gazeux et des NFC.
- **BE** : L'instrumentation (thermocouple, jauges de pression, relief valve) indiquera à quel moment la décharge du filtre doit être faite.
- **RBA** : Maintenance sur l'instrumentation et le filtre.

Analyse HAZOP

La gestion des risques de sécurité opérationnelle est abordée à l'aide d'une analyse de type « HAZard and OPerability Analysis » (HAZOP).

La Figure 3. 10 montre que la gravité est cotée de 1 à 5, la probabilité de A à E et que la sévérité augmente avec l'indice. L'intersection de la gravité d'un événement et de sa probabilité donne une idée sur le niveau de ce risque, soit élevé (rouge), moyen (jaune) ou bas (vert). L'analyse est effectuée sur deux nœuds, à savoir : le réacteur et le filtre. Les tableaux Tableau 3. *11* et Tableau 3. *12* donnent les résultats de cette analyse HAZOP.

MATRICE DE RISQUE D'UNE ORGANISATION									
					PROBABILITÉ				
Gravité	Personnes	Environnement	Biens	Réputation	**A** Improbable. On juge l'évènement possible mais qu'il ne surviendra pas pendant la vie utile de l'installation	**B** Peu probable. Pourrait se produire une fois entre 25 et 40 ans.	**C** Occasionnel. Pourrait se produire une fois entre 10 et 25 ans.	**D** Probable. Pourrait se produire une fois entre 1 et 10 ans.	**E** Fréquent. Se produit une fois par an ou plus
5. Catastrophique	Plusieurs pertes de vies ou blessures graves avec incapacité permanente	Conséquences très importantes de pollution de cours d'eau, de l'air et/ou du sol	Dommages importants. Perte totale des opérations pour une période de plus de 2 semaines. Coûts plus de 1 000 000 $	Impact médiatique international					

4. Majeur	Une perte de vie ou blessure grave avec incapacité permanente	Conséquences importantes de contamination de cours d'eau, de l'air et/ou du sol	Dommages majeurs. Perte totale des opérations pour 24heures à 2 semaines. Coûts entre 1 et 1 000 000 $	Impact médiatique national			**RISQUES ÉLEVÉS**		
3. Critique	Blessure ou effets graves sur la santé. Absence de longue durée.	Conséquences locales	Dommages locaux. Arrêt total des opérations pour 4 à 24heures. Coûts entre 250 000 et 500 000$	Impact médiatique régional		**RISQUES MOYENS (ALARP)**			
2. Marginal	Blessure mineure ou effets mineurs sur la santé. Absence de courte durée.	Effets mineurs	Dommages mineurs. Interruption mineure des opérations (moins de 4h). Coûts entre 100 000 et 250 000$	Impact médiatique local					
1. Négligeable	Blessures légères (premiers soins) ou effets légers sur la santé	Effets légers	Dommages légers. Pas d'arrêt des opérations. Coûts moins de 100 000$	Aucun impact médiatique	**RISQUES BAS**				
Risques élevés	Ce niveau de risque expose la compagnie à des niveaux intolérables pour les personnes, l'environnement, les biens (entreprises et tierces parties) et la réputation. Les dangers doivent être éliminés ou les risques réduits à des niveaux plus bas immédiatement. DES ACTIONS DOIVENT ÊTRE PRISES IMMÉDIATEMENT POUR RÉDUIRE LES RISQUES								

Risques moyens. Acceptable doit être géré au niveau ALARP	Les risques doivent être gérés en réduisant la sévérité des dangers ou leur probabilité au niveau le plus bas que raisonnablement possible de le faire (ALARP). LA RÉDUCTION DES RISQUES DOIT ÊTRE PLANIFIÉE ET DOCUMENTÉE.
Acceptable sans action correctives supplémentaires	Des mesures correctives supplémentaires ne sont pas essentielles mais peuvent être appliquées lorsque les ressources sont disponibles

Figure 3. 10 Matrice des risques.

HAZOP								
Nœud 1 : Réacteur (R1)								
Éléments / Paramètres				**Finalité / Activités**		**Origine**		**Destination**
Température: 600 °C Pression: 1 atm Entrée: CO_2+C_2H_4 Sortie : Gaz de synthèse+NFC+C_2H_4+CO_2				Production des NFC		Préchauffeur		Filtre
No.	**Déviation**	**Cause(s) plausible(s)**	**Conséquences**	**G**	**Dispositifs existants**	**F**	**R**	**Recommandations**
1	**Hausse de température**	Gaz alimenté très chaud, réaction non contrôlée (la réaction est légèrement exothermique)	Dommages aux instruments et au recouvrement interne du réacteur, perte de confinement, incendie, explosion	4	Thermocouples, alarme haute température	D		Inspection périodique du préchauffeur (origine) et maintenance préventive. Inspection périodique des instruments
2	**Baisse de température**	Gaz alimenté pas bien chauffé à cause de problèmes dans le préchauffeur	Altération de la qualité du carbone formé et du rendement	2	Thermocouples, alarme basse température	D		
3	**Hausse de pression**	Blocage de la ligne de sortie du réacteur (C2) à cause de l'accumulation des NFC	Dommages au réacteur, déformation, perte de confinement, fuite de gaz et propagation des NFC dans l'environnement, incendie, explosion	4	Détecteurs de pression, alarme haute pression, relief valve	D		Nettoyage et inspection périodique de la sortie du réacteur (ligne C2) et maintenance préventive

4	**Baisse de pression**	Faible débit de gaz à l'entrée, fuite de gaz.	Diminution de la production, incendie, explosion	4	Jauge de pression, alarme basse pression, valve de contrôle, débitmètre massique.	D		Nettoyage et inspection périodique d'entrée du réacteur (ligne C1). Inspection périodique des débitmètres massiques.

Tableau 3. 11 Analyse HAZOP, Nœud « réacteur ».

Tableau 3. 12 Analyse HAZOP, Nœud « filtre ».

HAZOP								
Nœud 2 : Filtre (F1)								
Éléments / Paramètres				**Finalité / Activités**		**Origine**		**Destination**
Température: 200 °C Pression: 1 atm Entrée: Gaz de synthèse+NFC+C_2H_4+CO_2, Sortie : Gaz de synthèse+C_2H_4+CO_2				Filtration des NFC		Réacteur		Condenseur
No.	**Déviation**	**Cause(s) plausible(s)**	**Conséquences**	**G**	**Dispositifs existants**	**F**	**R**	**Recommandations**
1	**Hausse de température**	Gaz provenant du réacteur à température très élevée	Dommages au filtre, déformation.	4	Thermocouples, alarme haute température	D		Inspection périodique du réacteur (origine) et maintenance préventive
2	**Baisse de température**	Gaz provenant du réacteur à faible température	Condensation de l'eau, colmatage du filtre, hausse de pression	4	Thermocouples, alarme basse température	D		
3	**Hausse de pression**	Blocage de la ligne de sortie du filtre (C8) à cause de l'accumulation des NFC, ou que l'épaisseur du gâteau est grande	Dommages au filtre, déformation, perte de confinement, fuite de gaz et propagation des NFC dans l'environnement, incendie, explosion	4	Système d'impulsions, détecteurs de pression, alarme haute pression, relief valve	D		Nettoyage et inspection périodique de la sortie du filtre (lignes C3 et C8) et maintenance préventive.
4	**Baisse de pression**	Fuite de gaz ou baisse de pression dans le réacteur	Incendie, explosion	4	Jauge de pression, alarme basse pression, détecteurs de gaz	D		Nettoyage et inspection périodique de toute la tuyauterie entourant le filtre et maintenance préventive

3.4. Problèmes techniques rencontrés et remédiation

Étant donné que la configuration du réacteur est toute nouvelle et qu'il s'agit de la première utilisation du système, plusieurs problèmes sont survenus qu'il fallait absolument résoudre « troubleshooting ». Il faut noter que ces problèmes sont survenus à la fois ou simultanément ce qui a compliqué la résolution.

La configuration initiale du réacteur est présenté en Figure 3. 11.

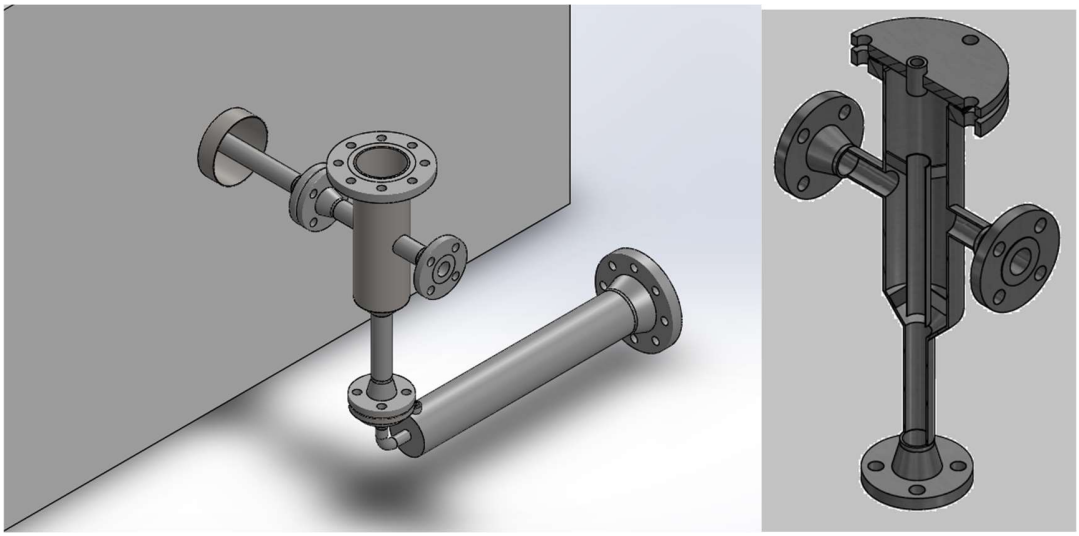

Figure 3. 11 Configuration et installation initiales du réacteur.

Pour pallier les différents problèmes ayant survenu lors des premières manipulations et permettre ainsi au système de fonctionner, nous avons dû apporter différentes modifications dans la configuration initiale du réacteur. Les différents problèmes rencontrés ainsi que les remédiations apportées sont :

3.4.1. Problème 1

Fuites en haut du réacteur et dans le bain de glycol

D'après l'étude hydrodynamique, le débit minimal de fluidisation est de 55 LPM. Pour délivrer ce haut débit, la pression dans les détendeurs des lignes doit être haute pour pouvoir pousser le gaz à travers les débitmètres massiques ce qui entraine une augmentation drastique de la pression dans le réacteur.

Dans le protocole de réaction, après la fermeture du réacteur, un test de fuite doit être fait et ce, afin d'assurer que le réacteur est bien étanche et de prévenir les fuites de gaz. En faisant

ce test, on a constaté la présence de fuites au niveau de la bride quand la pression dépasse 1,36 atmg (20 psig). Le problème de fuite a été attribué au nombre de boulons de la bride, qui était de 4. Pour une bride de ce diamètre, il faut que le nombre de boulons soit de 8. Par conséquent, la solution proposée est de percer la bride de quatre autres trous (Figure 3. 12).

Figure 3. 12 Bride du réacteur avant et après l'ajout des trous.

Un autre problème causé par la haute pression est l'occurrence d'une fuite au niveau du bain de glycol. Cette fuite est due au fait que le vaisseau n'est pas conçu pour fonctionner sous pression. Par conséquent, un débordement du glycol survenait et un risque de fuites de gaz toxique (CO) et inflammables (H_2, CH_4, C_2H_4) était très probable.

Pour contourner une telle situation , le bain de glycol a été contourné et un ajout du gel de silice dans le condenseur (Figure 3. 13) était suffisant pour la déshumidification quasi-totale du flux gazeux et ce, afin de protéger le GC.

Figure 3. 13 Bypass du bain de glycol.

3.4.2. Problème 2

Blocage majeur dans le tube inférieur du réacteur

Le test de fuite a été effectué à 1,5 atmg (22 psig). L'étape d'activation s'est déroulée normalement. Au bout de quelques minutes de réaction, la pression a monté graduellement jusqu'à atteindre la P_{max}. Après l'ouverture du réacteur, on a constaté la présence d'un bloc dense au niveau du tube inférieur causé par la formation du carbone et le compactage du lit.

Afin de maintenir le catalyseur dans le cylindre supérieur du réacteur, nous avons introduit dans le cylindre inférieur, une grille fine, fixée sur un support, de diamètre d'ouverture inférieur au diamètre du catalyseur (Figure 3. 14).

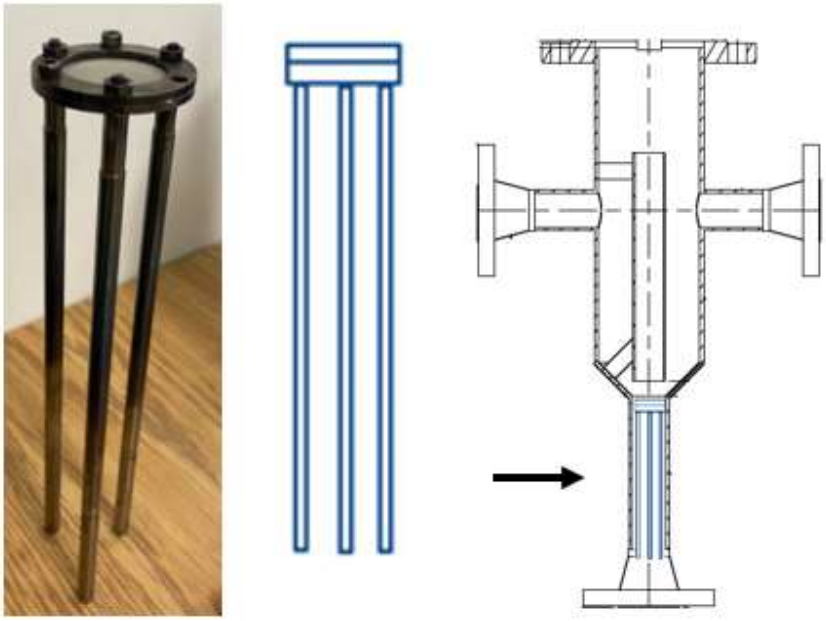

Figure 3. 14 Introduction de la grille dans le cylindre inférieur du réacteur.

3.4.3. Problème 3

Blocage dans le tube inférieur du réacteur

Malgré les solutions apportées aux problèmes suscités, la réaction devait être arrêtée du fait encore une fois de cette formation de carbone, du compactage du lit mais aussi de l'augmentation non contrôlée de la pression.

En fait, à force d'insérer et de retirer à chaque fois le support de la grille, le gap entre ce support et la paroi du cylindre inférieur est devenu large de tel sorte que le catalyseur a pu passer en dessous. Par conséquent, la réaction catalysée par les particules de catalyseur tombées a mené à la formation du carbone en dessous de la grille. Plusieurs solutions ont été essayées pour résoudre ce problème, à savoir :

1- Mettre une grille plus fine
2- Refaire un autre support plus serré

Ces solutions n'ayant pas abouti, une majeure modification au niveau de la configuration du réacteur a été faite. Il s'agissait notamment de couper le tube inférieur du réacteur pour éviter carrément l'utilisation du support (Figure 3. 15 et Figure 3. 16).

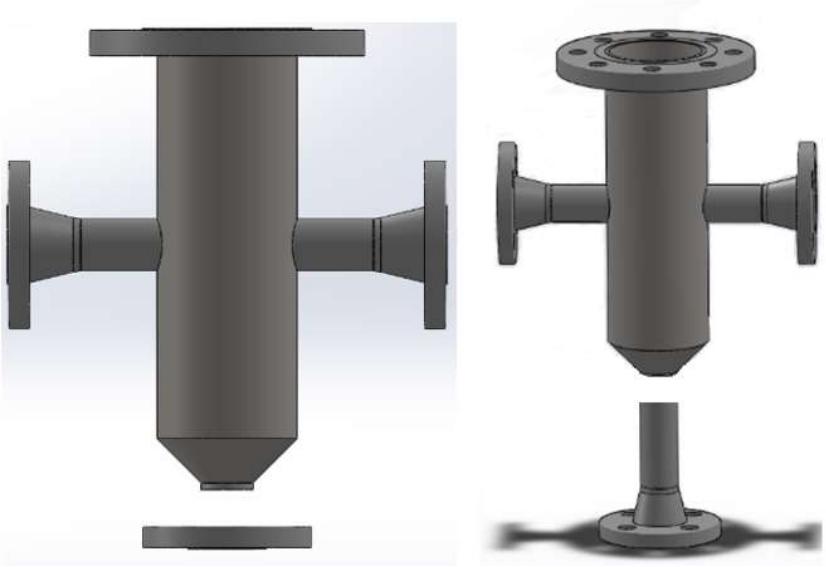

Figure 3. 15 Modification du réacteur.

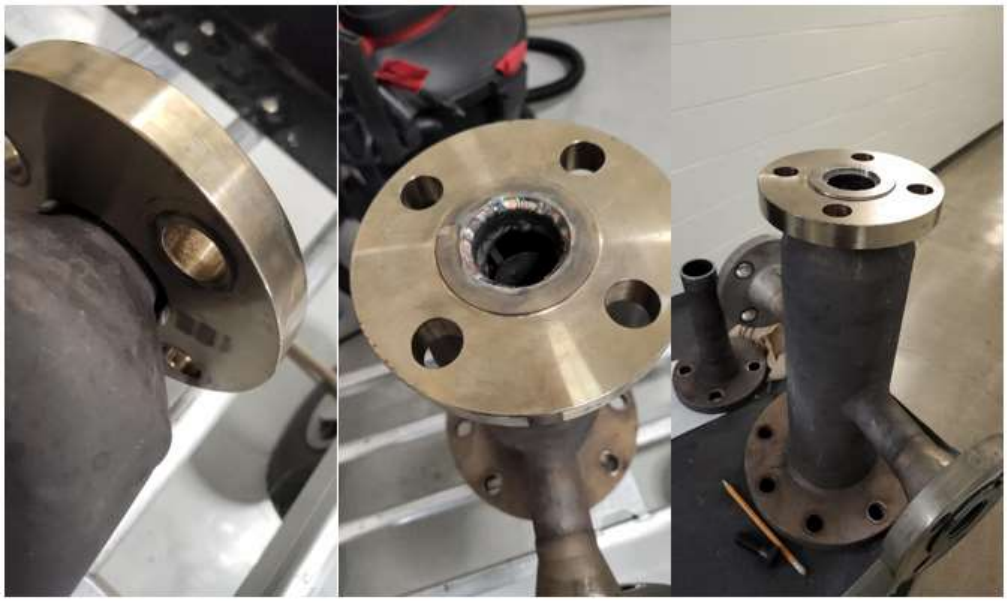

Figure 3. 16 État du réacteur après modification.

3.4.4. Problème 4

Hausse de pression

Malgré la modification apportée à la configuration du réacteur, le travail à haut débit en régime de fluidisation n'était pas possible à cause toujours de l'augmentation de la pression et de la présence d'une fuite au niveau de la grande bride. La raison semblait être la restriction causée par la diminution du diamètre de la tuyauterie, qui passe de 1,5 pouce à 3/8 après le filtre, à ¼ de pouce après le bain de glycol. La petite section de la tuyauterie de ¼ de pouce a été changée afin de réduire un peu ces restrictions, mais le résultat n'était pas très différent.

La solution trouvée était alors de travailler en alternance entre un lit fixe et un lit fluidisé. Le but était de débloquer le lit en le fluidisant par impulsions. En faisant les impulsions avec un haut débit d'azote, le carbone formé après un certain temps a pu être détaché des particules de catalyseur ce qui a empêché le lit de se compacter. Donc le risque d'une augmentation de la pression causée par le travail en régime de fluidisation en continu et le risque de compactage du le lit fixe ont été ainsi évités.

3.4.5. Problème 5

Entrainement du catalyseur

Comme autre problème rencontré, lors du fonctionnement du système en régime de fluidisation, est l'entrainement des particules de catalyseur et l'obstruction des tuyaux qui mènent au filtre. Ce problème a persisté même en travaillant en alternance entre un régime à lit fixe et un régime de fluidisation mais avec une moindre ampleur. La Figure 3. 17 met en relief la solution apportée par nos soins et qui consiste en l'introduction d'une grille.

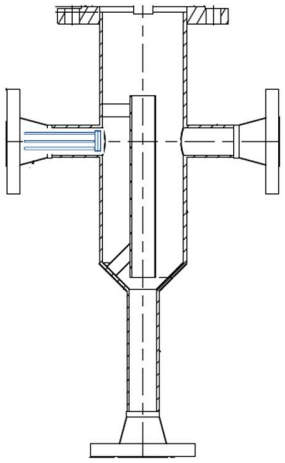

Figure 3. 17 Insertion de la grille à la sortie du réacteur.

Du fait de leur nature collante, les NFC ont tendance à s'agglomérer et à se déposer sur la grille ce qui provoque un blocage et une augmentation de la pression dans le système. Plusieurs grosseurs de grille ont été alors essayées en vain. Par conséquent, retirer carrément la grille semblait être la seule solution. Le travail en régime mixte a atténué un peu le problème d'entrainement et n'a pas causé un grand blocage et une restriction du passage du gaz ce qui pouvait provoquer une augmentation de la pression. Cependant, un nettoyage, en fin de chaque test, était nécessaire d'une part, pour récupérer à la fois le catalyseur et le carbone se trouvant dans les tuyaux et d'autre part, pour empêcher que le problème de blocage soit récurrent pour les prochains tests.

3.3.6. Autres problèmes

Éléments chauffants

Des rubans chauffants, composés de fils métalliques recouverts d'une gaine isolante en tissu de fibre de verre, ont été utilisés pour obtenir la température désirée au sein du réacteur et du préchauffeur. Après réactions et refroidissements de l'équipement, ces gaines se sont solidifiées et commençaient à s'effriter d'où l'apparition de parties dénudées (Figure 3. 18) qui ont été la source de courts circuits au sein du système. Le changement fréquent de ces rubans chauffants a occasionné un surcout.

Figure 3. 18 Rubans chauffants dénudés.

Une solution permanente devait être trouvée pour assurer le chauffage du réacteur et du préchauffeur. Des bandes en céramique, constituées de bobines de résistance enfilée à travers des briques isolantes, ont été fabriquées à cet effet. Ces bandes ont été recouvertes d'une

gaine en acier inoxydable avec une couche d'isolant entre les deux parties (Figure 3. 19). En raison de leur construction qui s'adapte au réacteur et au préchauffeur, les bandes chauffantes en céramique ont été adéquates pour une installation et un retrait faciles.

Figure 3. 19 Bande chauffantes en céramique du préchauffeur.

Torchère

La torchère prévue pour bruler les gaz produits de ce procédé n'a pas été certifiée jusqu'à maintenant. La division de la santé et de la sécurité en milieu de travail de l'université de Sherbrooke a autorisé de faire des tests dans certaines conditions de débit et de temps par jour pour éviter d'évacuer des grandes quantités de gaz dans l'atmosphère en l'attente de la certification de la torchère.

Gaz pyrolytiques

Il a été prévu aussi d'utiliser un gaz produit de la pyrolyse des résidus plastiques provenant du pyrolyseur autothermique. Ce dernier n'est pas encore fonctionnel.

CHAPITRE 4
ÉTUDE PRÉLIMINAIRE

CHAPITRE 4 ÉTUDE PRÉLIMINAIRE

4.1. Avant-propos

Auteurs et affiliation

A. Azara : Étudiante en Doctorat, Université de Sherbrooke, Faculté de Génie, Département de Génie Chimique et Génie Biotechnologique.

M. Chamoumi : ex-étudiant en post-doctorat, Université de Sherbrooke, Faculté de Génie, Département de Génie Chimique et Génie Biotechnologique.

N. Abatzoglou : Professeur, Université de Sherbrooke, Faculté de Génie, Département de Génie Chimique et Génie Biotechnologique.

F. Gitzhofer : Professeur, Université de Sherbrooke, Faculté de Génie, Département de Génie Chimique et Génie Biotechnologique

E. H. Benyoussef : Professeur, École Nationale Polytechnique d'Alger, Département de Génie Chimique.

F. Mohellebi : Professeure, École Nationale Polytechnique d'Alger, Département de Génie Chimique.

Date d'acceptation : 09 décembre 2019

État de l'acceptation : version finale publiée

Revue : Catalysts

Référence : (Azara et al., 2019)

Titre français : Reformage à sec et craquage catalytique de l'éthylène pour la production des nanofilaments de carbone et de l'hydrogène en utilisant un catalyseur à base de résidus miniers.

Contribution au document :Cet article, entrant dans le cadre de cette thèse, porte sur l'élaboration de la production des NFC à échelle laboratoire via la réaction de reformage à sec de l'éthylène. Cette étude a servi à démontrer que le reformage à sec de l'éthylène donne de meilleurs résultats en termes de qualité des NFC que la simple décomposition de cet

hydrocarbure, ce qui a prouvé qu'en plus de l'avantage environnemental de l'utilisation du CO_2, il y'a l'avantage de l'amélioration de la qualité des NFC.

Résumé français :

Dans cette étude, des résidus miniers riches en fer (UGSO) ont été utilisés comme support pour préparer un nouveau catalyseur à base de Ni via un protocole de réaction à l'état solide. Ni-UGSO avec différents pourcentages en poids de Ni (5, 10 et 13) ont été testés pour le reformage à sec du C_2H_4 (DR) et le craquage catalytique (CC) après activation avec H_2. Les réactions ont été conduites dans un réacteur à lit fixe différentiel à 550–750 °C et à pression atmosphérique, en utilisant 0,5 g de catalyseur. Les gaz purs ont été alimentés à un rapport molaire de $C_2H_4/CO_2 = 3$ pour la réaction de DR et $C_2H_4/Ar = 3$ pour la réaction de CC. Le débit est défini par un GHSV = 4800 $mL_{STP}/h.g_{cat}$. Les performances du catalyseur sont évaluées en calculant la conversion de C2H4 ainsi que les rendements en carbone et en H_2. Tous les catalyseurs frais, activés et usés, ainsi que le carbone déposé, ont été caractérisés par différentes techniques de caractérisation à savoir : Brunauer-Emmett-Teller, diffraction des rayons X, microscopie électronique à balayage, spectrométrie de rayons X à dispersion d'énergie, la microscopie électronique à transmission, la réduction programmée de température et l'analyse thermogravimétrique. Les résultats montrent que les rendements les plus élevés en carbone et en H_2 sont obtenus avec Ni-UGSO 13 % à 750 °C pour la réaction CC et à 650 °C pour la réaction DR. Le carbone déposé s'est avéré être filamenteux et de différentes tailles. Les analyses des résultats montrent que le fer est responsable de la croissance des nanofilaments de carbone et que le nickel est responsable de la rupture des liaisons C–C. En termes de rendements de conversion et de rendement, les performances des formulations catalytiques testées s'avèrent au moins équivalentes aux performances des autres catalyseurs à base Ni décrits par la littérature.

4.2. Article: Catalytic Dry Reforming and Cracking of Ethylene for Carbon Nanofilaments and Hydrogen Production Using a Catalyst Derived from a Mining Residue

Abir Azara [1,2], El-Hadi Benyoussef [2], Faroudja Mohellebi [2], Mostafa Chamoumi [1], François Gitzhofer [1] and Nicolas Abatzoglou [1,*]

[1] Department of Chemical & Biotechnological Engineering, Université de Sherbrooke, 2500 Boulevard de l'Université, Sherbrooke, QC J1K 2R1, Canada; abir.azara@usherbrooke.ca (A.A.); Mostafa.Chamoumi@USherbrooke.ca (M.C.); francois.gitzhofer@usherbrooke.ca (F.G.)

[2] Laboratoire de Valorisation des Énergies Fossiles, École National Polytechnique, 10 Avenue Hassen Badi El Harrach BP182, Alger 16200, Algeria; el-hadi.benyoussef@enp.edu.dz (E.-H.B.); mohellebifaroudja@yahoo.fr (F.M.)

*Correspondence: Nicolas.Abatzoglou@USherbrooke.ca

Received: 7 November 2019; Accepted: 9 December 2019; Published: date

Abstract

In this study, iron-rich mining residue (UGSO) was used as a support to prepare a new Ni-based catalyst via a solid-state reaction protocol. Ni-UGSO with different Ni weight percentages wt.% (5, 10, and 13) were tested for C_2H_4 dry reforming (DR) and catalytic cracking (CC) after activation with H_2. The reactions were conducted in a differential fixed-bed reactor at 550–750 °C and standard atmospheric pressure, using 0,5 g of catalyst. Pure gases were fed at a molar ratio of $C_2H_4/CO_2 = 3$ for the DR reaction and $C_2H_4/Ar = 3$ for the CC reaction. The flow rate is defined by a GHSV = 4800 $mL_{STP}/h.g_{cat}$. The catalyst performance is evaluated by calculating the C_2H_4 conversion as well as carbon and H_2 yields. All fresh, activated, and spent catalysts, as well as deposited carbon, were characterized by Brunauer–Emmett–Teller (BET), X-ray diffraction (XRD), scanning electron microscopy (SEM), energy dispersive X-ray spectrometry (EDX), transmission electron microscopy (TEM), temperature programmed reduction (TPR), and thermogravimetric analysis (TGA). The results so far show that the highest carbon and H_2 yields are obtained with Ni-UGSO

13% at 750 °C for the CC reaction and at 650 °C for the DR reaction. The deposited carbon was found to be filamentous and of various sizes (i.e., diameters and lengths). The analyses of the results show that iron is responsible for the growth of carbon nanofilaments (CNF) and nickel is responsible for the split of C–C bonds. In terms of conversion and yield efficiencies, the performance of the catalytic formulations tested is proven at least equivalent to other Ni-based catalyst performances described by the literature.

Keywords: dry reforming; catalytic cracking; ethylene; carbon nanofilaments; hydrogen.

4.2.1. Introduction

Hydrogen is an energy vector and is mainly used in the synthesis of several chemicals such as methanol, ammonia, and liquid hydrocarbons via the Fischer–Tropsch process. Concerning carbon nanofilaments (CNF), several studies have shown that they have noteworthy properties, including high surface area, high mechanical resistance, and high electrical and thermal conductivities (Baker et al., 1975). This is why research efforts have focused on optimizing and controlling the formation of these types of carbon structures, instead of inhibiting their growth (Baker, 2016). Although, usually, carbon formation on catalysts causes the deactivation of the catalyst (Baker & Albright, 1983), CNF are shown to grow in such a way that the catalytically active sites maintain their activity (Jankhah et al., 2008a). CNF properties make them a good substitute to high-cost materials used currently in various applications such as reinforcement of composites (Zeng et al., 2004) , manufacturing of double-layer condensers (Tao et al., 2006) , fabrication of anodes in lithium batteries (Ji et al., 2009; Yoon et al., 2004) , adsorption (Fauteux-Lefebvre et al., 2015) , support for catalysts (Bezemer et al., 2006) , or catalysts themselves (Mestl et al., 2001) .

H_2 is generated mainly from hydrocarbons via thermocatalytic processes such as steam reforming (SR), autothermal reforming (ATR), partial oxidation (POX), dry reforming (DR), and catalytic decomposition or cracking (CC) (Bockris, 2013) . However, methane SR is the only industrial production technology used so far (Wei et al., 2012) . SR is an endothermic reaction and requires a high energy input. Temperatures as high as 950 °C and relatively high steam/C ratios are required to reach high H_2 yields and avoid carbon formation and, consequently, premature catalyst deactivation. In the last decade, many researches have focused on DR that uses CO_2 instead of H_2O to produce not only H_2 but also CNF. Hence,

DR reaction has not only economic interests but also an environmental interest, which is the contribution on the sequestration of CO_2—a greenhouse gas (Blanchard et al., 2008; Braidy et al., 2017; Chamoumi & Abatzoglou, 2016; Jankhah et al, 2008b) .

The feedstock composition, the choice of catalysts including the support and active metals, as well as the operating conditions, especially the temperature, are the main elements that have been largely studied to optimize H_2 and CNF production (Y. T. Shah & Gardner, 2014) . Methane (Hu & Lu, 2009; Pinilla et al., 2011; Takehira et al., 2005), n-octane (Nakagawa et al., 2005), ethanol (Jankhah et al, 2008b) , and biogas (Pinilla et al., 2017) are the main reactants used. The use of pyrolytically-produced gases has rarely been cited in the current literature. Arena et al. (Arena et al., 2006) have developed an innovative process for mass production of multiwall carbon nanotubes (MWCNT) by pyrolysis of virgin or recycled polyolefins. Regarding CNF production, the literature is rather scarce. Svinterekos et al. (Svinterikos & Zuburtikudis, 2016) used lignin (a natural polymer found in plants) combined with recycled polyethylene terephthalate (PET) to make precursor fibers that are used for the electrospinning of CNF. The work presented here is part of a larger research endeavor aimed at the conversion of waste plastic streams into added plus-value products such as CNF. Since the gases produced by plastic pyrolysis are composed mainly of unsaturated hydrocarbons, the first step of this study is focused on using C_2H_4 as a surrogate molecule. The dry reforming reaction of ethylene is not yet well reported in the literature; the products of this type of reaction are considerably dependent on the nature of the catalyst used. In the presence of a transition metal catalyst, carbon and synthesis gas are the products obtained from ethylene DR (Krylov et al., 1995) . However, the Mn and Cr oxides convert ethylene to butadiene and propylene. For example, with a MnO/SiO_2 catalyst at 850 °C, the products obtained are C_4H_6 with a selectivity of 25%, C_3H_6 with a selectivity of 18%, and traces of CH_4, C_3H_8, and C_4H_8 (Krylov et al., 1995) .

The theoretical reaction of ethylene DR is given by (4.1) below (Krylov et al., 1995) :

$$C_2H_4 + 2CO_2 \rightarrow 4CO + 2H_2 \ (\Delta H^{\circ}_{298} = 292{,}5 \text{ MJ/kmol}) \qquad (4.1)$$

Other known reactions that take place during ethylene DR are:

Ethylene decomposition:

$$C_2H_4 \rightarrow 2C + 2H_2 \ (\Delta H^{\circ}_{298} = -52{,}5 \text{ MJ/kmol}) \quad (4.2)$$

Reverse water gas shift reaction (RWGS):

$$CO_2 + H_2 \rightleftharpoons CO + H_2O \ (\Delta H^{\circ}_{298} = 41{,}0 \text{ MJ/kmol}) \quad (4.3)$$

Boudouard reaction:

$$2CO \rightleftharpoons CO_2 + C \ (\Delta H^{\circ}_{298} = -172{,}0 \text{ MJ/kmol}) \quad (4.4)$$

Carbon gasification:

$$C + H_2O \rightarrow CO + H_2 \ (\Delta H^{\circ}_{298} = 131{,}3 \text{ MJ/kmol}) \quad (4.5)$$

In general, at the temperatures used for these reactions and in the presence of the chosen catalysts, hydrocarbon molecules (HC) are converted into free radicals in the gas phase or at the catalyst's surface (intermediates). The reforming agent, CO_2 in the case of DR, is also dissociated into oxygen intermediates (O *) and CO. Oxygen-containing intermediates oxidize HC intermediates to produce CO and subsequently produce CO_2 and carbon via the Boudouard reaction (R4). The atomic carbon formed during the Boudouard reaction first diffuses and dissolves into the metal particles until saturation is reached and then the graphitic carbon starts precipitating to form CNF (Baker et al., 1982) . For the CC reaction, HC intermediates self-decompose to produce H_2 and carbon (Nguyen et al., 2016) and the atomic carbon formed follows the same process of diffusion, saturation, and finally precipitation (Romero et al., 2008).

Transition metal-based catalysts, particularly iron and nickel, are recognized for their ability to decompose carbonaceous gases into filamentous carbon and hydrogen. This capacity for carbon formation is due to the high diffusion rate of carbon in these metals at high temperatures.

The coefficients of diffusion of carbon into transition metals at 550 °C are $1{,}2 \times 10^{-7}$, $0{,}8 \times 10^{-7}$, and $0{,}2 \times 10^{-7}$ cm^2/s, for Ni, Fe, and Co, respectively (Romero et al., 2008). Consequently, the carbon yield would increase as follows: Ni-based catalyst > Fe-based catalyst > Co-based catalyst. This order, however, was not confirmed by Romero et al. (Romero et al., 2008) , who studied the influence of these active metals (Co, Ni, Fe) and the influence of the zeolite type support on the synthesis of highly graphitized carbon nanofibers produced from the catalytic decomposition of ethylene. They found that the order is rather Ni > Co > Fe. They affirmed that this difference is due to the zeolite support that has a

different synergistic effect, which explains the important role played by the support, on the activity of the catalyst.

Recently, our research group (GRTP-C & P) collaborated with Rio Tinto Iron and Titanium (RTIT) for the valorization of a mining residue (upgraded slag oxide (UGSO)) of the upgraded slag (UGS) process to produce titanium slag from ilmenite. Since UGSO is largely composed of iron oxides, in addition to Mg and Al oxides, it has been used to produce an effective Ni-functionalized spinel catalyst tested in methane DR, methane mixed reforming (Chamoumi et al., 2017) , and pyrolytic oils SR (Bali et al., 2018) . In this work, we investigate the efficiency of this new catalyst in ethylene DR and CC reactions to produce H_2 and CNF.

4.2.2. Results and Discussion

Fresh Catalyst Characterization

Table 4. 1 illustrates the BET surface area, average pore volume, and average pore diameter for UGSO and Ni-UGSO with different Ni wt.%. We can observe that Ni-UGSO has a smaller BET surface area, smaller pore volume, and smaller pore diameter than UGSO; this is due to the formation of other phases (spinels) as shown on the XRD pattern (Figure 4. 1) that cause a rearrangement of UGSO structure (the signification of each symbol in XRD patterns are presented in Table 4. 2). Regarding the effect of Ni wt.%, no statistically significant change was found. Generally, Ni addition leads to the reduction of specific surface area, pore volume, and pore size of the catalyst.

Table 4. 1 Textural properties of Ni-UGSO with different Ni contents (5, 10, and 13 wt.%).

Catalyst	BET Surface Area ($m^2 \cdot g^{-1}$)	Average Pore Volume ($cm^3 \cdot g^{-1}$) [a]	Average Pore Diameter (nm) [b]	FWHM (nm)	Ni spinel Crystal Size (nm) [c]
UGSO	5,0	0,026	20,1	–	–

Ni-UGSO 5%	2,9	0,013	18,2	0,429	3,38
Ni-UGSO 10%	2,7	0,013	19,2	0,426	3,41
Ni-UGSO 13%	2,9	0,013	17,7	0,429	3,38

[a] Pore volume was obtained from $P/P_0 = 0,97$. [b] Pore diameter was obtained from Barret–Joyner–Halenda (BJH) desorption method. [c] Ni crystallite size was calculated from Scherrer Equation.

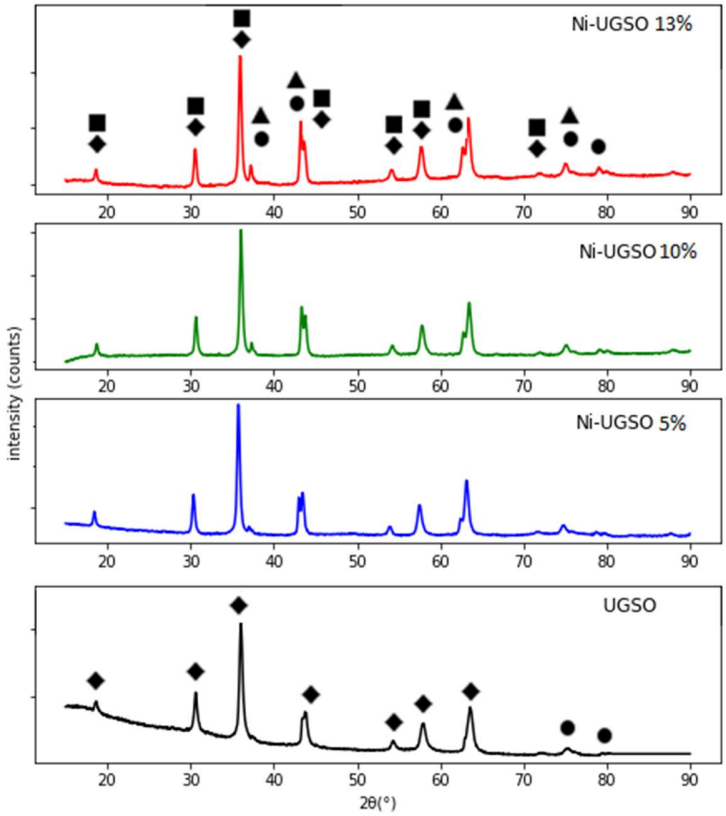

Figure 4. 1 XRD analysis of Ni-UGSO with different Ni contents (0, 5, 10, and 13 wt.%).

We can also observe that the $NiFe_2O_4$ crystal sizes are nanometric and there is no difference in the crystal size in function of wt.% of Ni on the catalyst.

XRD patterns of fresh catalysts with different wt.% of Ni are shown in, which shows that the patterns of the three catalysts are identical. The same family phases have been detected whatever the Ni percentage. In summary, the catalysts are mainly composed of two phases: spinels, in the most probable order of formation (figure of merit (FOM) smallest); $MgFeAlO_4$, $MgFe_2O_4$, Fe_3O_4, $NiFeAlO_4$, $AlFe_2O_4$, $NiFe_2O_4$; and monoxides (NiO, MgO), which coexist in their solid solution. When comparing to the pattern of fresh UGSO (Figure 4. 1), the new crystalline phases are a clear indication that the Ni has been well integrated into the structure of the UGSO.

Table 4. 2 XRD phase legend.

Symbol	Phase	Symbol	Phase
◆	$MgFeAlO_4$, $MgFe_2O_4$, Fe_3O_4, $AlFe_2O_4$,	☾	(FeNi)O
■	$NiFe_2O_4$, $FeNiAlO_4$	○	Fe
▲	NiO	◇	Ni
●	MgO	△	$FeNi_3$
⬠	Carbon	☆	Fe_2O_3
⊠	Fe_3C	▯	FeO

According to the TEM images shown in Figure 4. *2* (a), (c), the catalyst particles are faceted and have a size distribution ranging between 70 nm and 355 nm.

SAED patterns shown in Figure 4. *2* (b), (d) indicate that the catalyst is composed of the spinels $NiFe_2O_4$ and Fe_3O_4, and oxides NiO and (MgFe)O (Table 4. 3). These results corroborate the XRD analysis results.

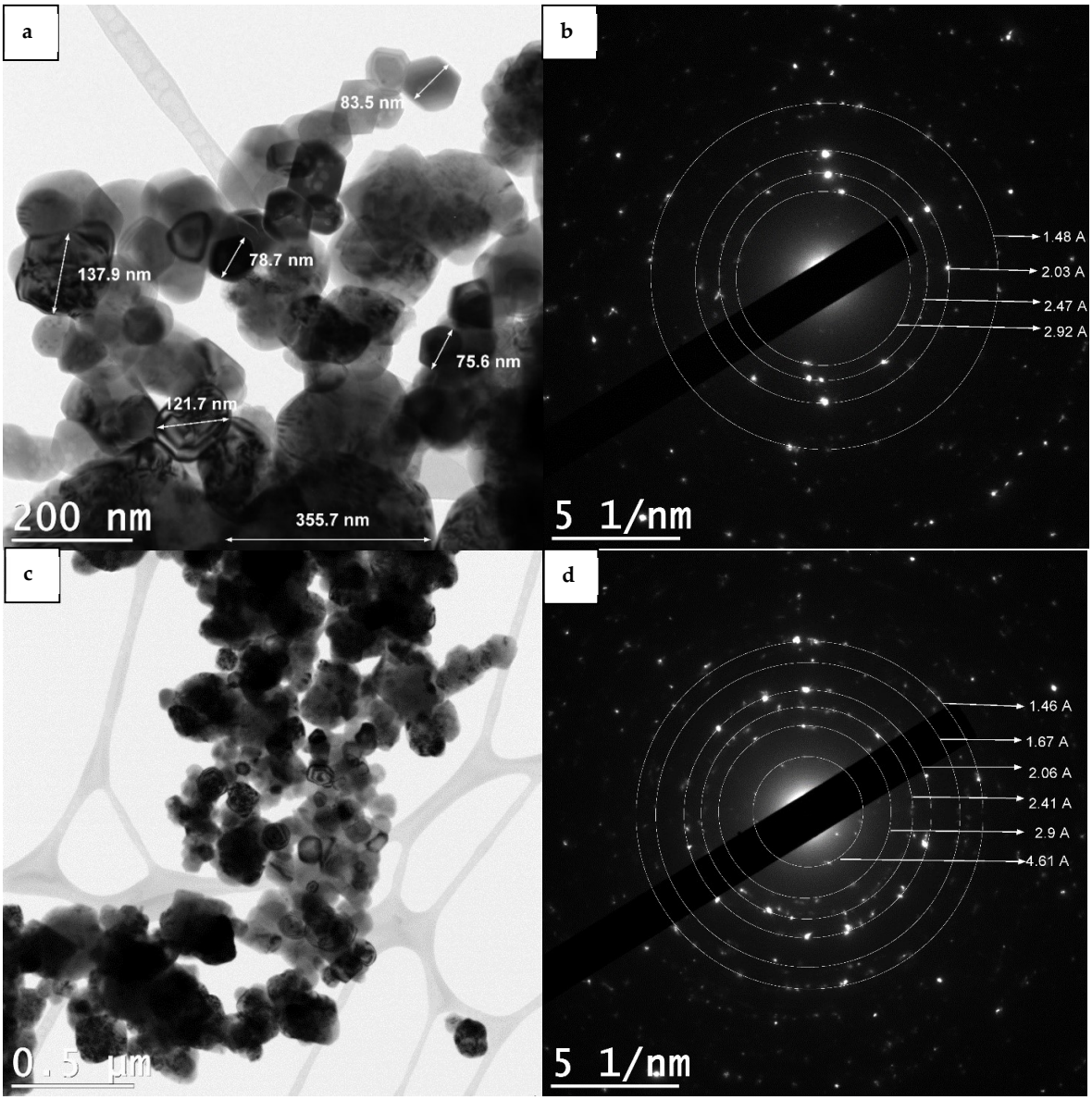

Figure 4. 2 TEM analysis of Ni-UGSO 13% (**a)** , (**c**) and its corresponding selected area electron diffraction (SAED) (**b)** , (**d**).

Table 4. 3 Indexation of d-spacing measured by SAED.

Measured D-Spacing (A°)	Indexation	Theoretical D-Spacing (A°)
1,48 and 1,46	(4 4 0) (MgFe)O/NiO	1,47
1,67	(4 2 2) $NiFe_2O_4/Fe_3O_4$	1,7
2,03 and 2,06	(4 0 0) (MgFe)O/NiO	2,08
2,47 and 2,41	(3 1 1) $NiFe_2O_4/Fe_3O_4$	2,51
2,9	(2 2 0) $NiFe_2O_4/Fe_3O_4$	2,94
4,61	(1 1 1) $NiFe_2O_4/Fe_3O_4$	4,8

Catalyst Activation and Characterization before DR and CC Reactions

Before the DR and CC reactions, Ni-UGSO was activated by H_2. Concerning structural properties, we notice that the activation has increased the BET surface area, pore volume, and pore diameter (Table 4. 4). The effect of the activation is the reduction of metal oxides into metal particles as we can see in XRD pattern (Figure 4. 3), especially into Ni and Fe metal and their alloys, which leads to a pore enlargement and a BET increase due to the nanometric size of the metallic species proved by TEM (Figure 4. 4).

Table 4. 4 Textural properties of Ni-UGSO 13% before and after activation.

Catalyst	BET Surface Area ($m^2 \cdot g^{-1}$)	Average Pore Volume ($cm^3 \cdot g^{-1}$) [a]	Average Pore Diameter (nm) [b]	FWMH	Ni Crystallite Size (nm) [c]
Fresh Ni-UGSO 13%	2,87	0,013	17,7	0,43	3,4
Activated Ni-UGSO 13%	4,81	0,024	19,1	1,39	1,2

[a] Pore volume was obtained from $P/P_0 = 0,97$.

[b] Pore diameter was obtained from Barret–Joyner–Halenda (BJH) desorption method. [c] Ni crystallite size was calculated from Scherrer Equation.

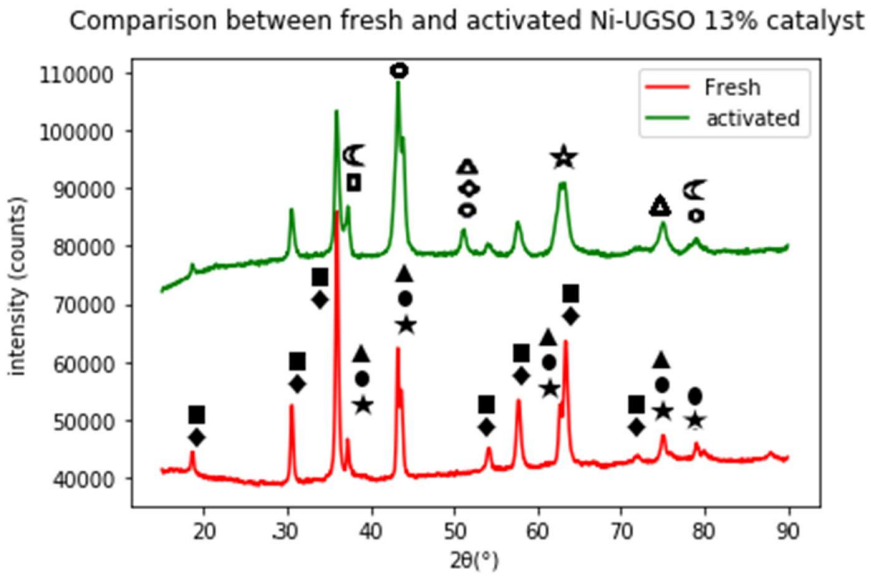

Figure 4. 3 XRD analysis of Ni-UGSO 13% before and after activation.

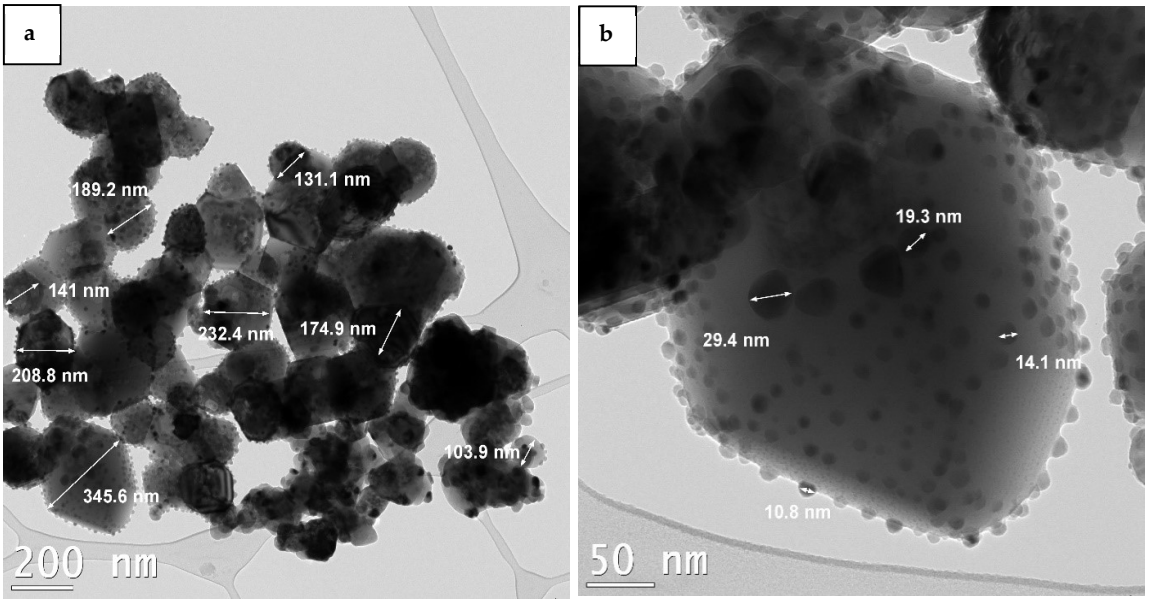

Figure 4. 4 TEM analysis of activated Ni-UGSO 13%, (a) support particle size and (b) crystallite size.

When comparing the XRD patterns of the catalyst structure before and after activation by H_2, we can observe the appearance of peaks attributed to the metallic phases Ni, Fe, and their alloys. Yu et al. (Yu et al., 2005) have shown that the reduction of catalysts containing Ni

and Fe leads to the formation of their alloys such as tarnite and kamacite, and the proportion of Ni:Fe on the alloy after reduction depends on their initial mass ratio. We can also observe the presence of FeO, which means that the magnetite has been reduced partially into wüstite and iron.

TPR analysis was used to determine the reduction temperatures of the different metal species present in the catalyst. The TPR profiles for the three different catalysts with different wt.% (Figure 4. 5) have the same shape with three distinctive peaks. The difference is in the amount of H_2 consumed, which, as expected, increases with the wt.% of Ni in the catalyst.

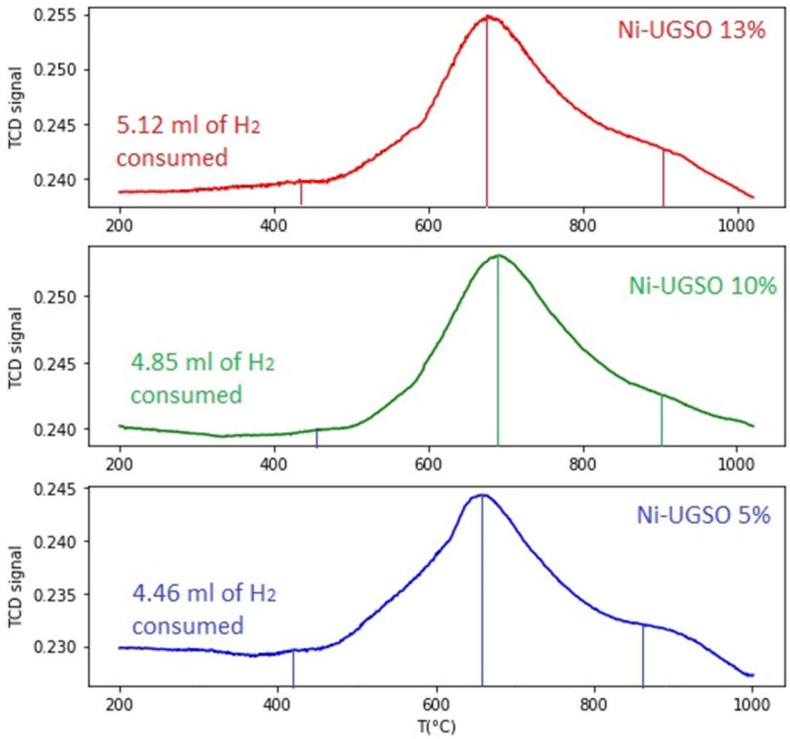

Figure 4. 5 TPR analysis for Ni-UGSO with different Ni contents (5, 10, and 13 wt.%).

In fact, the reduction temperature of metals depends on their interaction with the support and their location, as well as the structure to which it belongs (oxide or spinel). The reduction of Ni-UGSO by H_2 essentially leads to the formation of metallic Fe and Ni particles in addition to their solid solution. Al and Mg are resistant to reduction and remain in their oxidized state.

The analysis of the Ni-UGSO 13% TPR pattern depicts the main reduction peak (the one in the middle) and two others. The first peak can be attributed to the reduction of free NiO (not

in interaction with all other phases) and the reduction of Fe^{3+} to Fe^{2+}. The second peak can be assigned to the reduction of both Fe^{3+} species to Fe^{2+} and Fe, and Ni^{2+} to Ni (NiO moderately interacting with other phases). The third peak can be attributed to the reduction of NiO strongly interacting with MgO or having a strong interaction with spinel $MgFeAlO_4$ (Chamoumi et al., 2017) .

As shown in Figure 4. 4, the reduction of the catalyst by H_2 led to the formation of metal crystallites with different sizes on the surface of crystals that have not been reduced (Al and Mg oxides). Similar results were found by Romero et al. (Romero et al., 2008) , who studied the reduction of zeolite-supported Ni- and Fe-based catalysts. They observed Fe and Ni crystallites with different distributions formed on the surface of the zeolite. In fact, the activation of catalysts by H_2 led to the reduction of oxides into small metallic particles, which are the active phase for the growth of CNF.

As depicted in Figure 4. 4 (b), the crystallite sizes are in the range of 10–30 nm. Yu et al. (Yu et al., 2005) have found that the reduction of the Ni:Fe (6:1) catalyst has an average crystallite size of 6 nm with a Gaussian-like distribution. The difference observed when comparing our results with those in the literature might be due to a different Ni:Fe ratio and/or to the reduction conditions (nature of the substrate and rate of heat and mass transfer). Some sintering seems to have taken place due to reduction because, if we compare Figure 4. 4 (a) and Figure 4. *2*, , we notice that the support particle size has increased (100–400 nm).

Measured D-Spacing (A°)	**Indexation**	**Theoretical D-Spacing (A°)**
1,48 and 1,46	(4 4 0) (MgFe)O/NiO	1,47
1,67	(4 2 2) NiFe2O4/Fe3O4	1,7
2,03 and 2,06	(4 0 0) (MgFe)O/NiO	2,08
2,47 and 2,41	(3 1 1) NiFe2O4/Fe3O4	2,51
2,9	(2 2 0) NiFe2O4/Fe3O4	2,94
4,61	(1 1 1) NiFe2O4/Fe3O4	4,8

The EDX pattern (Figure 4. 6) shows that these crystallites are composed mainly of Ni and Fe and no O has been detected. This proves that these crystallites are metallic, and they are Ni, Fe, and/or Ni–Fe alloys, thus corroborating the already presented XRD results.

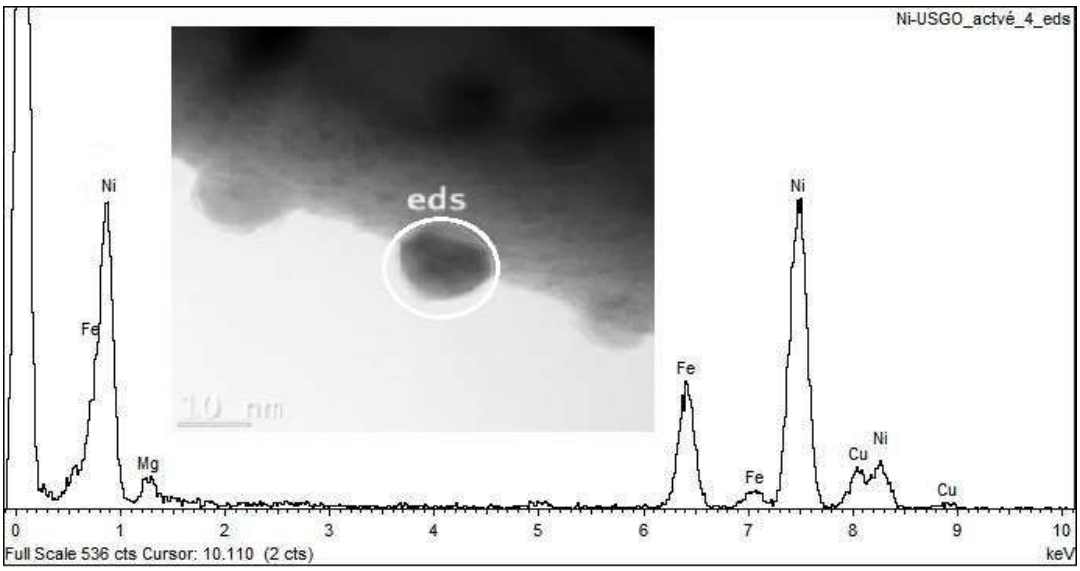

Figure 4. 6 EDX analysis of activated Ni-UGSO 13%.

Ni-UGSO Catalyst Performance

Thermodynamic Investigation

FactSage software was used to study the thermodynamic equilibrium of the C_2H_4 CC and DR reactions at different conditions of temperature (450–850 °C) and molar ratios C_2H_4/CO_2 (1/1-3/1) at atmospheric pressure. Equilibrium composition, heat, and enthalpy of the reaction, as well as the amount of deposited carbon, were studied during this research. This investigation allowed us to choose the experimental conditions. The results are shown in Figure 4. 7 to Figure 4. 9.

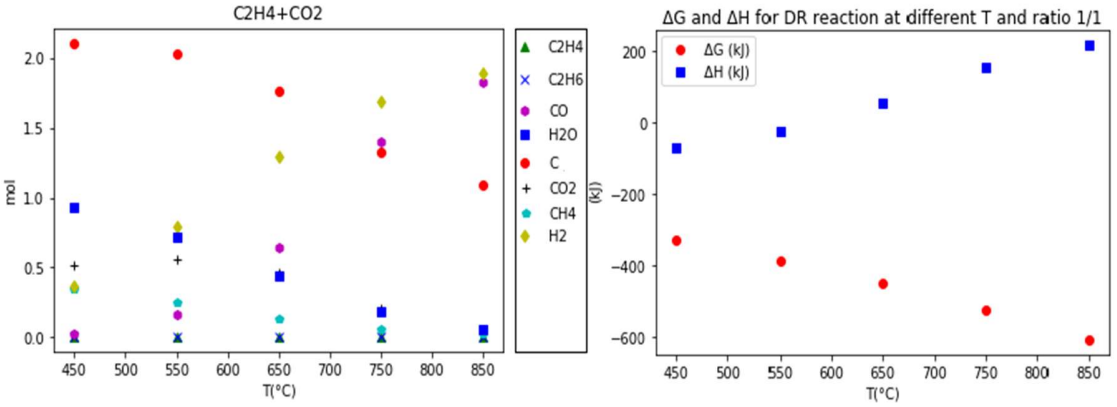

Figure 4. 7 Thermodynamic study of DR reaction at different temperature at ratio 1/1.

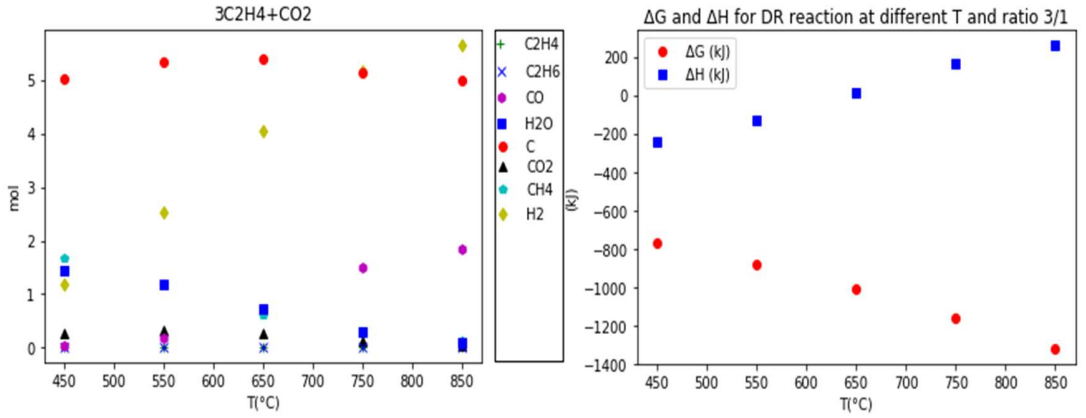

Figure 4. 8 Thermodynamic study of DR reaction at different temperature at ratio 3/1.

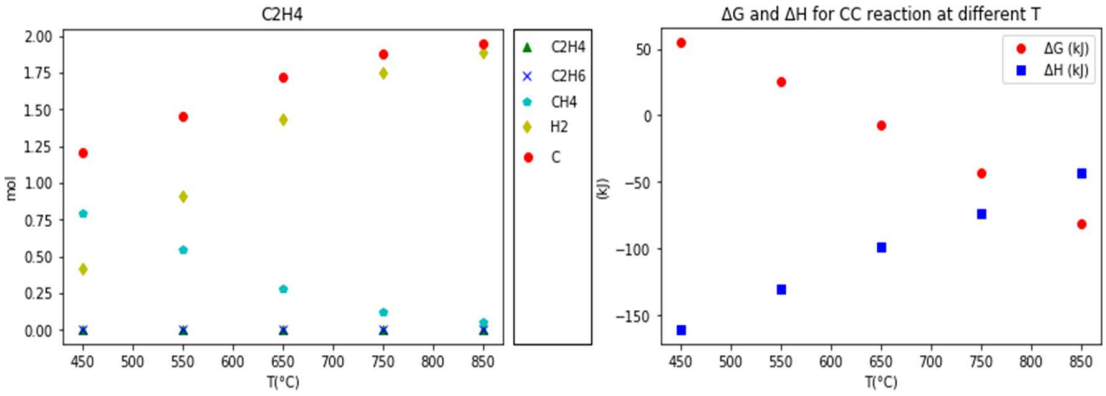

Figure 4. 9 Thermodynamic study of CC reaction at different temperature.

ΔH is negative for the CC reaction, which means that the reaction is exothermic, and it increases with the increase of temperature (Figure 4. 9). The DH of the DR reaction is

negative for temperatures below 600 °C for both ratios. This means that at temperatures higher than 600 °C the reaction is endothermic. The heat of this reaction increases with the increase of the amount of ethylene in the feedstock.

The decline of ΔG with temperature illustrates that the equilibrium is displaced toward the products. For the CC reaction, at temperatures below 700 °C, ΔG is positive and, therefore, the reaction is not taking place. For the DR reaction, ΔG is higher at higher C_2H_4/CO_2 ratios, which means that conversion is favored.

For the CC reaction, H_2 and carbon amounts at the equilibrium increase with temperature (Figure 4. 9). However, for the DR reaction, the H_2 amount increases with the temperature for both ratios, while the C amount decreases with the temperature at ratio 1/1 and reaches its maximum at 650 °C at a ratio of 3/1.

Based on these results, the three following temperatures have been chosen to be studied experimentally: 550 °C, 650 °C, and 750 °C. Since we want to maximize carbon and H_2 production, a 3/1 ratio of C_2H_4/CO_2 was chosen.

Study of CC Reaction

The effect of temperature and Ni percentage on CNF and H_2 yields, as well as carbon growth rate, are presented in Figure 4. 10 and Table 4. 5, respectively.

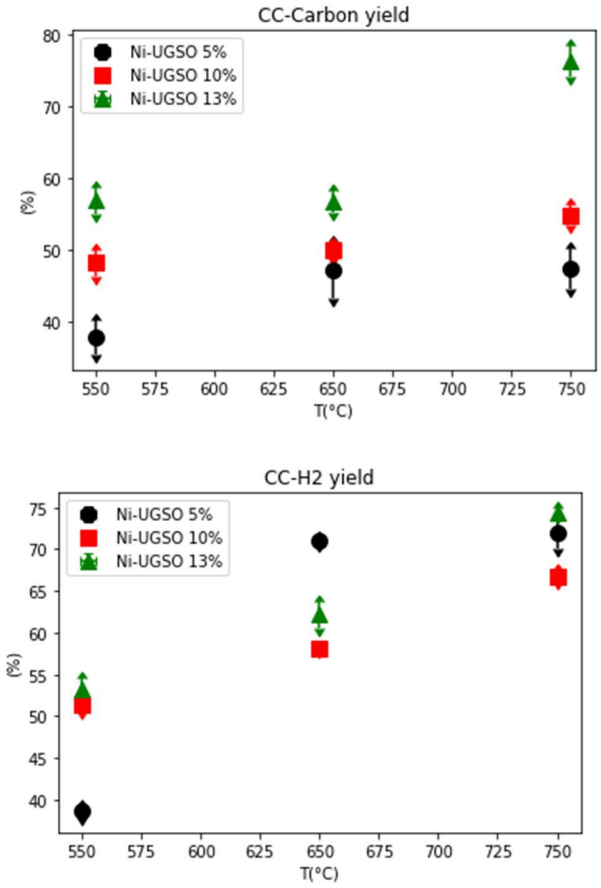

Figure 4. 10 Carbon and H_2 yields for the CC reaction using Ni-UGSO with different Ni wt.% (5, 10, and 13) at T = 550 °C, 650 °C, and 750 °C for 2 h time-on-stream (TOS).

Table 4. 5 Carbon growth rate for the CC reaction using Ni-UGSO with different Ni wt.% (5, 10, and 13) at T = 550 °C, 650 °C, and 750 °C for 2 h TOS.

Catalyst	**Carbon Growth Rate ($g_C \cdot g_{cat}^{-1} \cdot h^{-1}$) At**		
	550 °C	650 °C	750 °C
Ni-UGSO 5%	1,4	1,7	1,8
Ni-UGSO 10%	1,8	1,8	1,9
Ni-UGSO 13%	2,1	2,2	2,8

Yu et al. (Yu et al., 2005) , who used a bimetallic catalyst of Ni–Fe with different Ni loading levels, found that productivity is higher for higher T and higher Ni loading. This work shows that C and H_2 yields increase with temperature (Figure 4. 10). This is in accordance with the previously reported literature (Yu et al., 2005) . Moreover, the carbon growth rate increases with T because the solubility and diffusion of the carbon in the solid metallic phases also increases with T (Chesnokov & Buyanov, 2000). This effect is even more pronounced at higher percentages of Ni in the catalyst.

Since the highest carbon and H_2 yields were observed at T = 650 °C and wt.% of Ni = 13%, the reaction results at these conditions are presented in detail in Table 4. 6 and Figure 4. 11.

Table 4. 6 General experimental results for CC reaction using Ni-UGSO 13% at 750 °C for 2 h TOS.

C_2H_4 (mL/min)	**30**
Ar (mL/min)	10
Catalyst weight (g)	0,5
TOS (min)	120
$GHSV_{STP}$ ($mL \cdot h^{-1}$. g)	4800
C_2H_4/Ar	3
Ar/C_2H_4	0,33
Carbon (g)	2,8
Carbon production rate ($g_C \cdot g_{cat}^{-1} \cdot min^{-1}$)	0,047
Carbon production rate ($g_C \cdot g_{cat}^{-1} \cdot h^{-1}$)	2,8
Carbon yield (%)	76,3
Total H_2 yield (%)	74,5
Total C_2H_4 conversion (%)	92,2
Mass balance error for C (%)	3,31
Mass balance error for H (%)	0,08

Overall, the highest carbon and H_2 yields, Y_{H2} = 74,5% and Y_C = 76,3%, respectively, are observed at T = 750 °C and 13% of Ni. Thus, the carbon turnover frequency (TOF) expressed per mass of catalysts was 2,8 $g_C \cdot g_{cat}^{-1} \cdot h^{-1}$ at a flow rate of 30 mL/min (Table 4. 6**)**. When compared to the catalysts used in the literature, this catalyst has shown similar to better

performance. Yu et al. (Yu et al., 2005) have produced 3 $g_C \cdot g_{cat}^{-1} \cdot h^{-1}$ and 2,55 $g_C \cdot g_{cat}^{-1} \cdot h^{-1}$ using bimetallic catalysts Ni–Fe(6-1) and Ni–Fe(5-5), respectively, with a feed of $C_2H_4/CO/H_2$ (30/10/10). Diaz et al. (Díaz et al., 2008) studied Ni-SiO_2 catalyst for the catalytic decomposition of ethylene to produce carbon, between 600 °C and 700 °C. They obtained the maximum of carbon at 600 °C with 2 $g_C \cdot g_{cat}^{-1} \cdot h^{-1}$ for 60 mL/min of C_2H_4.

Figure 4. 11 shows that the steady-state has been reached very fast during the first 20 min of TOS. The conversion of C_2H_4 is nearly 100% and starts slightly decreasing in the last 20 min. The hydrogen yield is also constant around 80% for 120 min while the rate of carbon formation is also high and equal to 2,82 $g_C.g_{ca}^{-1}.h^{-1}$. The observed high and constant rates of carbon and H_2 formation are due to the high activity of the catalyst at the beginning of the reaction; moreover, even though carbon was formed, the catalyst did not show any deactivation during the TOS of operation. The latter can be explained by the type of carbon formed. Indeed, the carbon formed was analyzed by SEM and it has been proven that it was under the form of CNF (Figure 4. 12), which was not affecting considerably the access of the reactants at the surface of the catalyst.

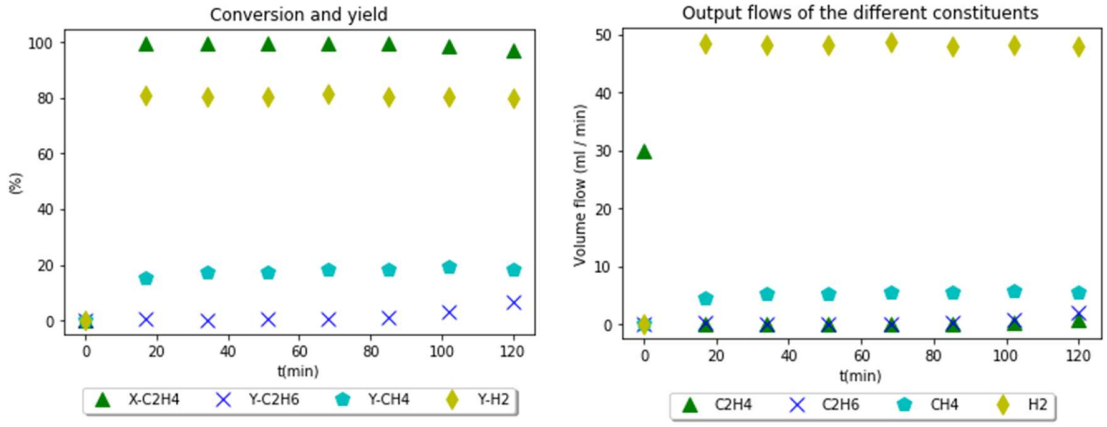

Figure 4. 11 Experimental results for CC reaction using Ni-UGSO 13% at 750 °C.

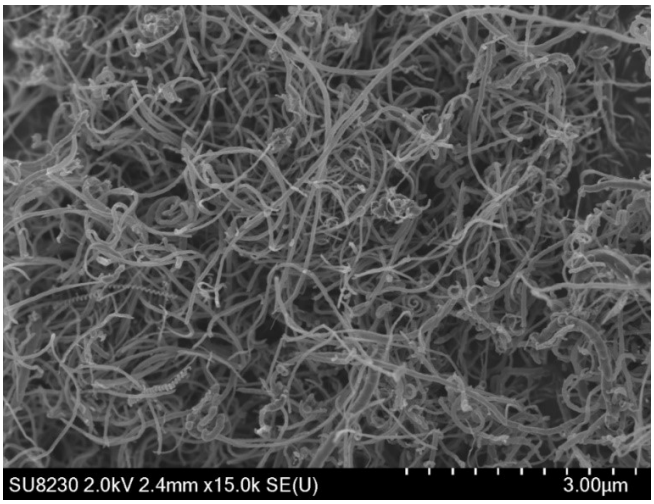

Figure 4. 12 SEM analysis of CNF produced at 750 °C using Ni-UGSO 13% for CC reaction.

Study of DR Reaction

The effect of temperature and Ni percentage on CNF and H_2 yields, as well as carbon growth rate, are illustrated in Figure 4. 13 and Table 4. 7, respectively.

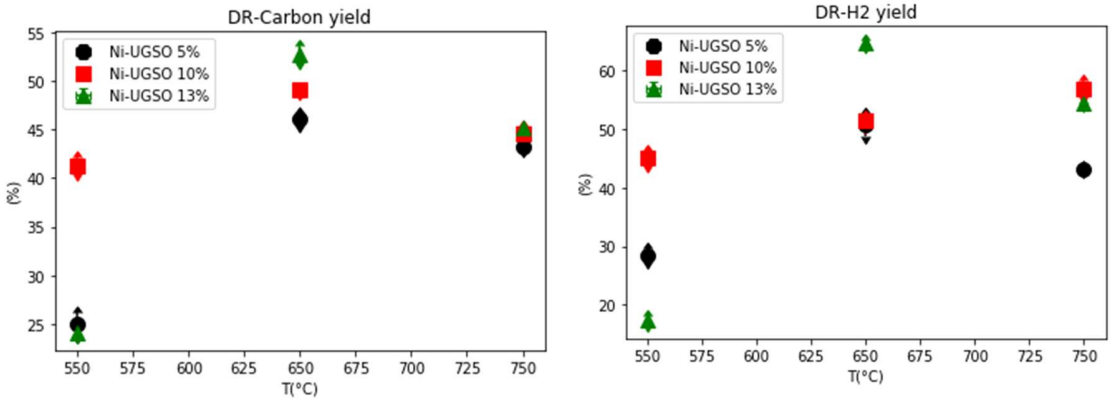

Figure 4. 13 Carbon and H_2 yield for the DR reaction using Ni-UGSO with different Ni wt.% (5, 10, and 13) at T = 550 °C, 650°C, and 750 °C for 2 h TOS.

Table 4. 7 Carbon growth rate for the DR reaction using Ni-UGSO with different Ni wt.% (5, 10, and 13) at T = 550 °C, 650 °C, and 750 °C for 2 h TOS.

Catalyst	**Carbon Growth Rate ($g_C \cdot g_{cat}^{-1} \cdot h^{-1}$) At**		
	550 °C	**650 °C**	**750 °C**
Ni-UGSO 5%	1,1	2,0	1,8

Ni-UGSO 10%	1,7	2,1	1,9
Ni-UGSO 13%	0,9	2,3	2,0

Figure 4. 13 shows that the carbon yield for all Ni contents has a maximum at 650 °C. Although it seems that the same applies to the H_2 yield, the latter keeps increasing in the case of the 10% Ni content catalyst. The amount of Ni active sites is a parameter that plays a significant role in terms of catalytic activity. The BET results in Table 4. 1 show that the specific surface and the average pore volume is not a function of the Ni content in the range between 5 and 13 wt.%. The small difference observed in the case of 10 wt.% Ni catalyst is within the experimental error and cannot be used as a differentiation argument. In light of the above, the difference in H_2 yield observed in the case of the 10 wt.% Ni catalysts might be explained in the following way:

- As expected by thermodynamic calculations, the temperature around 600 °C is optimal for carbon production and this is clearly shown by the experiments in Figure 4. *13*;
- At higher temperatures (i.e., 750 °C), carbon production decreases, but the H_2 yield must increase. Although this is the trend observed with the 10 wt.% Ni catalyst, in the case of 5 wt. % Ni, this increase is nil. In the case of 13 wt.% Ni, we observe the opposite. The most plausible speculation is that, at 5 wt.% Ni, the active catalytic sites are low, while, at 13 wt.% Ni, the Ni distribution is less than optimal. It is well known that in almost all heterogeneous catalysts there is an optimal active metal content below which and above which the catalytic activity decreases.

Since the target of the manuscript is the comparison of two regimes with a number of Ni-UGSO formulations, there are no available surface data to support further discussion. Our continuous efforts are now focusing namely on these aspects. Both carbon and hydrogen yields are maximal at 650 °C. This behavior can be explained by carbon and H_2 formation and consumption reactions. In fact, carbon is produced from C_2H_4 decomposition and Boudouard reaction and consumed by the gasification reaction, while H_2 is produced by C_2H_4 decomposition and consumed by RWGS reaction. C_2H_4 decomposition and RWGS reactions are favored by high temperatures. Boudouard has a thermodynamic maximum of carbon

formation around 550 °C. At T lower than 650 °C, the formation rate exceeds the consumption rate. Concerning the effects of Ni, the yield of carbon and H_2 increases with the increase of the Ni weight percentage in the catalyst, and this is attributed to the higher catalytic activity at higher Ni loading levels and consequently faster reaction rates. We can notice an exception for Ni-UGSO 13% at T = 550 °C where the yields are very low. This could be explained by the fact that the catalyst at such a low T with such a high load of Ni has not reached its highest activity within 2 h. Since the highest carbon and H_2 yields were observed at T = 650 °C and wt.% of Ni = 13%, the reaction results at these conditions are presented in detail in Table 4. 8 and Figure 4. 14.

Table 4. 8 General experimental results for the DR reaction at 650 °C and Ni-UGSO 13% for 2 h TOS.

C_2H_4 (mL/min)	**30**
CO_2 (mL/min)	10
Catalyst weight (g)	0,5
TOS (min)	120
$GHSV_{STP}$ ($mL \cdot h^{-1} \cdot g^{-1}$)	4800
C_2H_4/CO_2	3
CO_2/ C_2H_4	0,33
Carbon (g)	2,25
Carbon production rate ($g_C \cdot g_{cat}^{-1} \cdot min^{-1}$)	0,0375
Carbon production rate ($g_C \cdot g_{cat}^{-1} \cdot h^{-1}$)	2,25
Carbon yield (%)	53,6
Total H_2 yield (%)	67,5
Total C_2H_4 conversion (%)	91,3
Total CO_2 conversion (%)	88,5
Mass balance error for C (%)	9,16
Mass balance error for H (%)	1,46
Mass balance error for O (%)	8,81

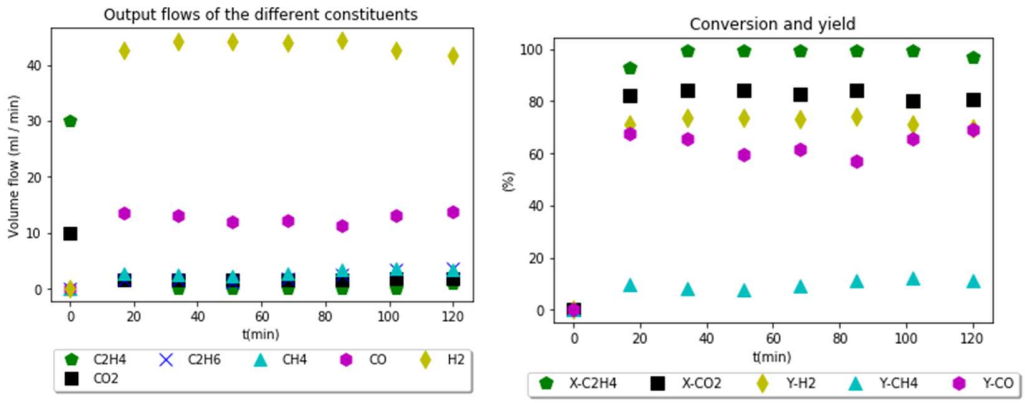

Figure 4. 14 Experimental results for DR reaction using Ni-UGSO 13% at 650 °C for 2 h TOS.

Ni-based catalysts have been used in the past for DR reactions, especially for methane and ethanol, but there are few studies on ethylene dry reforming. Jankhah et al. (Jankhah et al., 2008b) examined in detail the dry reforming reaction of ethanol using activated stainless-steel strips as a catalyst (strip surface of 0,04 m^2). Experiments have shown that the results that give the best yields of carbon and H_2 are obtained at a temperature of 550 °C. They have obtained a carbon rate equal to 3,6 $g \cdot h^{-1}$ and an H_2 yield of 76,33%. Since this catalyst is 2D and not 3D, the equivalent carbon TOF is related to the catalyst surface and not to the weight and is equal to 90 $g \cdot h^{-1} \cdot m^{-2}$. We observed that, during the first 100 min, the conversion of C_2H_4 is near 100% and starts slightly decreasing during the last 20 min. Hydrogen yield is constant for 120 min and equal to 65% (Figure 4. 14), and the rate of carbon formation is high and equal to 2,25 $g_C \cdot g_{cat}^{-1} \cdot h^{-1}$. These high and constant rates of carbon and H_2 formation are due to the high activity of the catalyst and can be explained by the following: the H_2 formed contributes to the additional activation of the catalyst through the reduction of iron oxides. This is proven by the presence of Fe and Ni metal peaks and the disappearance of iron oxide peaks on used catalyst XRD (Figure 4. 16). It has been demonstrated that the carbon under the form of catalytically induced CNF itself has catalytic properties (Jankhah et al., 2008a) . Although the activity measured through carbon TOF per mass of CNF is lower, if the TOF is calculated per mass of carbides content of the CNF, it is shown to be higher. This explains, at least partially, why the catalytic activity remains high even when the catalyst surface is covered by CNF. The carbon formed was analyzed by SEM and it has been proven that it is mainly under the form of CNF (Figure 4. 15).

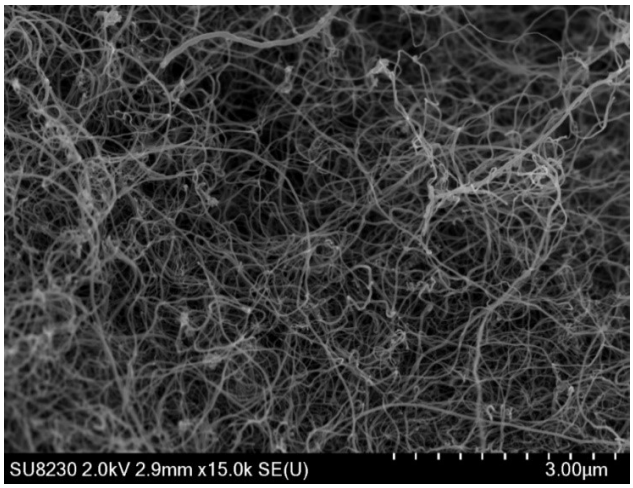

Figure 4. 15 SEM analysis of CNF produced at 650 °C using Ni-UGSO 13% for DR reaction for 2 h TOS.

Characterization of CNF and Spent Catalyst

XRD Analysis

Figure 4. 16 shows the XRD of deposited carbon on the used catalyst after the DR and CC reactions. The peak at 2θ = 26° confirms that the carbon formed is graphitic, no peaks of oxides have been detected, and only Ni and Fe were present in the patters, which proves that their oxides were reduced during the reactions. Carbide formation was expected because carbides are known to be the precursor of CNF especially with iron-based catalysts. Fe_3C is metastable under the reaction conditions so it is decomposed to CNF and α-Fe (Ermakova et al., 2001) . Nickel plays a key role in the formation of CNF because, when UGSO was used alone, catalyst activity was low (Chamoumi et al., 2017) . When nickel was added, the quantity and quality of CNF were found to have improved. Nickel catalyzes the C–C bond cleavage, thus producing carbon species radicals and atomic carbon that diffuses and dissolves in the iron to form a solid solution of iron carbides (Sacco et al., 1984) .

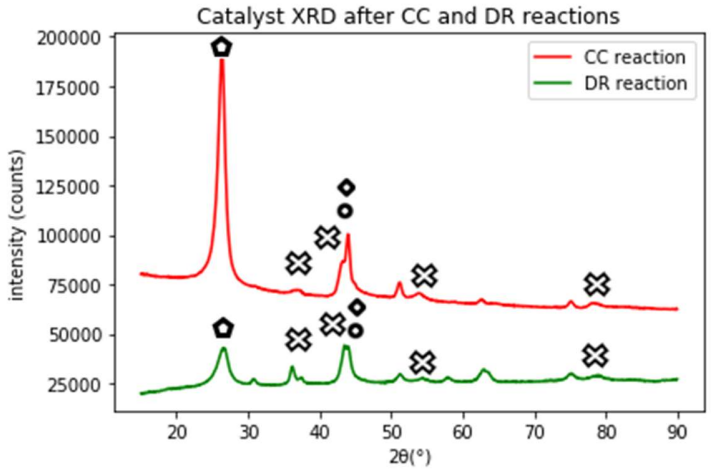

Figure 4. 16 XRD analysis of Ni-UGSO 13% after the CC reaction at 750 °C and after the DR reaction at 650 °C for 2 h TOS.

TGA

Figure 4. 17 shows the results of TGA analysis. For the DR sample, at T up to 450 °C, a mass gain of 0,25% was detected. Between 450 °C and 765 °C, there was a mass loss of about 60%; finally, between 765 °C and 890 °C, a mass gain of 0,05% was observed. For the CC sample, up until 500 °C, a mass gain of 0,23% was measured. From 500 °C to 750 °C, there was a mass loss of 88.62% and, finally, between 750 °C and 900 °C, a mass gain of 0,05% was observed.

The higher the temperature of oxidation, the higher the degree of structural order. Thus, as can be seen in Figure 4. 17, the oxidation of CNF produced by DR (CNF-DR) begins at a temperature lower than that in the case of CNF formed by CC (CNF-CC) (450 °C vs. 500 °C). In the literature, it has been reported that the oxidation of graphite and C_{60} in TGA occurs at 645 °C and 420 °C, respectively (Pang et al., 1993) . The oxidation temperature of CNF-CC is similar to that reported for CNT (Pradhan & Sharon, 2002) and higher than that reported by Sui et al. (Sui et al., 2001) . They are all lower than the graphite oxidation temperature. Serp et al. (Serp et al., 2003) have confirmed that CNT and CNF are more reactive than graphite. They have shown that CNF samples with 10% of remaining metal (produced from ethylene on Fe/SiO_2 catalysts) present a maximum gasification rate at 650 °C. The single-wall carbon nanotube (SWCNT), which is the carbon nanostructure that has the least remaining metal percentage (less than 1% of metal) and the least defects on its

surface, presents a maximum gasification rate at 800 °C. MWCNT, with 3% and 7,5% of residual metal, presents a maximum rate at 650 °C and 550 °C, respectively. According to these findings, the presence of defects on the CNF surface and the presence of residual metal within the carbon nanostructures that can catalyze carbon gasification cause a shift to lower temperatures. While the oxidation resistance of the DR carbon and the CC carbon is different, we can say that either CNF-DR carbon is more structured than CNF-CC, or that it contains more metal, or even that their surfaces are not the same, which means that they are two distinct types of CNF. The TEM analyses reported below help us to identify the type of CNF produced. It is well known that there are different types of CNF depending on the arrangement of the graphene plans. Accordingly, CNF are classified into three categories: platelets, fishbone, and stacked-cup CNF (Baker, 2016) .

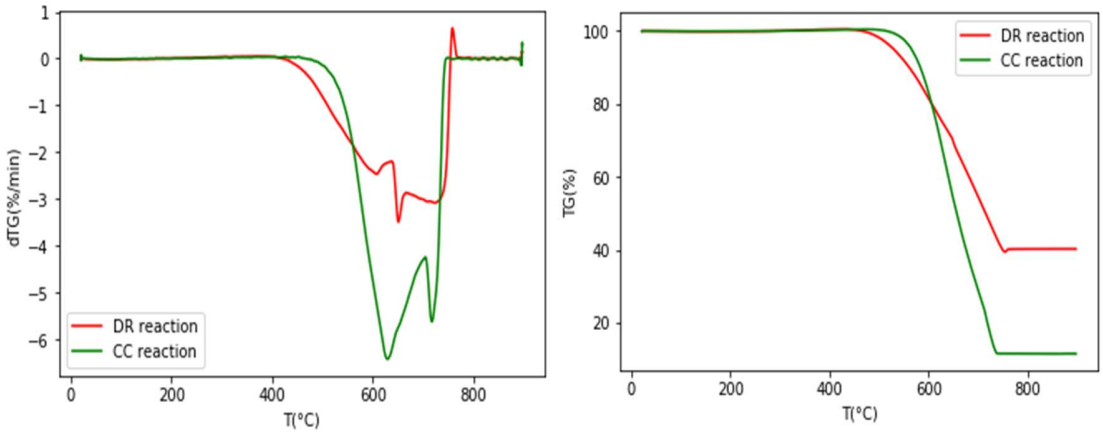

Figure 4. 17 TGA analysis of Ni-UGSO 13% after CC reaction at 750 °C and after DR reaction at 650 °C for 2 h TOS.

SEM-EDX Analysis

SEM images have shown that, in this experiment, the carbon is under the form of filaments of varying diameters. For CNF-DR, the diameter range is 15–50 nm (Figure 4. *18*) and for CNF-CC it is 25–75 nm (Figure 4. 19). Using backscattered electron imaging (Figure 4. 20), we can see that the metal particles are located on the top of the nanofilaments.

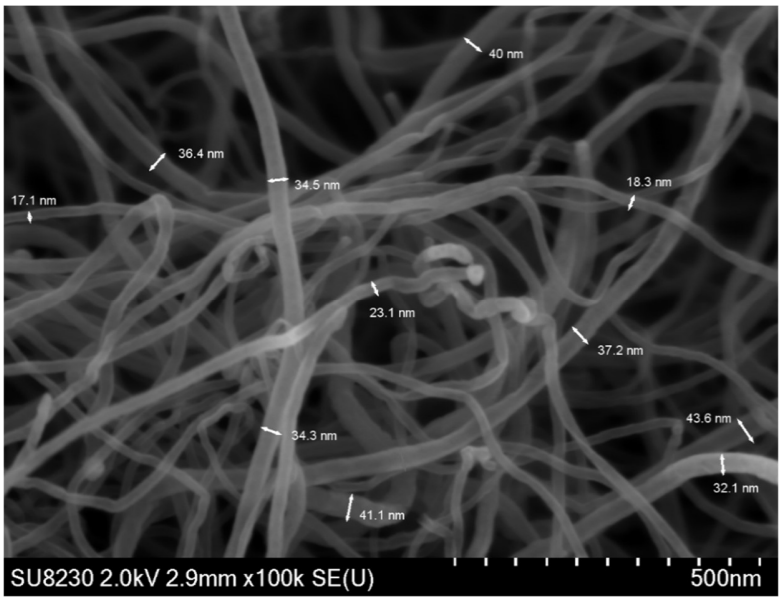

Figure 4. 18 SEM analysis of carbon deposited on Ni-UGSO 13% after DR reaction at 650 °C for 2 h TOS.

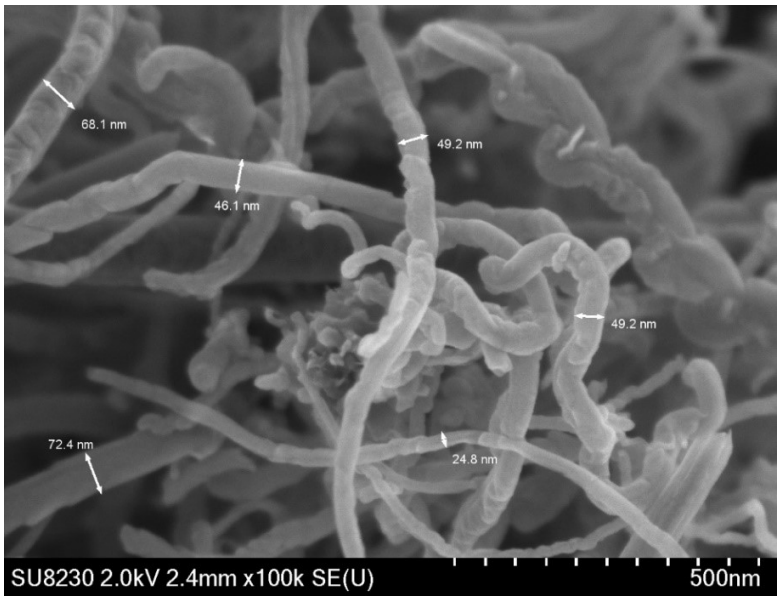

Figure 4. 19 SEM analysis of carbon deposited on Ni-UGSO 13% after the CC reaction at 750 °C for 2 h TOS.

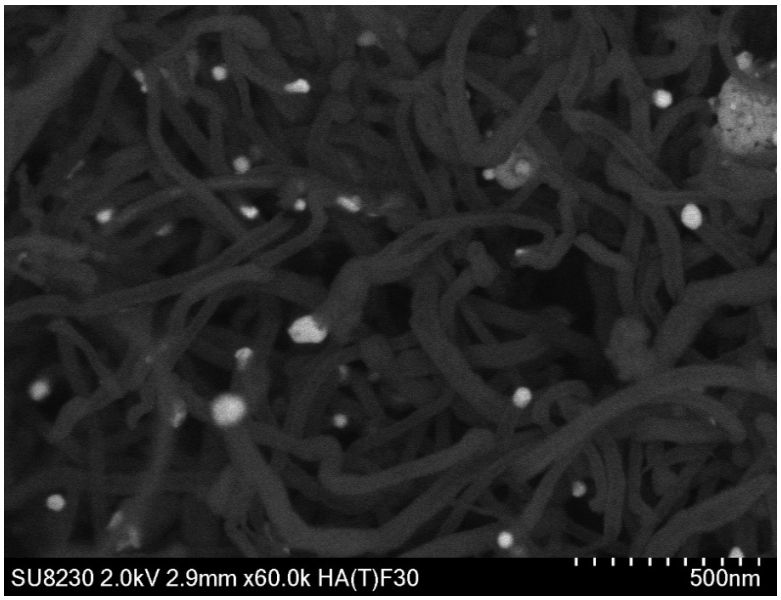

Figure 4. 20 SEM analysis (using backscattered electron imaging) of carbon deposited on Ni-UGSO 13% after DR reaction at 650 °C for 2 h TOS.

The EDX images presented in Figure 4. 21 and Figure 4. 22 give a chemical analysis of the spent catalyst and carbon deposited. We notice on the spectrum that the peaks of carbon are intense for both reactions, which proves the existence of carbon corresponding to CNF, as we can see on the SEM images.

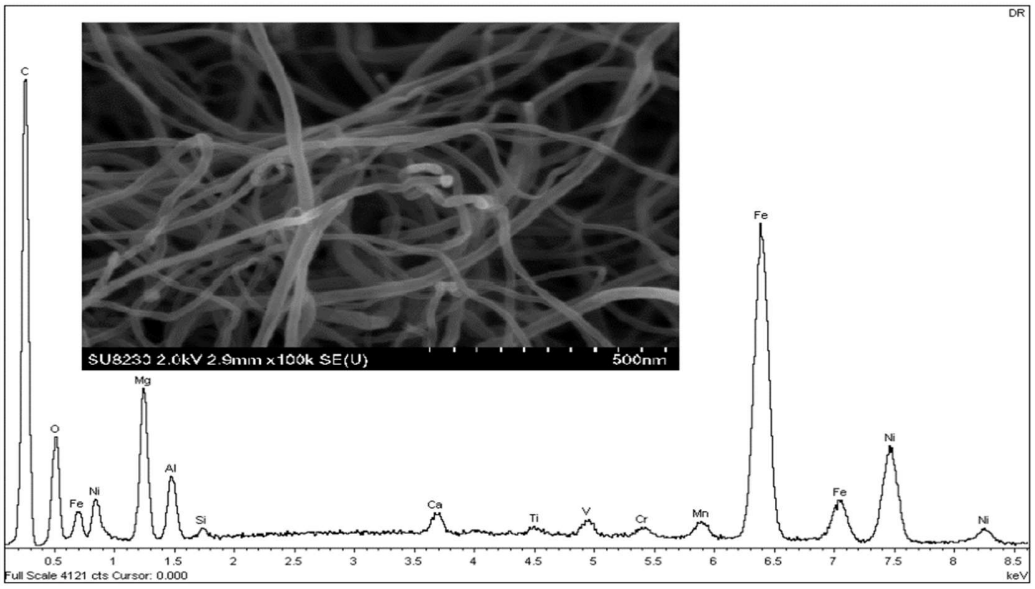

Figure 4. 21 EDX analysis of carbon deposited on Ni-UGSO 13% after the DR reaction at 650 °C for 2 h TOS.

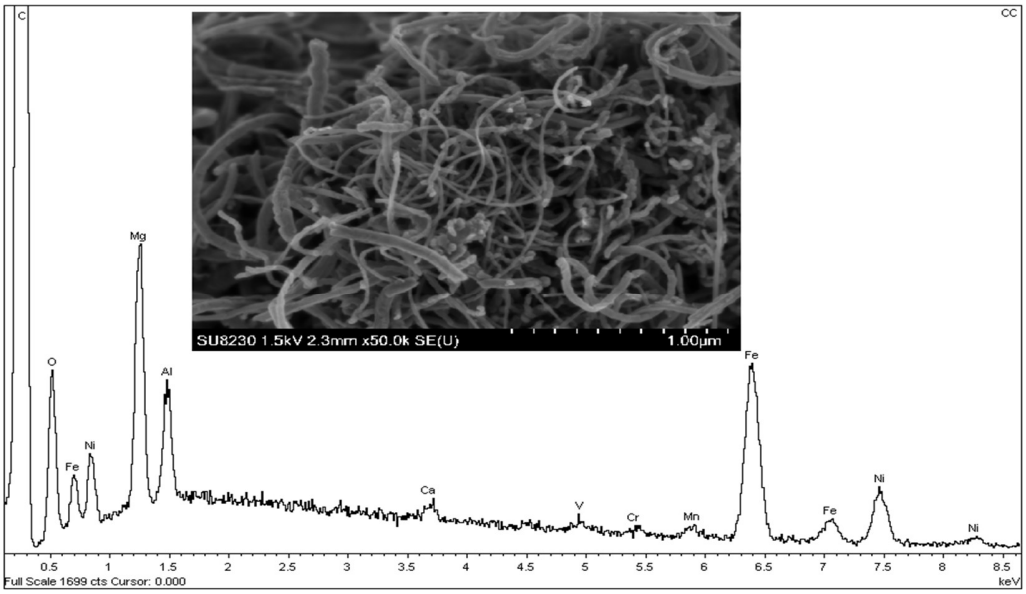

Figure 4. 22 EDX analysis of carbon deposited on Ni-UGSO 13% after the CC reaction at 750 °C for 2 h TOS.

TEM-EDX Analysis

DR Reaction Sample

Examination of the carbon formed in TEM demonstrated that the carbon formed consists entirely of cylindrical and straight CNF. However, all CNF produced are of the fishbone type (graphene sheets at a certain angle relative to the hollow core fiber main axis). Romero et al. (Romero et al., 2008) have indicated in their article that Fe-based catalysts are responsible for the growth of two types of CNF, tubular (sheets parallel to fiber axis), and platelets; while Ni-based catalysts are responsible for the growth of fishbone type CNF only. However, in an earlier work of our research group (Jankhah et al., 2008b) where steel was used as a dry reforming catalyst to produce CNF, it has been found that different forms of CNF were formed during the reactions, including fishbone ones. Yu et al. (Yu et al., 2005) have done a study in conditions similar to ours, which consists of decomposing a $C_2H_4/H_2/CO$ mixture with a Ni–Fe bimetallic catalyst and have found that the CNF formed during their study were of the fishbone type. They have reported that the fishbone is probably formed when a Boudourd reaction took place. In light of these results, we can deduce that the catalyst is not the only factor that influences the type of carbon formed; other factors, such as the type of gas supplied and the temperature, also have an influence as discussed further.

When the graphitic sheets stack with one another, the angle formed between the sheets and the fiber axis was not always the same for all of the produced CNF. Different angles (11°, 17°, 23°) are observed. It also seems that the diameter of the hollow core depends on this angle: the bigger the angle, the smaller the diameter (Figure 4. 23). Since the catalyst's structure changes over TOS, it is rather impossible to control the width of the CNF as it is also discussed further.

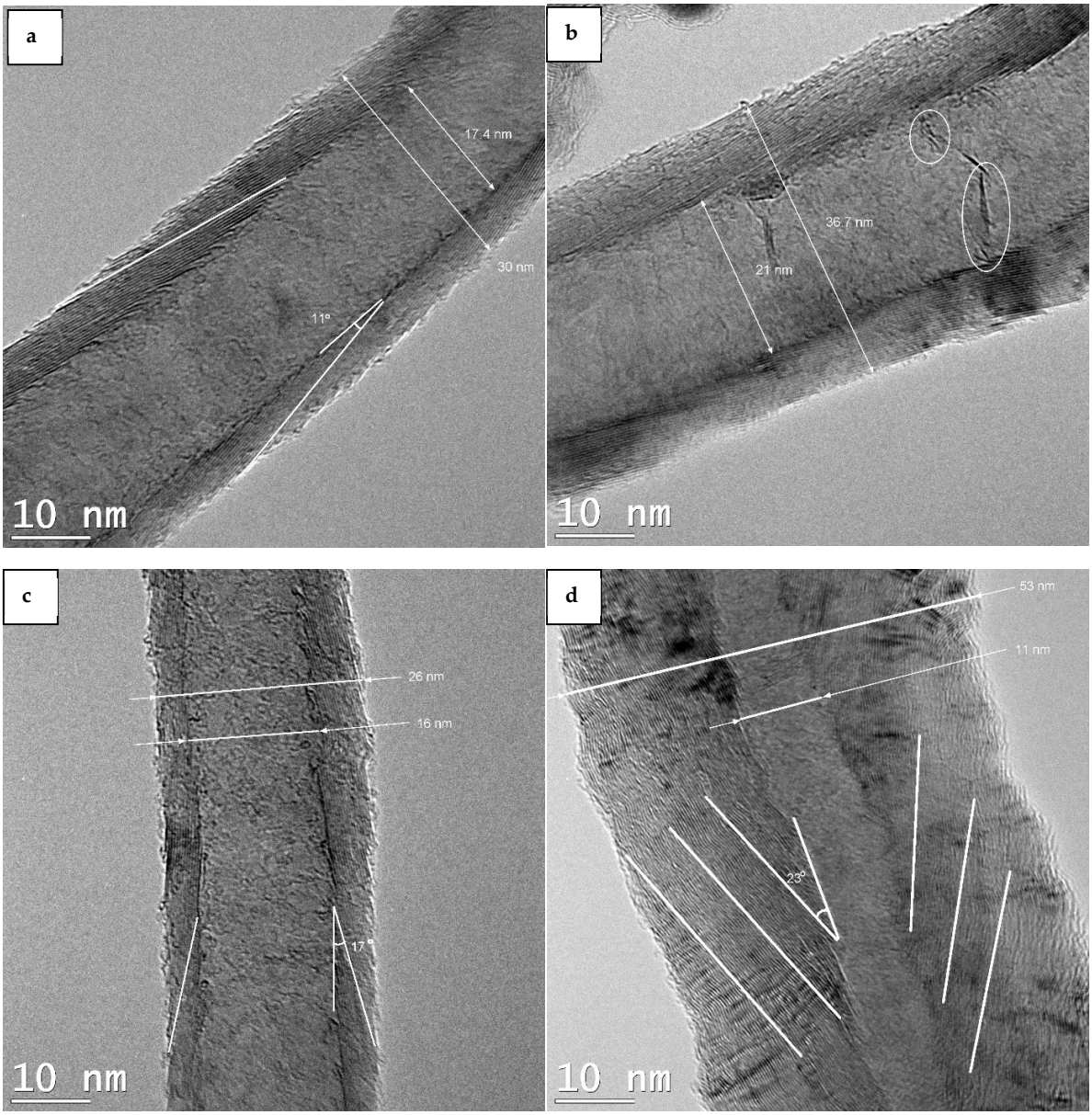

Figure 4. 23 TEM analysis of carbon deposited on Ni-UGSO 13% after the DR reaction at 650 °C for 2 h TOS, (a) CNF with d=30 nm, (b) CNF with d=36,7 nm, (c) CNF with d=26 nm, (d) CNF with d=53 nm.

The distance between the graphitic sheets is 0,340 nm (Figure 4. 24), which is higher than the corresponding distance of graphite (0,335 nm). This means that CNF have structural defects and their structure is only ordered locally, not globally (Romero et al., 2008) . These defects are shown in as waved lines. The fact that the CNF are less ordered and have defects has been verified by TGA profiles (Figure 4. 17), where the latter demonstrates that lower temperatures are necessary to oxidize CNF. Some zones that are darker than others can also be observed; they are due to layers not being stacked identically, and whose local density is different. The degree of graphitization (g) is calculated using this Equation: $d_{hkl} = 3{,}354 + 0{,}086\,(1-g)$, where d_{hkl} is the interplanar distance (Narkiewicz et al., 2010). Thus, the g -value of the CNF produced in this study is g = 46,5%. Romero et al. (Romero et al., 2008) have found that CNF produced from ethylene decomposition over a Fe-Ni-based catalyst have an interplanar distance of 3,42 Å, therefore g = 23%, which means that they are less graphitized than those obtained in this work.

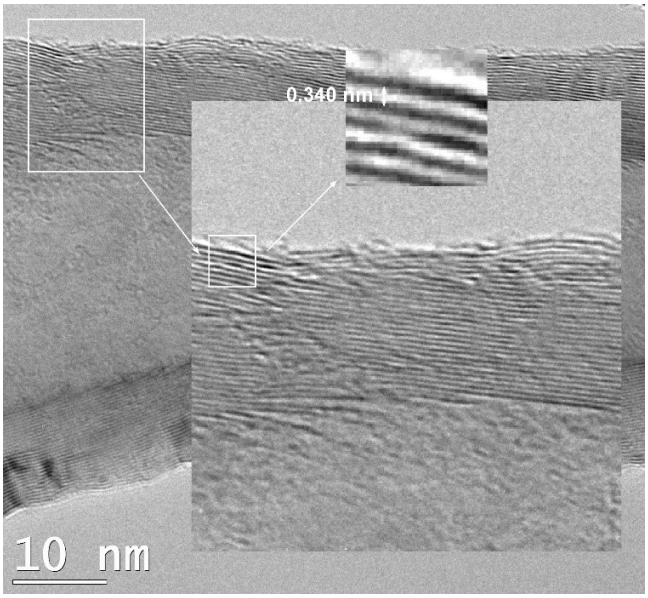

Figure 4. 24 Interplanar distance of graphene sheets.

SAED analysis confirmed that the interplanar distance of CNF is 0,340 nm. The second d_{hkl} can be attributed to planes (102), (220), and (031) of Fe_3C according to JCPDF File # 35-0772, or to planes (111) and (110) of Ni and Fe, respectively. From the presence of Fe_3C, it can be deduced that CNF have grown on Fe. The existence of the Ni atoms in the metallic particles at the bottom of the CNF, as it is proven by SAED (Figure 4. 25) and confirmed by

the EDX analysis (Figure 4. 21), confirms that the Ni has mainly participated in one of the stages of the growth of the CNF, which is the decomposition of the HC, while the iron is the main contributor in the second and third stages (dissolution and precipitation). In fact, it is known that Ni and Fe differ in their ability to decompose HC and solubilize carbon. Ni rapidly dehydrogenates the adsorbed HC while Fe is slower, and iron solubilizes carbon better than Ni. Indeed, the solubility of the carbon in the Ni in the range of temperature at which we worked is very low. Lander et al. (Lander et al., 1952) have experimentally developed an Equation that gives the solubility of carbon in nickel between 700 °C and 1300 °C, which is as follows: $lnS = 2.48 - \frac{4,880}{T}$, where S is the solubility in grams of carbon per 100 gr of nickel and the temperature is in °C. The S value at 700 °C is relatively low (2,5%). This will also be discussed further.

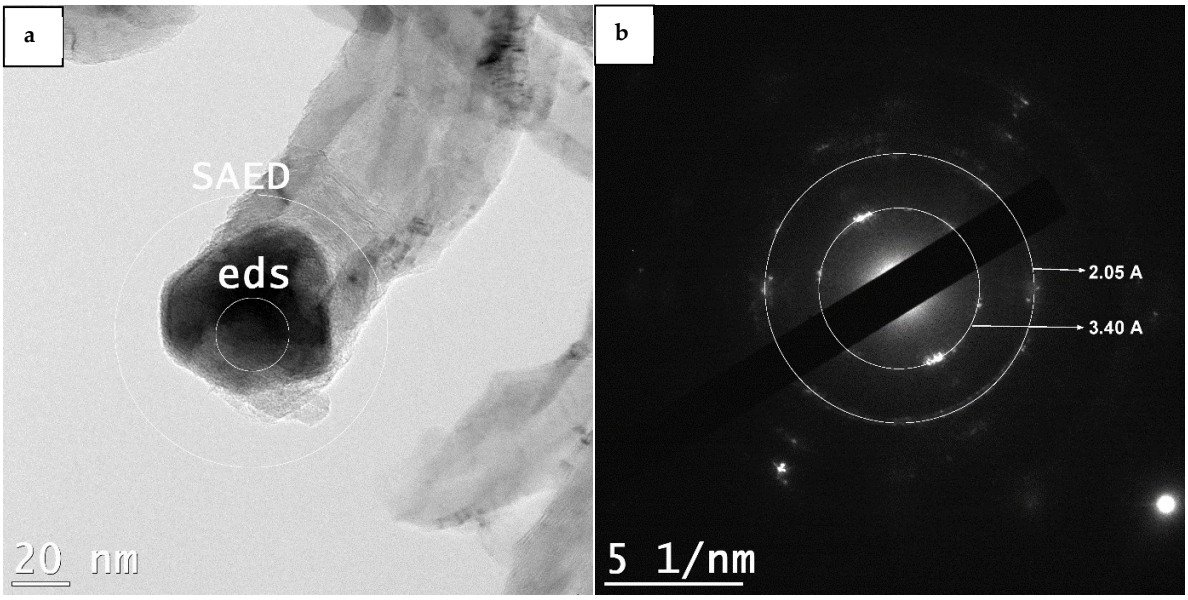

Figure 4. 25 (**a**) Metallic particle at the tip of CNF (**b**) SAED of this particle.

CC Reaction Sample

For the CC reaction, we observed that there are different types of CNF, such as the tubular shape (layers are parallel to fiber axis like MWCNT) with a hollow core (

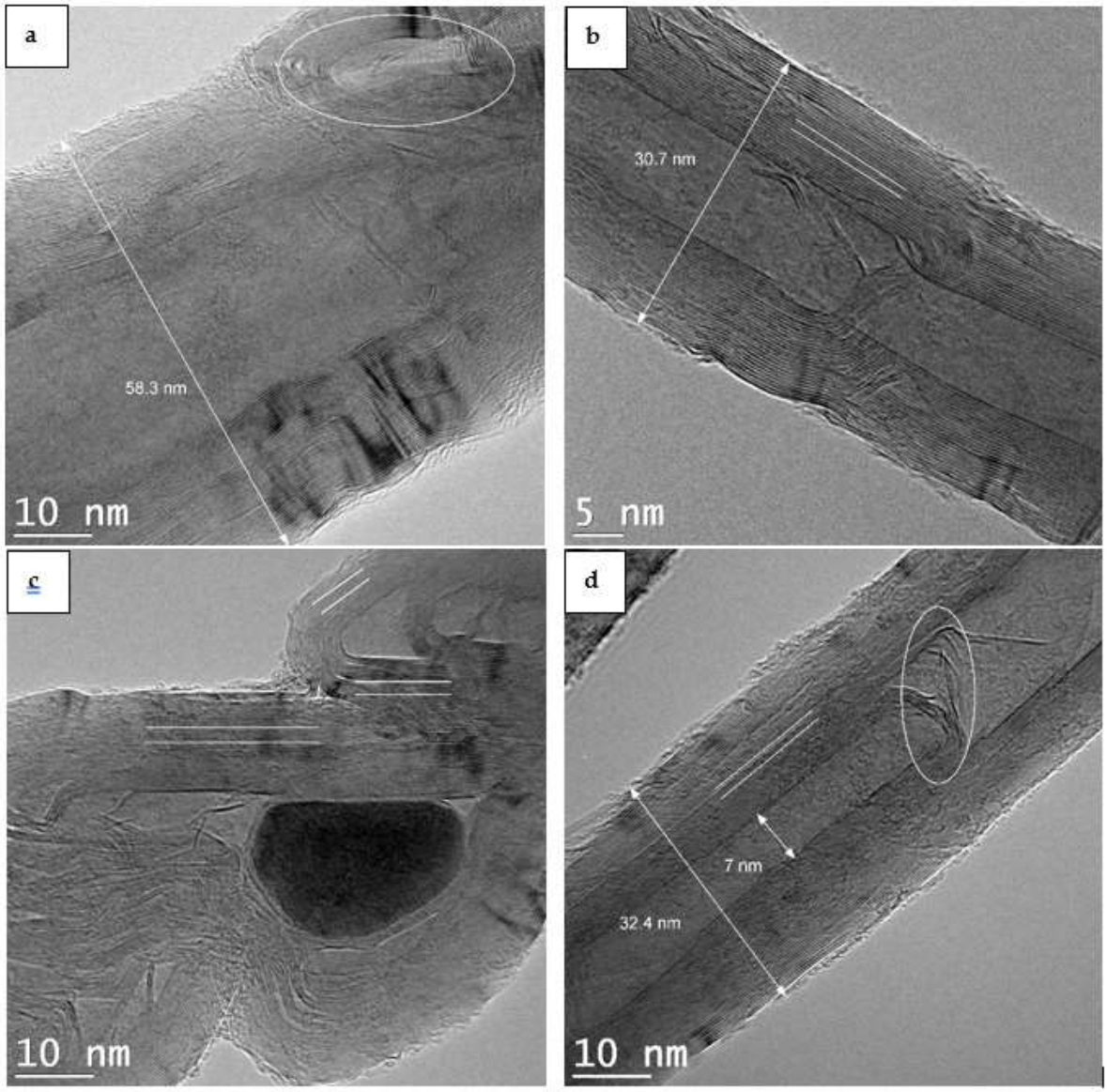

Figure 4. *26* (b), (d)), where we can also observe that some layers have torn ends. It seems that the sheets tended to connect to fill the inside of the CNF structure. Another type of

structure is the bamboo type (

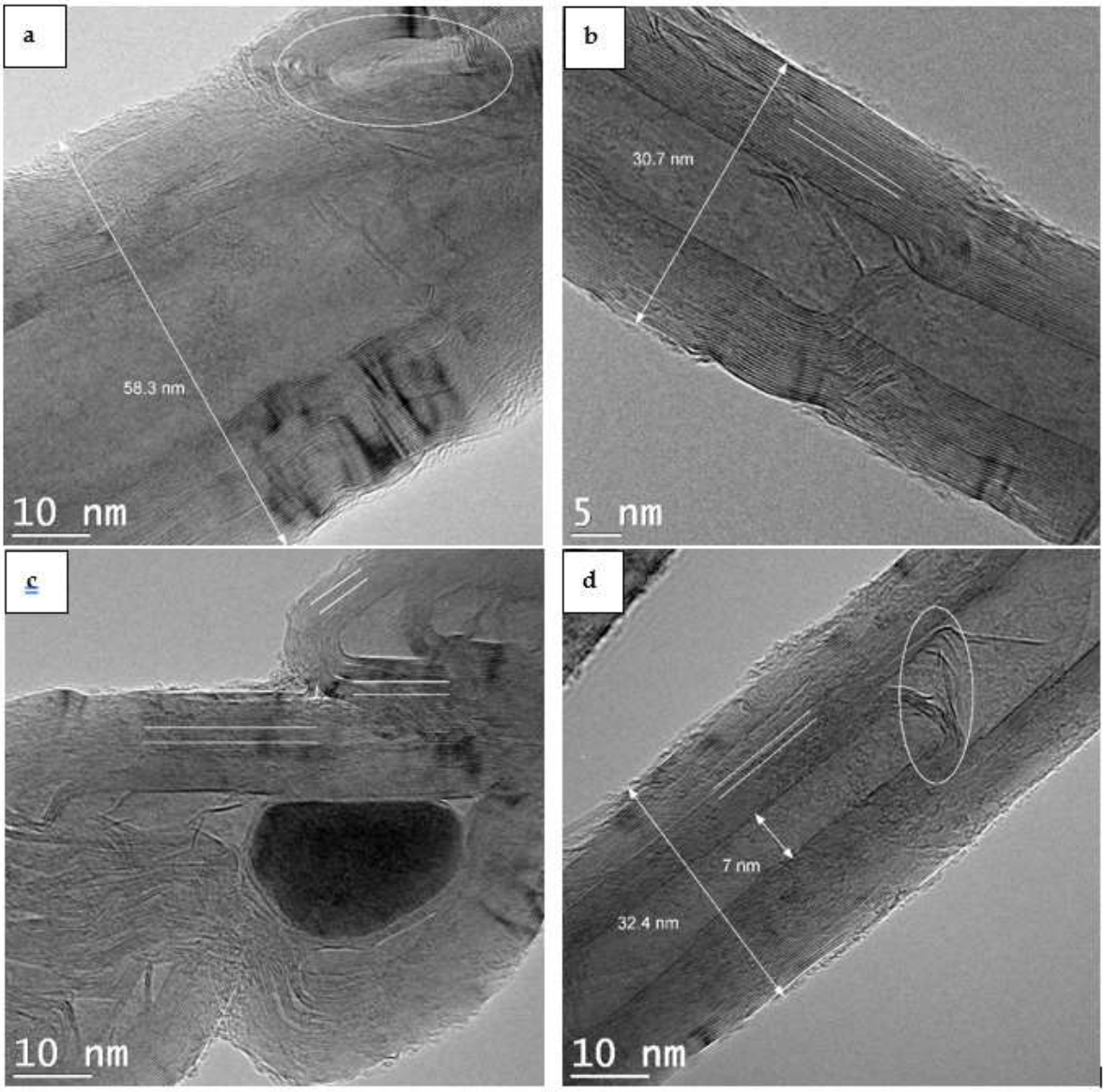

Figure 4. *26* (c)). We were also able to observe that CNF formed with irregular stacking of graphene planes (

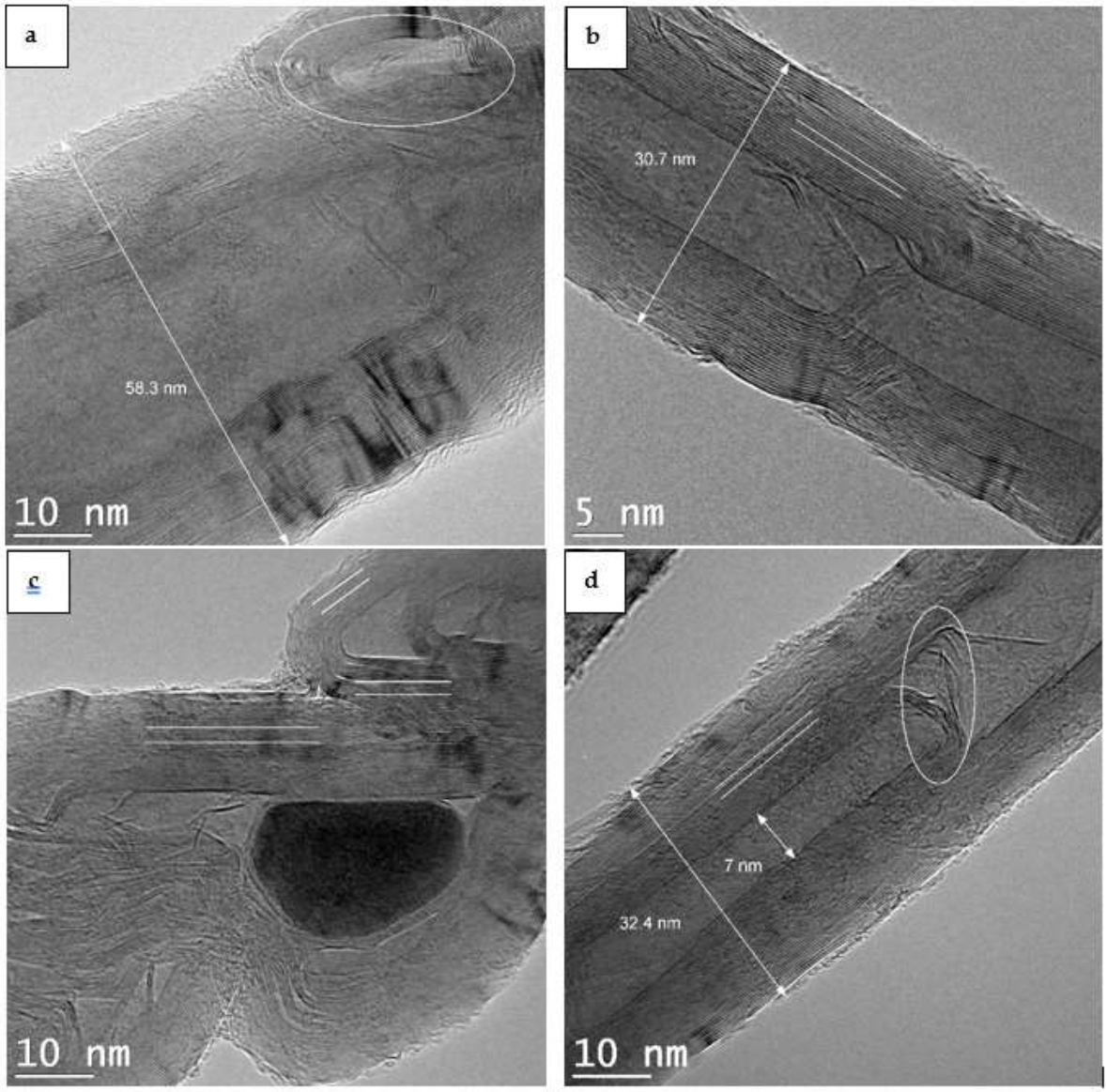

Figure 4. *26* (a)), and we can observe that the graphene planes started out parallel to one another and that the angle of inclination with the fiber axis subsequently changed. The appearance of these CNF is quite similar to those formed by the decomposition of C_2H_4/H_2 over Fe:Ni catalyst studied by Park and Baker (Park & Baker, 2000) .

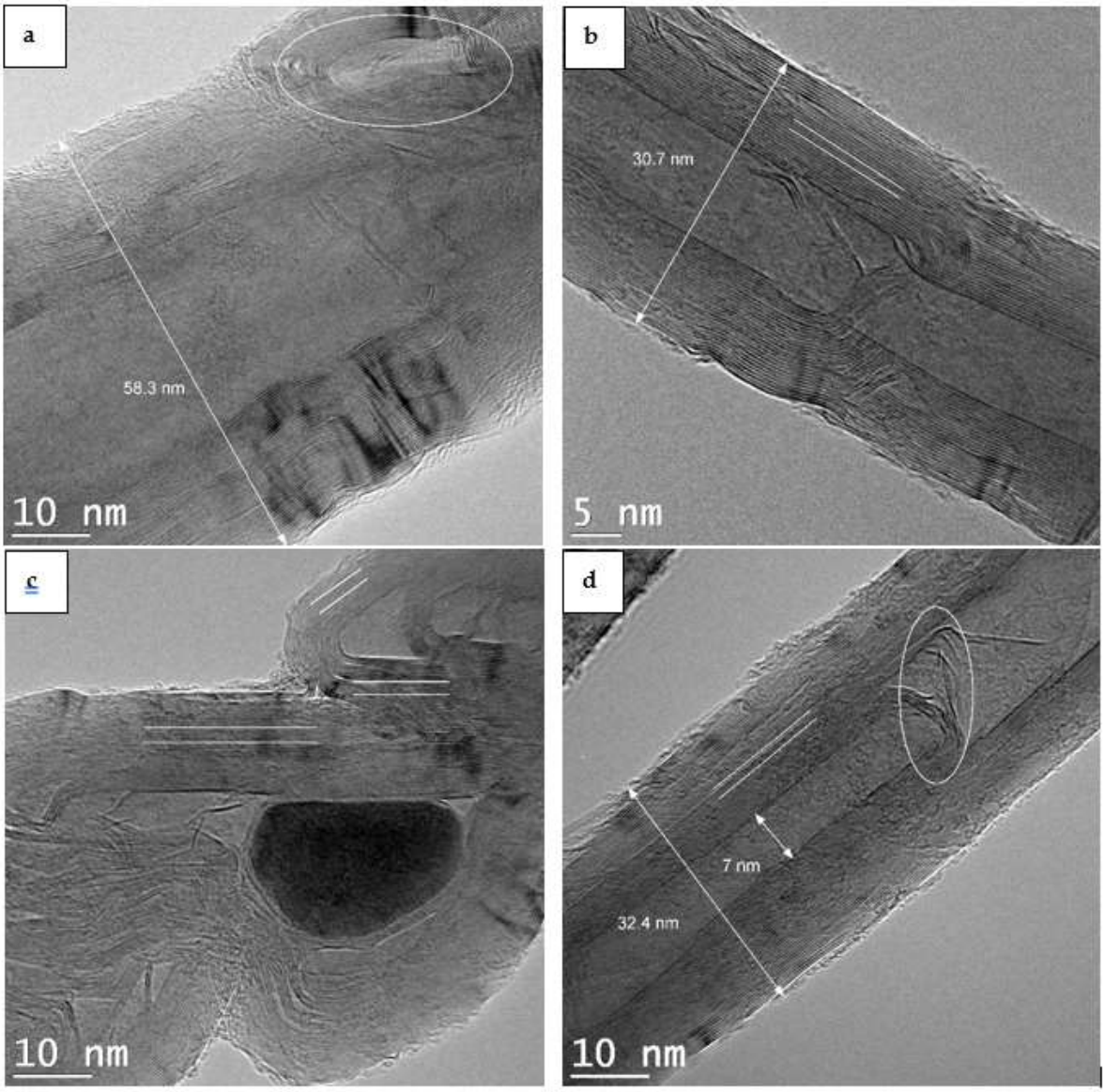

Figure 4. 26 TEM analysis of carbon deposited on Ni-UGSO 13% after CC reaction at 750 °C for 2 h TOS, (a) CNF formed with irregular stacked graphene planes, (b) and (d) tubular CNF with hollow core, (c) bamboo CNF.

In Figure 4. 27, we observe that the metal particle is not on the tip of the filament contrary to what was found in DR, but it is encapsulated inside the filament. This could be explained by the fragmentation of the main particle, as its fragments could have been entrained within the body structure of the filament during the growth phase. The same behavior was found by Park and Baker (Park & Baker, 2000) who worked in conditions similar to those used for this work (decomposition of C_2H_4 over Ni–Fe catalyst). The metal particle that was

encapsulated by the CNF during the CC reaction appears to have a smooth globular morphology, in contrast to the structure of the catalyst particles at the end of the CNF produced in the DR reaction, which have more angular forms.

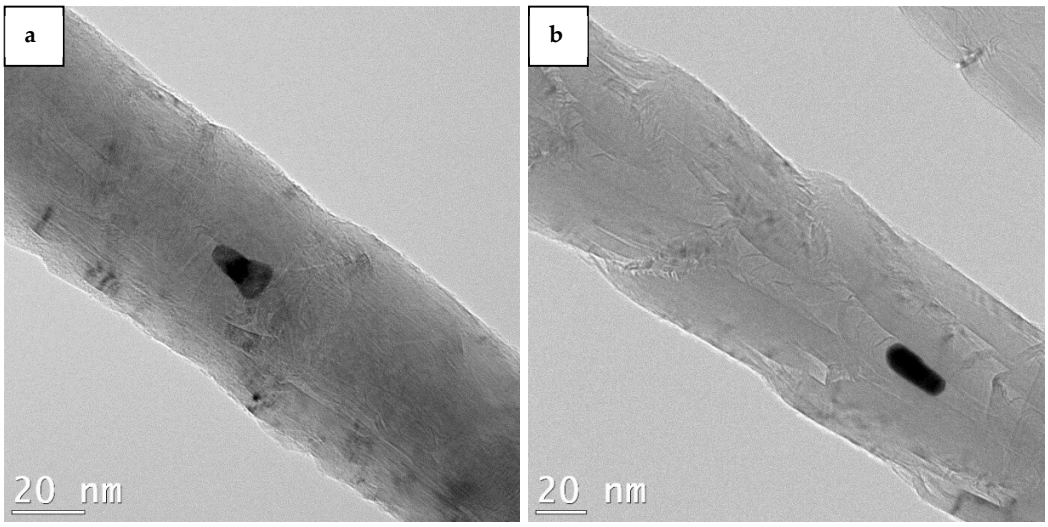

Figure 4. 27 TEM analysis showing a catalyst particle inserted in two different nanofilaments.

The EDX analysis presented in Figure 4. 28 shows Fe and Ni peaks in the pattern as well as C peak, which proves that the metallic particle is composed of both metals and encapsulated by carbon.

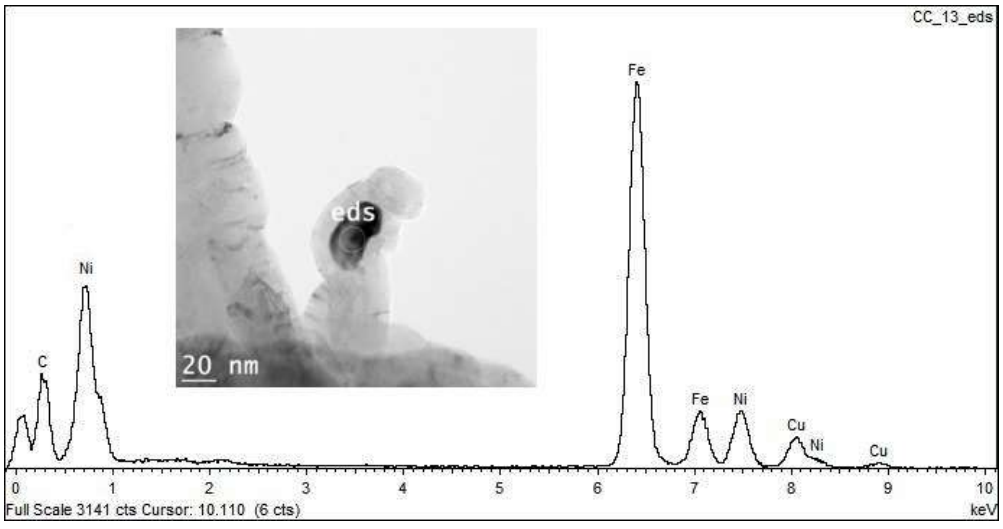

Figure 4. 28 EDX analysis of carbon deposited on Ni-UGSO 13% after CC reaction at 750 °C for 2 h TOS.

Mechanistic Understanding for the Growth of CNF

The results of this study, which aimed to test the catalytic performance of a new catalyst derived from a mining residue (Ni-UGSO), have shown that Ni-UGSO is also a good catalyst for CNF production from ethylene cracking and dry reforming.

The influence of the catalyst composition as well as of the precursor gas composition and reaction conditions are discussed below.

Influence of the Catalyst on the Growth of CNF

The effects of Ni and Fe on the growth of CNF is different depending on whether it is a CC reaction (decomposition of C_2H_4) or a DR reaction (decomposition of C_2H_4 and disproportionation of CO). Park and Baker (Park & Baker, 2000) have mentioned in their work that Ni-based catalysts are good for the decomposition of ethylene but were not as potent for catalyzing the Boudouard reaction, whereas Fe-based catalysts exhibited the opposite behavior. This fact was verified by our work, where we found that Ni is responsible for ethylene decomposition while Fe is responsible for the growth of CNF. They studied a bimetallic Ni–Fe catalyst for the decomposition of C_2H_4 and CO in the temperature range 600–725 °C, and they proved that increasing the ambient temperature improves the decomposition of C_2H_4 while the Boudouard reaction is favored thermodynamically by temperatures of around 550 °C.

It has also been found that the crystallographic orientation of the metal atoms plays an important role in the ability of the catalyst to decompose the reactive gases (Koestner et al., 1982) . Zhu et al. (Zhu & White, 1989) showed that the Ni (111) plane adsorbs ethylene and acetylene dissociatively, which was proven in this work by SAED results where the Ni (111) facet was found on the metal particle on the top of CNF (Figure 4. 25). Their calculations show that the rate of diffusion of carbon on the Ni (110) plane is the fastest step. However, the carbon deposited on the facet (110) is poorly crystallized because the distance of this plane does not correspond to that required for forming a graphite network. To form a good crystalline carbon structure, the atoms resulted from the decomposition of HC must first diffuse through Ni to dissolve and then precipitate onto the adequate Fe (110) facet (Table 4. 9), which is required to form a graphite network. The energy difference between poor and well-crystallized carbon is the driving force that leads to transfer from one side of a metal to another (Koestner et al., 1982).

Table 4. 9 Indexation of D-spacing measured by SAED.

Measured D-Spacing (Å)	Indexation (Park & Baker, 2000)	Theoretical D-Spacing (Å) (Park & Baker, 2000)
	(111) Ni	2,03
	(110) Fe	2,04
2,05	(102) Fe_3C	2,07
	(220) Fe_3C	2,03
	(031) Fe_3C	2,01
3,40	(200) carbon	3,35

Influence of Catalyst Particle Sizes on the CNF Diameter

Rodriguez (Rodriguez, 1993) has studied the interaction between a metallic surface and carbon. Figure 4. *29* is a schematic representation of the forces involved in the interaction of a metal catalyst particle with a graphite support in the presence of a gaseous environment. The contact angle θ is determined by the surface energy of the graphite support (Y_{SG}), the surface energy of the metal (Y_{MG}), and the metal-graphite interfacial energy (Y_{MS}), and is expressed in terms of Young's Equation:

$$Y_{SG} = Y_{MS} + Y_{MG} \cos \theta \qquad (4.\ 1)$$

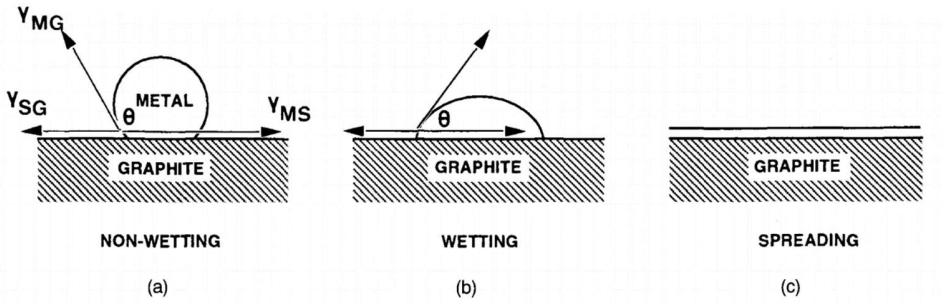

Figure 4. 29 Interaction between surface metal and graphite (Rodriguez, 1993).

It presents changes in the shape of the metal particles as a function of the catalyst wetting degree on the graphite:

- When weak forces occur between the metal and the graphite, the resulting contact angle is higher than 90° and there is no wetting;
- When strong forces occur between the two components, the contact angle is lower than 90° and wetting occurs;

- When the adhesion exceeds the cohesion inside the particle ($Y_{MS} > Y_{SG} + Y_{MG}$), the metal spreads over the graphite support surface.

Two forms of catalyst particles associated with nanotubular carbon products, which are clearly different from one another, are commonly observed and presented in the literature (Chitrapu et al., 1992) : one is conical and the other one is spherical. The conical particles are usually found at the end of the nanofilaments, as it was proven in this work (Figure 4. 25), and the almost spherical particles are observed at the end of the nanotubes (Audier et al., 1980) . For conical particles, the adhesion exceeds the cohesion inside the particle, which leads the metal to spread on the graphite surface and, after precipitation, the carbon takes the form of piled up stacked cones from the particle, determining the shape of the particle's bottom (Figure 4. 30). In addition, when weak forces occur between the metal and the graphite and the contact angle is >90°, nanotubes are formed (Figure 4. 30).

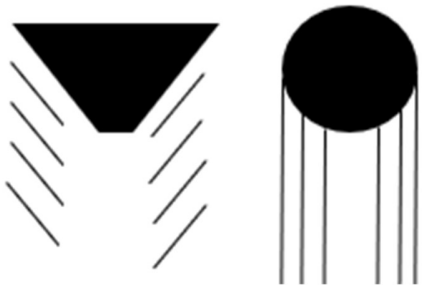

Figure 4. 30 Conical and spherical metal particles on the top of CNF and CNT, respectively.

A sequence of "stop-action" images (Audier et al., 1980) shows that after a few seconds of initial growth, the particle is pushed upward by the carbon flux and lengthens. As growth continues, the surface in contact with the carbon begins to tilt upward until it forms a conical or tear-shaped form, the tip of the cone being oriented toward the growing carbon nanostructure and pointing in the direction of carbon diffusion. This observation leads to the conclusion that the commonly accepted belief that the catalyst particle determines the size and shape of the product is false. It is more likely the opposite (Nolan et al., 1998) .

Influence of Gas Composition on CNF Growth

The type of CNF formed is different for DR reactions and CC reactions; nevertheless, it also depends on other factors, namely the metal type and temperature. Luo et al. (Luo et al., 2000)

have used Ni–La_2O_3 in a flow of CH_4/N_2, CO/N_2, and $CO_2/CH_4/N_2$, and they observed the production of both encapsulating carbon and CNF. The former was mostly formed in a CH_4/N_2 atmosphere whereas the latter was formed in a CO/N_2 or $CO_2/CH_4/N_2$ atmosphere. These results are in accordance with our findings. When using only C_2H_4, CNF with irregular forms as well as encapsulated carbon was formed; while, during DR reactions (where CO is present), only fishbone-type CNF were formed.

In fact, the composition of the gas affects the composition of the surface of metal particles because of the preferential segregation behavior of one of these components, which affects the arrangement of the atoms in the crystallographic face. This critical characteristic determines the mode of adsorption and decomposition of the reactive gas (Krishnankutty et al., 1996) . It has been found that when CO is present in the reactive gas, particles tended to have a faceted form, which leads to the formation of fishbone CNF (Krishnankutty et al., 1996) .

CNF Precursor

As it appeared on the images of the TEM analysis (Figure 4. 25), the metal is located in the tip of carbon nanofilaments, which indicates that carbon has grown in a crystallographic face of the metal. Several authors have tried to find which phase is the one responsible for CNF growth. First, Baker et al. (Baker et al., 1972) report an activation energy that suggests that carbon diffuses through the reduced metal and, therefore, they indicate that the reduced metal is the growth crystal. Subsequently, Oberlin et al. (Oberlin et al., 1976) studied CNF growth on iron. They used TEM to identify growth crystals and reported that cementite and alpha iron were the only ones present in their work, which led them to conclude that not only is the active metal responsible for the growth of CNF but that it also contributed to the formation of metal carbides. In other research, in order to confirm which solid phase of iron is the most catalytic for carbon formation, Sacco et al. (Sacco et al., 1984) worked on phase diagrams. They experimented by heating iron foils under a stream of hydrogen at 900 K, then fed hydrocarbon gas mixtures of different compositions into the reactor for each experiment. They had a mass gain that corresponds to carbon formation only in the area where Fe_3C is thermodynamically favored. Mass gain does not occur in α-Fe region, which proves that carbides, at least initially, are needed for carbon formation. In another study, it was shown

that Fe_3C supported on graphite and exposed to acetylene did not catalyze carbon formation (Baker et al., 1982) . There are two assumptions to explain this: Fe_3C does not catalytically break up acetylene, or it is necessary to have a Fe_3C/Fe dual phase metal interface to provide the solubility difference needed for carbon diffusion and thus the growth of the nanofilament. The results found in this work, which confirm the presence of the Fe_3C peaks in the XRD pattern and SAED, confirm the assumption that the Fe_3C is the responsible growth crystal for CNF.

4.2.3. Experimental

Materials

The targeted feedstock was gases derived from plastic pyrolysis, which are largely composed of unsaturated HC. The initial step, which is presented in this work, was the use of ethylene as a representative molecule.

UGSO—upgraded slag oxide—is a residue of the UGS process, which has been developed by RTIT to produce, from ilmenite, the world's richest titanium slag (95% of TiO_2). This mining residue is composed largely of Fe, Al, and Mg oxides as determined by inductively coupled plasma mass spectrometry (ICP-MS) elemental analysis shown in Table 4. 10. To produce a reforming catalyst, the UGSO is doped with Ni (Chamoumi et al., 2017). Blank experiments have shown that UGSO itself has no significant catalytic activity (Chamoumi et al., 2017).

Table 4. 10 Average elemental analysis of the upgraded slag oxide (UGSO) residue (Chamoumi et al., 2017).

Component	Fe	Mg	Al	Ca	Mn	V	Ti	Cr	Na	Si	K	P	Zr	Zn
(wt.%) [a]	31,2	17,5	5,4	1,1	1,0	0,9	0,6	0,5	0,2	0,1	0,02	0,04	0,01	0,01

[a] The balance is oxygen.

Set-Up

Reactions (DR, CC, and activation reaction) were conducted in a differential fixed-bed reactor, which is a quartz tube of approximately 25 cm of length and 15 mm of internal diameter, put in an oven with temperature control. The catalyst was deposited at the bottom

of the tube between two pieces of quartz wool and placed in the oven. Gases were fed from commercial gas (supplied by Praxair) cylinders: C_2H_4 (99%), CO_2 (99%) for the DR reaction, C_2H_4 (99%), Ar (99%) for CC reaction, and H_2 (99%) and Ar (99%) for the activation reaction. Three AALBORG mass flow meters were used to control the gas flow at the inlet (Figure 4. 31). The flow rate of the products was measured using a bubble flow meter and its composition was analyzed by gas chromatography (GC Varian CP-3800) with a measurement error varying between 1% and 2.5% depending on the analyzed gases (i.e., H_2 had the highest error proven during calibration tests).

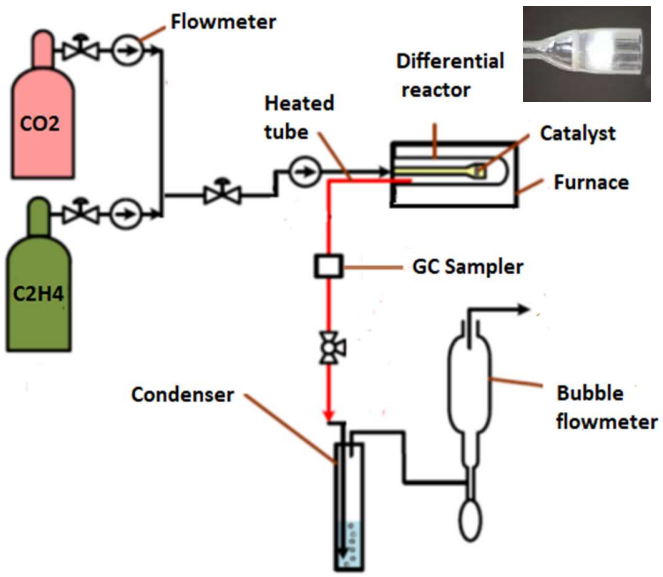

Figure 4. 31 Reaction set-up (Chamoumi et al., 2017).

Experimental Methodology

Preparation of Ni-UGSO

Ni-UGSO is prepared via a solid-state reaction developed by Chamoumi et al. (Chamoumi & Abatzoglou, 2016). In summary, UGSO was first milled and sieved in a 53 µm sieve, which was the smallest size obtained with our dry powder sieving equipment. Nitrate hexahydrate $Ni(NO_3)_2 \cdot 6H_2O$ was used as a Ni precursor; the latter was mixed with the UGSO in the targeted proportion. A small quantity of water was added, and the mixture was then milled and homogenized softly in a mortar at ambient temperature. The resulting milled mixture was oven-dried at 105 °C for 4 h and then calcined at 900 °C for 12 h. After

calcination, the catalyst was sieved down to 53 µm and was used in the catalytic tests as powder dispersed in the quartz wool placed in the differential reactor.

Activation of Ni-UGSO

The Ni-UGSO was activated by H_2. The evolution of the catalyst structure was studied using TPR, TEM and XRD analysis. The catalyst was activated under a flow of 75% H_2 and 25% Ar for a time-on-stream (TOS) of 2 h. Table 4. 11 shows the activation test conditions.

Table 4. 11 Activation test conditions.

Catalyst	H_2 Flow Rate (mL/min) [a]	Ar Flow Rate (mL/min) [a]	Catalyst Weight (g)	TOS (h)	GHSV ($mL \cdot h^{-1} \cdot g^{-1}$)	T (°C)
Ni-UGSO (wt.% = 5, 10, 13)	30	10	0,5	2	4800	650

[a] Gases are fed at atmospheric pressure.

Dry Reforming (DR) and Catalytic Cracking (CC) Reactions

Ni-UGSO was used as a catalyst for ethylene DR and CC. The influence of two factors was studied: temperature; and weight percentage of Ni in the catalyst (wt.%).

In order to choose the temperature range for the tests, a study of thermodynamic equilibrium was done at temperatures ranging from 350 °C to 850 °C. The wt.% of Ni in the catalyst, 13%, was chosen because the theoretical calculations based on the average UGSO composition show that this Ni content is necessary if all available Fe and Al oxides form spinels with Ni (Chamoumi et al., 2017). Nevertheless, since the catalytic activity comes from the local reduction of Ni and Fe into their metallic forms, as well as the concentration of these species at the surface of their support, lower Ni percentage were tested as well. Therefore, 10% and 5% were chosen arbitrarily as intermediate and lower wt.% of Ni.

A 3^2 fully reproduced factorial design of experiments (18 runs) were conducted for each study (nine tests with their duplicates). The experiments were conducted at atmospheric pressure after the activation step. Reaction conditions are summarized in the Table 4. 12 et Table 4. *13*.

Table 4. 12 Ethylene dry reforming (DR) reaction conditions.

Catalyst	C_2H_4 Flow Rate (mL/min) [a]	CO_2 Flow Rate (mL/min) [a]	Catalyst Weight (g)	TOS (h)	GHSV ($mL \cdot h^{-1} \cdot g^{-1}$)	T (°C)
Ni-UGSO (wt.% = 5, 10, 13)	30	10	0,5	2	4800	550, 650, 750

[a] Gases are fed at atmospheric pressure.

Table 4. 13 Ethylene catalytic cracking (CC) reaction conditions.

Catalyst	C_2H_4 Flow Rate (mL/min) [a]	Ar Flow Rate (mL/min) [a]	Catalyst Weight (g)	TOS (h)	GHSV ($mL \cdot h^{-1} \cdot g^{-1}$)	T (°C)
Ni-UGSO (wt.% = 5, 10, 13)	30	10	0,5	2	4800	550, 650, 750

[a] Gases are fed at atmospheric pressure.

Characterization Techniques

Several techniques were used to characterize fresh, activated, and spent catalysts. The information derived from the results of these techniques allows the understanding and interpretation of the phenomena that occur during the activation, DR, and CC reactions.

XRD

XRD analysis was used to identify fresh catalyst crystalline structure and to study transformations that might have occurred on this crystalline structure during and after activation, DR reactions, and CC reactions. The diffractometer used was Philips X'Pert PRO equipped with a Cu tube as its X-ray source and a Ni filter that was used to only let through Kα1 radiations from Cu (1,5418 Å) produced at 40 kV and 50 mA. The anti-dispersion slit was set at 1/2 and the diverged slit at 1/4. The analysis was carried out with a scanning angle of 2θ ranging from 15° to 90°.

Crystallite size can be calculated using Scherrer Equation:

$$L_c = \frac{K \times \lambda}{d \times cos\,\theta} \qquad (2.\ 5)$$

L_c—crystallite size (nm);

K—0,9;

λ—1,5418 (Å) for Cu Kα1;

d—FHMW (full width at half maximum) calculated using Origin software (nm);

θ—angle (rad).

SEM and EDX

Scanning electron microscopy was used to characterize CNF and to study their morphology. The microscope used was a Hitachi Cold FE SU-823000 characterized by a 0,5 nm resolution at 30 kV and 3 nm resolution at 0,05 kV. It was equipped with a secondary electron (SE) lower detector, an SE/backscattered electron (BSE) upper detector, an SE/BSE top detector with energy filtration of BSE, a five quadrant BSE detector, a STEM (scanning transmission electron microscopy) detector for bright/dark fields, and a drift silicon detector energy dispersive X-ray spectrometry (SDD-EDS) detector, which was used to study the elemental composition and mapping of the sample.

TEM Coupled with EDX and Selected Area Electron Diffraction (SAED)

The microscope used was the Jeol JEM-2100F analytical transmission electron microscope equipped with a field effect gun operating at an acceleration voltage of 200 kV. Capable of imaging resolutions of 0,1 nm, this microscope was also equipped with an EDX spectrometer for chemical analysis. It also allowed the evaluation of crystallography using electron diffraction.

TPR

TPR was performed using a Chemisorb 2750 system (Micrometrics) equipped with a thermal conductivity detector (TCD). Tests were done after calibration of H_2 consumption. Fifteen milligrams of the studied catalyst were put on quartz wool and deposited in the tube reactor. A gas mixture consisting of 10% *v*/*v* of H_2 in Ar was fed in the TPR apparatus at a controlled flow rate of 40 mL/min. The sample was heated up to 1000 °C at a ramp rate of 2 °C/min in a temperature-controlled oven. The sensor was put in a cold trap Dewar flask containing isopropanol in liquid nitrogen in order to protect it from H_2O formed during reduction.

ChemiSoft TCx software (Micromeritics) was used to calculate the peak area which is proportional to H_2 consumption.

TGA

TGA was done using a Setaram Setsys 24 analyzer under 20% O_2 and 80% Ar in a temperature range between 20 °C and 1000 °C. For carbon deposited quantification, the TGA was carried out at a heating rate of 10 °C/min.

BET

Specific surface area, pore volume, and pore average size were calculated by multipoint BET method. It was performed using an Accelerated Surface Area and Porosimetry System (ASAP 2020 V4.01).

Reaction Metrics

The performance of the catalyst was evaluated by calculating: C_2H_4 conversions ($X_{C_2H_4}$), H_2 yield (Y_{H_2}), carbon yield (Y_C), and carbon growth rate ($g_C \cdot g_{cat}^{-1} \cdot h^{-1}$) in accordance with Algorithm 1 below:

Algorithm 1

$$X_{C_2H_4}\ (\%) = \frac{(F_{C2H4,in} - F_{C2H4,out})}{F_{C2H4,in}}$$

$$Y_{H_2}\ (\%) = \frac{F_{H_2}}{2 \times F_{C_2H_4}\text{in}} \times 100$$

$$Y_C\ (\%) = \frac{m_{C_{deposit}}}{m_{C,in}} \times 100$$

$$m_{C_{deposit}} = m_{catalyst,tf} - m_{catalyst,t0}$$

For DR: $m_{C,in} = ((2^* F_{C2H4,in}\text{*time} + F_{CO2,in}\text{*time})) * M_C$

For CC: $m_{C,in} = ((2^* F_{C2H4,in}\text{*time})) * M_C$

Carbon growth rate ($g_c \cdot g_{cat}^{-1} \cdot h^{-1}$) $= \frac{m_{C_{deposit}}}{t \times m_{catalyst,t0}}$

where:

$F_{C2H4,in}$ and $F_{C2H4,out}$ respectively denote the molar flow rates of C_2H_4 at the inlet and the outlet of the reactor,

F_{H_2} the molar flow rates of H_2 at the outlet of the reactor

$m_{C,in}$ the mass of carbon fed.

$m_{C_{deposit}}$ the mass of solid carbon deposit on the catalyst

M_C the molar mass of C = 12,0107 g/mol

4.2.4. Conclusion

Ni-UGSO was prepared from a mining residue UGSO and then used to produce CNF and H_2 via CC and DR reactions. When mining residues are involved in formulations, there is a concern regarding the variability of its composition. Prior to the present study and the ones published previously (Chamoumi et al., 2017), four different batches of UGSO have been used to prepare the same catalytic formulations. The elemental analyses of the UGSO have shown that the variations were typically lower than 5% and the subsequent tests demonstrated that the observed conversion and yields deviations were lower than the overall experimental error and, consequently, not statistically significant.

Ni-UGSO 13% at 750 °C for the CC reaction and at 650 °C for the DR reaction exhibited the best performance in terms of H_2 and CNF yields. The literature has already provided the first insight into the factors influencing the formation of CNF and the mechanism of their formation, but the current work reveals the complexity of the latter. Although it is widely thought that the diameter of the CNF depends on the size of the catalyst particles, a more careful literature review along with the results of this work proves that other factors are also important. It has also been proven that carbides are the precursors of CNF and that the CNF-DR have higher structural order than CNF-CC. The type of CNF is also different. TEM images have shown that CNF-DR are fishbone shaped and CNF-CC form into tubular (MWNT) and stacked-cup structures. The results show that Fe is the main precursor of the CNF growth while Ni is more contributing to the split of C–C bonds. In terms of conversion and yield efficiencies, the performance of the catalytic formulations tested is proven at least equivalent to other Ni-based catalyst performances described by the literature. The experiments reported were conducted in a lab scale (g-lab) fixed-bed reactor and serve as a preliminary study. Ongoing work focuses on the production of CNF and H_2 in a kg-lab scale fluidized bed reactor to prove the feasibility at a larger scale towards eventual process commercialization.

CHAPITRE 5

ÉTUDE HYDRODYNAMIQUE ET RÉSULTATS EXPÉRIMENTAUX À L'ÉCHELLE PILOTE

CHAPITRE 5 ÉTUDE HYDRODYNAMIQUE ET RÉSULTATS EXPÉRIMENTAUX À L'ÉCHELLE PILOTE

5.1. Avant-propos

Auteurs et affiliation

A. Azara : Étudiante en Doctorat, Université de Sherbrooke, Faculté de Génie, Département de Génie Chimique et Génie Biotechnologique.

J. Blanchard : partenaire industriel, KWI Polymers, Boibriand, Sherbrooke.

N. Abatzoglou : Professeur, Université de Sherbrooke, Faculté de Génie, Département de Génie Chimique et Génie Biotechnologique.

F. Gitzhofer : Professeur, Université de Sherbrooke, Faculté de Génie, Département de Génie Chimique et Génie Biotechnologique

E. H. Benyoussef : Professeur, École Nationale Polytechnique d'Alger, Département de Génie Chimique.

F. Mohellebi : Professeure, École Nationale Polytechnique d'Alger, Département de Génie Chimique.

Date d'acceptation : soumis pas encore accepté.

État de l'acceptation : soumis pas encore accepté.

Revue : ENP Engineering Science journal

Référence : n.d.

Titre français : Production de nanofilaments de carbone et d'hydrogène en utilisant une nouvelle configuration de réacteur : étude hydrodynamique et résultats expérimentaux.

Contribution au document : cet article porte sur les principaux résultats de l'étude hydrodynamique effectuée avec le banc d'essai à froid et qui a servi à la concrétisation et la compréhension du concept du réacteur en visualisant les phénomènes qui existent entre la

phase solide et la phase gaz. Enfin, la preuve de fonctionnalité de ce nouveau procédé a été prouvée par le présentation des résultats expérimentaux obtenus en utilisant le réacteur pilote.

Résumé français :

Une nouvelle configuration de réacteur combinant deux lits, un lit fluidisé central et un lit mobile annulaire, a été conçue pour la production de nanofilaments de carbone et d'hydrogène par reformage à sec de gaz issus de la pyrolyse de déchets plastiques. Cette combinaison permet une récupération facile de ces nanomatériaux et, puisque le mélange de catalyseur et de carbone formé est fluidisé en continu, elle évite également le colmatage. La compréhension de l'hydrodynamique est cruciale pour choisir les conditions de fonctionnement optimales. Ainsi, un réacteur en Plexiglas à froid de même taille a été construit et utilisé. Étant donné que les gaz produits par la pyrolyse du plastique sont principalement composés d'hydrocarbures insaturés, la configuration du réacteur prototype a été exploitée en utilisant l'éthylène comme molécule représentative. Les résultats expérimentaux préliminaires du fonctionnement du réacteur avec de l'éthylène obtenus jusqu'à présent sont très prometteurs et confirment l'opérabilité du procédé. L'étape suivante consiste à fonctionner en continu plus longtemps pour atteindre une production de 1 kg/h de nanofilaments de carbone.

5.2. Article : Production of hydrogen and carbon nanofilaments using a novel reactor configuration: hydrodynamic study and experimental results

Abir Azara, Jasmin Blanchard, Faroudja Mohellebi, El Hadi Benyoussef, François Gitzhofer and Nicolas Abatzoglou

Abstract− A novel reactor configuration combining two beds, a central fluidized bed and an annular mobile bed, was designed for the production of hydrogen and carbon nanofilaments via dry reforming of gases produced from the pyrolysis of plastic waste. This combination allows for easy recovery of these nanomaterials and, since the mixture of catalyst and carbon formed is continuously fluidized, it also prevents blockage. Understanding the hydrodynamics is crucial for choosing the optimal operating conditions. Thus, a cold mock-up unit of the same size has been built and used. Since the gases produced by plastic pyrolysis are mainly composed of unsaturated hydrocarbons, the prototype reactor setup has been operated using ethylene as a surrogate molecule. The preliminary experimental results of the reactor operation with ethylene obtained so far are very promising and confirm the operability of the process. Next step is to operate continuously for longer time and reach a production of 1kg/h of carbon nanofilaments.

Keywords− Carbon nanofilaments, Fluidized bed, Hydrodynamics, Hydrogen, Reactor.

Nomenclature

CNF	Carbon Nanofilaments.
DR	Dry reforming
FBR	Fluidized bed reactor
FEG	Field emission gun
FCC	Fluid catalytic cracking
SBE	Spouted bed reactor
SEM	Scanning electron microscopy
TOS	Time-on-stream
XRD	X-Ray diffraction

5.2.1. Introduction

Various types of reactors are used for thermocatalytic reactions such as dry reforming (DR). The most conventional ones are: fixed bed (Binhang et al., 2016; Drif et al., 2015;

Fakeeha et al., 2018), fluidized bed (FBR) (Pinilla et al., 2007, 2010; Ugarte et al., 2017), rotary (Pinilla et al., 2009, 2011; Pirard et al., 2013) and membrane reactors (Alexandrov et al., 2017; Múnera et al., 2003; Sumrunronnasak et al., 2016). Fixed bed reactors have several problems, and their use remains limited on a laboratory scale because it is easier at this scale to provide a high energy supply in order to overcome the endothermicity of DR reaction. Nevertheless, this heat transfer represents a major drawback at industrial scale and still remains a major techno-economic challenge for the large-scale industrial processes (Aiello et al., 2000).

Fluidized bed reactor (FBR) is also widely studied (Pinilla et al., 2007). This type of reactor promotes heat and mass exchange between the gas and catalyst particles, thus ensuring a good mass transfer and a nearly uniform temperature in the reactor. In addition, this type of configuration makes it easy to add and remove catalyst, allowing for easier process scale-up (Azara et al., 2022; G. S. Bajad et al., 2017; Barbarias et al., 2018; R.-X. Yang et al., 2015).

There are also membrane reactors which have been extensively studied in the literature and applied to reforming processes of hydrocarbons and oxygenated hydrocarbons (Alexandrov et al., 2017; El et al., 2008; Godini et al., 2013; B. Lee et al., 2016; Sumrunronnasak et al., 2016). The interest of this type of reactor consists in the selective separation of the hydrogen from the products in order to push the balance in the direction of the products and, thus, increase the yields. This is particularly interesting for industrial reforming because at the desired high-pressure operation the conversion even at equilibrium is typically lower than 75%.

When it comes to produce carbon, the fixed bed also presents the risk of blockage due to the accumulation of carbon on the catalyst particles. In the case of fluidized beds, the friction between the catalyst particles allows the carbon to detach and be carried away with the gas. There are several types of FBR configurations, such as: fluid catalytic cracking FCC riser reactors, spouted bed reactors SBR (Weinberg et al., 1988) and SPR with a draft tube which are called also Wurster type FBR (Wurster, 1966). However, FBR also presents some drawbacks, such as the variation of the bed density, particles attrition and the rupture of carbon nanostructures are the main drawbacks (Pinilla et al., 2009; Pirard et al., 2013).

Researchers have long wanted to improve conventional fluidized bed reactors to ensure and optimize the operability of the process at industrial scale, which has resulted in many innovative reactor configurations. For example, Bajad et al. (G. S. Bajad et al., 2017) developed a new reactor configuration consisting of co-central compartments for the conversion of plastic waste into liquid hydrocarbons, carbon nanotubes and hydrogen-rich syngas (Figure 5. 1). The advantage of this configuration is that the heat has been provided in the annulus to heat both compartments and reduce the need for energy. The reactor presented in this work is also a novel configuration. It is a combination of a fixed bed and a moving bed. The advantage of this configuration is that it facilitates the recovery of CNF which is done mechanically during the fluidized bed phase.

Understanding the hydrodynamics of reactors with new configuration is important for choosing the optimal operating conditions for appropriate operation. Using a cold mock-up on Plexiglas is an efficient means to visualize the complex phenomena that occur between the gas phase and solid particles. It helps also when retrofit modifications to an existing reactor is required (Sundaresan, 2013).

The purpose of this work is to present a comprehensive study of the reactor hydrodynamics and to present the proof of the scale-up process operability by presenting the first experimental results.

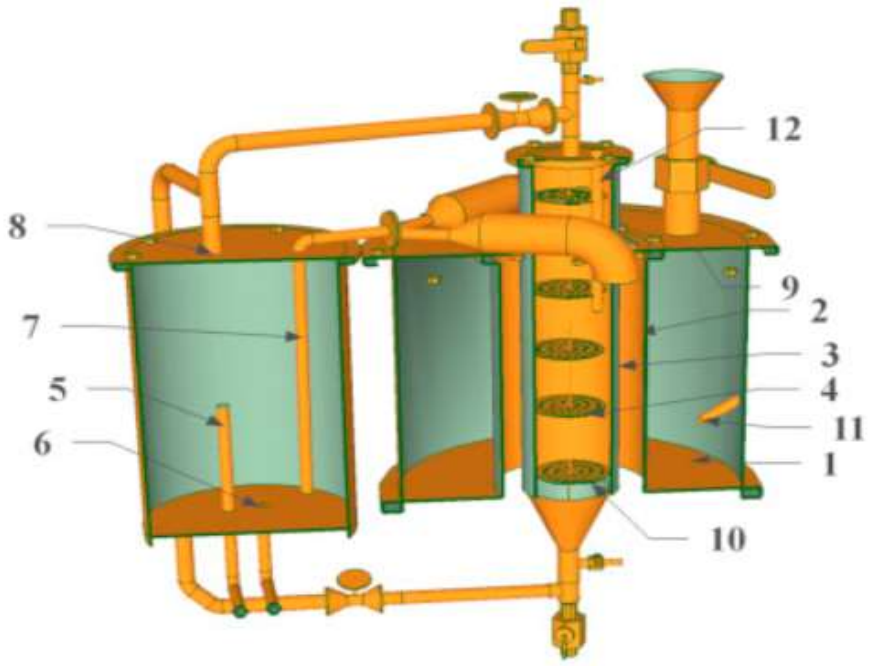

Figure 5. 1 Reactor cut section showing inner chambers and catalyst tray arrangement. (1 – pyrolysis chamber, 2 – heating chamber, 3 – CNT chamber, 4 – catalyst tray, 5 – oil drain line, 6 – water drain line, 7 – pyrolysis gas line to condenser, 8–non condensable gases to CNT chamber, 9 – Plastic feeder, 10 – first tray, 11 & 12 – thermo well) (G. S. Bajad et al., 2017).

5.2.2. Cold mock-up and Hydrodynamic study

Experimental set-up

The prototype of a plexiglass reactor, used in this study to analyze the behavior of the gas phase and the solid phase inside the reactor, is presented in Figure 5. 2 **خطأ! لم يتم العثور على مصدر المرجع.** and the dimensions are presented in Table 5. 1. it is composed of two concentric cylinders, two lateral outlets and a conical base. The gas enters from the bottom through a distribution grid to ensure a uniform supply and exits through one of the two side outlets, the other outlet being closed. A grid is also located at the outlet to prevent the catalyst from being carried outside, however allowing the gas to exit freely.

Figure 5. 2 Reactor mock-up

Table 5. 1 Prototype dimensions

External cylinder diameter (cm)	12
Internal cylinder diameter (cm)	3,8
Entrance diameter (cm)	3,8
Exit diameter (cm)	4
External cylinder height (cm)	38
internal cylinder height (cm)	27
Wall thickness (cm)	0,16
Angle of the conic base	45 °

Experimental conditions

The study of the pressure drop of the bed as a function of the superficial gas velocity is the conventional method which can give an idea of the fluidization regime. The compressed air from the main line first passes through a mass flow meter (0-100 LPM), then passes through the pipe towards the reactor inlet; the gas flow is distributed using a perforated plate

located at the reactor inlet. The outlet is linked to a pipe which is connected to the vacuum. The reactor has two gauges to measure the pressure at the top and bottom and therefore calculate the pressure drop. The two pressure sensors are connected to the computer via two acquisition cards. The pressure measurements are read directly on the screen. Particles of 300 microns and density equal to 1657 kg/m^3 were used as solid phase. A graduated scale was stuck at the external surface to measure the height of the reactor.

Results and Discussion

There are three different regions in the reactor: the spout (S), the annulus (A) and the fountain (F) as presented in Figure 5. 3.

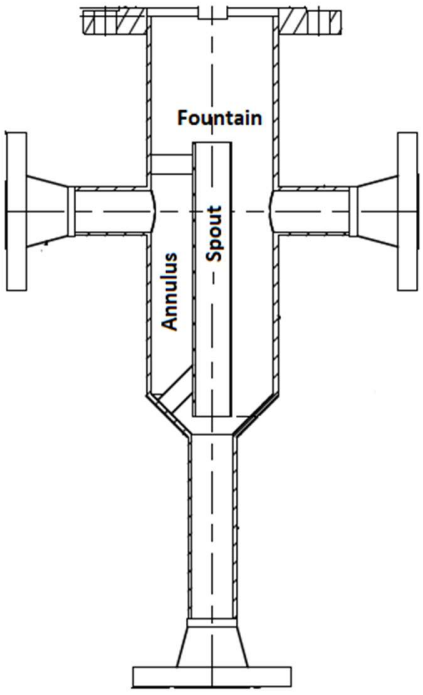

Figure 5. 3 Different regions in the reactor

First, the movement of the catalyst was observed by visually following the profile over time of a layer of the same material but of a different color which was deposited at the surface of the bed in the annular section before the beginning of the tests. We observed that the

movement of the solid is circular. The gas has two ways to reach the outlets: (a) by passing through the catalytic bed in the annular section towards the two outlets or (b) continue vertically to the end of the inner cylinder and then change direction towards the two outlets. If the gas flow is high enough along the entire length of the inner cylinder, the solid particles are fluidized (spout region S) and spring out like a fountain (fountain region F). In parallel with this movement, the solid particles in the annular region fall into the part below the inner cylinder to be entrained again allowing a slow downward movement of the catalyst in the annular part (region A). The latter, as shown in Figure 5. 4 has been clearly proven by the descent of the colored layer. Over time, the color of particles becomes homogenous; because the colored layer reaches the bottom, and it is fluidized too; this oscillatory movement finishes by homogenizing the fluidized granular material. Since one of the two outlets has been used in our runs the descent on one side is faster than the other. In fact, at industrial scale this lack of symmetry can be remedied by collecting the outlet gas flow through a radially positioned grid into another external annular section.

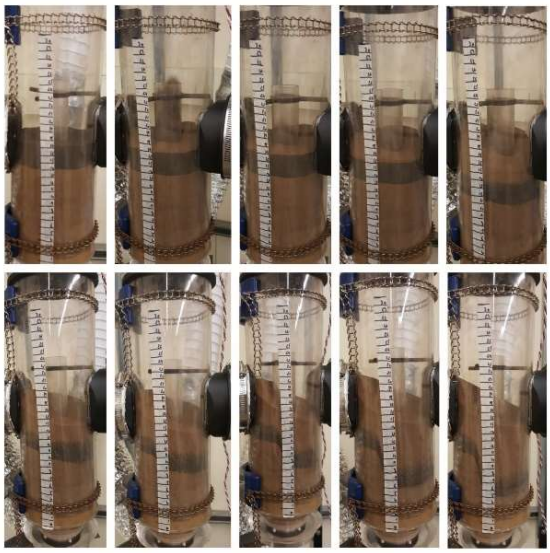

Figure 5. 4 visualization of catalyst movement

The bed pressure drop was measured over fluidizing velocity in small steps for different solid heights (Figure 5. 5). The results of the pressure drop profile corroborate with the visual observations. We observe the existing of three distinct zones:

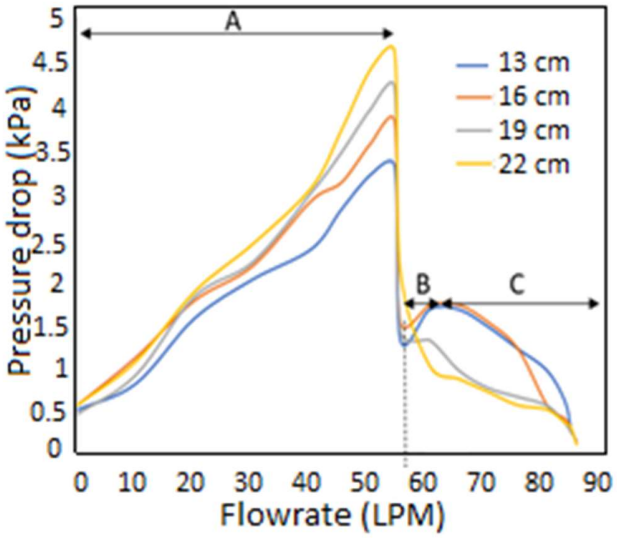

Figure 5. 5 Pressure profile

Zone A: blocking period

We notice that the pressure drop increases with the flow rate for the 4 bed heights; and it is higher with a higher height (mass) of the bed. The explanation is that the catalyst particles which are below the inner cylinder block the flow of gas as long as the weight of the catalytic bed is higher than the pressure drop due to the flow through the bed. Thus, pressure drop increases over flow rate.

Zone B: explosion period

We notice that after the plug, the pressure drop drops suddenly, because the plug is pushed away.

- 13 and 16 cm: the pressure drop increases a little bit.
- 19 cm: the pressure drop remains constant.
- 22 cm: the pressure drop continues to fall with the same slope.

For this period, the pressure is high enough to burst the plug and its force exceeds the weight of the bed in the inner cylinder causing the bed to expand rapidly in the inner cylinder and the solids to spurt out. The net decrease is attributed to the fact that the mass of the fluidized material in the inner cylinder is lower during the operation in zone B than that during zone A conditions. In other words the amount of the fluidized material expelled equals the amount

of that re-entering the inner concentric tube and it is lower than the amount placed initially in the bed.

Zone C: recirculation period

- 13 and 16 cm: pressure drop remains constant for a while and then decreases.
- 19 cm: after the explosion period, pressure drop decreases directly for high flow rates.
- 22 cm: after the explosion period, pressure drop decreases with a slower slope when increasing the flow rate.

During this period, the solids of the annular region fall in the lower part of the inner cylinder to be fluidized and entrained which makes a periodic oscillatory movement of entrainment of the solids characterized by a slow downward movement of the bed in the annular part and an entrainment in the inner cylinder .

The minimum flow rate to pass from zone A to zone B is near 55 SLPM for nearly all heights tested.

5.2.3. Scale up process

Materials

The targeted feedstock is gases derived from plastic pyrolysis, which are largely composed of unsaturated HC. The initial step, which is presented in this work, is the use of ethylene as a surrogate molecule.

The catalyst used is Fe supported on alumina. Since the aim is to test the operation of the reactor; the use of a well-known catalyst was recommended.

P&ID

The set-up presented in Figure 5. 6 is composed of three operation sections, the first one is reaction section, where the reaction is conducted in the novel reactor vessel (R1), covered by a heating jacket with temperature control. The catalyst is deposited inside the reactor and gases are fed from commercial gas cylinders (supplied by LINDE): C_2H_4 (99%), CO_2 (99%) and then preheated. Three ALICAT mass flow controllers were used to control the gas flows at the inlet. The CNF are removed from the catalyst due to the friction and entrained with the exiting gas to enter the filtration section where they are retrieved from the gas using metallic

filters at an efficiency as high as approximately 90%. This filter is cleaned up periodically using N_2 pulsations and the CNF are collected in reservoir R2 in the recovery section. The filtration section and recovery sections are inside an appropriate designed space with negative pressure which is suitable for handling nanomaterials. The last section comprises the exchanger for the quenching of gaseous stream and the final conditioning through the glycol bath for the complete removal of water vapors prior to final disposal through a flameless and smokeless flare. The flow rate of the products is measured using a totalizer and its composition is analyzed by gas chromatography (Scion 400 Series GC).

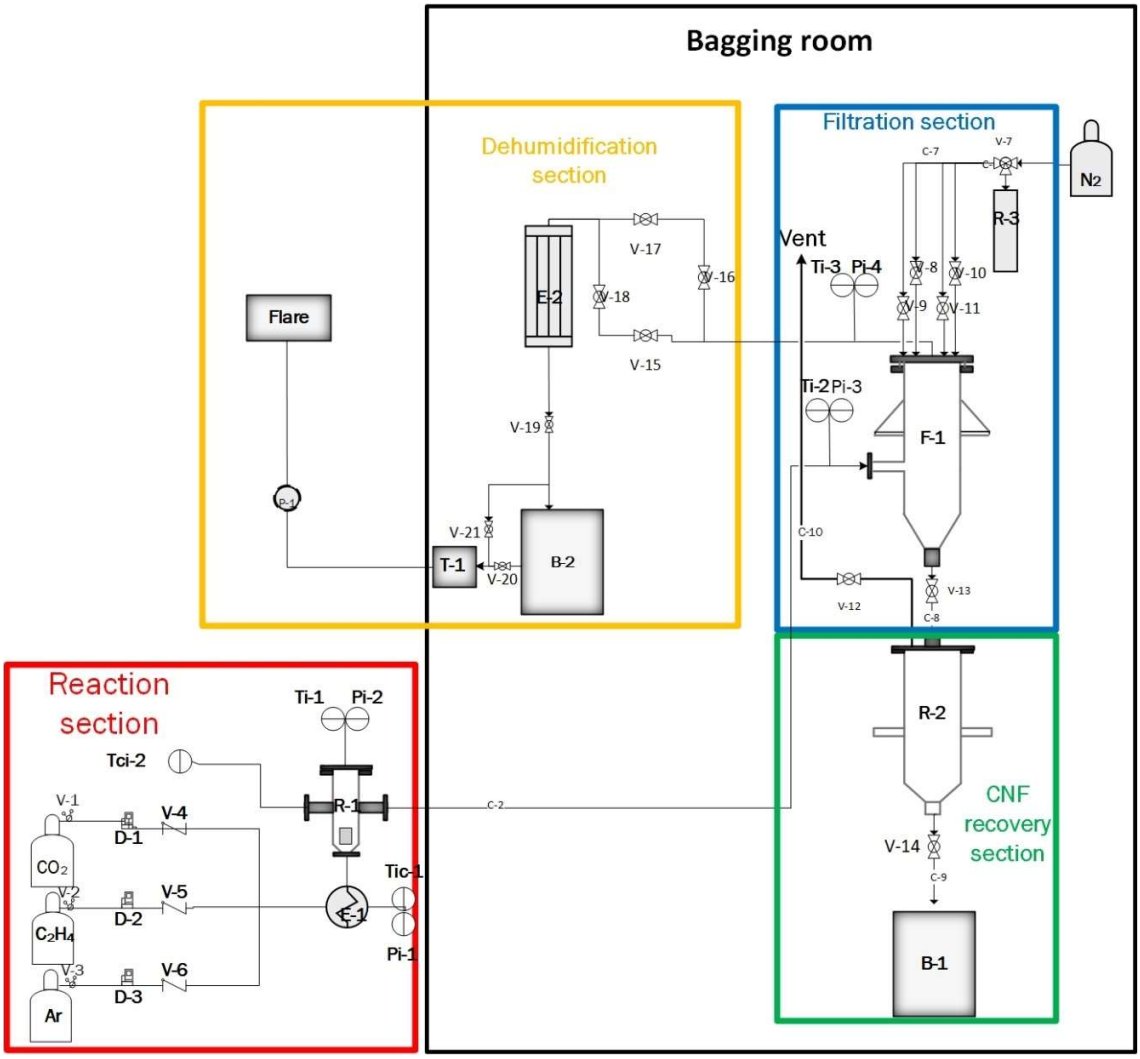

Figure 5. 6 P&ID of the scale up process

Experimental methodology

Preparation of the catalyst

The catalyst used is Fe supported on alumina and it was prepared via wet impregnation. Iron nitrate ($Fe(NO_3)_3.9H_2O$) is dissolved in water (volume greater than pore volume) then the alumina is added. The mixture is stirred for 4 hours until it becomes a "slurry". The slurry is dried at 105°C overnight to remove remaining solvent. The catalyst is then calcined under an air atmosphere for 3 hours at 750 at 2° C./min. Finally, the catalyst is ground and sieved down to 250 microns.

Activation of the catalyst

The catalyst was activated under a flow of 50% H_2 and 50% Ar for a time-on-stream (TOS) of 0,5 hour. Table 5. 2 shows the activation test conditions.

Table 5. 2 Activation conditions

Catalyst	**H_2 flow rate (SLPM)**	**N_2 flow rate (SLPM)**	**Catalyst Weight (kg)**	**TOS (h)**	**T(°C)**
Fe/Al_2O_3 (10 wt%)	**1**	**3**	**0,5**	**0,5**	**550**

Reaction and CNF and H_2 production

CNF were produced via ethylene DR reaction. The reaction conditions are presented in Table 5. 3**.**

The reaction temperature was chosen following a study of thermodynamic equilibrium at temperatures ranging from 350 °C to 850 °C. The study is presented in the Results and Discussion section. Even though it was found in the hydrodynamic study that the minimum fluidization flow (transition from zone A to zone B) is approximately 55 SLPM, the total flow used is 4 SLPM. This is due to the high pressure generated by the very high flow rate feed, a that the reactor is designed to operate at a pressure of 4 atm. On the other hand, to ensure the detachment of the carbon from the catalyst particles, pulses were made every 10 minutes using nitrogen to fluidize the bed for two minutes.

Table 5. 3 Reaction conditions

Catalyst	C_2H_4 flow rate (SLPM)	CO_2 flow rate (SLPM)	Catalyst Weight (kg)	TOS (h)	T(° C)
Fe/Al_2O_3 (10 wt%)	**3**	**1**	**0,5**	**6**	**600**

Characterization techniques

Two techniques were used to characterize the catalysts and carbon produced. X-Ray diffraction (XRD) analysis was used to identify the catalyst crystalline structure before and after reaction. The diffractograph used is Philips X'pert PRO equipped with a Cu tube as its X-ray source and a Ni filter which is used to only let through Kα1 radiations from Cu (1,5418 Å) produced at 40 kV and 50 mA. The anti-dispersion slit was set at 1/2 and the divergence slit at 1/4. The analysis is carried out with a scanning angle 2θ ranging from 15 to 90°. Scanning electron microscopy (SEM) was used to characterize the carbons formed and to study their morphology. The microscope used is a S-4700 Hitachi with field emission gun (FEG). It is equipped with detectors for secondary electrons (SE) and backscattered electrons (BSE). the working distance is 2,5-12mm and the accelerating voltage ranges from 1kV to 30kV. The magnification is up to 200,000X with resolution down to 5 nm.

Reaction metrics

The extent of the reaction is evaluated by calculating: C_2H_4 conversions ($X_{C_2H_4}$), H_2 yield (Y_{H_2}) and carbon yield (Y_C).

$$X_{C_2H_4}\ (\%) = \frac{(F_{C2H4,in} - F_{C2H4,out})}{F_{C2H4,in}} \qquad (5.\ 1)$$

$$Y_{H_2}\ (\%) = \frac{F_{H2}}{2 \times F_{C2H4,in}} \times 100 \qquad (5.\ 2)$$

$$Y_C\ (\%) = \frac{m_{C\ deposit}}{m_{C,in}} \times 100 \qquad (5.\ 3)$$

$$m_{C_{deposit}} = m_{catalyst,tf} - m_{catalyst,t0} \qquad (5.\ 4)$$

$$m_{C,in} = ((2 * F_{C2H4,in} * time + F_{CO\ ,in} * time)) * M_C \qquad (5.\ 5)$$

Where:

$F_{C2H4,in}$ and $F_{C2H4,out}$ respectively denote the molar flow rates of C_2H_4 at the inlet and the outlet of the reactor,

F_{H2} the molar flow rate of H_2 at the outlet of the reactor

$m_{C,in}$ the mass of carbon fed.

$m_{c\ deposit}$ the mass of solid carbon deposit on the catalyst

$m_{catalyst,tf}$ the mass of the catalyst after reaction

$m_{catalyst,t0}$ the mass of the catalyst before reaction

M_C the molar mass of C = 12,0107 $g.mol^{-1}$

Results and Discussion

Thermodynamic investigation

FactSage software was used to study the thermodynamic equilibrium of the C_2H_4 DR reactions at different conditions of temperature (450-850 °C) and molar ratios C_2H_4/CO_2 (1/1-3/1), at atmospheric pressure. Equilibrium composition as well as the amount of deposited carbon were estimated. This investigation allowed us to choose the experimental conditions which optimize carbon and synthesis gas ($CO+H_2$) yields. The most useful results are shown in Figure 5. 7 and Figure 5. 8.

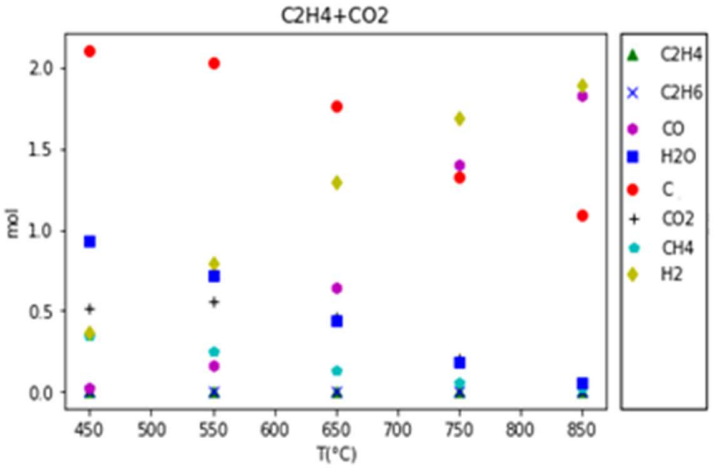

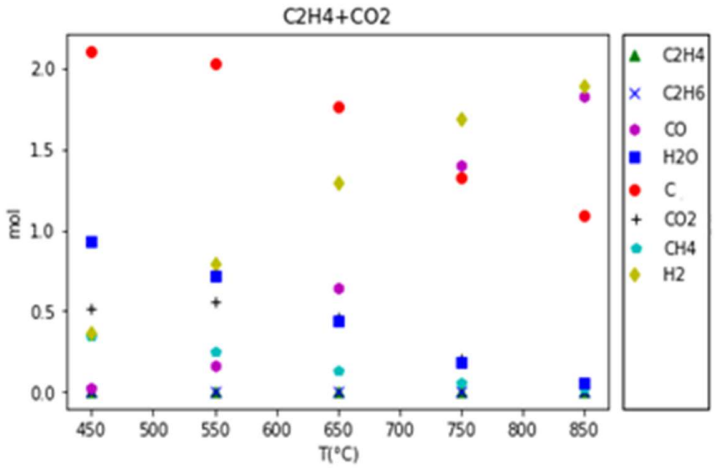

Figure 5. 7 Product composition for ethylene DR at ratio 1/1.

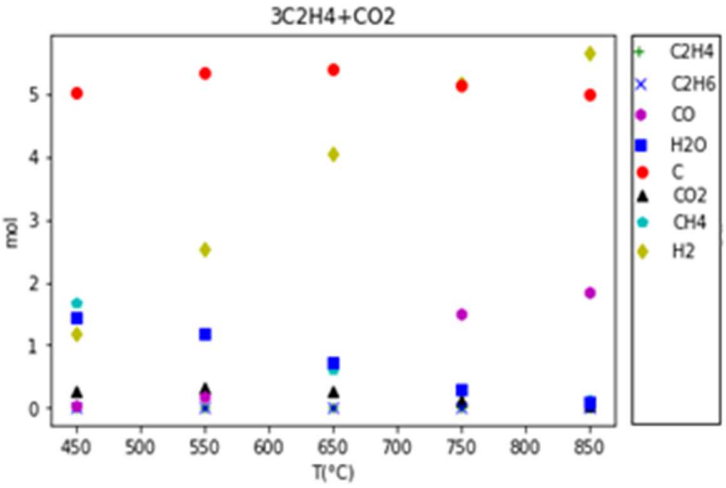

Figure 5. 8 Product composition for ethylene DR at ratio 3/1

We can observe that H_2 amount increases with temperature for both ratios, while C amount decreases with temperature at ratio 1/1; and reaches its maximum at temperature between 600-650 °C at a ratio of 3/1. Based on these results, 600 °C was chosen as the reaction temperature. Since we want to maximize carbon and H_2 production, a 3/1 ratio of C_2H_4/CO_2 was chosen.

Experimental results

The results of the reaction at 600 °C and ratio 3/1 are presented in Table 5. 4.

Table 5. 4 General experimental results for the DR reaction at 600 °C and Fe-Al_2O_3 10% for 4h TOS.

C_2H_4 (SLPM)	3
CO_2 (SLPM)	1
Catalyst weight (kg)	0,5
TOS (hours)	6
$GHSV_{STP}$ ($l.h^{-1}.\ kg^{-1}$)	480
C_2H_4/CO_2	3
Carbon (g)	615
Carbon growth rate ($kg_C.kg_{cat}^{-1}.h^{-1}$)	0,2
Carbon yield (%)	53,2
Total H_2 yield (%)	46,4
Total C_2H_4 conversion (%)	73,0
Total CO_2 conversion (%)	69,9
Mass balance error for C (%)	6,3
Mass balance error for H (%)	4,0
Mass balance error for O (%)	4,3

The carbon formed was analyzed by SEM and it has been proven that it is filamentous as shown in Figure 5. *9*.

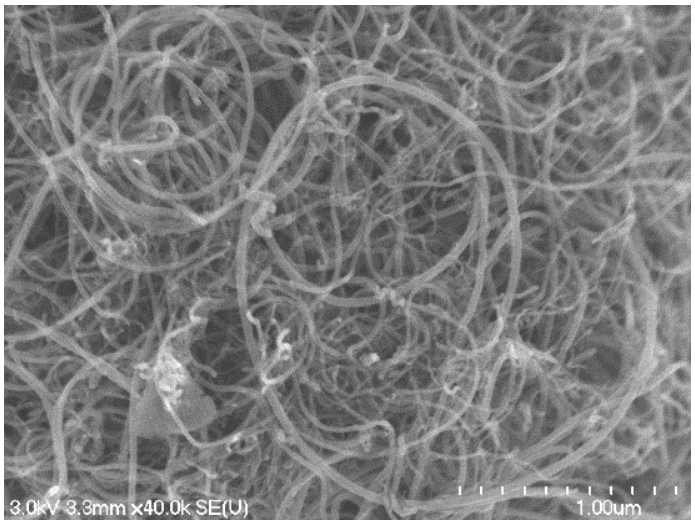

Figure 5. 9 SEM image of deposited carbon.

Figure 5. 10 and Figure 5. 11 show the XRD of the fresh catalyst and deposited carbon on used catalyst after the DR reactions, respectively.

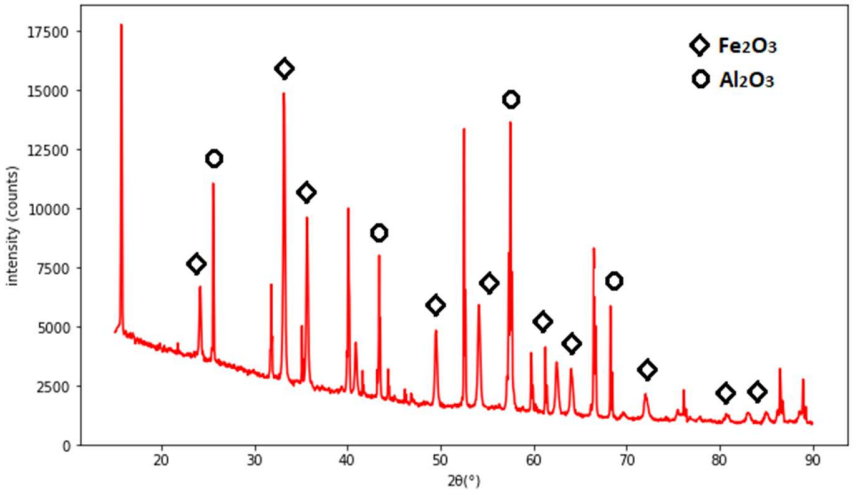

Figure 5. 10 XRD of fresh catalyst

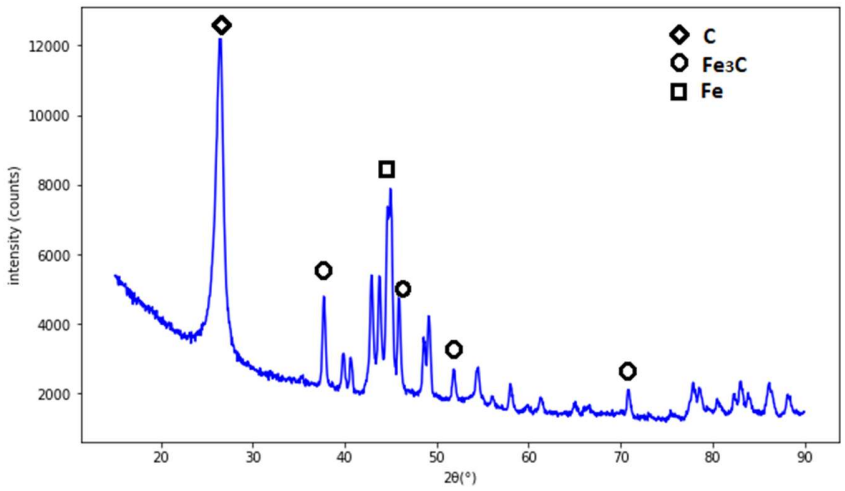

Figure 5. 11 XRD of the spent catalyst

Discussion

The production of CNF at a pilot scale in a continuous mode has not been reported in the literature. In this work, we managed to operate a kilo lab scale reactor. The carbon produced in the reactor has been removed from the catalyst particles thanks to the friction between the particles which are in continuous movement between the two beds. The CNF with nanometric size were entrained with the exist gaseous stream and retrieved in the filter.

The carbon and H_2 yields are 53% and 46% respectively. These high rates are due to the suitable activity of the iron-based catalyst. Although the first reduction step with H_2 activated the catalyst, the H_2 formed at the beginning of the reaction contributes to catalyst activation by further reduction of iron oxides. This is proven by the presence of Fe metal peaks and the disappearance of iron oxide peaks on used catalyst XRD (Figure 5. 11). Also, carbon itself may contribute to the catalytic activity. It has been demonstrated that the carbon under the form of catalytically induced CNF itself has catalytic properties (Jankhah et al., 2008b).

The XRD of used catalyst after the reaction, proves the deposition of carbon. The peak at $2\theta=26°$ confirms that the carbon formed is graphitic. Moreover, no peaks of oxides have been found and only Fe was present in the diffractograms; the latter prove that Fe oxides were reduced during the reactions. Carbide formation was expected, because carbides are known to be the precursor of CNF especially with iron based catalyst; Fe_3C is metastable under the reaction conditions and it is decomposed to CNF and α-Fe (Ermakova et al., 2001). Consequently, carbides co-exist along with CNF and Fe^0.

The SEM analyses reported above help us to identify the morphology of carbon produced. It is well known that there are different types of carbon that can be produced, pyrolytic, encapsulating and filamentous. Filamentous carbon is formed from the catalytic decomposition of HC, pyrolytic carbon is formed from HC thermal decomposition at high T, and encapsulating carbon is usually formed at relatively low T when the adsorbed HC accumulate on the surface of the catalyst and the C_nH_m* radicals slowly polymerize (Dupuis, 2005). Figure 5. 9 shows clearly that the carbon formed is filamentous with different width and length.

5.2.4. Conclusion

Compared with waste plastics, CNF and H_2 are high-added-value products. Many efforts have been deployed to produce them at industrial scale with an optimized process in terms of energy efficiency, continuity and the facility of the system operation. This work is part of such an endeavor. The reactor conceived, built and operated is a novel configuration which has several advantages: especially in terms of recovery of carbon nanofilaments.

The process development unit used in this study is at pilot kg-lab scale, with the use of half a kg of catalyst and a total flow rate of reactants of 4 SLPM. Even though some problems occurred, the system worked very well, and more than 600 g of carbon was produced. The main drawback is that the scale is still low and after some hours of operation there is a tendency of carbon accumulation at the relatively small orifices. Nevertheless, this study proved the concept at nearly kg-lab scale and further improvement will come along with a bigger scaleup which is the intention of the research and industrial partner for the next steps towards commercialization.

CHAPTRE 6

CONCLUSION

CHAPITRE 6 CONCLUSION

6.1. Conclusion générale

Ce projet de recherche a plusieurs dimensions : technologique, économique et environnemental. La dimension technologique réside dans l'utilisation d'un réacteur ayant une nouvelle configuration innovante constituée d'un lit fluidisé et d'un lit mobile et présentant des avantages intéressants en termes de production et récupération des NFC. La dimension économique est assurée par l'introduction des NFC dans les matrices polymériques ce qui va réduire le cout de production en substituant aux additifs onéreux utilisés actuellement. En effet, les NFC vont conférer aux polymères des propriétés mécaniques et thermiques améliorées, ce qui les rend plus rapides à mettre en œuvre (temps de refroidissement réduit); et également des propriétés électriques intéressantes (antistatique permanent, localisable, etc.). En plus, les déchets plastiques non recyclables et le CO_2 utilisés comme source de carbone, présentent des entrants à faible coût. Enfin, ces NFC sont considérés comme des produits verts car ils sont produits à partir de déchets en utilisant un procédé qui vise à éliminer les GES, ce qui donne à ce projet une dimension environnementale aussi.

Le projet se décompose en deux volets essentiels : volet réacteur et volet production des NFC. Concernant le volet réacteur, une nouvelle configuration a été développée au cours de ce projet, les étapes de construction commençaient par le dimensionnement, la fabrication de réacteur en respectant les normes ASME, la conception d'un banc d'essai à froid pour l'étude fluido-dynamique. Ce volet comporte aussi la mise en marche de tout le procédé et l'évaluation de son fonctionnent tout en appliquant un protocole de sécurité. Le dimensionnement du réacteur passe par plusieurs étapes. Les vitesses minimale et maximale de fluidisation ont été calculées afin de choisir la vitesse de gaz nécessaire pour être en régime de fluidisation bouillonnant. Pour que les particules puissent jaillir, il faut que la hauteur du cylindre interne soit inférieure à la hauteur totale du lit en régime bouillonnant (HCI < HL + TDH). Le diamètre du cylindre interne ainsi que la hauteur sont alors calculés. Le débit de gaz alimenté au réacteur se divise en deux courants à l'entrée, dépendamment de la perte de charge à travers les deux passages. Sachant que la perte de charge dans le cylindre externe est égale à la somme de la perte de charge dans le cylindre interne et la perte de charge du

transit du gaz du cylindre interne à la sortie, les autres dimensions ont été calculées par itération jusqu'à satisfaire l'égalité des pertes de charge. Le réacteur a été construit chez la compagnie Pro-Par Inc. qui est un fabricant québécois des réservoirs d'entreposage. Comme le procédé est à l'échelle pilote, un nouvel espace plus spacieux a été construit par l'université de Sherbrooke pour abriter les travaux de mise à l'échelle. Après l'inauguration du nouveau laboratoire, l'installation de tous les équipements a commencé. Les différents équipements ont été placés à leurs endroits respectifs, les tuyaux de raccordement entre chacun ont été installés, les supports métalliques ont été construits et positionnés adéquatement et les différents instruments de mesure et de contrôle ont été placés. Le procédé est composé de 4 sections. La première étant la section de la réaction où se trouve le réacteur. Les gaz sont alimentés à partir des cylindres de gaz commerciaux. Des débitmètres massiques sont utilisés pour contrôler le débit de gaz entrant dans le préchauffeur. Ce dernier précède le réacteur et sert à préchauffer le mélange de gaz réactif. La chaleur est fournie au préchauffeur et au réacteur à l'aide de bandes chauffantes en céramiques qui enveloppent les deux équipements. La bride en haut du réacteur est amovible et permet l'introduction du catalyseur au début du test ainsi que la vidange et le nettoyage du réacteur à la fin du test. Le gaz à la sortie du réacteur passe à la section de filtration entrainant avec lui les NFC. Quatre cartouches métalliques installées dans une enceinte sont utilisées pour filtrer le gaz et récupérer les NFC. Le gâteau formé est délogé par des impulsions de gaz en utilisant un système qui comporte un cylindre pressurisé de N_2, un vérin, une vanne à bille à trois voies et quatre vannes à bille. Un réservoir se trouve juste en dessous du filtre pour récupérer le gâteau délogé. Le filtre et le réservoir se trouvent dans une salle d'ensachage à pression négative ce qui empêche la diffusion de l'air en cas de propagation des NFC au cours des manipulations. L'air est aussi évacué en continu pour réduire les NFC en suspension et donc limiter le risque de contamination des personnes qui entrent dans la pièce. L'évacuation est reliée à un filtre pour décontaminer l'air évacué. Toute personne qui travaille dans cette salle doit être équipée des équipements de protection individuelle en particulier un adducteur d'air qui protège contre l'inhalation des NFC. La dernière section est le conditionnement de l'effluent gazeux : elle comprend un condenseur pour déshumidifier le gaz et un bain de glycol pour enlever toute trace d'eau ou autres impuretés. Un totalisateur est utilisé pour mesurer le débit à la sortie, et un point de prélèvement sert à prélever le gaz pour analyser sa composition à l'aide d'un

chromatographe, et une torchère sans flamme et sans fumée permet de bruler le gaz avant son évacuation dans l'atmosphère.

Un protocole de sécurité d'opération a été établi afin que les manipulations se déroulent en toute sécurité, étant donné que le procédé présente beaucoup de risques de santé et de sécurité. Des analyses What-if et HAZOP ont été réalisées sur les sections de réaction et de filtration. Les principales déviations qui peuvent avoir lieu sont la baisse ou la hausse de la température et de la pression. Ceci peut être causé par plusieurs facteurs, comme le blocage des lignes à cause de l'accumulation du carbone, manque ou défaillance de contrôle de température ou de pression, problèmes au niveau de l'alimentation des gaz. Les dangers majeurs qui peuvent survenir sont les fuites des gaz toxiques et inflammables, l'incendie, l'explosion et propagation des NFC. Pour mitiger ces risque, il faut établir et mettre en place des pratiques de travail sécuritaire avec des équipement d'échelle pilote kg-lab (instrumentation, nettoyage, inspection et maintenance) et lors de la manipulation des NFC (lieux adéquats, EPI).

Un prototype en plexiglas de même configuration et de mêmes dimensions que le réacteur a été utilisé dans l'étude hydrodynamique pour comprendre le comportement de la phase gazeuse et de la phase solide à l'intérieur du réacteur. En premier lieu, le mouvement du catalyseur a été observé en suivant visuellement le profil dans le temps d'une couche du même matériau mais de couleur différente qui a été déposée à la surface du lit dans la section annulaire avant le début des essais. En alimentant le gaz, il a été observé que la couche colorée descend au fil du temps, et après un certain temps, la couleur du lit devient homogène. En effet, la couche colorée arrive au fond, tombe dans la partie sous le cylindre interne et se fluidise avant de jaillir et tomber dans le lit dans l'annulaire. Ainsi, le mouvement du solide dans le réacteur est caractérisé par un profil circulaire oscillatoire. Ensuite, la variation de la perte de charge du lit en fonction de la vitesse superficielle des gaz a été étudiée pour identifier les différents régimes ayant lieu dans le réacteur. Trois régimes ont été observés : le régime de blocage, le régime d'explosion et le régime de recirculation. Lors du régime de blocage, les particules de catalyseur qui se trouvent sous le cylindre interne bloquent l'écoulement de gaz et la perte de charge augmente. Ce régime dure tant que le poids du lit catalytique est supérieur à la perte de charge due à l'écoulement à travers le lit. Lorsque la pression est suffisamment élevée et que sa force dépasse le poids du lit dans le cylindre

interne, le bouchon éclate. Ensuite, le lit expand rapidement dans le cylindre interne et les solides jaillissent. La perte de pression soudaine est attribuée au fait que la masse du solide fluidisé dans le cylindre interne est plus faible comparativement à la quantité placée initialement dans le lit. Enfin, les solides effectuent un mouvement oscillatoire périodique caractérisé par un profil lent de descente du lit dans la partie annulaire et un entraînement dans le cylindre interne, et accompagné d'une perte de pression avec l'augmentation du débit alimenté.

Des problèmes au cours des premières manipulations du système sont survenus et ont empêché le bon déroulement des tests. Les deux principaux problèmes sont la hause de pression et la fuite au niveau du réacteur et du bain de glycol. La bride avait seulement 4 boulons et il a fallu en ajouter quatre autres pour améliorer le scellage et l'étanchéité avec le réacteur. Concernant le bain de glycol, le vaisseau n'était pas conçu pour fonctionner sous pression, la seule solution était donc de l'écarter du procédé. Après ces modifications, des tests ont été réalisés. Le problème de la hausse de pression persistait, et une analyse de cause a révélé qu'un bloc de carbone produit formait des bouchons et empêchait le passage du gaz. Ce problème est arrivé à plusieurs reprises. Le premier était le blocage au niveau du tube inférieur du réacteur qui contenait du catalyseur. La solution proposée était d'introduire une grille (fixée dans un support) fine avec un diamètre inférieur au diamètre du catalyseur pour maintenir le catalyseur dans le cylindre supérieur du réacteur. Cependant, le vide entre le support et la paroi du réacteur devenait de plus en plus grand à force de l'introduire et de le retirer, ce qui a laissé des particules de catalyseurs tomber dans le tube inférieur et le problème de blocage est survenu à nouveau. La décision majeure de couper le tube inférieur du réacteur pour éliminer ce problème définitivement a été prise. Malgré la modification de la configuration du réacteur, le travail à haut débit en régime de fluidisation n'était pas possible à cause de l'augmentation de la pression et la fuite au niveau du couvercle du réacteur. La solution était de travailler en alternance entre un lit fixe et un lit fluidisé pour éviter le travail à haute pression et pour assurer le détachement du carbone et débloquer le lit en le fluidisant par impulsions. Un autre problème s'agissait de l'entrainement des particules de catalyseur à la sortie ce qui bloquait la tuyauterie connectant le réacteur et filtre. En régime d'alternance, ce problème n'était pas prononcé mais le nettoyage après chaque test était indispensable pour ne pas altérer le déroulement du test suivant.

Quant au volet de production des NFC, il a été réalisé sur deux montages : des expériences ont été menées dans un réacteur différentiel à lit fixe à l'échelle du laboratoire (g-lab) et les travaux subséquents ont été effectués dans un réacteur hybride combinant un lit mobile à un lit fluidisé à l'échelle pilote du laboratoire (kg-lab) afin de prouver la faisabilité à plus grande échelle d'une éventuelle commercialisation du procédé. Le craquage catalytique ainsi que le reformage à sec du C_2H_4 ont été réalisés dans le réacteur différentiel dans le but de faire ressortir l'impact de l'ajout du CO_2 sur la qualité et la quantité des NFC formés. Les résultats ont montré que les rendements les plus élevés en carbone et en H_2 ont été obtenus à des température moins élevées pour la réaction du reformage à sec (650 °C pour la réaction du reformage et 750 °C pour la réaction de craquage catalytique). En outre, le carbone déposé s'est avéré être de meilleur ordre structural dans le cas du reformage à sec. L'étude a également démontré que le fer est le principal précurseur de la croissance de NFC tandis que le nickel contribue davantage à la scission des liaisons C-C. Concernant les test effectués dans le réacteur hybride, la matière première utilisée était également le C_2H_4 comme molécule représentative du gaz produit de la pyrolyse des déchets plastiques. Un demi-kg de catalyseur et un débit total de réactifs de 4 SLPM ont été utilisés pour la production des NFC dans le réacteur hybride. Même si quelques problèmes sont survenus, le système a très bien fonctionné et plus de 600 g de carbone ont été produits. Le principal inconvénient est que l'échelle est encore faible et après quelques heures de fonctionnement, il y a une tendance à l'accumulation de carbone au niveau des orifices relativement petits. Néanmoins, cette étude a prouvé le concept à l'échelle du laboratoire et des améliorations supplémentaires s'accompagneront d'une mise à l'échelle plus importante, ce qui est l'intention du partenaire de recherche et industriel pour les prochaines étapes vers la commercialisation.

6.2. Recommandations pour le procédé

D'autres modifications pourraient être faites au niveau de l'installation actuelle pour améliorer encore le procédé avec les équipements existants, en revanche, pour pouvoir industrialiser le procédé, une mise à échelle plus importante s'impose. Les recommandations suivantes peuvent être utiles tant pour le procédé actuel que pour les procédés à des échelles plus grandes.

Le plus gros problème rencontré étant la hausse de pression, un nouveau réacteur de plus grandes dimensions et qui fonctionne dans une plage de pression plus large doit être construit selon les normes ASME des vaisseaux sous pression et pourrait remplacer le réacteur actuel. Le bain de glycol aussi doit être remplacé par un vaisseau sous pression. Ceci va donner une plus grande marge de travail dans le cas où la pression augmente à cause du blocage occasionné par l'accumulation du carbone.

Pour pallier le problème d'entrainement du solide, la sortie du réacteur doit être plus haute. Un cyclone suivant le réacteur s'avère nécessaire pour séparer le catalyseur du gaz, ce dernier plein de NFC va continuer son chemin vers le filtre. En ce qui concerne l'obturation des tuyaux , il faut que la plupart des tuyaux reliant les différents équipements de l'installation soient plus courts et de plus gros diamètre. Comme montré dans le nouvelle installation proposée (Figure 6. 1), le réacteur dans le salle principale peut se trouver sur une mezzanine pour être dans la même hauteur que le cyclone. Ce dernier se trouve dans la salle d'ensachage à côté du filtre qui lui aussi se trouve sur la mezzanine déjà existante.

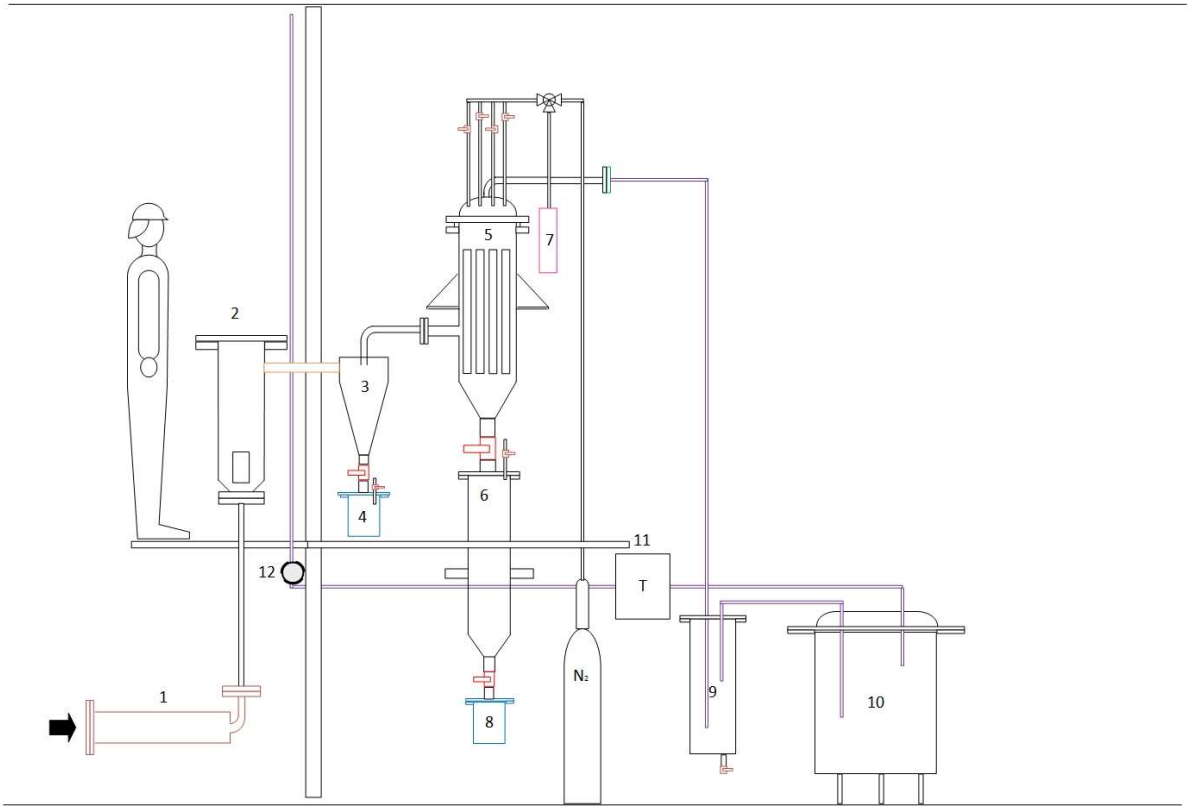

Figure 6. 1 Schéma proposé du diagramme bloc du procédé. 1-Préchauffeur, 2-Réacteur, 3-Cyclone, 4-Contenant du catalyseur, 5-Filtre, 6-Resrvoire de récupération des NFC, 7-Vérin, 8-Contenant des NFC, 9-Condenseur, 10-Bain de glycol, 11-Totalisateur, 12-Point d'échantillonnage.

Le cyclone pourrait être aussi connecté au réacteur pour faire un lit fluidisé circulant permettant ainsi de réintroduire le catalyseur dans le système (Figure 6. 2).

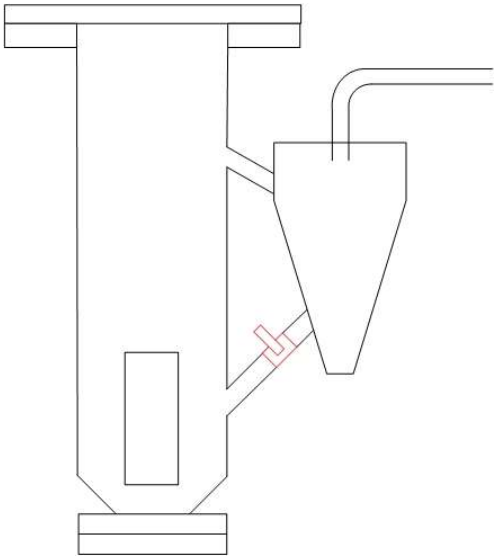

Figure 6. 2 Lit circulant.

Concernant la configuration du réacteur, elle pourra être modifiée selon les technologies qui existent déjà dans la littérature. Dans ce qui suit, plusieurs idées tirées de la littérature seront présentées et qui pourraient être utiles pour configurer un réacteur qui répond aux besoins et qui limite les problèmes rencontrés avec la configuration actuelle.

Dans un lit à jaillissement classique, une fraction importante du gaz d'entrée est déviée vers le lit annulaire de solides. Ce gaz a un temps de séjour beaucoup plus long que celui du gaz de jaillissement non dévié. Un type de réacteur appelé *Internal Circulating Fluidized Bed* (ICFB) représente une modification du lit fluidisé jaillissant avec tube d'aspiration ayant des caractéristiques spécialement conçues pour éliminer le problème de contournement de gaz (Milne et al., 1992). Il est composé de cylindres concentriques et le lit dans l'annulaire est un lit mobile et celui dans le tube d'aspiration est fluidisé, ce qui est le même concept que le réacteur présenté dans cette étude à l'exception de trois différences. La première différence réside dans le tube d'aspiration, auquel un « té » peut être installé au sommet pour fonctionner comme un dispositif de séparation des solides (Figure 6. 3). Milne et al. (Milne et al., 1999) ont proposé un autre type de séparateur, il s'agit d'un séparateur centrifuge gaz/solides qui sépare le gaz du tube central des particules qui retournent vers le lit annulaire (Figure 6. 4). La seconde différence est que le tube d'aspiration est fixé directement sur l'entrée des gaz et un certain nombre d'orifices sont positionnés dans la paroi du tube près de

sa base pour permettre l'échange du gaz et du solide entre l'annulaire et le tube. Les solides pénètrent dans le tube d'aspiration par les orifices et sont entraînés. La troisième différence est que le gaz est aussi introduit par un distributeur dans la région annulaire entourant le tube central. Une fraction de ce gaz auxiliaire s'écoule à travers les orifices dans le tube central, favorisant ainsi l'afflux radial de solides et assurant des débits élevés de circulation des solides. Ceci est la caractéristique du lit jet-fluide (*spout-fluid beds*) qui est un type de lit à jaillissant dans lequel, en plus de l'orifice central, un fluide auxiliaire s'écoule à travers une série de trous dans un distributeur dans la base conique (Sutkar et al., 2013).

L'ajout d'un dispositif de séparation à la tête du tube central semble être un moyen efficace pour empêcher l'entrainement des particules de catalyseur. Il peut même remplacer le cyclone proposé pour la séparation gaz-solide et réduire ainsi les couts d'investissement et d'opération. La configuration du lit jet-fluide est aussi intéressante. Le distributeur dans l'annulaire peut être alimenté avec du gaz réactif qui va rentrer en contact avec le catalyseur dans l'annulaire et la formation du carbone aura lieu. Le gaz de fluidisation rentrant par l'entrée principale pourrait être le gaz réactif lui-même comme il peut être un gaz inerte qui va servir comme fluide fluidisant qui va assurer le détachement des NFC.

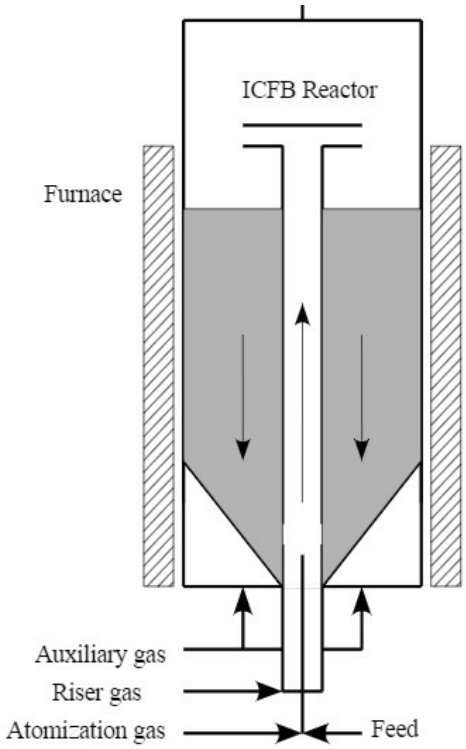

Figure 6. 3 ICBF schematic diagram type 2 (Milne et al., 1992).

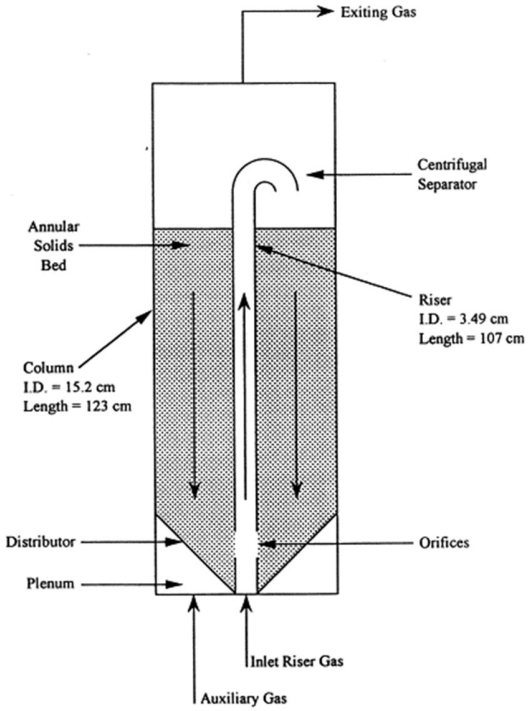

Figure 6. 4 Schematic diagram of the ICFB (Milne et al., 1999).

Un autre type de réacteur qui permet aussi d'éviter l'entrainement du solide est le lit jaillissant conteneur de fontaine (*Fountain Contained Conical Spouted Bed*) (Lopez et al., 2017). Ce type de réacteur assure une augmentation du temps de séjour et un contact direct supplémentaire avec les particules de catalyseur dans la fontaine du lit. La modification la plus importante réside dans le confinement de la fontaine, qui a été réalisé en soudant un tube au couvercle du réacteur, l'extrémité inférieure du tube étant proche de la surface du lit (Figure 6. 5). Ce dispositif a été conçu à l'origine dans le but de manipuler des matériaux fins en retenant les particules dans la région de la fontaine, et donc en évitant leur entraînement hors du lit (Lopez et al., 2017).

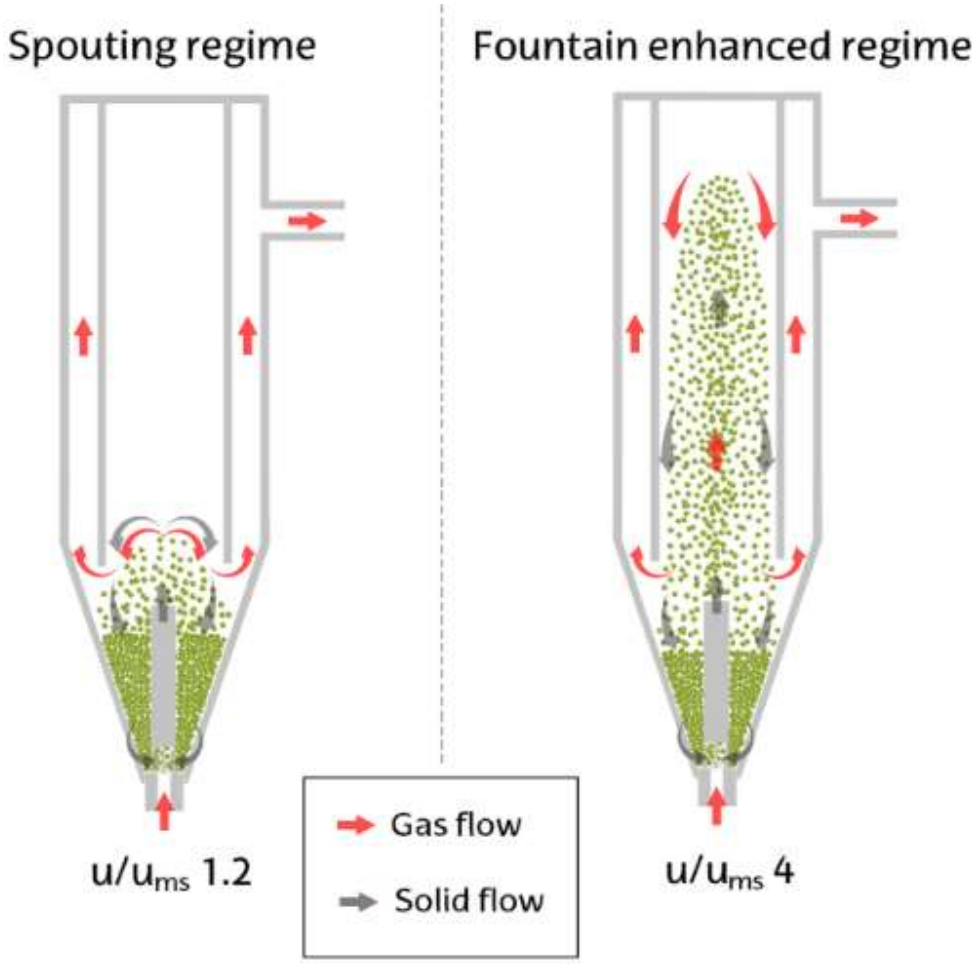

Figure 6. 5 Schémas du jaillissement conventionnel et des régimes améliorés de la fontaine (Lopez et al., 2017).

LISTE DES RÉRÉNCES

Liste des références

Aboul-Enein, A. A., Adel-Rahman, H., Haggar, A. M., & Awadallah, A. E. (2017). Simple method for synthesis of carbon nanotubes over Ni-Mo/Al2O3 catalyst via pyrolysis of polyethylene waste using a two-stage process. *Fullerenes, Nanotubes and Carbon Nanostructures*, *25*(4), 211-222. https://doi.org/10.1080/1536383X.2016.1277422

Aboul-Enein, A. A., & Awadallah, A. E. (2018). Production of nanostructured carbon materials using Fe–Mo/MgO catalysts via mild catalytic pyrolysis of polyethylene waste. *Chemical Engineering Journal*, *354*, 802-816. https://doi.org/10.1016/j.cej.2018.08.046

Aboul-Enein, A. A., & Awadallah, A. E. (2019). Production of nanostructure carbon materials via non-oxidative thermal degradation of real polypropylene waste plastic using La2O3 supported Ni and Ni–Cu catalysts. *Polymer Degradation and Stability*, *167*, 157-169. https://doi.org/10.1016/j.polymdegradstab.2019.06.015

Aboul-Enein, A. A., Awadallah, A. E., Abdel-Rahman, A. A.-H., & Haggar, A. M. (2018). Synthesis of multi-walled carbon nanotubes via pyrolysis of plastic waste using a two-stage process. *Fullerenes, Nanotubes and Carbon Nanostructures*, *26*(7), 443-450. https://doi.org/10.1080/1536383X.2018.1447929

Acomb, J. C., Wu, C., & Williams, P. T. (2014). Control of steam input to the pyrolysis-gasification of waste plastics for improved production of hydrogen or carbon nanotubes. *Applied Catalysis B: Environmental*, *147*, 571-584. https://doi.org/10.1016/j.apcatb.2013.09.018

Acomb, J. C., Wu, C., & Williams, P. T. (2015). Effect of growth temperature and feedstock:catalyst ratio on the production of carbon nanotubes and hydrogen from the pyrolysis of waste plastics. *Journal of Analytical and Applied Pyrolysis*, *113*, 231-238. https://doi.org/10.1016/j.jaap.2015.01.012

Acomb, J. C., Wu, C., & Williams, P. T. (2016). The use of different metal catalysts for the simultaneous production of carbon nanotubes and hydrogen from pyrolysis of plastic feedstocks. *Applied Catalysis B: Environmental*, *180*, 497-510. https://doi.org/10.1016/j.apcatb.2015.06.054

Ago, H., Uehara, N., Yoshihara, N., Tsuji, M., Yumura, M., Tomonaga, N., & Setoguchi, T. (2006). Gas analysis of the CVD process for high yield growth of carbon nanotubes over metal-supported catalysts. *Carbon*, *44*(14), 2912-2918. https://doi.org/10.1016/j.carbon.2006.05.049

Aiello, R., E Fiscus, J., Zur Loye, H.-C., & D Amiridis, M. (2000). Hydrogen production via the direct cracking of methane over Ni/SiO2 : Catalyst deactivation and regeneration. *Applied Catalysis A: General*, *192*, 227-234. https://doi.org/10.1016/S0926-860X(99)00345-2

Alexandrov, A. V., Gavrilova, N. N., Kislov, V. R., & Skudin, V. V. (2017). Comparison of membrane and conventional reactors under dry methane reforming conditions. *Petroleum Chemistry*, *57*(9), 804-812. https://doi.org/10.1134/S0965544117090031

Al-Saleh, M. H., & Sundararaj, U. (2011). Review of the mechanical properties of carbon nanofiber/polymer composites. *Composites Part A: Applied Science and Manufacturing*, *42*(12), 2126-2142. https://doi.org/10.1016/j.compositesa.2011.08.005

Al-Salem, S. M., Antelava, A., Constantinou, A., Manos, G., & Dutta, A. (2017). A review on thermal and catalytic pyrolysis of plastic solid waste (PSW). *Journal of Environmental Management*, *197*, 177-198. https://doi.org/10.1016/j.jenvman.2017.03.084

Alstrup, I. (1988). A new model explaining carbon filament growth on nickel, iron, and Ni-Cu alloy catalysts. *Journal of Catalysis*, *109*, 241.

Arena, U., Mastellone, M. L., Camino, G., & Boccaleri, E. (2006). An innovative process for mass production of multi-wall carbon nanotubes by means of low-cost pyrolysis of polyolefins. *Polymer Degradation and Stability*, *91*(4), 763-768. https://doi.org/10.1016/j.polymdegradstab.2005.05.029

Argyle, M. D., & Bartholomew, C. H. (2015). Heterogeneous Catalyst Deactivation and Regeneration : A Review. *Catalysts*, *5*(1), 145-269. https://doi.org/10.3390/catal5010145

Arnaiz, N., Gomez-Rico, M. F., Martin Gullon, I., & Font, R. (2013). Production of Carbon Nanotubes from Polyethylene Pyrolysis Gas and Effect of Temperature. *Industrial & Engineering Chemistry Research*, *52*(42), 14847-14854. https://doi.org/10.1021/ie401688n

Audier, M., Coulon, M., & Bonnetain, L. (1983a). Disproportionation of CO on iron-cobalt alloys—I : Thermodynamic study. *Carbon*, *21*(2), 93-97. https://doi.org/10.1016/0008-6223(83)90162-8

Audier, M., Coulon, M., & Bonnetain, L. (1983b). Disproportionation of CO on iron-cobalt alloys—II : Kinetic study on iron-cobalt alloys of different compositions. *Carbon*, *21*(2), 99-103. https://doi.org/10.1016/0008-6223(83)90163-X

Audier, M., Coulon, M., & Bonnetain, L. (1983c). Disproportionation of CO on iron-cobalt alloys—III : Kinetic laws of the carbon growth and catalyst fragmentation. *Carbon*, *21*(2), 105-110. https://doi.org/10.1016/0008-6223(83)90164-1

Audier, M., Coulon, M., & Oberlin, A. (1980). Relative crystallographic orientations of carbon and metal in a filamentous catalytic carbon. *Carbon*, *18*(1), 73-76. https://doi.org/10.1016/0008-6223(80)90080-9

Avdeeva, L. B., Reshetenko, T. V., Fenelonov, V. B., Chuvilin, A. L., & Ismagilov, Z. R. (2004). Gasification behavior of catalytic filamentous carbon. *Carbon*, *42*(12-13), 2501-2507. https://doi.org/10.1016/j.carbon.2004.05.049

Azara, A., Belbessai, S., & Abatzoglou, N. (2022). A review of filamentous carbon nanomaterial synthesis via catalytic conversion of waste plastic pyrolysis products. *Journal of Environmental Chemical Engineering*, *10*(1), 107049. https://doi.org/10.1016/j.jece.2021.107049

Azara, A., Benyoussef, E.-H., Mohellebi, F., Chamoumi, M., Gitzhofer, F., & Abatzoglou, N. (2019). Catalytic Dry Reforming and Cracking of Ethylene for Carbon Nanofilaments and Hydrogen Production Using a Catalyst Derived from a Mining Residue. *Catalysts*, *9*(12), 1069. https://doi.org/10.3390/catal9121069

Bahome, M. C., Jewell, L. L., Hildebrandt, D., Glasser, D., & Coville, N. J. (2005). Fischer–Tropsch synthesis over iron catalysts supported on carbon nanotubes. *Applied Catalysis A: General*, *287*(1), 60-67. https://doi.org/10.1016/j.apcata.2005.03.029

Bahome, M. C., Jewell, L. L., Padayachy, K., Hildebrandt, D., Glasser, D., Datye, A. K., & Coville, N. J. (2007). Fe-Ru small particle bimetallic catalysts supported on carbon

nanotubes for use in Fischer–Tröpsch synthesis. *Applied Catalysis A: General*, *328*(2), 243-251. https://doi.org/10.1016/j.apcata.2007.06.018

Bajad, G. S., Vijayakumar, R. P., Gupta, A. G., Jagtap, V., & Singh, Y. pal. (2017). Production of liquid hydrocarbons, carbon nanotubes and hydrogen rich gases from waste plastic in a multi-core reactor. *Journal of Analytical and Applied Pyrolysis*, *125*, 83-90. https://doi.org/10.1016/j.jaap.2017.04.016

Bajad, G., Vijayakumar, R. P., Rakhunde, P., Hete, A., & Bhade, M. (2017). Processing of mixed-plastic waste to fuel oil, carbon nanotubes and hydrogen using multi–core reactor. *Chemical Engineering and Processing: Process Intensification*, *121*, 205-214. https://doi.org/10.1016/j.cep.2017.09.011

Baker, R. T. K. (1989). Catalytic growth of carbon filaments. *Carbon*, *27*(3), 315-323. https://doi.org/10.1016/0008-6223(89)90062-6

Baker, R. T. K. (2016). Carbon Nanofibers. In *Reference Module in Materials Science and Materials Engineering*. Elsevier. https://doi.org/10.1016/B978-0-12-803581-8.02294-3

Baker, R. T. K., & Albright, L. F. (1983). *Coke Formation on Metal Surfaces,* (M. J. Comstock, Éd.; Vol. 202). American Chemical Society. https://doi.org/10.1021/bk-1983-0202.fw001

Baker, R. T. K., Alonzo, J. R., Dumesic, J. A., & Yates, D. J. C. (1982). Effect of the surface state of iron on filamentous carbon formation. *Journal of Catalysis*, *77*(1), 74-84. https://doi.org/10.1016/0021-9517(82)90148-8

Baker, R. T. K., Barber, M. A., Harris, P. S., Feates, F. S., & Waite, R. J. (1972). Nucleation and growth of carbon deposits from the nickel catalyzed decomposition of acetylene. *Journal of Catalysis*, *26*(1), 51-62. https://doi.org/10.1016/0021-9517(72)90032-2

Baker, R. T. K., Buschow, K. H. J., Cahn, R. W., Flemings, M. C., Ilschner, B., Kramer, E. J., Mahajan, S., & Veyssière, P. (2001). Carbon Nanofibers. In *Encyclopedia of Materials : Science and Technology* (p. 932-941). Elsevier. https://doi.org/10.1016/B0-08-043152-6/00178-9

Baker, R. T. K., Gadsby, G. R., Thomas, R. B., & Waite, R. J. (1975). The production and properties of filamentous carbon. *Carbon*, *13*(3), 211-214. https://doi.org/10.1016/0008-6223(75)90234-1

Baker, R. T. K., Harris, P. S., Thomas, R. B., & Waite, R. J. (1973). Formation of filamentous carbon from iron, cobalt and chromium catalyzed decomposition of acetylene. *Journal of Catalysis*, *30*, 86.

Bali, A., Blanchard, J., Chamoumi, M., & Abatzoglou, N. (2018). Bio-Oil Steam Reforming over a Mining Residue Functionalized with Ni as Catalyst : Ni-UGSO. *Catalysts (2073-4344)*, *8*(1), 1-24. https://doi.org/10.3390/catal8010001

Barbarias, I., Lopez, G., Artetxe, M., Arregi, A., Bilbao, J., & Olazar, M. (2018). Valorisation of different waste plastics by pyrolysis and in-line catalytic steam reforming for hydrogen production. *Energy Conversion and Management*, *156*, 575-584. https://doi.org/10.1016/j.enconman.2017.11.048

Bazargan, A., & McKay, G. (2012). A review – Synthesis of carbon nanotubes from plastic wastes. *Chemical Engineering Journal*, *195-196*, 377-391. https://doi.org/10.1016/j.cej.2012.03.077

Bezemer, G. L., Radstake, P. B., Koot, V., van Dillen, A. J., Geus, J. W., & de Jong, K. P. (2006). Preparation of Fischer–Tropsch cobalt catalysts supported on carbon

nanofibers and silica using homogeneous deposition-precipitation. *Journal of Catalysis*, *237*(2), 291-302. https://doi.org/10.1016/j.jcat.2005.11.015

Bhaskar, T., Uddin, M. A., Kaneko, J., Kusaba, T., Matsui, T., Muto, A., Sakata, Y., & Murata, K. (2003). Liquefaction of mixed plastics containing PVC and dechlorination by calcium-based sorbent. *Energy and Fuels*, *17*(1), 75-80. Scopus. https://doi.org/10.1021/ef020091g

Binhang, Y., Xiaofang, Y., Jie, W., Siyy, Y., MyatNeoZin, M., Elaine, G., Zhenhua, X., Shyam, K., Wenquian, X., & Jingguang G., C. (2016). *Dry Reforming of Ethane and Butane with CO2 over PtNi/CeO2 Bimetallic Catalysts*. ACS Catal. 6, 11, 7283-7292.

Bitter, J. H., van der Lee, M. K., Slotboom, A. G. T., van Dillen, A. J., & de Jong, K. P. (2003). Synthesis of Highly Loaded Highly Dispersed Nickel on Carbon Nanofibers by Homogeneous Deposition–Precipitation. *Catalysis Letters*, *89*(1), 139-142. https://doi.org/10.1023/A:1024744131630

Blanchard, J., Oudghiri-Hassani, H., Abatzoglou, N., Jankhah, S., & Gitzhofer, F. (2008). Synthesis of nanocarbons via ethanol dry reforming over a carbon steel catalyst. *Chemical Engineering Journal*, *143*(1), 186-194. https://doi.org/10.1016/j.cej.2008.04.012

Bockris, J. O. M. (2013). The hydrogen economy : Its history. *International Journal of Hydrogen Energy*, *38*(6), 2579-2588. https://doi.org/10.1016/j.ijhydene.2012.12.026

Boehm, H. P. (1973). Carbon from carbon monoxide disproportionation on nickel and iron catalysts : Morphological studies and possible growth mechanisms. *Carbon*, *11*(6), 583-590. https://doi.org/10.1016/0008-6223(73)90323-0

Borsodi, N., Szentes, A., Miskolczi, N., Wu, C., & Liu, X. (2016). Carbon nanotubes synthetized from gaseous products of waste polymer pyrolysis and their application. *Journal of Analytical and Applied Pyrolysis*, *120*, 304-313. https://doi.org/10.1016/j.jaap.2016.05.018

Braidy, N., Bastien, S., Blanchard, J., Fauteux-Lefebvre, C., Achouri, I. E., & Abatzoglou, N. (2017). Activation mechanism and microstructural evolution of a YSZ/Ni-alumina catalyst for dry reforming of methane. *Catalysis Today*, *291*, 99-105. https://doi.org/10.1016/j.cattod.2017.03.006

Breuer, O., & Sundararaj, U. (2004). Big returns from small fibers : A review of polymer/carbon nanotube composites. *Polymer Composites*, *25*(6), 630-645. Scopus. https://doi.org/10.1002/pc.20058

Cargnello, M., Doan-Nguyen, V. V. T., Gordon, T. R., Diaz, R. E., Stach, E. A., Gorte, R. J., Fornasiero, P., & Murray, C. B. (2013). Control of metal nanocrystal size reveals metal-support interface role for ceria catalysts. *Science (New York, N.Y.)*, *341*(6147), 771-773. https://doi.org/10.1126/science.1240148

Chambers, A., & Baker, R. T. K. (1997). Influence of Chlorine on the Decomposition of Ethylene over Iron and Cobalt Particles. *The Journal of Physical Chemistry B*, *101*(9), 1621-1630. https://doi.org/10.1021/jp963031i

Chambers, A., Rodriguez, N. M., & Baker, R. T. K. (1996). Influence of Silver Addition on the Catalytic Behavior of Cobalt. *The Journal of Physical Chemistry*, *100*(10), 4229-4236. https://doi.org/10.1021/jp9531570

Chamoumi, M., & Abatzoglou, N. (2016). NiFe2O4 production from α-Fe2O3 via improved solid state reaction : Application as catalyst in CH4 dry reforming. *The*

Canadian Journal of Chemical Engineering, *94*(9), 1801-1808. https://doi.org/10.1002/cjce.22561

Chamoumi, M., Abatzoglou, N., Blanchard, J., Iliuta, M.-C., & Larachi, F. (2017). Dry reforming of methane with a new catalyst derived from a negative value mining residue spinellized with nickel. *Catalysis Today*, *291*, 86-98. https://doi.org/10.1016/j.cattod.2017.02.018

Chen, J., Li, Y., Ma, Y., Qin, Y., & Chang, L. (2001). Formation of bamboo-shaped carbon filaments and dependence of their morphology on catalyst composition and reaction conditions. *Carbon*, *39*(10), 1467-1475. https://doi.org/10.1016/S0008-6223(00)00274-8

Chen, L., Xia, K., Huang, L., Li, L., Pei, L., & Fei, S. (2013). Facile synthesis and hydrogen storage application of nitrogen-doped carbon nanotubes with bamboo-like structure. *International Journal of Hydrogen Energy*, *38*(8), 3297-3303. https://doi.org/10.1016/j.ijhydene.2013.01.055

Chen, X., Wang, R., Xu, J., & Yu, D. (2004). TEM investigation on the growth mechanism of carbon nanotubes synthesized by hot-filament chemical vapor deposition. *Micron*, *35*(6), 455-460. https://doi.org/10.1016/j.micron.2004.02.006

Cheng, J., Zhang, X., Luo, Z., Liu, F., Ye, Y., Yin, W., Liu, W., & Han, Y. (2006). Carbon nanotube synthesis and parametric study using CaCO3 nanocrystals as catalyst support by CVD. *Materials Chemistry and Physics*, *95*(1), 5-11. https://doi.org/10.1016/j.matchemphys.2005.04.043

Chesnokov, V. V., & Buyanov, R. A. (2000). The formation of carbon filaments upon decomposition of hydrocarbons catalysed by iron subgroup metals and their alloys. *Russian Chemical Reviews*, *69*(7), 623-638. https://doi.org/10.1070/RC2000v069n07ABEH000540

Cheung, C. L., Kurtz, A., Park, H., & Lieber, C. M. (2002). Diameter-Controlled Synthesis of Carbon Nanotubes. *The Journal of Physical Chemistry B*, *106*(10), 2429-2433. https://doi.org/10.1021/jp0142278

Chitrapu, P., Lund, C. R. F., & Tsamopoulos, J. A. (1992). A model for the catalytic growth of carbon filaments. *Carbon*, *30*(2), 285-293. https://doi.org/10.1016/0008-6223(92)90091-A

Coleman, J. N., Khan, U., & Gun'ko, Y. K. (2006). Mechanical reinforcement of polymers using carbon nanotubes. *Advanced Materials*, *18*(6), 689-706. Scopus. https://doi.org/10.1002/adma.200501851

Couteau, E., Hernadi, K., Seo, J. W., Thiên-Nga, L., Mikó, Cs., Gaál, R., & Forró, L. (2003). CVD synthesis of high-purity multiwalled carbon nanotubes using CaCO3 catalyst support for large-scale production. *Chemical Physics Letters*, *378*(1), 9-17. https://doi.org/10.1016/S0009-2614(03)01218-1

Dai, H., Rinzler, A. G., Nikolaev, P., Thess, A., Colbert, D. T., & Smalley, R. E. (1996). Single-wall nanotubes produced by metal-catalyzed disproportionation of carbon monoxide. *Chemical Physics Letters*, *260*(3), 471-475. https://doi.org/10.1016/0009-2614(96)00862-7

David Moy, W., & Asif Chishti, L. (1998). *US Patent for Fibril aggregates and method for making same Patent* (Patent Nº 5,726,116).

Day, M., & Wiles, D. M. (1984). Influence of temperature and environment on the thermal decomposition of poly(ethylene terephthalate) fibres with and without the flame

retardant tris(2,3-dibromopropyl) phosphate. *Journal of Analytical and Applied Pyrolysis*, *7*(1), 65-82. https://doi.org/10.1016/0165-2370(84)80041-8
Dębek, R., Galvez, M. E., Launay, F., Motak, M., Grzybek, T., & Da Costa, P. (2016). Low temperature dry methane reforming over Ce, Zr and CeZr promoted Ni–Mg–Al hydrotalcite-derived catalysts. *International Journal of Hydrogen Energy*, *41*(27), 11616-11623. https://doi.org/10.1016/j.ijhydene.2016.02.074
DeLorme, M. P., Muro, Y., Arai, T., Banas, D. A., Frame, S. R., Reed, K. L., & Warheit, D. B. (2012). Ninety-Day Inhalation Toxicity Study With A Vapor Grown Carbon Nanofiber in Rats. *Toxicological Sciences*, *128*(2), 449-460. https://doi.org/10.1093/toxsci/kfs172
Desmaris, V., Saleem, M. A., & Shafiee, S. (2015). Examining Carbon Nanofibers : Properties, growth, and applications. *IEEE Nanotechnology Magazine*, *9*(2), 33-38. https://doi.org/10.1109/MNANO.2015.2409394
DeWhitt, K. C. (2012). *SYSTEMS AND METHODS FOR RECYCLING PLASTIC* (Patent Nº US8193403B2).
Díaz, M. C., Blackman, J. M., & Snape, C. E. (2008). Maximising carbon nanofiber and hydrogen production in the catalytic decomposition of ethylene over an unsupported Ni-Cu alloy. *Applied Catalysis A: General*, *339*(2), 196-208. https://doi.org/10.1016/j.apcata.2008.01.017
Drif, A., Bion, N., Brahmi, R., Ojala, S., Pirault-Roy, L., Turpeinen, E., Seelam, P. K., Keiski, R. L., & Epron, F. (2015). Study of the dry reforming of methane and ethanol using Rh catalysts supported on doped alumina. *Applied Catalysis A: General*, *504*, 576-584. https://doi.org/10.1016/j.apcata.2015.02.019
Dunlap, B. I. (1994). Relating carbon tubules. *Physical Review B*, *49*(8), 5643-5651. https://doi.org/10.1103/PhysRevB.49.5643
Dupuis, A.-C. (2005). The catalyst in the CCVD of carbon nanotubes—A review. *Progress in Materials Science*, *50*(8), 929-961. https://doi.org/10.1016/j.pmatsci.2005.04.003
El, K., Da, S., Ja, D., Wd, P., Le, M., Jgg, C., & Dj, B. (2008). The role of rhenium in the conversion of glycerol to synthesis gas over carbon supported platinum-rhenium catalysts. *Journal of Catalysis*, *260*(1), 164-177.
Endo, M., Kim, Y. A., Hayashi, T., Nishimura, K., Matusita, T., Miyashita, K., & Dresselhaus, M. S. (2001). Vapor-grown carbon fibers (VGCFs) : Basic properties and their battery applications. *Carbon*, *39*(9), 1287-1297. https://doi.org/10.1016/S0008-6223(00)00295-5
Endo, M., & Koyama, T. (1977). Growth mechanism and some properties of vapor-grown carbon fibers. *Solid State Physics*, 1-12.
Ermakova, M. A., Ermakov, D. Y., Chuvilin, A. L., & Kuvshinov, G. G. (2001). Decomposition of Methane over Iron Catalysts at the Range of Moderate Temperatures : The Influence of Structure of the Catalytic Systems and the Reaction Conditions on the Yield of Carbon and Morphology of Carbon Filaments. *Journal of Catalysis*, *201*(2), 183-197. https://doi.org/10.1006/jcat.2001.3243
Fakeeha, A. H., Ibrahim, A. A., Khan, W. U., Seshan, K., Al Otaibi, R. L., & Al-Fatesh, A. S. (2018). Hydrogen production via catalytic methane decomposition over alumina supported iron catalyst. *Arabian Journal of Chemistry*, *11*(3), 405-414. https://doi.org/10.1016/j.arabjc.2016.06.012

Fauteux-Lefebvre, C., Abatzoglou, N., Blais, S., Braidy, N., & Hu, Y. (2015). Iron oxide-functionalized carbon nanofilaments for hydrogen sulfide adsorption : The multiple roles of carbon. *Carbon*, *95*, 794-801. https://doi.org/10.1016/j.carbon.2015.08.117

Finegan, I. C., & Tibbetts, G. G. (2001). Electrical conductivity of vapor-grown carbon fiber/thermoplastic composites. *Journal of Materials Research*, *16*(6), 1668-1674. Scopus. https://doi.org/10.1557/JMR.2001.0231

Futaba, D. N., Goto, J., Yasuda, S., Yamada, T., Yumura, M., & Hata, K. (2009a). General Rules Governing the Highly Efficient Growth of Carbon Nanotubes. *Advanced Materials*, *21*(47), 4811-4815. https://doi.org/10.1002/adma.200901257

Futaba, D. N., Goto, J., Yasuda, S., Yamada, T., Yumura, M., & Hata, K. (2009b). A Background Level of Oxygen-Containing Aromatics for Synthetic Control of Carbon Nanotube Structure. *Journal of the American Chemical Society*, *131*(44), 15992-15993. https://doi.org/10.1021/ja906983r

Gavillet, J., Loiseau, A., Journet, C., Willaime, F., Ducastelle, F., & Charlier, J.-C. (2001). Root-Growth Mechanism for Single-Wall Carbon Nanotubes. *Physical Review Letters*, *87*(27), 275504. https://doi.org/10.1103/PhysRevLett.87.275504

Godini, H. R., Xiao, S., Kim, M., Görke, O., Song, S., & Wozny, G. (2013). Dual-membrane reactor for methane oxidative coupling and dry methane reforming : Reactor integration and process intensification. *Chemical Engineering and Processing: Process Intensification*, *74*, 153-164. https://doi.org/10.1016/j.cep.2013.09.007

Gong, J., Feng, J., Liu, J., Jiang, Z., Chen, X., Mijowska, E., Wen, X., & Tang, T. (2014). Catalytic carbonization of polypropylene into cup-stacked carbon nanotubes with high performances in adsorption of heavy metallic ions and organic dyes. *Chemical Engineering Journal*, *248*, 27-40. https://doi.org/10.1016/j.cej.2014.01.107

Gong, J., Liu, J., Jiang, Z., Chen, X., Wen, X., Mijowska, E., & Tang, T. (2015). New insights into the role of lattice oxygen in the catalytic carbonization of polypropylene into high value-added carbon nanomaterials. *New Journal of Chemistry*, *39*(2), 962-971. https://doi.org/10.1039/C4NJ01735H

Gong, J., Liu, J., Jiang, Z., Wen, X., Mijowska, E., Tang, T., & Chen, X. (2015). A facile approach to prepare porous cup-stacked carbon nanotube with high performance in adsorption of methylene blue. *Journal of Colloid and Interface Science*, *445*, 195-204. https://doi.org/10.1016/j.jcis.2014.12.078

Gong, J., Liu, J., Wan, D., Chen, X., Wen, X., Mijowska, E., Jiang, Z., Wang, Y., & Tang, T. (2012). Catalytic carbonization of polypropylene by the combined catalysis of activated carbon with Ni2O3 into carbon nanotubes and its mechanism. *Applied Catalysis A: General*, *449*, 112-120. https://doi.org/10.1016/j.apcata.2012.09.028

Guellati, O., Janowska, I., Bégin, D., Pham-Huu, C., Guerioune, M., Mekhalif, Z., Delhalle, J., Moldovan, S., & Ersen, O. (2012). Influence of ethanol in the presence of H2 on the catalytic growth of vertically aligned carbon nanotubes. *Applied Catalysis. A: General*, *423-424*, 7-14. https://doi.org/10.1016/j.apcata.2012.02.036

Hammer, L., Landskron, H., Nichtl-Pecher, W., Fricke, A., Heinz, K., & Müller, K. (1993). Hydrogen-induced restructuring of close-packed metal surfaces : H/Ni(111) and H/Fe(110). *Physical Review B*, *47*(23), 15969-15972. https://doi.org/10.1103/PhysRevB.47.15969

Hapipi, A. M., Suda, H., Uddin, A., & Kato, Y. (2018). Dechlorination of Polyvinyl Chloride under Superheated Steam with Catalysts and Adsorbents. *Energy & Fuels*, *32*, 7792-7799. https://doi.org/10.1021/acs.energyfuels.8b00838

Hossain, M. S., Tryk, D., & Yeager, E. (1989). The electrochemistry of graphite and modified graphite surfaces : The reduction of O2. *Electrochimica Acta*, *34*(12), 1733-1737. https://doi.org/10.1016/0013-4686(89)85057-1

Hou, P. X., Bai, S., Yang, Q. H., Liu, C., & Cheng, H. M. (2002). Multi-step purification of carbon nanotubes. *Carbon*, *40*(1), 81-85. https://doi.org/10.1016/S0008-6223(01)00075-6

Hu, X., & Lu, G. (2009). Syngas production by CO2 reforming of ethanol over Ni/Al2O3 catalyst. *Catalysis Communications*, *13*(10), 1633-1637. https://doi.org/10.1016/j.catcom.2009.04.030

Jankhah, S., Abatzoglou, N., & Gitzhofer, F. (2008). Thermal and catalytic dry reforming and cracking of ethanol for hydrogen and carbon nanofilaments' production. *International Journal of Hydrogen Energy*, *33*(18), 4769-4779. https://doi.org/10.1016/j.ijhydene.2008.06.058

Jankhah, S., Abatzoglou, N., Gitzhofer, F., Blanchard, J., & Oudghiri-Hassani, H. (2008). Catalytic properties of carbon nano-filaments produced by iron-catalysed reforming of ethanol. *Chemical Engineering Journal*, *139*(3), 532-539. https://doi.org/10.1016/j.cej.2007.08.031

Ji, L., Lin, Z., Medford, A. J., & Zhang, X. (2009). Porous carbon nanofibers from electrospun polyacrylonitrile/SiO2 composites as an energy storage material. *Carbon*, *47*(14), 3346-3354. https://doi.org/10.1016/j.carbon.2009.08.002

Jia, Z., Kou, K., Qin, M., Wu, H., Puleo, F., & Liotta, L. (2017). Controllable and Large-Scale Synthesis of Carbon Nanostructures : A Review on Bamboo-Like Nanotubes. *Catalysts*, *7*(9), 256. https://doi.org/10.3390/catal7090256

Jiang, K., Feng, C., Liu, K., & Fan, S. (2007). A vapor-liquid-solid model for chemical vapor deposition growth of carbon nanotubes. *Journal of Nanoscience and Nanotechnology*, *7*(4-5), 1494-1504. https://doi.org/10.1166/jnn.2007.332

Jourdain, V., Kanzow, H., Castignolles, M., Loiseau, A., & Bernier, P. (2002). Sequential catalytic growth of carbon nanotubes. *Chemical Physics Letters*, *364*(1), 27-33. https://doi.org/10.1016/S0009-2614(02)01309-X

Kaimal, V. K., & Vijayabalan, P. (2015). A detailed study of combustion characteristics of a DI diesel engine using waste plastic oil and its blends. *Energy Conversion and Management*, *105*, 951-956. https://doi.org/10.1016/j.enconman.2015.08.043

Kang, Z., Wang, E., Mao, B., Su, Z., Gao, L., Lian, S., & Xu, L. (2005). Controllable Fabrication of Carbon Nanotube and Nanobelt with a Polyoxometalate-Assisted Mild Hydrothermal Process. *Journal of the American Chemical Society*, *127*(18), 6534-6535. https://doi.org/10.1021/ja051228v

Karayıldırım, T., Yanık, J., Yüksel, M., Sağlam, M., & Haussmann, M. (2005). Degradation of PVC Containing Mixtures in the Presence of HCl Fixators. *Journal of Polymers and the Environment*, *13*(4), 365-374. https://doi.org/10.1007/s10924-005-5531-2

Kawaguchi, M., Nozaki, K., Motojima, S., & Iwanaga, H. (1992). A growth mechanism of regularly coiled carbon fibers through acetylene pyrolysis. *Journal of Crystal Growth*, *118*(3), 309-313. https://doi.org/10.1016/0022-0248(92)90077-V

Kaya, B., Irmak, S., Hasanoğlu, A., & Erbatur, O. (2015). Developing Pt based bimetallic and trimetallic carbon supported catalysts for aqueous-phase reforming of biomass-derived compounds. *International Journal of Hydrogen Energy*, *40*(10), 3849-3858. https://doi.org/10.1016/j.ijhydene.2015.01.131

Keith, J. M., Janda, N. B., King, J. A., Perger, W. F., & Oxby, T. J. (2005). Shielding effectiveness density theory for carbon fiber/nylon 6,6 composites. *Polymer Composites*, *26*(5), 671-678. Scopus. https://doi.org/10.1002/pc.20139

Kim, M. S., Rodriguez, N. M., & Baker, R. T. K. (1991). The interaction of hydrocarbons with copper-nickel and nickel in the formation of carbon filaments. *Journal of Catalysis*, *131*(1), 60-73. https://doi.org/10.1016/0021-9517(91)90323-V

Kim, M. S., Rodriguez, N. M., & Baker, R. T. K. (1992). The role of interfacial phenomena in the structure of carbon deposits. *Journal of Catalysis*, *134*(1), 253-268. https://doi.org/10.1016/0021-9517(92)90226-8

Kim, M. S., Rodriguez, N. M., & Baker, R. T. K. (1993). The Interplay Between Sulfur Adsorption and Carbon Deposition on Cobalt Catalysts. *Journal of Catalysis*, *143*(2), 449-463. https://doi.org/10.1006/jcat.1993.1289

Kim, P., Shi, L., Majumdar, A., & McEuen, P. L. (2001). Thermal Transport Measurements of Individual Multiwalled Nanotubes. *Physical Review Letters*, *87*(21), 215502. https://doi.org/10.1103/PhysRevLett.87.215502

Koestner, R. J., Frost, J. C., Stair, P. C., Van Hove, M. A., & Somorjai, G. A. (1982). Evidence for the formation of stable alkylidyne structures from C3 and C4 unsaturated hydrocarbons adsorbed on the Pt(111) single crystal surface. *Surface Science*, *116*(1), 85-103. https://doi.org/10.1016/0039-6028(82)90680-X

Krishnankutty, N., Rodriguez, N. M., & Baker, R. T. K. (1996). Effect of Copper on the Decomposition of Ethylene over an Iron Catalyst. *Journal of Catalysis*, *158*(1), 217-227. https://doi.org/10.1006/jcat.1996.0021

Krivoruchko, O. P., & Zaikovskii, V. I. (1998). Formation of Liquid Phase in the Carbon-Metal System at Unusually Low Temperature. *Kinetics and Catalysis*, *39*(4). https://www.elibrary.ru/item.asp?id=13304186

Krylov, O. V., Mamedov, A. Kh., & Mirzabekova, S. R. (1995). Oxidation of Hydrocarbons and Alcohols by Carbon Dioxide on Oxide Catalysts. *Industrial & Engineering Chemistry Research*, *34*(2), 474-482. https://doi.org/10.1021/ie00041a007

Kunwar, B., Cheng, H. N., Chandrashekaran, S. R., & Sharma, B. K. (2016). Plastics to fuel : A review. *Renewable and Sustainable Energy Reviews*, *54*, 421-428. https://doi.org/10.1016/j.rser.2015.10.015

Lai, M., Li, J., Yang, J., Liu, J., Tong, X., & Cheng, H. (2004). The morphology and thermal properties of multi-walled carbon nanotube and poly(hydroxybutyrate-co-hydroxyvalerate) composite. *Polymer International*, *53*(10), 1479-1484. https://doi.org/10.1002/pi.1566

Lamouroux, E., Serp, P., & Kalck, P. (2007). Catalytic Routes Towards Single Wall Carbon Nanotubes. *Catalysis Reviews*, *49*(3), 341-405. https://doi.org/10.1080/01614940701313200

Lamouroux, E., Serp, P., Kihn, Y., & Kalck, P. (2007). Identification of key parameters for the selective growth of single or double wall carbon nanotubes on FeMo/Al2O3 CVD catalysts. *Applied Catalysis A: General*, *323*, 162-173. https://doi.org/10.1016/j.apcata.2007.02.019

Lander, J. J., Kern, H. E., & Beach, A. L. (1952). Solubility and Diffusion Coefficient of Carbon in Nickel : Reaction Rates of Nickel-Carbon Alloys with Barium Oxide. *Journal of Applied Physics*, *23*(12), 1305-1309. https://doi.org/10.1063/1.1702064

Lee, B., Lee, S., & Lim, H. (2016). Numerical modeling studies for a methane dry reforming in a membrane reactor. *Journal of Natural Gas Science and Engineering*, *34*, 1251-1261. https://doi.org/10.1016/j.jngse.2016.08.019

Lee, S., Yoshida, K., & Yoshikawa, K. (2015). Application of Waste Plastic Pyrolysis Oil in a Direct Injection Diesel Engine : For a Small Scale Non-Grid Electrification. *Energy and Environment Research*, *5*(1), p18. https://doi.org/10.5539/eer.v5n1p18

Leturia, M., & Saleh, K. (2014). *Fluidisation gaz-solide—Bases et théorie*. Techniques de l'ingénieur.

Li, H., Li, J., & Gu, C. (2005). Local field emission from individual vertical carbon nanofibers grown on tungsten filament. *Carbon*, *43*(4), 849-853. https://doi.org/10.1016/j.carbon.2004.11.021

Li, Y., Chen, J., Ma, Y., Zhao, J., Qin, Y., & Chang, L. (1999). Formation of bamboo-like nanocarbon and evidence for the quasi-liquid state of nanosized metal particles at moderate temperatures. *Chemical Communications*, *12*, 1141-1142. https://doi.org/10.1039/A902281C

Li, Y., Li, D., & Wang, G. (2011). Methane decomposition to COx-free hydrogen and nano-carbon material on group 8–10 base metal catalysts : A review. *Catalysis Today*, *162*(1), 1-48. https://doi.org/10.1016/j.cattod.2010.12.042

Li, Y., Liu, J., Wang, Y., & Wang, Z. L. (2001). Preparation of Monodispersed Fe−Mo Nanoparticles as the Catalyst for CVD Synthesis of Carbon Nanotubes. *Chemistry of Materials*, *13*(3), 1008-1014. https://doi.org/10.1021/cm000787s

Liu, J., Jiang, Z., Yu, H., & Tang, T. (2011). Catalytic pyrolysis of polypropylene to synthesize carbon nanotubes and hydrogen through a two-stage process. *Polymer Degradation and Stability*, *96*(10), 1711-1719. https://doi.org/10.1016/j.polymdegradstab.2011.08.008

Liu, W.-W., Aziz, A., Chai, S.-P., Mohamed, A. R., & Hashim, U. (2013, juin 27). *Synthesis of Single-Walled Carbon Nanotubes : Effects of Active Metals, Catalyst Supports, and Metal Loading Percentage* [Research Article]. Journal of Nanomaterials; Hindawi. https://doi.org/10.1155/2013/592464

Liu, X., Shen, B., Wu, Z., Parlett, C. M. A., Han, Z., George, A., Yuan, P., Patel, D., & Wu, C. (2018). Producing carbon nanotubes from thermochemical conversion of waste plastics using Ni/ceramic based catalyst. *Chemical Engineering Science*, *192*, 882-891. https://doi.org/10.1016/j.ces.2018.07.047

Liu, X., Zhang, Y., Nahil, M. A., Williams, P. T., & Wu, C. (2017). Development of Ni- and Fe- based catalysts with different metal particle sizes for the production of carbon nanotubes and hydrogen from thermo-chemical conversion of waste plastics. *Journal of Analytical and Applied Pyrolysis*, *125*, 32-39. https://doi.org/10.1016/j.jaap.2017.05.001

Loiseau, A., Gavillet, J., Ducastelle, F., Thibault, J., Stéphan, O., Bernier, P., & Thair, S. (2003). Nucleation and growth of SWNT : TEM studies of the role of the catalyst. *Comptes Rendus Physique*, *4*(9), 975-991. https://doi.org/10.1016/j.crhy.2003.10.022

López, A., Marco, I. De, Caballero, B. M., Laresgoiti, M. F., & Adrados, A. (2011). Dechlorination of fuels in pyrolysis of PVC containing plastic wastes. *Fuel*

Processing Technology, *92*(2), 253-260. https://doi.org/10.1016/j.fuproc.2010.05.008
Lopez, G., Artetxe, M., Amutio, M., Alvarez, J., Bilbao, J., & Olazar, M. (2018). Recent advances in the gasification of waste plastics. A critical overview. *Renewable and Sustainable Energy Reviews*, *82*, 576-596. https://doi.org/10.1016/j.rser.2017.09.032
Lopez, G., Cortazar, M., Alvarez, J., Amutio, M., Bilbao, J., & Olazar, M. (2017). Assessment of a conical spouted with an enhanced fountain bed for biomass gasification. *Fuel*, *203*, 825-831. https://doi.org/10.1016/j.fuel.2017.05.014
Lu, C., & Liu, J. (2006). Controlling the Diameter of Carbon Nanotubes in Chemical Vapor Deposition Method by Carbon Feeding. *The Journal of Physical Chemistry B*, *110*(41), 20254-20257. https://doi.org/10.1021/jp0632283
Luo, J. Z., Yu, Z. L., Ng, C. F., & Au, C. T. (2000). CO2/CH4 Reforming over Ni–La2O3/5A : An Investigation on Carbon Deposition and Reaction Steps. *Journal of Catalysis*, *194*(2), 198-210. https://doi.org/10.1006/jcat.2000.2941
Martin-Gullon, I., Vera, J., Conesa, J. A., González, J. L., & Merino, C. (2006). Differences between carbon nanofibers produced using Fe and Ni catalysts in a floating catalyst reactor. *Carbon*, *44*(8), 1572-1580. https://doi.org/10.1016/j.carbon.2005.12.027
Mestl, G., Maksimova, N. I., Keller, N., Roddatis, V. V., & Schlögl, R. (2001). Carbon Nanofilaments in Heterogeneous Catalysis : An Industrial Application for New Carbon Materials? *Angewandte Chemie International Edition*, *40*(11), 2066-2068. https://doi.org/10.1002/1521-3773(20010601)40:11<2066::AID-ANIE2066>3.0.CO;2-I
Miandad, R., Barakat, M. A., Aburiazaiza, A. S., Rehan, M., Ismail, I. M. I., & Nizami, A. S. (2017). Effect of plastic waste types on pyrolysis liquid oil. *International Biodeterioration & Biodegradation*, *119*, 239-252. https://doi.org/10.1016/j.ibiod.2016.09.017
Milne, B. J., Behie, L. A., & Berruti, F. (1999). Recycling of waste plastics by ultrapyrolysis using an internally circulating fluidized bed reactor. *Journal of Analytical and Applied Pyrolysis*, *51*(1), 157-166. https://doi.org/10.1016/S0165-2370(99)00014-5
Milne, B. J., Berruti, F., Behie, L. A., & De Bruijn, T. J. W. (1992). The internally circulating fluidized bed (ICFB) : A novel solution to gas bypassing in spouted beds. *The Canadian Journal of Chemical Engineering*, *70*(5), 910-915. https://doi.org/10.1002/cjce.5450700512
Ministère. (2020). - *Règlement sur la santé et la sécurité du travail*. LégisQuébec. http://www.legisquebec.gouv.qc.ca/fr/showdoc/cr/S-2.1,%20r.%2013
Moisala, A., Nasibulin, A., & Kauppinen, E. (2003). The role of metal nanoparticles in the catalytic production of single-walled carbon nanotubes : A review. *Journal of Physics: Condensed Matter*, *15*(42), S3011-S3035. https://doi.org/10.1088/0953-8984/15/42/003
Monthioux, M., Noé, L., Dussault, L., Dupin, J.-C., Latorre, N., Ubieto, T., Romeo, E., Royo, C., Monzón, A., & Guimon, C. (2007). Texturising and structurising mechanisms of carbon nanofilaments during growth. *Journal of Materials Chemistry*, *17*(43), 4611-4618. https://doi.org/10.1039/B707742D
Moo, J. G. S., Veksha, A., Oh, W.-D., Giannis, A., Udayanga, W. D. C., Lin, S.-X., Ge, L., & Lisak, G. (2019). Plastic derived carbon nanotubes for electrocatalytic oxygen

reduction reaction : Effects of plastic feedstock and synthesis temperature. *Electrochemistry Communications*, *101*, 11-18. https://doi.org/10.1016/j.elecom.2019.02.014

Müller, K. (1993). Hydrogen-induced reconstruction of transition metal surfaces. *Progress in Surface Science*, *42*(1), 245-255. https://doi.org/10.1016/0079-6816(93)90073-5

Múnera, J., Irusta, S., Cornaglia, L., & Lombardo, E. (2003). CO2 reforming of methane as a source of hydrogen using a membrane reactor. *Applied Catalysis A: General*, *245*(2), 383-395. https://doi.org/10.1016/S0926-860X(02)00640-3

Nahil, M. A., Wu, C., & Williams, P. T. (2015). Influence of metal addition to Ni-based catalysts for the co-production of carbon nanotubes and hydrogen from the thermal processing of waste polypropylene. *Fuel Processing Technology*, *130*, 46-53. https://doi.org/10.1016/j.fuproc.2014.09.022

Nakagawa, K., Nishitani-Gamo, M., Ogawa, K., & Ando, T. (2005). Catalytic growth of carbon nanofilament in liquid hydrocarbon. *Catalysis Letters*, *101*(3-4), 191-194. https://doi.org/10.1007/s10562-005-4890-6

Narkiewicz, U., Podsiadły, M., Jędrzejewski, R., & Pełech, I. (2010). Catalytic decomposition of hydrocarbons on cobalt, nickel and iron catalysts to obtain carbon nanomaterials. *Applied Catalysis A: General*, *384*(1), 27-35. https://doi.org/10.1016/j.apcata.2010.05.050

National Institute for Occupational Safety and Health. (2018). *Current intelligence bulletin 65 : Occupational exposure to carbon nanotubes and nanofibers*. Consulté 20 avril 2020, à l'adresse https://www.cdc.gov/niosh/docs/2013-145/default.html

Nguyen, H. N. T., Berguerand, N., & Thunman, H. (2016). Mechanism and Kinetic Modeling of Catalytic Upgrading of a Biomass-Derived Raw Gas : An Application with Ilmenite as Catalyst. *Industrial & Engineering Chemistry Research*, *55*(20), 5843-5853. https://doi.org/10.1021/acs.iecr.6b00650

Nishibata, H., Uddin, A., & Kato, Y. (2020). Simultaneous degradation and dechlorination of poly (vinyl chloride) by a combination of superheated steam and CaO catalyst/adsorbent. *Polymer Degradation and Stability*, *179*, 109-225. https://doi.org/10.1016/j.polymdegradstab.2020.109225

Nolan, P. E., Lynch, D. C., & Cutler, A. H. (1998). Carbon Deposition and Hydrocarbon Formation on Group VIII Metal Catalysts. *The Journal of Physical Chemistry B*, *102*(21), 4165-4175. https://doi.org/10.1021/jp980996o

Oberlin, A., Endo, M., & Koyama, T. (1976). Filamentous growth of carbon through benzene decomposition. *Journal of Crystal Growth*, *32*(3), 335-349. https://doi.org/10.1016/0022-0248(76)90115-9

Panahi, A., Wei, Z., Song, G., & Levendis, Y. A. (2019). Influence of Stainless-Steel Catalyst Substrate Type and Pretreatment on Growing Carbon Nanotubes from Waste Postconsumer Plastics. *Industrial & Engineering Chemistry Research*, *58*(8), 3009-3023. https://doi.org/10.1021/acs.iecr.8b05770

Pang, L. S. K., Saxby, J. D., & Chatfield, S. P. (1993). Thermogravimetric analysis of carbon nanotubes and nanoparticles. *The Journal of Physical Chemistry*, *97*(27), 6941-6942. https://doi.org/10.1021/j100129a001

Park, C., & Baker, R. T. K. (2000). Carbon Deposition on Iron–Nickel During Interaction with Ethylene–Carbon Monoxide–Hydrogen Mixtures. *Journal of Catalysis*, *190*(1), 104-117. https://doi.org/10.1006/jcat.1999.2735

Pinilla, J. L., de Llobet, S., Moliner, R., & Suelves, I. (2017). Ni-Co bimetallic catalysts for the simultaneous production of carbon nanofibres and syngas through biogas decomposition. *Applied Catalysis B: Environmental*, *200*, 255-264. https://doi.org/10.1016/j.apcatb.2016.07.015

Pinilla, J. L., Lázaro, M. J., Suelves, I., Moliner, R., & Palacios, J. M. (2010). Characterization of nanofibrous carbon produced at pilot-scale in a fluidized bed reactor by methane decomposition. *Chemical Engineering Journal*, *156*(1), 170-176. https://doi.org/10.1016/j.cej.2009.10.032

Pinilla, J. L., Moliner, R., Suelves, I., Lázaro, M. J., Echegoyen, Y., & Palacios, J. M. (2007). Production of hydrogen and carbon nanofibers by thermal decomposition of methane using metal catalysts in a fluidized bed reactor. *International Journal of Hydrogen Energy*, *32*(18), 4821-4829. https://doi.org/10.1016/j.ijhydene.2007.08.013

Pinilla, J. L., Utrilla, R., Lázaro, M. J., Moliner, R., Suelves, I., & García, A. B. (2011). Ni- and Fe-based catalysts for hydrogen and carbon nanofilament production by catalytic decomposition of methane in a rotary bed reactor. *Fuel Processing Technology*, *92*(8), 1480-1488. https://doi.org/10.1016/j.fuproc.2011.03.009

Pinilla, J. L., Utrilla, R., Lázaro, M. J., Suelves, I., Moliner, R., & M. Palacios, J. (2009). A novel rotary reactor configuration for simultaneous production of hydrogen and carbon nanofibers. *International Journal of Hydrogen Energy*, *34*, 8016-8022. https://doi.org/10.1016/j.ijhydene.2009.07.057

Pirard, S. L., Delafosse, A., Toye, D., & Pirard, J.-P. (2013). Modeling of a continuous rotary reactor for carbon nanotube synthesis by catalytic chemical vapor deposition : Influence of heat exchanges and temperature profile. *Chemical Engineering Journal*, *232*, 488-494. https://doi.org/10.1016/j.cej.2013.07.077

Plastics. (2021). American Chemistry Council. Consulté 25 septembre 2021, à l'adresse https://www.americanchemistry.com/chemistry-in-america/chemistry-in-everyday-products/plastics

Pradhan, D., & Sharon, M. (2002). Carbon nanotubes, nanofilaments and nanobeads by thermal chemical vapor deposition process. *Materials Science and Engineering: B*, *96*(1), 24-28. https://doi.org/10.1016/S0921-5107(02)00309-4

Pyrograf®-III. (2018). Patented Pyrograf Products. Consulté 1 mai 2018, à l'adresse https://apsci.com/products/pyrograf/

Raghubanshi, H., & Dikio, E. D. (2015). Synthesis of Helical Carbon Fibers and Related Materials : A Review on the Past and Recent Developments. *Nanomaterials*, *5*(2), 937-968. https://doi.org/10.3390/nano5020937

Ramachandran, C. N., & Sathyamurthy, N. (2006). Introducing a twist in carbon nanotubes. *Current Science*, *91*(11), 1503-1505.

Reyniers, M.-F. S. G., & Froment, G. F. (1995). Influence of Metal Surface and Sulfur Addition on Coke Deposition in the Thermal Cracking of Hydrocarbons. *Industrial & Engineering Chemistry Research*, *34*(3), 773-785. https://doi.org/10.1021/ie00042a009

Rodriguez, N. M. (1993). A review of catalytically grown carbon nanofibers. *Journal of Materials Research*, *8*(12), 3233-3250. https://doi.org/10.1557/JMR.1993.3233

Rodriguez, N. M., Chambers, A., & Baker, R. T. K. (1995). Catalytic Engineering of Carbon Nanostructures. *Langmuir*, *11*(10), 3862-3866. https://doi.org/10.1021/la00010a042

Romero, A., Garrido, A., Nieto-Márquez, A., Sánchez, P., Lucas, A. de, & Valverde, J. L. (2008). Synthesis and structural characteristics of highly graphitized carbon nanofibers produced from the catalytic decomposition of ethylene : Influence of the active metal (Co, Ni, Fe) and the zeolite type support. *Microporous and Mesoporous Materials*, *110*(2), 318-329. https://doi.org/10.1016/j.micromeso.2007.06.031

Rostrup-Nielsen, J. R. (1984). Catalytic Steam Reforming. In J. R. Anderson & M. Boudart (Éds.), *Catalysis : Science and Technology Volume 5* (p. 1-117). Springer. https://doi.org/10.1007/978-3-642-93247-2_1

Saad, J. M., Nahil, M. A., & Williams, P. T. (2015). Influence of process conditions on syngas production from the thermal processing of waste high density polyethylene. *Journal of Analytical and Applied Pyrolysis*, *113*, 35-40. http://dx.doi.org/10.1016/j.jaap.2014.09.027

Saad, J. M., Nahil, M. A., Wu, C., & Williams, P. T. (2015). Influence of nickel-based catalysts on syngas production from carbon dioxide reforming of waste high density polyethylene. *Fuel Processing Technology*, *138*, 156-163. https://doi.org/10.1016/j.fuproc.2015.05.020

Sacco, A., Thacker, P., Chang, T. N., & Chiang, A. T. S. (1984). The initiation and growth of filamentous carbon from α-iron in H2, CH4, H2O, CO2, and CO gas mixtures. *Journal of Catalysis*, *85*(1), 224-236. https://doi.org/10.1016/0021-9517(84)90125-8

Schaper, A. K., Hou, H., Greiner, A., & Phillipp, F. (2004). The role of iron carbide in multiwalled carbon nanotube growth. *Journal of Catalysis*, *222*(1), 250-254. https://doi.org/10.1016/j.jcat.2003.11.011

Scheirs, J. (2006). Overview of commercial pyrolysis processes for waste plastics. In J. Scheirs & W. Kaminsky (Éds.), *Feedstock recycling and pyrolysis of waste plastics* (p. 381-433). John Wiley & Sons.

Serp, P., Corrias, M., & Kalck, P. (2003). Carbon nanotubes and nanofibers in catalysis. *Applied Catalysis A: General*, *253*(2), 337-358. https://doi.org/10.1016/S0926-860X(03)00549-0

Setton, R., & Setton, N. (1997). Carbon nanotubes : III. Toroidal structures and limits of a model for the construction of helical and S-shaped nanotubes. *Carbon*, *35*(4), 497-505. https://doi.org/10.1016/S0008-6223(97)83726-8

Shaffer, M. S. P., & Windle, A. H. (1999). Fabrication and characterization of carbon nanotube/poly(vinyl alcohol) composites. *Advanced Materials*, *11*(11), 937-941. Scopus. https://doi.org/10.1002/(SICI)1521-4095(199908)11:11<937::AID-ADMA937>3.0.CO;2-9

Shah, K. A., & Tali, B. A. (2016). Synthesis of carbon nanotubes by catalytic chemical vapour deposition : A review on carbon sources, catalysts and substrates. *Materials Science in Semiconductor Processing*, *41*, 67-82. https://doi.org/10.1016/j.mssp.2015.08.013

Shah, Y. T., & Gardner, T. H. (2014). Dry Reforming of Hydrocarbon Feedstocks. *Catalysis Reviews*, *56*(4), 476-536. https://doi.org/10.1080/01614940.2014.946848

Shaikjee, A., & Coville, N. J. (2012). The synthesis, properties and uses of carbon materials with helical morphology. *Journal of Advanced Research*, *3*(3), 195-223. https://doi.org/10.1016/j.jare.2011.05.007

Shen, Y., & Lua, A. C. (2015). Synthesis of Ni and Ni–Cu supported on carbon nanotubes for hydrogen and carbon production by catalytic decomposition of methane. *Applied Catalysis B: Environmental*, *164*, 61-69. https://doi.org/10.1016/j.apcatb.2014.08.038

Shvedova, A. A., Kisin, E., Murray, A. R., Johnson, V. J., Gorelik, O., Arepalli, S., Hubbs, A. F., Mercer, R. R., Keohavong, P., Sussman, N., Jin, J., Yin, J., Stone, S., Chen, B. T., Deye, G., Maynard, A., Castranova, V., Baron, P. A., & Kagan, V. E. (2008). Inhalation vs. aspiration of single-walled carbon nanotubes in C57BL/6 mice : Inflammation, fibrosis, oxidative stress, and mutagenesis. *American Journal of Physiology-Lung Cellular and Molecular Physiology*, *295*(4), L552-L565. https://doi.org/10.1152/ajplung.90287.2008

Siew, K. W., Lee, H. C., Khan, M. R., Gimbun, J., & Cheng, C. K. (2015). CO2 reforming of glycerol over La-Ni/Al2O3 catalyst : A longevity evaluative study. *Journal of Energy Chemistry*, *24*(3), 366-373. https://doi.org/10.1016/S2095-4956(15)60324-2

CCHST. (2020). *Poussières combustibles : Réponses SST*. Consulté 10 mai 2020, à l'adresse https://www.cchst.ca/oshanswers/chemicals/combustible_dust.html

Sui, Y. C., Acosta, D. R., González-León, J. A., Bermúdez, A., Feuchtwanger, J., Cui, B. Z., Flores, J. O., & Saniger, J. M. (2001). Structure, Thermal Stability, and Deformation of Multibranched Carbon Nanotubes Synthesized by CVD in the AAO Template. *The Journal of Physical Chemistry B*, *105*(8), 1523-1527. https://doi.org/10.1021/jp002408o

Sumrunronnasak, S., Tantayanon, S., Kiatgamolchai, S., & Sukonket, T. (2016). Improved hydrogen production from dry reforming reaction using a catalytic packed-bed membrane reactor with Ni-based catalyst and dense PdAgCu alloy membrane. *International Journal of Hydrogen Energy*, *41*(4), 2621-2630. https://doi.org/10.1016/j.ijhydene.2015.10.129

Sundaresan, S. (2013). Role of hydrodynamics on chemical reactor performance. *Current Opinion in Chemical Engineering*, *2*(3), 325-330. https://doi.org/10.1016/j.coche.2013.06.003

Sutkar, V. S., Deen, N. G., & Kuipers, J. A. M. (2013). Spout fluidized beds : Recent advances in experimental and numerical studies. *Chemical Engineering Science*, *86*, 124-136. https://doi.org/10.1016/j.ces.2012.06.022

Svinterikos, E., & Zuburtikudis, I. (2016). Carbon nanofibers from renewable bioresources (lignin) and a recycled commodity polymer [poly(ethylene terephthalate)]. *Journal of Applied Polymer Science*, *133*(37). https://doi.org/10.1002/app.43936

Syamsiro, M., Saptoadi, H., Norsujianto, T., Noviasri, P., Cheng, S., Alimuddin, Z., & Yoshikawa, K. (2014). Fuel Oil Production from Municipal Plastic Wastes in Sequential Pyrolysis and Catalytic Reforming Reactors. *Energy Procedia*, *47*, 180-188. https://doi.org/10.1016/j.egypro.2014.01.212

Takehira, K., Ohi, T., Shishido, T., Kawabata, T., & Takaki, K. (2005). Catalytic growth of carbon fibers from methane and ethylene on carbon-supported Ni catalysts. *Applied Catalysis A: General*, *283*(1), 137-145. https://doi.org/10.1016/j.apcata.2004.12.044

Tang, Y., & Luo, W. (2018). Synthesis And Characterization Of Bamboo-like Multi-walled Carbon Nanotubes By Alcohothermal Process. *IOP Conference Series: Earth and Environmental Science*, *186*, 012058. https://doi.org/10.1088/1755-1315/186/2/012058

Tao, X. Y., Zhang, X. B., Zhang, L., Cheng, J. P., Liu, F., Luo, J. H., Luo, Z. Q., & Geise, H. J. (2006). Synthesis of multi-branched porous carbon nanofibers and their application in electrochemical double-layer capacitors. *Carbon*, *44*(8), 1425-1428. https://doi.org/10.1016/j.carbon.2005.11.024

Teo, K., Singh, C., Chhowalla, M., & Milne, W. I. (2003). Catalytic synthesis of carbon nanotubes and nanofibers. *Encyclopedia of Nanoscience and Nanotechnology*, *10*(1), 1-22. https://scholar.google.ca/scholar?q=Catalytic+synthesis+of+carbon+nanotubes+and+nanofibers&hl=fr&as_sdt=0&as_vis=1&oi=scholart

Teunou, E., & Poncelet, D. (2002). Batch and continuous fluid bed coating – review and state of the art. *Journal of Food Engineering*, *53*(4), 325-340. https://doi.org/10.1016/S0260-8774(01)00173-X

Tibbetts, G. G., Lake, M. L., Strong, K. L., & Rice, B. P. (2007). A review of the fabrication and properties of vapor-grown carbon nanofiber/polymer composites. *Composites Science and Technology*, *67*(7-8), 1709-1718. Scopus. https://doi.org/10.1016/j.compscitech.2006.06.015

Ting, J.-M., & Liu, R.-M. (2003). Carbon nanowires with new microstructures. *Carbon*, *41*(3), 601-603. https://doi.org/10.1016/S0008-6223(02)00394-9

Torres, D., Pinilla, J. L., Lázaro, M. J., Moliner, R., & Suelves, I. (2014). Hydrogen and multiwall carbon nanotubes production by catalytic decomposition of methane : Thermogravimetric analysis and scaling-up of Fe–Mo catalysts. *International Journal of Hydrogen Energy*, *39*(8), 3698-3709. https://doi.org/10.1016/j.ijhydene.2013.12.127

Ugarte, P., Durán, P., Lasobras, J., Soler, J., Menéndez, M., & Herguido, J. (2017). Dry reforming of biogas in fluidized bed : Process intensification. *International Journal of Hydrogen Energy*, *42*(19), 13589-13597. https://doi.org/10.1016/j.ijhydene.2016.12.124

Veksha, A., Giannis, A., & Chang, V. W.-C. (2017). Conversion of non-condensable pyrolysis gases from plastics into carbon nanomaterials : Effects of feedstock and temperature. *Journal of Analytical and Applied Pyrolysis*, *124*, 16-24. https://doi.org/10.1016/j.jaap.2017.03.005

Veksha, A., Giannis, A., Oh, W.-D., Chang, V. W.-C., & Lisak, G. (2018). Upgrading of non-condensable pyrolysis gas from mixed plastics through catalytic decomposition and dechlorination. *Fuel Processing Technology*, *170*, 13-20. https://doi.org/10.1016/j.fuproc.2017.10.019

Vincent, C. (2008). *Le composite cuivre / nanofires de carbone* [Thèse de doctorat]. Université Sciences et Technologies, Bordeaux 1, 157.

Vinciguerra, V., Buonocore, F., Panzera, G., & Occhipinti, L. (2003). Growth mechanisms in chemical vapour deposited carbon nanotubes. *Nanotechnology*, *14*(6), 655-660. https://doi.org/10.1088/0957-4484/14/6/317

Wagner, R. S., & Ellis, W. C. (1964). Vapor-liquid-solid mechanism of single crystal growth. *Applied Physics Letters*, *4*(5), 89-90. https://doi.org/10.1063/1.1753975

Wampler, T. P. (1989). Thermometric behavior of polyolefins. *Journal of Analytical and Applied Pyrolysis*, *15*, 187-195. https://doi.org/10.1016/0165-2370(89)85032-6

Wang, P., Xiao, P., Zhong, S., Chen, J., Lin, H., & Wu, X.-L. (2016). Bamboo-like carbon nanotubes derived from colloidal polymer nanoplates for efficient removal of

bisphenol A. *Journal of Materials Chemistry A*, *4*(40), 15450-15456. https://doi.org/10.1039/C6TA06971A

Wei, Z., Sun, J., Li, Y., Datye, A. K., & Wang, Y. (2012). Bimetallic catalysts for hydrogen generation. *Chemical Society Reviews*, *41*(24), 7994-8008. https://doi.org/10.1039/C2CS35201J

Weinberg, F. J., Bartleet, T. G., Carleton, F. B., Rimbotti, P., Brophy, J. H., & Manning, R. P. (1988). Partial oxidation of fuel-rich mixtures in a spouted bed combustor. *Combustion and Flame*, *72*(3), 235-239. https://doi.org/10.1016/0010-2180(88)90124-1

Wen, X., Chen, X., Tian, N., Gong, J., Liu, J., Rümmeli, M. H., Chu, P. K., Mijiwska, E., & Tang, T. (2014). Nanosized Carbon Black Combined with Ni2O3 as "Universal" Catalysts for Synergistically Catalyzing Carbonization of Polyolefin Wastes to Synthesize Carbon Nanotubes and Application for Supercapacitors. *Environmental Science & Technology*, *48*(7), 4048-4055. https://doi.org/10.1021/es404646e

Winey, K. I., & Vaia, R. A. (2007). Polymer Nanocomposites. *MRS Bulletin*, *32*(4), 314-322. https://doi.org/10.1557/mrs2007.229

Wiśniewski, M., Terzyk, A. P., Gauden, P. A., Kaneko, K., & Hattori, Y. (2012). Removal of internal caps during hydrothermal treatment of bamboo-like carbon nanotubes and application of tubes in phenol adsorption. *Journal of Colloid and Interface Science*, *381*(1), 36-42. https://doi.org/10.1016/j.jcis.2012.05.036

Wu, C., Nahil, M. A., Miskolczi, N., Huang, J., & Williams, P. T. (2014). Processing Real-World Waste Plastics by Pyrolysis-Reforming for Hydrogen and High-Value Carbon Nanotubes. *Environmental Science & Technology*, *48*(1), 819-826. https://doi.org/10.1021/es402488b

Wu, C., Nahil, M. A., Miskolczi, N., Huang, J., & Williams, P. T. (2016). Production and application of carbon nanotubes, as a co-product of hydrogen from the pyrolysis-catalytic reforming of waste plastic. *Process Safety and Environmental Protection*, *103*, 107-114. https://doi.org/10.1016/j.psep.2016.07.001

Wu, C., & Williams, P. T. (2010a). Pyrolysis–gasification of post-consumer municipal solid plastic waste for hydrogen production. *International Journal of Hydrogen Energy*, *35*(3), 949-957. https://doi.org/10.1016/j.ijhydene.2009.11.045

Wu, C., & Williams, P. T. (2010b). Pyrolysis–gasification of plastics, mixed plastics and real-world plastic waste with and without Ni–Mg–Al catalyst. *Fuel*, *89*(10), 3022-3032. https://doi.org/10.1016/j.fuel.2010.05.032

Wurster, D. E. (1966). *Particle coating process* (United States Patent Nº US3253944A). https://patents.google.com/patent/US3253944A/en

Xie, X.-L., Mai, Y.-W., & Zhou, X.-P. (2005). Dispersion and alignment of carbon nanotubes in polymer matrix : A review. *Materials Science and Engineering R: Reports*, *49*(4), 89-112. Scopus. https://doi.org/10.1016/j.mser.2005.04.002

Xu, X., Tan, H., Xi, K., Ding, S., Yu, D., Cheng, S., Yang, G., Peng, X., Fakeeh, A., & Kumar, R. V. (2015). Bamboo-like amorphous carbon nanotubes clad in ultrathin nickel oxide nanosheets for lithium-ion battery electrodes with long cycle life. *Carbon*, *84*, 491-499. https://doi.org/10.1016/j.carbon.2014.12.040

Xu, Y.-Q., Flor, E., Schmidt, H., Smalley, R. E., & Hauge, R. H. (2006). Effects of atomic hydrogen and active carbon species in 1mm vertically aligned single-walled carbon nanotube growth. *Applied Physics Letters*, *89*(12), 123116. https://doi.org/10.1063/1.2349280

Yang, R. T., & Chen, J. P. (1989). Mechanism of carbon filament growth on metal catalysts. *Journal of Catalysis*, *115*(1), 52-64. https://doi.org/10.1016/0021-9517(89)90006-7

Yang, R.-X., Chuang, K.-H., & Wey, M.-Y. (2015). Effects of Nickel Species on Ni/Al2O3 Catalysts in Carbon Nanotube and Hydrogen Production by Waste Plastic Gasification : Bench- and Pilot-Scale Tests. *Energy and Fuels*, *29*(12), 8178-8187. https://doi.org/10.1021/acs.energyfuels.5b01866

Yao, D., & Wang, C.-H. (2020). Pyrolysis and in-line catalytic decomposition of polypropylene to carbon nanomaterials and hydrogen over Fe- and Ni-based catalysts. *Applied Energy*, *265*, 114819. https://doi.org/10.1016/j.apenergy.2020.114819

Yao, D., Wu, C., Yang, H., Zhang, Y., Nahil, M. A., Chen, Y., Williams, P. T., & Chen, H. (2017). Co-production of hydrogen and carbon nanotubes from catalytic pyrolysis of waste plastics on Ni-Fe bimetallic catalyst. *Energy Conversion and Management*, *148*, 692-700. https://doi.org/10.1016/j.enconman.2017.06.012

Yao, D., Yang, H., Chen, H., & Williams, P. T. (2018). Investigation of nickel-impregnated zeolite catalysts for hydrogen/syngas production from the catalytic reforming of waste polyethylene. *Applied Catalysis B: Environmental*, *227*, 477-487. https://doi.org/10.1016/j.apcatb.2018.01.050

Yao, D., Zhang, Y., Williams, P. T., Yang, H., & Chen, H. (2018). Co-production of hydrogen and carbon nanotubes from real-world waste plastics : Influence of catalyst composition and operational parameters. *Applied Catalysis B: Environmental*, *221*, 584-597. https://doi.org/10.1016/j.apcatb.2017.09.035

Yoon, S. H., Park, C. W., Yang, H., Korai, Y., Mochida, I., Baker, R. T. K., & Rodriguez, N. M. (2004). Novel carbon nanofibers of high graphitization as anodic materials for lithium ion secondary batteries. *Carbon*, *42*(1), 21-32. https://doi.org/10.1016/j.carbon.2003.09.021

Yoshida, H., Shimizu, T., Uchiyama, T., Kohno, H., Homma, Y., & Takeda, S. (2009). Atomic-Scale Analysis on the Role of Molybdenum in Iron-Catalyzed Carbon Nanotube Growth. *Nano Letters*, *9*(11), 3810-3815. https://doi.org/10.1021/nl9019903

Yu, Z., Chen, D., Tøtdal, B., & Holmen, A. (2005). Parametric study of carbon nanofiber growth by catalytic ethylene decomposition on hydrotalcite derived catalysts. *Materials Chemistry and Physics*, *92*(1), 71-81. https://doi.org/10.1016/j.matchemphys.2004.12.032

Zeng, J., Saltysiak, B., Johnson, W. S., Schiraldi, D. A., & Kumar, S. (2004). Processing and properties of poly(methyl methacrylate)/carbon nano fiber composites. *Composites Part B: Engineering*, *35*(2), 173-178. https://doi.org/10.1016/S1359-8368(03)00051-9

Zhang, Y., Nahil, M. A., Wu, C., & Williams, P. T. (2017). Pyrolysis–catalysis of waste plastic using a nickel–stainless-steel mesh catalyst for high-value carbon products. *Environmental Technology*, *38*(22), 2889-2897. https://doi.org/10.1080/09593330.2017.1281351

Zheng, G.-B., Kouda, K., Sano, H., Uchiyama, Y., Shi, Y.-F., & Quan, H.-J. (2004). A model for the structure and growth of carbon nanofibers synthesized by the CVD method using nickel as a catalyst. *Carbon*, *42*(3), 635-640. https://doi.org/10.1016/j.carbon.2003.12.077

Zhou, Q., Tang, C., Wang, Y.-Z., & Zheng, L. (2004). Catalytic degradation and dechlorination of PVC-containing mixed plastics via Al–Mg composite oxide catalysts. *Fuel*, *83*(13), 1727-1732. https://doi.org/10.1016/j.fuel.2004.02.015

Zhu, X.-Y., & White, J. M. (1989). Interaction of ethylene and acetylene with Ni(111) : A SSIMS study. *Surface Science*, *214*(1), 240-256. https://doi.org/10.1016/0039-6028(89)90421-4

Zhuo, C., Wang, X., Nowak, W., & Levendis, Y. A. (2014). Oxidative heat treatment of 316L stainless steel for effective catalytic growth of carbon nanotubes. *Applied Surface Science*, *313*, 227-236. https://doi.org/10.1016/j.apsusc.2014.05.189

ANNEXE A

ANNEXE A DIMENSIONNEMENT DU RÉACTEUR

Un rappel sur la fluidisation et les équations utilisées pour le dimensionnement du réacteur sont présentés dans ce qui suit :

A.1. Phénomène de fluidisation

La fluidisation consiste à faire passer verticalement et vers le haut, à une vitesse superficielle U, un fluide (gaz ou liquide) à travers un lit de particules reposant sur une grille horizontale située au fond d'une colonne afin de mettre en suspension ces particules. Avec l'augmentation progressive du débit de fluide, on réalise que pour les plus faibles vitesses, la couche de solide reste sur la grille sans mouvements visibles, les particules forment un lit fixe. A partir d'une certaine vitesse, les forces de frottement deviennent suffisantes pour équilibrer le poids du solide par unité d'aire de section droite, la couche de particules se dilate légèrement mais le lit reste fixe : c'est le point initial de fluidisation. La vitesse correspondante est désignée par la vitesse minimale de fluidisation U_{mf}.

Il existe plusieurs types de configurations de réacteur a lit fluidisé telles que : les réacteurs de craquage catalytique fluide (FCC), les réacteurs à lit jaillissant (SBR) (Weinberg et al., 1988) et SPR avec un tube d'aspiration à l'intérieur (*draft tube*) qui sont également appelés : Wurster (Teunou & Poncelet, 2002).

A.2. Régimes de fluidisation

Selon la vitesse de fluidisation et la nature des particules solides, on peut observer différents régimes de fluidisation présentés sur la Figure A. 1. Pour une vitesse inférieure à U_{mf}, le lit reste fixe et conserve son aspect compact. La perte de charge due aux frottements avec la surface des grains reste inférieure au poids du lit rapporté à la section droite de la colonne et augmente avec l'augmentation de la vitesse du gaz. À la U_{mf} , le poids des particules est précisément compensé par ces forces de frottement, les particules bougent légèrement et se mettent en suspension. La porosité et la hauteur du lit augmentent légèrement: c'est le début de la fluidisation.

À une vitesse légèrement supérieure à U_{mf}, la formation de bulles a lieu. La vitesse superficielle de gaz à partir de laquelle ces bulles apparaissent est appelée vitesse minimale de bullage et est notée U_{mb}. Il s'agit du régime de fluidisation bouillonnante. Au fur et à mesure que la vitesse augmente encore, les bulles qui montent fusionneront et grossiront, et la taille des bulles peut devenir presque la même que le diamètre du lit, c'est ce qu'on appelle le pistonnage. L'écoulement est sous forme de bouchons fluides et est accompagné de larges fluctuations de la perte de pression. Si le débit de gaz est suffisamment élevé, la surface supérieure du lit disparaît et, au lieu de bulles, on observe un mouvement turbulent d'amas solides et de vides de gaz de tailles et de formes variées. Il s'agit du régime de fluidisation turbulente. Lorsque la vitesse terminale de chute libre des particules (U_t) est dépassée, le lit devient entraîné et on a un lit fluidisé en phase diluée dispersée, ce qui revient à un transport pneumatique de solides. On appelle ce régime le lit transporté. Il est également possible de récupérer les particules dans des dispositifs annexes (cyclones) afin de les réintroduire dans le lit fluidisé. On parle alors de lit fluidisé circulant.

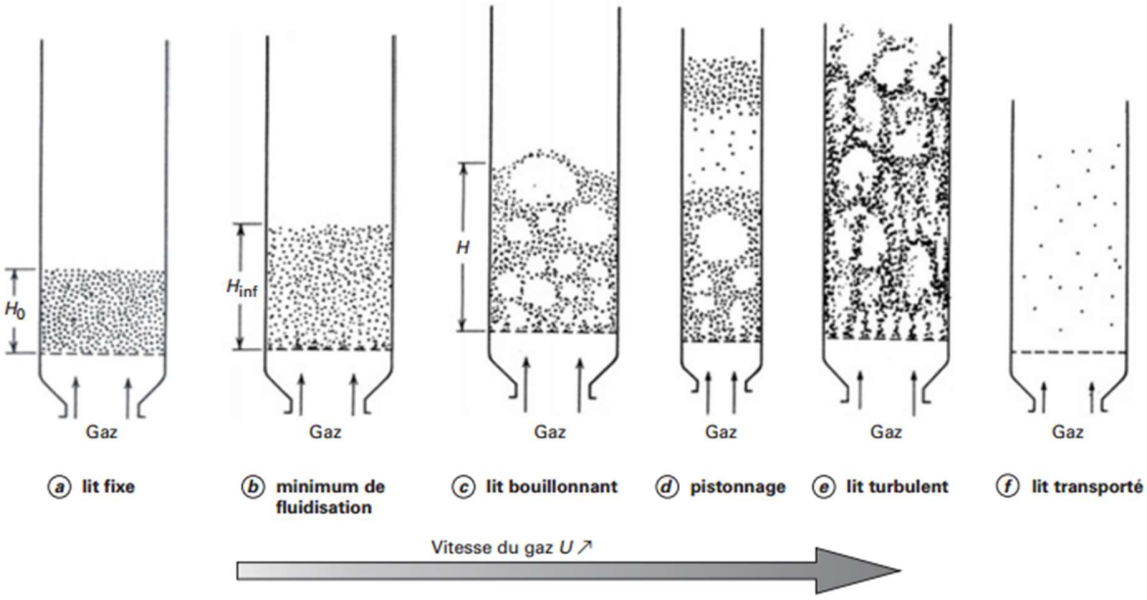

Figure A. 1 Différents régimes de fluidisation (Leturia & Saleh, 2014).

L'Évolution de la perte de charge d'un lit fluidisé en fonction de la vitesse du gaz est présentée dans la Figure A. 2.

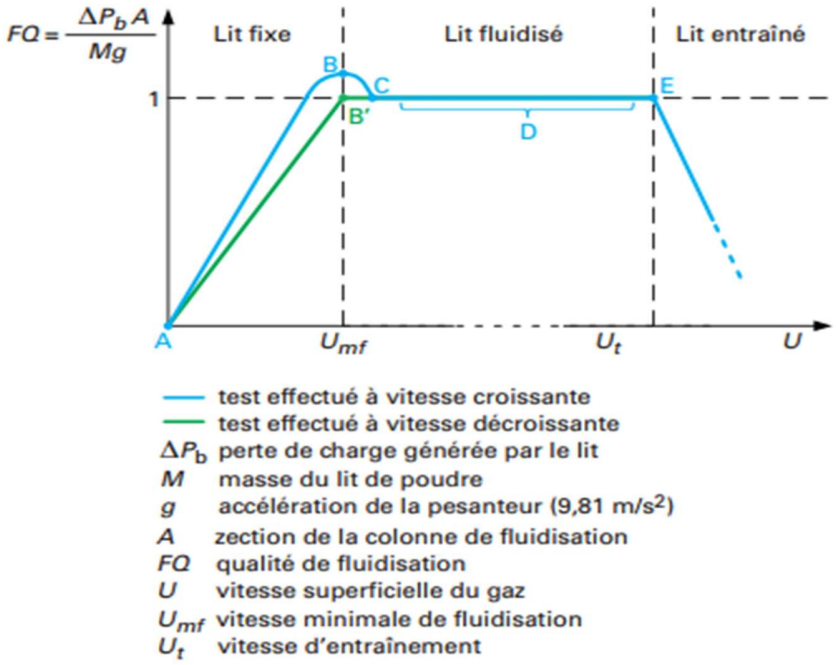

Figure A. 2 Perte de charge d'un lit fluidisé (Leturia & Saleh, 2014).

ABC : correspond à la perte de charge du lit fixe, pour une vitesse inférieure à U_{mf}, la perte de charge augmente avec la vitesse du gaz, elle obéit à la relation d'Ergun.

$$\frac{\Delta P}{Z} = 150\,\frac{(1-\varepsilon)^2}{\varepsilon^3}\,\frac{\mu_f\, U}{(d_p\,\Psi)^2} + 1{,}75\,\frac{(1-\varepsilon)}{\varepsilon^3}\,\frac{\rho_f\, U^2}{(d_p\,\Psi)} \qquad \text{(A. 1)}$$

ΔP : perte de charge

Z : hauteur du lit

ε : porosité du lit

μ_f : viscosité du gaz

d_p: $diamètre\ des\ particules$

U : vitesse du gaz

ρ_f : masse volumique du gaz

CDE : Lorsque $U = U_{mf}$, la perte de charge devient égale au poids du lit par unité d'aire de section droite Ω. Ensuite, cette perte de charge reste constante et égale au poids du lit sur une large plage de vitesses comprises entre U_{mf} et U_t .

$$\Delta P = \frac{poid\ de\ la\ couche\ de\ particules}{section\ deroite\ du\ lit} \qquad \text{(A. 2)}$$

Cependant, la porosité et la hauteur du lit augmentent avec le débit.

Les forces exercées sur la couche de particules (ρ_s) en suspension homogène dans le fluide (ρ_f , μ_f) sont les suivantes :

Poids du solide :

$$\rho_s(1-\varepsilon)\Omega\, Z\, g \qquad \text{(A. 3)}$$

Poussée d'Archimède :

$$\rho_f(1-\varepsilon)\Omega\, Z\, g \qquad \text{(A. 4)}$$

Forces de pression :

$$\Delta P\ \Omega \qquad \text{(A. 5)}$$

Bilan de force :

$$\rho_f(1-\varepsilon)\Omega\, Z\, g + \Delta P\ \Omega - \rho_s(1-\varepsilon)\Omega\, Z\, g = 0$$

$$\frac{\Delta P}{Z} = \left(\rho_s - \rho_f\right)(1-\varepsilon)\, g \qquad \text{(A. 6)}$$

E : au fur et à mesure de l'envol des particules qui quittent le réacteur, la perte de charge diminue jusqu'à atteindre une valeur correspondant à un écoulement de gaz dans un fût vide.

A.3. Zones présentes dans le lit fluidisé

Le lit fluidisé est divisé généralement en deux zones, une zone dense et une zone de désengagement comme montré dans Figure A. 3.

La couche fluidisée qui contient la majorité du solide représente la zone dense et le zone située entre la surface du lit dense et la sortie du courant gazeux correspond à la zone de désengagement appelée *freebord.* Dans cette zone, la concentration du solide est d'autant plus grande que le régime de fluidisation est turbulent et diminue de façon exponentielle avec la hauteur jusqu'à une valeur limite ou la concentration du solide reste constante, c'est la hauteur limite de désengagement TDH (*Transport Disengaging Height*). Pour des vitesses de gaz relativement élevées, la surface supérieure du lit s'estompe et devient floue. L'espace surmontant la surface du lit dense est alors caractérisé par une diminution rapide de la concentration en solide. Cette région est appelée *splash zone*.

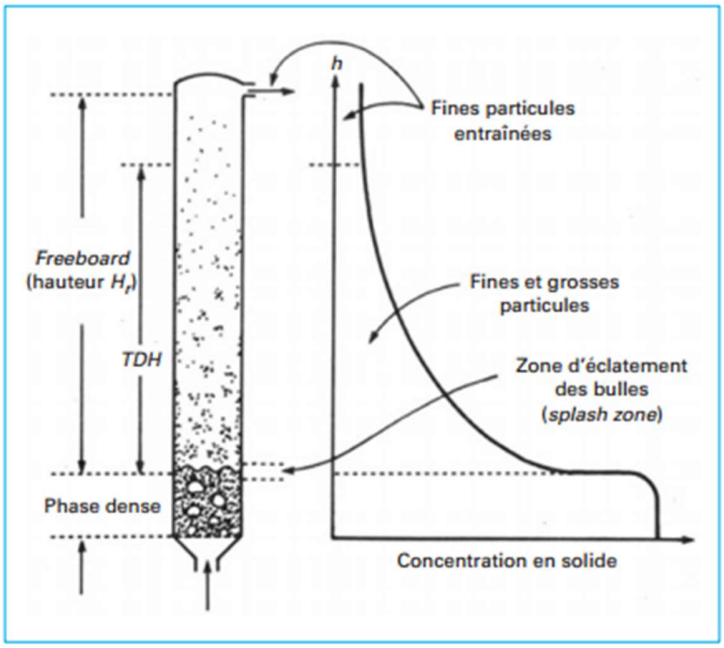

Figure A. 3 Différentes zones présentes dans un lit fluidisé (Leturia & Saleh, 2014).

L'éjection des particules de la phase dense vers le *freeboard* est directement liée à l'éclatement des bulles à la surface du lit. La littérature fait état de trois mécanismes principaux :

- L'éjection des particules situées à la surface du lit au moment de l'éclatement d'une bulle (Figure A. 4-a)
- L'éjection des particules transportées dans le sillage d'une bulle isolée (Figure A. 4-b) ;
- L'éjection des particules transportées dans le sillage de deux bulles qui coalescent au moment où elles arrivent à la surface du lit (Figure A. 4-c)

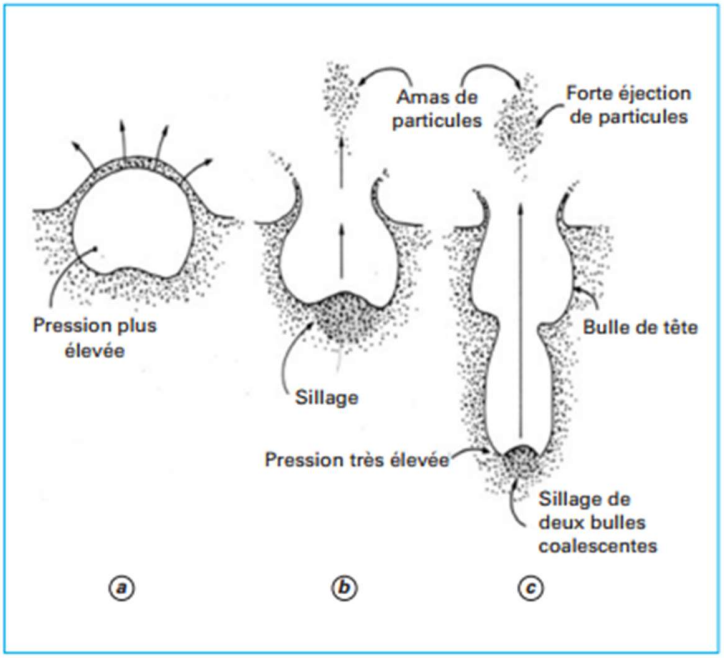

Figure A. 4 Mécanismes d'éjection des particules de la phase dense vers le *freeboard* (Leturia & Saleh, 2014).

A.4. Calcul de de la vitesse minimale de fluidisation

La vitesse minimale de fluidisation est un des paramètres essentiels pour caractériser le phénomène de fluidisation. Cette caractéristique qui marque la transition entre l'état fixe et l'état fluidisé du lit peut être déterminée en mesurant les pertes de charge totale à travers le lit fluidisé à débit décroissant.
Le minimum de fluidisation est défini comme étant le point d'intersection entre la droite linéaire correspondant au lit fixe et le palier constant correspondant au lit fluidisé (Figure A. 2).

Au niveau du minimum de fluidisation, la perte de charge est donnée par ces deux équations :

$$\frac{\Delta P}{Z_{mf}} = \left(\rho_s - \rho_f\right)(1 - \varepsilon_{mf}) \qquad \text{(A. 7)}$$

$$\frac{\Delta P}{Z_{mf}} = 150\,\frac{(1-\varepsilon_{mf})^2}{\varepsilon^3{}_{mf}}\,\frac{\mu_f\, U_{mf}}{(d_p\,\Psi)^2} + 1{,}75\,\frac{(1-\varepsilon)}{\varepsilon^3{}_{mf}}\,\frac{\rho_f\, {U_{mf}}^2}{(d_p\,\Psi)} \qquad \text{(A. 8)}$$

En réarrangeant ces deux équations on trouve :

$$Ar = 150\,\frac{(1-\varepsilon_{mf})}{\varepsilon^3{}_{mf}\,\Psi^2}\,Re_{mf} + 1{,}75\,\frac{1}{\varepsilon^3{}_{mf}\,\Psi}\,{Re_{mf}}^2 \qquad \text{(A. 9)}$$

Tels que :

$$Ar = \frac{\rho_f\,(\rho_s - \rho_f)\,g\,d_p^3}{\mu^2} \qquad \text{(A. 10)}$$

$$Re_{mf} = \frac{\rho_f\ U_{mf}\ d_p}{\mu} \qquad \text{(A. 11)}$$

Ar : nombre d'Archimède

Re_{mf} : nombre de Reynolds au minimum de fluidisation

ε_{mf} : porosité du lit au minimum de fluidisation, et pour la calculer, la corrélation (A.12) est utilisée :

$$\varepsilon_{mf} = 0{,}586 * \psi - 0{,}72 * \left(\frac{{\mu_f}^2}{\rho_f\,\eta\,dp^3}\right)^{0{,}029} * \left(\frac{\rho_f}{\rho_s}\right)^{0{,}021} \qquad \text{(A. 12)}$$

Il est possible de résoudre l'équation (A.9) (équation du second degré en Re_{mf}) afin de calculer la vitesse minimale de fluidisation U_{mf}.

A.5. Vitesse maximale de fluidisation ou vitesse terminale de chute libre

Les particules peuvent être entraînées par le gaz et quitter le lit fluidisé si la vitesse du gaz est supérieure à U_t de ces particules. U_t correspond à la vitesse limite de gaz à laquelle la force de traînée compense exactement le poids apparent de la particule.

Poids du solide :

$$\rho_s\,V_s\,g \qquad \text{(A. 13)}$$

Poussée d'Archimède :

$$\rho_f V_s\,g \qquad \text{(A. 14)}$$

Force de trainée :

$$\frac{1}{2}\,\rho_f\,U_t^2\,(A\,f) \qquad \text{(A. 15)}$$

Bilan des forces

$$\Sigma\,F = 0$$

$$P - F_A - F_T = 0$$

$$\rho_s\,V_s\ g - \rho_f\,V_s\,g - \frac{1}{2}\,\rho_f\,U_t^2\,(A\,f) = 0$$

$$\rho_s\,\frac{1}{6}\,\pi\,d_p^3\,g - \rho_s\,\frac{1}{6}\,\pi\,d_p^3\,g - \frac{1}{2}\,\rho_f\,U_t^2\,(\frac{1}{4}\,\pi\,d_p^2\,f) = 0$$

$$U_t{}^2 = \frac{4}{3}\,\mathrm{g}\,\mathrm{d_p}\,\frac{(\rho_p - \rho_f)}{\rho_f}\,\frac{1}{f} \qquad \text{(A. 16)}$$

$$\eta = g\left(\rho_p - \rho_f\right) \qquad \text{(A. 17)}$$

$$Ut^2 = \frac{4}{3} d_p \frac{\eta}{\rho_f} \frac{1}{f} \qquad \text{(A. 18)}$$

Le coefficient de friction f (également appelé coefficient de trainée C_D) dépend du régime d'écoulement (Tableau A. 1).

Tableau A. 1 Différentes formules de f selon le régime (Leturia & Saleh, 2014).

Régime	Laminaire, loi de Stokes	Intermédiaire d'Allen	Turbulent, loi de Newton
Re_t	<0,3	0,3< Re_t <500	500< Re_t <2×10^5
f	$\frac{24}{Re_t}$	$\frac{24}{Re_t}(1 + 0{,}15Re_t^{0{,}687})$	0,44

Re_t : nombre de Reynolds aux conditions d'entrainement.

A.6. Régime bouillonnant

Selon la théorie des deux phases, la zone dense d'un lit fluidisé en régime bouillonnant comporte deux phases distinctes comme montré dans la Figure A. 5:

- La phase émulsion qui comporte les particules solides et le gaz interstitiel circulant à U_{mf}, le taux de vide reste égal celui au minimum de fluidisation.
- La phase bulle qui correspond au débit de gaz en excès par rapport au minimum de fluidisation.

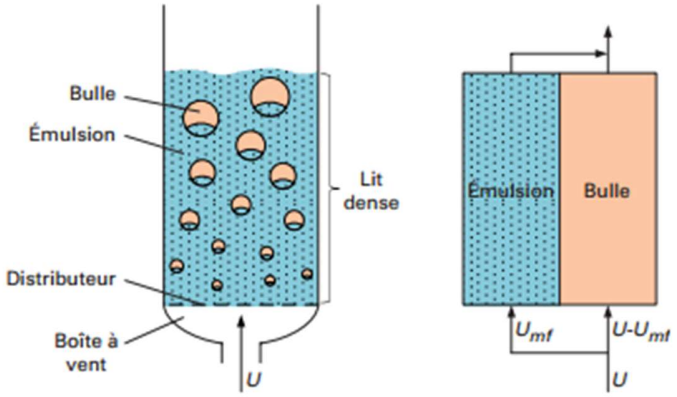

Figure A. 5 Lit fluidisé en régime bouillonnant- théorie des deux phases (Leturia & Saleh, 2014).

La taille des bulles (d_b) augmente au fur et à mesure que les bulles s'élèvent dans le lit et sa valeur initiale dépend du type de distributeur. De nombreuses corrélations sont proposées dans la littérature pour calculer le diamètre moyen des bulles sur une section droite du lit.

La corrélation de Darton donnée par l'équation (A.19) calcule le diamètre des bulles de fluide d_b à une hauteur h du lit (Leturia & Saleh, 2014):

$$d_b(cm) = \frac{0{,}54(U_0 - U_{minf})^{0,4}(HL + 4\sqrt{5{,}52.10^{-5}})}{g^{0,2}} \qquad \text{(A. 19)}$$

La vitesse d'ascension des bulles (U_b) dépend de leur taille, elle est plus élevée quand le diamètre des bulles est plus grand. Elle peut être calculée en utilisant plusieurs corrélations. La plus utilisée est la corrélation de Davidson et Harrison (Leturia & Saleh, 2014), équation A.20.:

$$U_b = U_0 - U_{mf} + (0{,}711)(g d_b)^{1/2} \qquad \text{(A. 20)}$$

A.7. Étapes de calcul

Contraintes

- La vitesse du gaz dans le cylindre central doit être entre 3 et 5 fois la vitesse minimale de fluidisation.
- Le débit total Q doit être inférieur à 250L/min.
- La vitesse à la sortie doit être maintenue inferieure a 2m/s.
- Le débit dans le cylindre extérieur doit donner une vitesse inférieure à celle de fluidisation.
- La perte de charge dans le cylindre externe ΔP_{ext} est égale la somme de la perte de charge dans le cylindre interne ΔP_{int} et la perte de charge de la transition entre le cylindre interne et la sortie du réacteur $\Delta P_{transit}$.

Données

- Diamètre des particules d_p (m)
- Masse volumique du gaz ρ_f (kg.m^{-3})
- Masse volumique du solide en ρ_s (kg.m^{-3})
- Masse du catalyseur W (kg)
- Viscosité du gaz en μ_f (kg·m^{-1}·s^{-1})
- Porosité du lit au repos ε
- Sphéricité

Calcul de la vitesse minimale de fluidisation

Le minimum de fluidisation est donné par les équations de (A.7) à (A.12).

La résolution de l'équation (A.9) qui est une équation de second degré donne Re_{mf}, aboutit à :

$$U_{mf} = \frac{Re_{minf} * \mu_f}{\rho_f * d_p} \qquad \text{(A. 21)}$$

Calcul de la vitesse maximale de fluidisation

U_t est donnée par l'équation (A.18). Le coefficient de friction f est considéré en régime turbulent.

Choix de U_0, Q, Q_1 et Q_2

La vitesse choisie doit être comprise entre $\mathbf{U_{mf} < U_0 < U_t}$.

Le régime de bullage est remarqué à une vitesse légèrement supérieure à U_{mf}, soit 3 à 4 fois U_{mf}.
Un choix initial de partage de débit est fait, et réitéré jusqu'à satisfaire la contrainte d'égalité des pertes de pression.

$$Q_1 = x\,Q \qquad \text{(A. 22)}$$

$$Q_2 = y\,Q \qquad \text{(A. 23)}$$

Calcul du diamètre

Pour calculer le diamètre, on a utilisé les relations suivantes :

$$A_{CI} = \frac{Q_{int}}{U_0} = \frac{\pi\, {D_{CI}}^2}{4} \qquad \text{(A. 24)}$$

$$D_{CI} = \left(\frac{4\,Q_{int}}{\pi \times U_0}\right)^{0,5} \qquad \text{(A. 25)}$$

Calcul de la hauteur du cylindre interne

La hauteur totale du lit en régime bouillonnant est égale à la somme de la hauteur de la phase dense HL et la hauteur de la zone de désengagement TDH. Pour que les particules puissent jaillir, il faut que la hauteur du cylindre interne soit inférieure à la hauteur totale du lit en régime bouillonnant, c'est-à-dire inférieure à la somme HL + TDH.

- Calcul du HL

La hauteur de la phase dense est pratiquement égale à la hauteur du lit au minimum de fluidisation

$$(Z_{mf}\,A_c)\,(1-\varepsilon_{minf})\,\rho_s = W \qquad \text{(A. 26)}$$

$$HL = Z_{mf} = \frac{W}{A_c\,(1-\varepsilon_{minf})\rho_s} \qquad \text{(A. 27)}$$

- Calcul du TDH

En ce qui concerne le désengagement, les équations de (A.19) et (A.20) sont utilisées pour le calcul de d_b et U_b.

Enfin, la hauteur de désengagement TDH se calcule par la relation de Baron :

$$TDH = 0{,}22\,{U_b}^2 \qquad \text{(A. 28)}$$

Calcul de la perte de charge dans le cylindre interne

Après le minimum de fluidisation, la perte de charge reste constante et est donnée par l'équation (A.8).

Calcul de la perte de charge de transition entre le cylindre interne et la sortie du réacteur et la perte de charge vers la sortie

ΔP_{ext} et $\Delta P_{transit}$ peuvent être aussi calculées en utilisant l'équation d'Ergun.

$$\frac{\Delta P_{ext}}{L_{1a}} = 150\,\frac{(1-\varepsilon_{mf})^2}{\varepsilon^3_{mf}}\,\frac{\mu_f\, U_1}{(d_p\,\Psi)^2} + 1{,}75\,\frac{(1-\varepsilon)}{\varepsilon^3_{mf}}\,\frac{\rho_f\, {U_1}^2}{(d_p\,\Psi)} \qquad \text{(A. 29)}$$

$$\frac{\Delta P_{transit}}{L_{3a}} = 150\,\frac{(1-\varepsilon_{mf})^2}{\varepsilon^3_{mf}}\,\frac{\mu_f\, U_3}{(d_p\,\Psi)^2} + 1{,}75\,\frac{(1-\varepsilon_{mf})}{\varepsilon^3_{mf}}\,\frac{\rho_f\, {U_3}^2}{(d_p\,\Psi)} \qquad \text{(A. 30)}$$

- Calcul du L_{1a} et L_{3a}

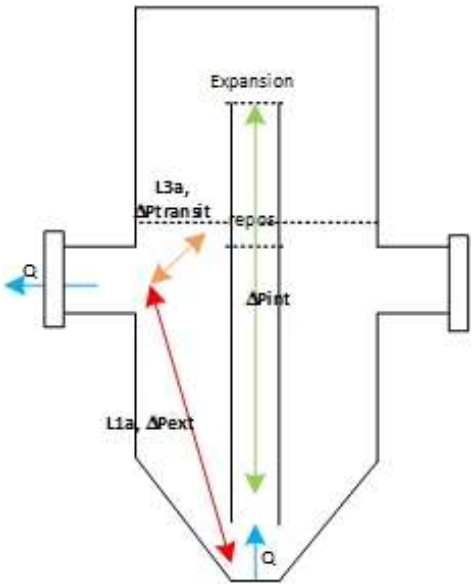

Figure A. 6 Distances parcourues par le gaz

Les distances L_{1a} et L_{3a} (Figure A. 6) représentent les hypoténuses de deux triangles, donc ils sont calculés en utilisant le théorème de Pythagore.

$$L_{1a} = \left(\frac{D_{ce}}{2}^2 + HS^2\right)^{0,5} \qquad \text{(A. 31)}$$

$$L_{1a} = \left(\frac{D_{ce}}{2}^2 + (Z_{mf} - HS)^2\right)^{0,5} \qquad \text{(A. 32)}$$

- Calcul de A_{ext}, U_1 et U_3

$$A_{ext} = \frac{\pi}{4}\left(D_{CE}^2 - D_{CI}^2\right) \qquad \text{(A. 33)}$$

$$U_1 = \frac{Q_1}{A_{ext}} \qquad \text{(A. 34)}$$

$$U_3 = \frac{Q_2}{A_{ext}} \qquad \text{(A. 35)}$$

Calcul du diamètre de la sortie

$$A_S = \frac{Q_{sortie}}{U_{sortie}} \qquad \text{(A. 36)}$$

$$Ds = \left(\frac{4A_s}{\pi}\right)^{0,5} \qquad \text{(A. 37)}$$

Application numérique

Le calcul a été réalisé en utilisant Python, et est présenté en dessous

```
@author: azaa3101
"""
import sympy as sp
from math import pi
#%% Données
dp = 1.5*10**(-4)                #diamètre des particules (m)
rhof = 1.316                     #masse volumique du gaz en (kg.m-3)
rhos = 1300                      #masse volumique du solide en (kg.m-3)
muf = 1.147*10**(-5)             #viscosité du gaz en (kg·m−1·s−1)
g = 9.8                          #m.s-2
nu = g*(rhos-rhof)
e = 0.4                          #porosité
s = 1                            #sphéricité
Qtot = 1.66*10**-3               #débit volumique total (m3/s)
Qint = 0.25*Qtot                 #débit volumique dans le cylindre interne (m3/s)
Qext = Qtot-Qint                 #débit volumique dans le cylindre interne (m3/s)
#%%Calcul de la vitesse minimale de fluidisation
emin=0.586*(s**(-0.72))*((muf**2/(rhof*nu*dp**3))**0.029)*((rhof/rhos)**0.021)
Ar = (rhof*nu*(dp**3))/(muf**2)          # nombre adimensionnel Archimède
B = (150*(1-emin))/((s**2)*(emin**3))
A = 1.75/(s*(emin**3))
Rminf = sp.symbols("Rminf")              # nombre adimensionnel Reynolds au minf
eq = sp.Eq(Ar, A*Rminf**2+ B*Rminf)
Rminf = sp.solve(eq,Rminf)
Uminf = (Rminf[1]*muf)/(dp*rhof)         # vitesse minimale de fluidisation
print('Uminf=',Uminf, 'm/s')
```

#%%Calcul de la vitesse maximale de fluidisation

```
f = 0.44                                    #régime turbulent
Ut = (4/3)*dp*(nu/rhof)*(1/f)
print('Ut=',Ut, 'm/s')
```

#%%Choix de la vitesse du gaz

```
U0= 4*Uminf          #régime de bullage observé a une vitesse 3 ou 4 fois la vitesse de fluidisation
```

#%%Calcul du diamètre du cylindre interne

```
Aci = Qint/U0
Dci = ((4*Aci)/pi)**0.5
print('Dci=',Dci*100, 'cm')
```

#%%Calcul de la hauteur du cylindre interne

```
W=1
Zminf= W/(Aci*(1-emin)*rhos)
HL=Zminf          #la hauteur de la phase dense du lit est presque égale à la hauteur au minimum de fluidisation
db = (0.54*((U0-Uminf)**0.4)*(HL+4*((0.0000551)**0.5)))/(g**0.2)
Ub = U0-Uminf+0.711*(g*(db))**0.5
TDH=0.22*Ub**2
HCI=HL+(TDH/2)       #la hauteur du cylindre interne doit être inférieure à HL+TDH
print('HCI=',100*HCI,'cm')
```

#%%Choix de HTS et HS

```
HTS = 0.01
HS=(HCI+HTS)/2
print('HS=',HS*100,'cm')
```

#%%Calcul de la perte de charge dans le cylindre interne

```
deltaPint=Zminf*(150*((1-emin)**2/emin**3)*((muf*Uminf)/(s*dp)**2)+1.75*((1-emin)/emin**3)*((rhof*(Uminf**2))/(s*dp)))
print('DeltaPinter=',deltaPint)
```

#%%Calcul des pertes de charges extérieure et de transit

```
Dce = 0.2
```

```
Aext=(pi/4)*(Dce**2-Dci**2)

U1 = Qext/Aext

U3 = Qint/Aext

L1= (((Dce**2)/2)+HS**2)**0.5

L3= (((Dce**2)/2)+(Zminf-HS)**2)**0.5

deltaPtransit=L3*(150*((1-emin)**2/emin**3)*((muf*U3)/(s*dp)**2)+1.75*((1-
emin)/emin**3)*((rhof*(U3**2))/(s*dp)))

deltaPext=L1*(150*((1-emin)**2/emin**3)*((muf*U1)/(s*dp)**2)+1.75*((1-
emin)/emin**3)*((rhof*(U1**2))/(s*dp)))

print('DeltaPext=',deltaPext)

print('DeltaPinter+DeltaPtransit=',deltaPint+deltaPtransit)
```

#%%Calcul du diamètre de la sortie

```
Qs=Qtot

Us= 2

As=Qs/Us

Ds=(4*As/pi)**0.5

print('Ds=',Ds*100,'cm')
```

#%%fin du programme.

ANNEXE B

ANNEXE B PROTOCOLE DE LA RÉACTION

B.1. Préparation de la réaction

Taches	Faite
Porter les EPI	
Placer le catalyseur dans le réacteur	
Fermer la grande bride à l'aide d'une barre dynamométrique (il faut appliquer un couple de 250 livres-pieds pour pouvoir atteindre l'étanchéité à 1,5 atm)	

B.2. Inspection des fuites avec N_2 et mise en marche pour la période de chauffage sous atmosphère inerte

Taches	Faite
Brancher les câbles dans les prises de courant et allumer le panneau central ainsi que le panneau NFC	
Activer la section d'alimentation et d'acquisition de données pour le montage des NFC	
S'assurer que la bonbonne de N_2 à l'extérieur est ouverte	
S'assurer que les vannes pneumatiques à l'extérieur sont actionnées par l'air comprimé	
Définir la consigne du débit de N_2 dans le débit mètre massique du N_2 (D3)	
Ouvrir les valves d'alimentation de N_2 (V-3 et V_s-16) V_s-16 : c'est la vanne dans la ligne de N_2 qui vient du montage de pyrolyse	
Ouvrir les vannes : V-12, V-15 et V-15' (ou V-16 et V-16'), V-19	
S'assurer que les valves suivantes sont fermées : V-7 à V-11 (vannes d'impulsion), V-13, V-14, V-16 et V-16' (ou V-15 et V-15'), V-17 et V-18 (vannes du bypass du bain de glycol) , et celles venant du montage du reformeur et du pyrolyseur connectés au bain de glycol	
Démarrer le D3 de N_2 avec la consigne choisie	
Fermer V-19 et attendre quelques minutes le temps que la pression augmente dans le système (22 psig max) **NB** : la pression indiquée dans le lecteur sur le panneau est en psig	

Maintenir le système quelques temps	
Vérifier avec le snoop partout où il y'a des jonctions, s'il y'a des fuites dans l'installation. Colmater les fuites le cas échéant **NB** : ces étapes précédentes doivent être faites la veille du test, le lendemain matin, il faut venir tôt au labo pour commencer le chauffage et lancer le test (voir étapes suivantes).	
Enclencher la mise en route des bandes chauffantes (définir les consignes de température dans le panneau)	
Démarrer l'acquisition sur l'ordinateur dans la salle du GC	

B.3. Opération en régime permanent avec les réactifs

Taches	Faite
Vérifier les consignes de température et de pression, une fois la température de consigne est atteinte, suivre les étapes suivantes	
Vérifier la pression dans les bonbonnes des gaz régulièrement	
Vérifier si les bonbonnes de l'extérieur sont ouvertes et que les valves pneumatiques sont actionnées	
Vérifier que la valve est ouverte du côté droit (et non pas du côté gauche qui est le côté du méthane)	
Vérifier que c'est bien le gaz H_2 qui est alimenté et il faut diminuer la pression de sortie car le détendeur de gaz est conçu pour le C_2H_4 et non pas le H_2 **NB** : les bonbonnes de H_2 et de C_2H_4 sont connectées toutes à la ligne du C_2H_4, donc durant l'activation il faut ouvrir juste les bonbonnes de H_2 et s'assurer que les bonbonnes de C_2H_4 sont fermées, et durant la réaction ça sera le contraire.	
Définir la consigne de débit de N_2 dans le débit mètre massique du N_2 (D3)	
Définir la consigne de débit de H_2 dans le débit mètre massique (D2) **NB** : ne pas oublier de changer le type de gaz alimenté dans basic configuration du débitmètre pour le H_2.	
Ouvrir la vanne d'alimentation de H_2, V-02	
Démarrer D2 avec la consigne choisie	
Laisser le catalyseur s'activer durant le temps voulu	
À la fin de l'activation, fermer V-02, arrêter D2 et laisser seulement le N_2 jusqu'à atteindre la T de réaction si elle est différente de la T d'activation	

Une fois la T de réaction est atteinte, entamer la réaction en suivant les étapes suivantes	
Changer le type de gaz alimenté dans D2 du H_2 au C_2H_4, ensuite fermer la bonbonne de H_2 et ouvrir celle de C_2H_4	
Alimenter les gaz réactifs en suivant les étapes suivantes	
Définir la consigne de débit de CO_2 dans le débit mètre massique du CO_2 (D1)	
Définir la consigne de débit de C_2H_4 dans le débit mètre massique du C_2H_4 (D2)	
Ouvrir les valves d'alimentation des gaz réactifs V-01, V-02	
Démarrer D1, D2 avec les consignes choisies	
Prendre régulièrement les mesures de température et de pressions affichées sur le panneau (si l'acquisition électronique sur l'ordinateur ne marche pas)	
Faire les impulsions avec le N_2 chaque 15 minutes	
Vérifier régulièrement la perte de pression dans le réacteur (Pi-2 – Pi-1) **NB** : si la pression Pi-2 dépasse 22 psig, arrêter immédiatement.	
Vérifier souvent les fuites avec le détecteur mobile	
Vérifier régulièrement la perte de pression dans le filtre (Pi-4 – Pi-3) si elle augmente, il faut faire décharge du filtre en suivant les étapes suivantes	
Ouvrir V-07 pour remplir le vérin, ensuite fermer-la	
Ouvrir V-13	
Ouvrir V-08	
Changer la direction de V-07 vers le filtre pour faire des impulsions dans la première chandelle **NB** : pour chaque chandelle, refaire cette démarche au moins 3 fois, pour s'assurer que tout le gâteau soit délogé.	
Fermer V-08 et V-07	
Répéter la procédure pour les trois autres chandelles	
Faire un échantillonnage dans le point P1 chaque 10 minutes, et injecter dans le GC	
À chaque échantillonnage, mesurer le débit volumique mesuré par le totalisateur	

B.4. Fin des tests et mise au repos

Taches	Faite
Arrêter l'alimentation des gaz réactifs (CO_2 et C_2H_4) en mettant toutes les consignes à zéro (D1, D2) et en fermant les valves V-01 et V-02	
Arrêter le chauffage	
Laisser seulement le N_2 s'écouler jusqu'à ce que tout le gaz réactif soit évacué (il faut faire des injections gaz dans le GC jusqu'à ce que le résultat donne 0 de H_2)	
Après refroidissement, suivez le protocole de nettoyage et de vidange	

ANNEXE C

ANNEXE C PROTOCOLE DE NETTOYAGE ET DE VIDANGE

Tache	Description
  	Collecter les outils nécessaires et les mettre tous dans le cubicule(Sac ziploc, Tie-wrap, Clés, Pince, Tige, Spatule, Carton). Porter les EPI (couvre chaussures/Tyvek ou sarrau/gants)
  	Enlever toute la laine de quartz qui couvre le top du réacteur et la sortie aussi. La mettre dans le carton prévu pour ça
 	Enlever la partie femelle du connecteur du thermocouple
 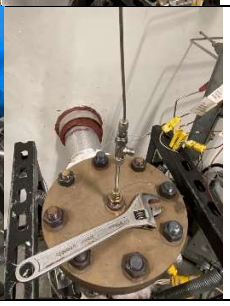	Enlever le connecteur de la gauge de pression

	Ouvrir le réacteur à l'aide d'une clé dynamométrique. Ne jamais utiliser le drill électrique, soit pour fermer ou pour ouvrir. Demander l'aide au besoin.
 	Mettre les boulons et les écrous dans le contenant. Enlever la bride et le joint d'étanchéité et les mettre sur le contenant aussi comme montré dans les photos.
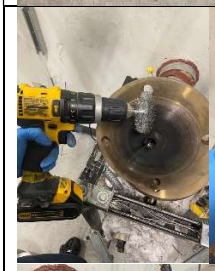    	Nettoyer bien les brides des 2 cotés.3

	Une fois le réacteur est ouvert, il faut porter l'adducteur d'air
 	S'il y'a du carbone accumulé à la sortie, utiliser un marteau et une tige pour le défaire
 	Utiliser l'aspirateur pour aspirer le catalyseur
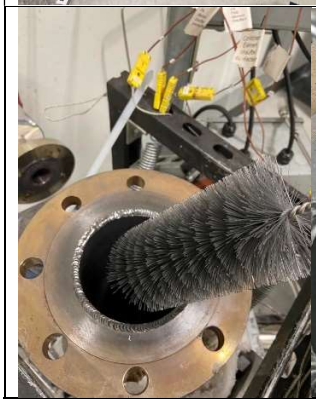 	Utiliser la brosse pour nettoyer les parois du réacteur

 	S’assurer que le réacteur est bien vidé et bien nettoyé (utiliser à plusieurs reprise l’aspirateur jusqu’à être sûr qu’il n’en reste rien). Ouvrir ensuite la sortie.
    	Mettre des sacs ziploc autour des brides pour éviter que le carbone tombe par terre. Faire des impulsions dans le filtre (sans ouvrir la valve entre le filtre et le réservoir) pourque le carbone résiduel dans les tuyaux tombe dans le sac ziploc. S’assurer que tout le carbone est récupéré dans les sacs, ensuite les enlever. (étape*)
 	Utiliser l’aspirateur pour aspirer ce qui reste dans le tuyau de la sortie

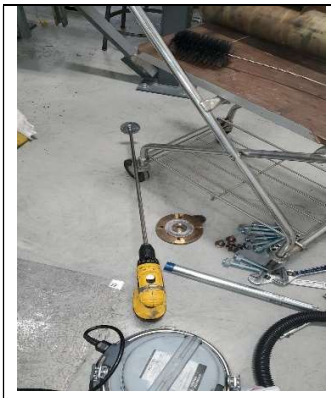	Ouvrir les tuyaux vertical de l'autre côté dans la salle d'ensachage, et utiliser la brosse avec les sections détachables pour le nettoyer complètement avant refermer le tout.
  	Ouvrir l'aspirateur pour récupérer le mélange de catalyseur+carbone qui a été aspiré

 	Prendre l'aspirateur et récupérer le catalyseur+carbone sur le filtre HEPA bleu dans la salle du four (ne pas oublier de partir l'aspiration du filtre)
	Préparer l'aspirateur pour le prochain test en installant un nouveau sac
	Transvider le sac d'aspirateur dans un sac ziploc, y rajouter le carbone récupéré dans les deux sacs ziploc utilisée dans l'étape (*). Peser-le. Noter la masse.

	Faire la décharge du filtre en suivant les étapes dans le protocole de réaction
	Les sacs et les tie-wrap sont au-dessous de l'évier en face au filtre. Transvider le carbone dans un petit sac ziploc
     	Prendre des échantillons du carbone récupéré du réacteur et celui récupéré du filtre. Il faut bien les identifier. Les mettre dans un sac et les collecter tous dans le carton à côté du filtre bleu. Après 3 tests (dans 2 semaines) on fera la caractérisation de 6 échantillons de carbone et 3 échantillons de catalyseur.